Analysis of the timing of deformation, porphyroblast growth and metamorphic conditions in the Lukmanier Pass area, Switzerland

Implications for the origin of metamorphism in the Central Alps

Msc Thesis
Joep Kiers

Supervisors:
Prof. dr. Martyn R. Drury, Dr. Herman van Roermund, Dr. Oliver Plümper

January 2013

Department of Structural Geology and Tectonics
Faculty of Geosciences
Utrecht University

Universiteit Utrecht

Cover picture: figure of P58b-16 post-D2 M3 kyanite crystals on top of a cleavage domain in plain polarized light (ppl).

TABLE OF CONTENTS

1. Abstract

The Lukmanier Pass area is situated in the centre of the Penninic domain in the central Alps. This domain consists of crystalline basement and Mesozoic sedimentary units. These sediments have gone through complementary geodynamic processes, although there are regional heterogeneities observed. The complexity of the area can be visualized in a PT(t) path for the rock units in the area. The peak metamorphic pressure conditions are related to subduction of the margins of micro-continent Adria beneath the distal margins of the European crust. This is followed by continued exhumation of the Alpine orogen due to continental collision and nappe stacking. The blueschist-eclogite pressure dominated areas related to subduction (with phengite, glaucophane, carpholite and lawsonite) were later truncated by a Barrovian-type setting (with almandine, staurolite, kyanite and muscovite) related to orogenic build-up. In a final stage this setting was overprinted by a late stage heating event characterized by Buchan-type metamorphism (kyanite, ilmenite, muscovite and oligoclase porphyroblasts). The aim of this study is to analyse the mineralogical composition of P58b metapelitic samples in a Mesozoic sedimentary succession and link them to observed deformation phases in the central Alps. A PT(t) path was modelled based on EMP analyses and optical microscopy. The role of fluids in the rocks is also briefly mentioned, as fluids are an important medium in many geological processes. Since the metapelitic rocks contain many fluid-rich minerals, a water saturated system is assumed.

Our samples P58b were collected during a 4-day fieldtrip in the Lukmanier Pass area and are studied in the lab at the Earth Sciences institute at Utrecht University. They were analysed using optical microscopy for microstructural relationships, X-ray fluorescence (XRF) for bulk rock composition and EMP to acquire compositional information. The data obtained was processed to create P-T pseudosections to indicate mineral stability fields over a range of 0 - 20 kbar and 500 – 1000 K. This was done using thermodynamic software like Perple_X (Connolly, 2005). These results are compared by using the TheriakDomino software developed by De Capitani (1994 a.o.). Thereafter, a practical approach is used to calculate stable mineral assemblages. Geothermobarometry was applied to several mineral clusters to obtain PT relationships.

The metapelitic chemical bulk rock composition is relatively rich in Na, Fe and Al. The main porphyroblasts observed are almandine, ilmenite, kyanite, staurolite, muscovite and oligoclase. Inside the matrix, minerals like paragonite, biotite and chlorite indicated the enrichment in sodium and iron. Minor phases as magnetite, rutile and tourmaline are present in small volume-percentages. The garnet porphyroblasts showed a slightly chemical zonation. Microstructural relationships between the minerals and deformation phases showed a progressive development towards a higher metamorphic grade. The rocks underwent multiple deformation phases. According to the microstructural relationships, a late stage heating event would have influenced the region.

The rocks show Barrovian-type metamorphism under greenschist facies conditions, indicated by a stable mineral assemblage of almandine, ilmenite, muscovite, chlorite and kyanite. Towards peak metamorphic pressures at 10-12 kbar, amphibolite facies minerals like almandine, staurolite, kyanite and muscovite form a stable mineral assemblage. Isothermal retrograde metamorphism was subsequently followed by a Buchan-type late stage heating event which heated the rocks ≈ 100 ^{o}C up to 650-680 ^{o}C. This heating caused porphyroblasts

of oligoclase, ilmenite, kyanite and muscovite to grow which do not show any signs of deformation. In terms of geodynamics, this late stage heating event is most likely caused by a combination of geodynamical processes. Slab break-off at depth seems a viable mechanism to account for the relatively rapid rise in temperature, combined with accretion of large crustal masses with radiogenic heat production, like the Lepontine dome. However, regional influences increase the complexity of the area and more quantitative research is recommended to explain the evolution in the central Alps at Lukmanier Pass.

2. Introduction

The Alpine Orogeny is a complex mountain belt which is formed on the continent Europe by collision of the former European mainland and the Adria micro-continent north of paleo-Africa (fig. 2.1). Ongoing debate about the precise paleographic orientation of the (micro)-continents involved increases the complexity of the current tectonic setting (Wortmann et al., 2001, Pfiffner, 2010, e.o.). On the basis of extensive fieldwork and modeling studies an accepted subdivision of the Alpine orogeny is made (fig. 2.2). This subdivision is chiefly based on the stacking of different nappes on top of each other. The sliding horizons over which the movement has taken place are décollement zones like Triassic evaporites (Pfiffner, 2010). Classical structural domains, or nappe structures, which are distinguished from each other, are the (i) Helvetic-Dauphinois domain, (ii) Penninic zone, (iii) Austroalpine zone and (iv) Southalpine zone.

This study focuses on the area of the Lukmanier Pass, Ticino, Switzerland (fig. 2.2) located in the Penninic zone of the Alps. The area can roughly be subdivided into three main units called the Gotthard Massif, Mesozoic cover of the Gotthard Massif and Lucomagno Massif. In the north and west of the pass pre-Mesozoic rocks of the Gotthard Massif crop out (fig. 2.3). These rocks are influenced by Hercynian intrusives. Towards the south the Mesozoic cover rocks of the Gotthard Massif are heavily folded by several (pre-)Alpine deformational phases. The Mesozoic sediments are bound to the south by the Lucomagno Massif which thrusted over the pre-Hercynian crystalline basement. The Lucomagno nappe consists of pre-Mesozoic metamorphosed sediments and igneous rocks (Chadwick, 1968). A detailed description of the units will be outlined in chapter 3. Rock samples have been collected during a 1-day fieldtrip in 2005 to the Lukmanier Pass-area. The Mesozoic cover of the Gotthard Massif had special interest. The rocks are entirely of sedimentary origin and range from Lower Triassic (≈ 250 Ma) to Aalenian Middle Jurassic (≈ 170 Ma) (Chadwick, 1968). In the cover, the Liassic Inferno and Stgir Series contain metapelitic schists with well-developed porphyroblasts. A complete description of the Series is given in chapter 3.

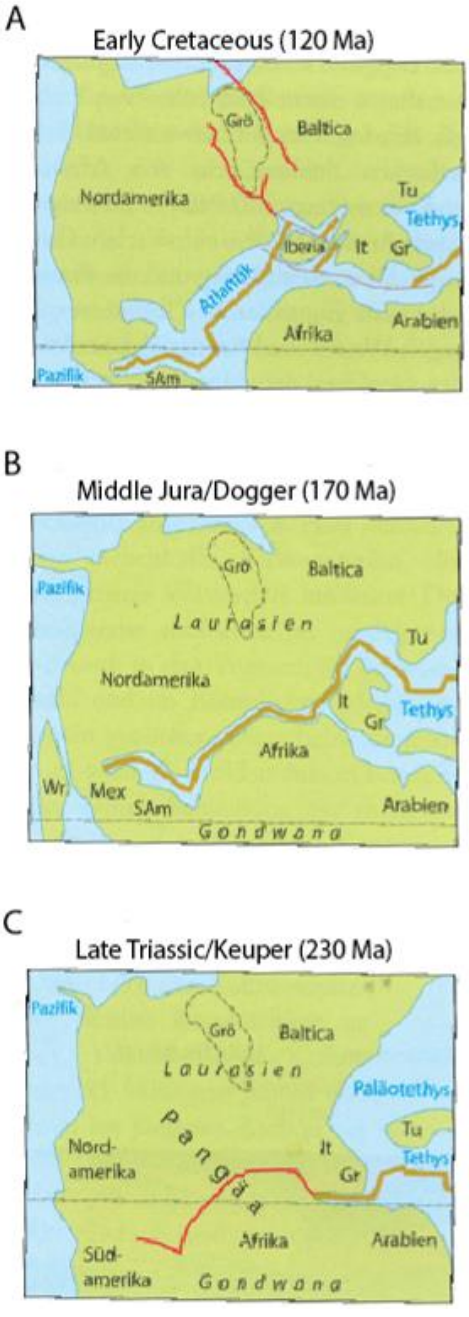

Figure 2.1. Plate reconstruction focused on the break-up of Pangea in three stages. A) Formation of Central Atlantic and drift of Africa from America, formation of Iberia and connection of Atlantic with Tethys. B) Development of rift throughout Pangea, closure of the Paleotethys and rift formation between Laurasia and Italy-Greece. C) Rift formation from Tethys ontwards, initial closure of Paleotethys. Grö: Greenland, It: Italy, Gr: Greece, Tu: Turkey, Sam: South-America, Wr: Wrangellia, Mex: Mexico. Modified from: Pfiffner, (2010).

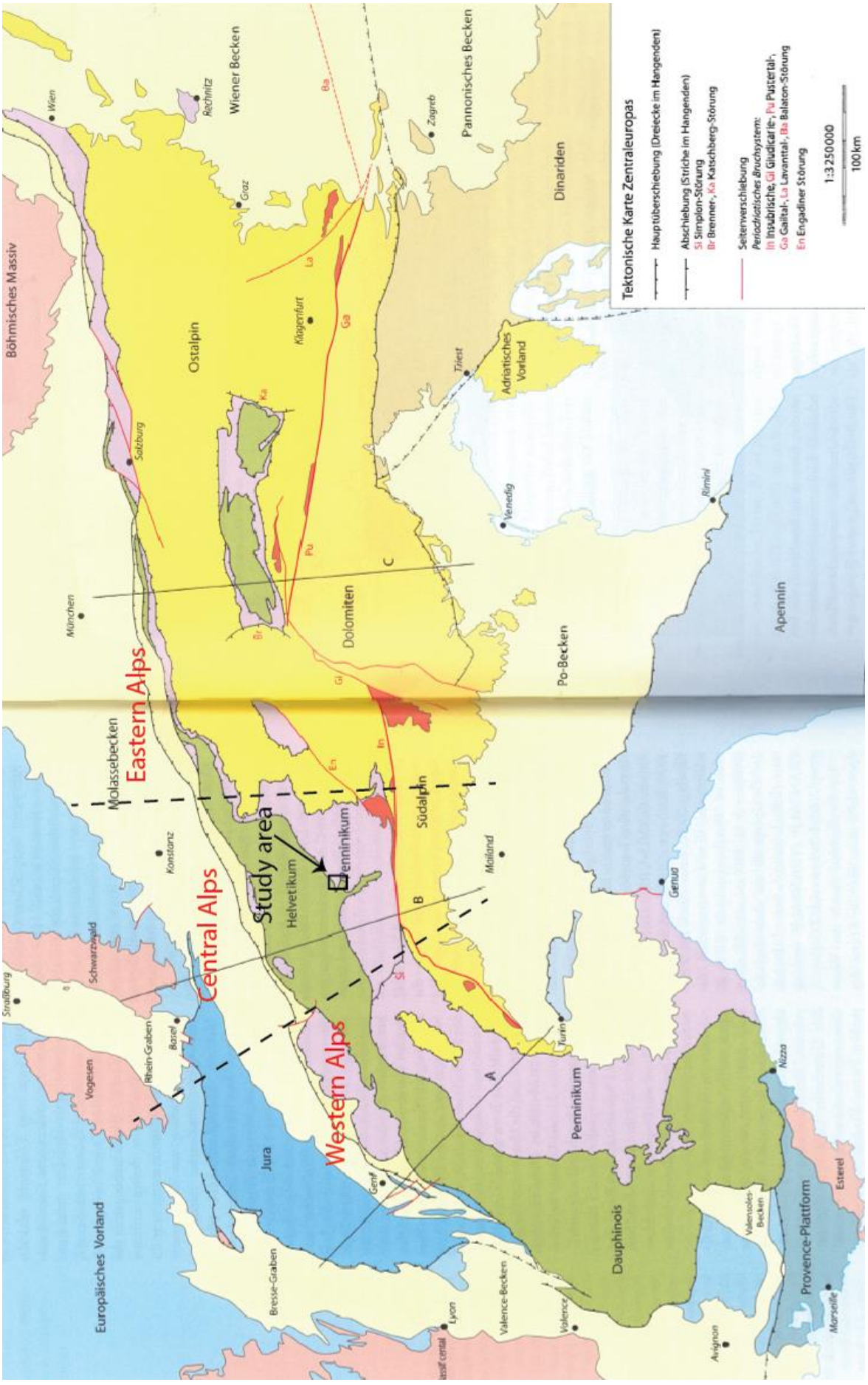

Figure 2.2. Tectonic map of the Alpine orogeny Main units are the Helvetic-Dauphinois domain, the Penninic zone, the Southalpine zone and the Eastalpine zone. The black box indicates the area of study. Modified after Pfiffner (2005).

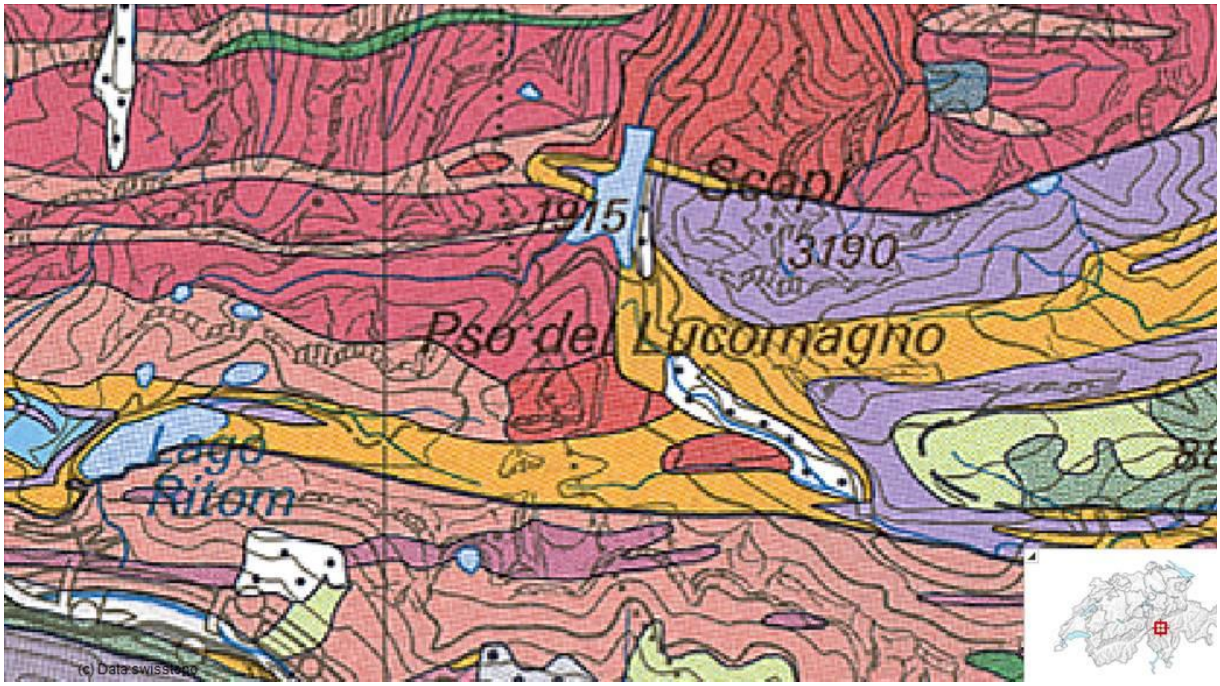

Figure 2.3. Geological map of the Lukmanier Pass area. dark green: amphibolites; blue: diorites Middle to Late Carboniferous; purple: Liassic cover rocks including Coroi, Inferno and Stgir Series; red: granites, granodiorites, Middle to Late Carboniferous; orange: Triassic cover rocks; pinkish: gneissic and schistose sediments; dotted white: moraine and rubble. From: Swiss Topo, ETH.

The metamorphic grade of the Lukmanier area increases towards the south. Just east of the pass lower grade blasts like zoisite, albite and muscovite are found, whereas more south in the direction of the Lucomagno nappe the presence of garnet, kyanite and staurolite blasts are common. The first part of this study is focused on the timing and growth of the mineral assemblage of the metapelitic schists. Main questions here are 1) the timing of growth of kyanite crystals and 2) to describe the mineral assemblage of the rock. Shortly, a brief analysis will be made on the influence of fluids present in the rocks. Do fluids influence the growth of minerals in particular, e.g. is the presence of fluids significant for the amount or composition of the minerals that grow. The fluids in this study are assumed to be water without CO_2. The main reason for this assumption is the presence of many fluid-rich minerals which devolatized at higher metamorphic grade and hence oversaturates the rocks in water.

The Penninic zone of the Alps was influenced by Eoalpine high-pressure metamorphism between 40 – 30 Ma due to subduction of multiple oceanic domains (Wiederkehr et al., 2008 a.o.). The high pressure peak was subsequently followed by a late stage heating at medium-pressure high-temperature conditions (e.g. Borghi et al., 1996; Brouwer, 2000; Brouwer et al., 2002 e.o.). Effects of the late stage heating, classically called the Lepontine overprint, can be recognized in the mineral composition of investigated rock samples. Some striking characteristics are observed in the late-growing minerals. The second part of this study tries to observe this late stage heating which could possibly be linked to a change in geodynamic setting.

The main aim of this MSc thesis is to reconstruct a pressure-temperature-time path for pelitic rocks in the Lukmanier Pass area. This is performed by analysis of bulk rock compositions of collected samples in combination with chemical analysis using the electron microprobe

(EMP). The EMP mineral chemical composition and chemical zoning of the porphyroblasts are used as geothermobarometers to resolve their P-T conditions of formation. Chemical analysis of minerals that grow post-deformational should resolve the question whether the rocks have undergone a late stage heating event or not. The analysis of P-T paths is mainly done using the Perple_X software developed by James Connolly at the ETH Zürich. This software is powerful in calculating PT-pseudosections to highlight the compositional and mineralogical variation with pressure and temperature of minerals and calculate their stability fields.

Subsequently, a thermodynamic reference frame is also build with TheriakDomino software developed by de Capitani, 1994. This program is comparable to Perple_X, except there exist differences in thermodynamic data and hence stability of minerals at certain pressure and temperature. Variation in stability influences the results. The main focus will however be Perple_X.

A second reference frame is made using P-T paths of Alpine retro-eclogite localities and the study of Wiederkehr et al. (2008) in the north-eastern section of the Lepontine Dome. The occurrence in the area makes the eclogites comparable to our own study. Studies of Spalla et al. (1996) and Bocchio et al. (1985) concentrate on eclogite lenses which have been exhumed in the central Alps around the Alpe Arami peridotite body. The metamorphic evolution of these high-pressure eclogites towards the surface gives insight in the regional tectonic evolution of the area, and hence their retrograde path could possibly be used as a comparison to our schists.

The conditions of the rock through geological time will briefly be analysed and possible geodynamic settings discussed. This will be done in a qualitative way. Several models have been proposed throughout the years to explain the late stage heating event observed in the Central Alps. These models include slab detachment and upwelling of the underlying hot lithosphere (Davies and Von Blanckenburg, 1995; Wortel and Spakman, 2000; Van de Zedde and Wortel, 2001), thermal evolution of wedged crustal material underlying the Central Alps, called tectonically accreted radiogenic material (TARM) as a cause of Barrovian high temperature-medium pressure metamorphism (Jamieson et al., 1998), orogenic collapse of the Alpine Orogeny (Platt, 1986; Ballèvre et al., 1990) and a heat pulse due to post-orogenic intrusions (Engi et al., 1995 e.o.). Finally some recommendations for future work will be *addressed* to give a better understanding and insight in the evolution of the Lukmanier area.

3. Geological setting

Some geological background is important to understand the geodynamical processes active during the evolution of the Alpine orogeny. In the first part an overview of the global paleogeography is given. Throughout geological time the main focus moves towards the pre-Alpine geography regarding the Tethys Ocean and the adjacent continents. Finally a description of the local geology in the Lukmanier Pass area is given. The main geological units are described and the location of rock P58b is presented.

3.1 History of the Alpine orogeny

The Alpine orogenic event that is observed nowadays consists of several mountain ranges in Europe, Asia and India, like the Himalayas, Pyrenees, Zagros, Alborz, Carpathians, Apennine and Alps. They were formed during the Late Cretaceous and are - mostly – still active in the Cenozoic. However, the first evidence which would lead to the Alpine orogenic event started in the Late Carboniferous as the Hercynian orogenic event. In the Late Carboniferous, all continental material from Laurasia and Gondwanaland had collided to form a great complex mountain belt which crossed the length of a new supercontinent, called Pangea (Rodgers, 1988). In the late Triassic Keuper FM (ca. 230 Ma) Pangea fell apart along a rift structure which formed a weak zone in the continent (fig 2.1C). This rift zone initiated in an arm in the west of the Tethys Ocean and developed between the continental masses of Arabia and Greece-Italy (Pfiffner, 2010) towards the Pacific in the west. Over time this rift developed throughout the continent of Pangea towards the west, to divide Africa and South America from North America. In the east, the developed spreading zone ceased south of Greece-Italy and divided Italy from Laurasia in the Dogger era around 170 Ma. In the Early Cretaceous the spreading zone was offset by several transform faults with a dextral movement direction (fig 2.1B). The main fault developed into the Mid-Atlantic Ridge and several small pieces caused the opening of smaller oceans like the Piemonte-Ligurian Ocean and Penninic Ocean which are connected by transform faults (Pfiffner, 2010).
In the Late Cretaceous, the spreading ridge divided North America from Eurasia around 140 Ma (fig 2.1A). The associated transform faults caused division of Iberia from Europe and the pre-African Adria plate. Wortmann et al. (2001) described the plate tectonic setting quite accurately, but debate is ongoing about the exact geometry of the continents and oceans at the Jurassic-Cretaceous boundary (Wortmann et al., 2001, Hauck, 1998, Stampfli, a.o.). Two small micro-continents are diverted from Iberia towards the North-West by the dextral movement along a transform fault. These micro-continents are Corsica-Sardinia and Briançonnais, which will eventually collide into one larger micro-continent (fig 3.1). To the Northwest of this micro-continent lies a continental margin which develops into the Valais through and separates the continent from the Eurasian mainland. Discussions exist about actual oceanic crust formation in the Valais trough or just continental margin sediment infill. Since some research claims to have found pillow basalts in the basin (Jamieson et al., 1998 a.o.), an oceanic evolution is likely. The precise location of the Briançonnais micro-continent has also been a topic of debate. Hauck (1998) obtained a paleopole from the Rhenodanubian Supergroup which is considered part of the micro-continent (Hesse, 1973, 1974). The latitude from this paleopole is interpreted to be south of the micro-continents of Corsica-Sardinia and the Valais trough.

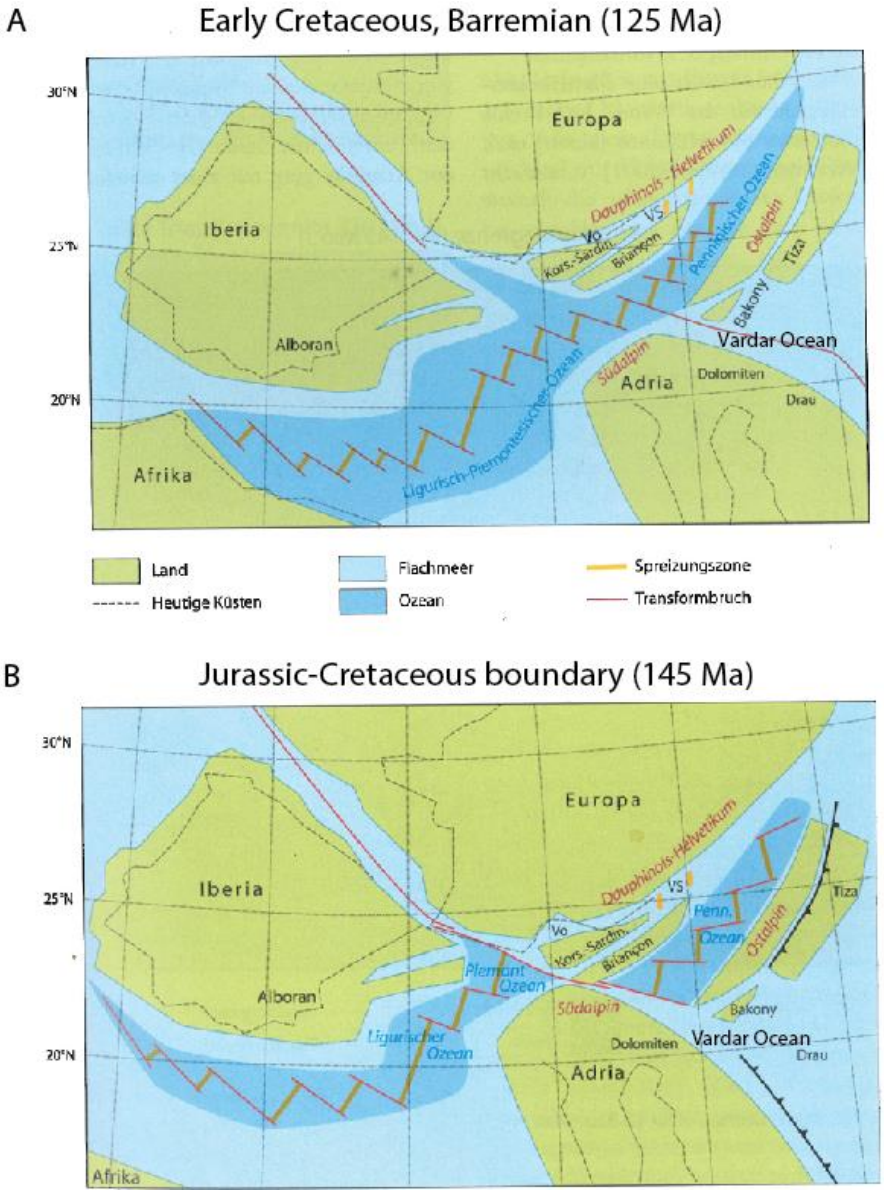

Figure 3.1. Pre-Alpine plate reconstructions. A) *The Piemonte-Ligurian ocean evolves and connects with the Penninic Ocean to form one spreading ridge. The Southern and Eastern Alps also align with each other. Modified after Wortmann et al., (2001).* B) *The Piemonte- and Ligurian Ocean divide the Iberian Peninsula from the Adria indenter. The Vocontian-through divides the European mainland from Corsica-Sardinia and the Valais-through separates Europe from the Briançonnais micro-continent. The Penninic Ocean separates the Eastern Alps from the micro-continents and the European mainland.*

To the southwest of the Penninic Ocean lies the Austroalpine micro-continent (fig 3.1B). This continent is considered to be different from the Southern Alps on the Adria continent due to the differences in rotation. The Austroalpine micro-continent rotates clockwise (Channell et al., 1990) relative to the Southern Alpine domain on Adria. However, their similar sedimentary successions and geochemical Middle Triassic volcanics give them a comparable origin. Therefore, the Vardar Ocean is placed between the two micro-continents (Wortmann et al., 2001) to account for the differences in rotation. This ocean should however converge

and close before the onset of the volcanics of the Middle Triassic. The switch from a relative southeast directed movement of Adria relative to Europe changed in the Early Cretaceous in a northeasterly direction. This was partly due to the onset of seafloor spreading in the North Atlantic Ocean (Wortmann, 2001; Rodgers, 1988 a.o.). As a consequence, the more translational motions between Europe, Iberia and Adria changed to a more rotational movement. This results ultimately into the compression between the continents and hence subduction of the intermediate oceans.

The Vardar Ocean was gradually subducted beneath the northeastward moving Adria micro-continent (Wortmann, 2001; fig 3.1A). After subduction, the contact between the Southern Alpine domain and Austroalpine domain changed to a more transpressional fault system in the Adria-Austroalpine transform fault (fig 3.1A). This compression leads to the onset of subduction of the Penninic Ocean beneath the Austroalpine margin. This agrees with the Mid-Cretaceous subduction along the Austroalpine margin (e.g., Schmid, 1973, Trümphy, 1992). More towards the west the Piemonte-Ligurian Ocean and the Penninic Ocean are coupled via a sinistral transform fault which is the continuation of the same fault that divides the Austroalpine from the Southern Alpine domain on Adria. Eventually the Ligurian Ocean would subduct beneath Iberia in the Late Cretaceous and cause a roll back system which transports it towards the African margin (Dewey et al., 1989). The Penninic Ocean is also subducted beneath the Austroalpine block (Adria) during the Late Cretaceous which caused a hard collision with the Briançonnais micro-continent. The Valais Through is closed in the Eocene around ± 43.2 Ma (Rubatto et al., 1997) when the Briançonnais/Adria continent collided with the European continent.

The arcuate shape of the Alps (fig. 2.2) is caused by an oblique collision of the Adria indenter and the European mainland. Recent measurements by Tesauro et al., 2005, of the movements of the plates indicate that the southern margin of the Alps is moving with 1.2 millimeter per year towards the NNW and the northern part only with 0.7 millimeter per year. This means that the Alpine orogeny is still evolving and it shortens with roughly 0.5 millimeter per year in a NNW-SSE direction.

The Alps can be subdivided into three main units (fig. 2.2). The Western Alps contain the French Alps and continue roughly towards the line Bern-Milan, but there is no hard limit dividing them. The Central Alps have a boundary in the east with the Eastern Alps which follows roughly the line St. Margrethen-Chur-Sondrio (Pfiffner, 2009). This subdivision is however of inferior importance to the subdivision in paleographic domains.

The Helvetic Zone. This part of the Alps forms the outer most northerly and westerly domains of the Alps and is covered with Mesozoic sediments which are deposited on the European continental margin. It is also referred to as the outer most margins of the Alps and lies south/southeast adjacent to the European foreland. This area is mainly reactivated by tectonic inversion due to the collision of Adria with the European mainland. The most important change in the domain since the Tertiary was the transition from a thin-skinned section (affected only overlying sediments) into a thick-skinned thrust system (included underlying basement) with Triassic evaporite gliding planes (Spalla et al., 1996). The sediments found in this part include platform carbonates and marls in the more distal regions (Maxelon et al., 2005). The most southerly located marls are referred to as Ultrahelvetic. In France, the Helvetics are also named Dauphinois Zone.

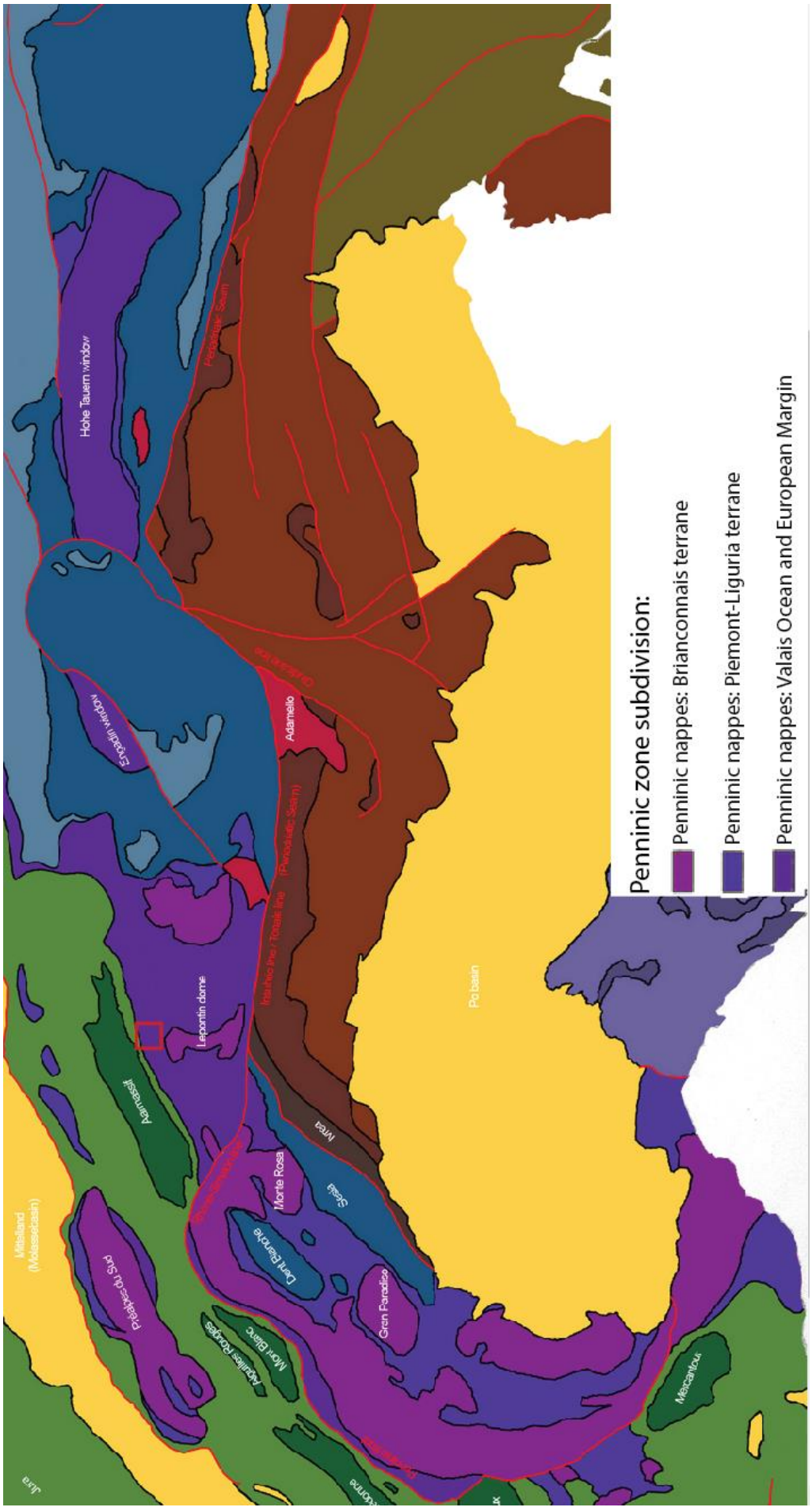

Figure 3.2. Overview of the Penninic zone with the three subdivisions North, Middle and South. The red box indicates the working area at the Lukmanier Pass.

The Penninic Zone. These rocks are more internally located (more towards the south and east compared to the Helvetics) and their associated sediments are deposited in the distal realm between the European mainland and Adria. It consists of ophiolites from the sutured Tethys Ocean and intensely deformed Mesozoic sediments from the continental margins of both continents. Gneissic material present belonged to the former Briançonnais micro-continent which is located in between these realms. A threefold division is in classical literature also named North, Middle and South Penninic and can be geographically related to the Valais Through, Briançonnais micro-continent and Piemonte-Ligurian Ocean (fig. 3.2).

The Austroalpine Zone. This zone is composed of the former Austroalpine continent southeast of the Penninic Ocean. It is geographically oriented southeast of the main orogenic belt. Parts of the zone are slid on top of the Penninic system and eroded away. Only small remnants are nowadays present (called: klippen) in the more central parts of the Penninic zone. In the current Alpine geometry the Austroalpine units crop out mostly in the Eastern Alps in eastern-Switzerland and Austria.

The Southalpine Zone. This zone is divided from the Eastern Alps by the Periadriatic Line which strikes roughly east-west across the Alps with components like the Insubric Line and the Pustertal transform fault (fig 3.2). The Southalpine zone is composed of material from the micro-continent Adria together with material of the Africa-paleocontinent. Their amalgamation was established before a hard collision with the European mainland took place. It evolved in the final stages of the Alpine orogenic setting during the Neogene as a thick-skinned thrust system, where basement (e.g. continental material) and Mesozoic cover sediments are involved and thrusted over the underlying Helvetic, Penninic and Austroalpine structures (fig. 3.5). Due to this late deformation the Southalpine zone shows only a weak Alpine overprint compared to the Penninic and Austroalpine domains (Pfiffner, 2010).

The focus of this study lies in the Penninic Zone (fig 3.2). This zone can be subdivided in Lower and Upper Penninic units as proposed by Milnes (1974b) on the basis of paleogeographical orientation. The Upper Penninic units would represent the rocks north of the Valais zone and are gradually changing into the Ultrahelvetic units. The Lower Penninic units encompass everything south of the Valais Ocean, which represents material derived from the Briançonnais micro-continent. The outline of the study area at Lukmanier Pass is indicated in figure 3.2 as a red square box.

3.2 Local geology

The Lukmanier pass area comprises three distinct geological domains. Petrologically and paleogeographically it is subdivided into the Gotthard Massif, the Mesozoic cover of the Gotthard Massif and the Lukmanier Massif in the Penninic domain of the central Alps (fig. 3.3). A detailed map of the area modified from Chadwick, 1968 can be found in figure 3.4.

3.2.1 The Gotthard Massif

The northern boundary of the Lukmanier area is part of the Ultrahelvetic domain. It formed part of the European lower crust before it was significantly reworked during subsequent orogenic events (Pfiffner, 2010). The Gotthard Massif itself is roughly 100 km long and 10 km wide and is separated by the Mesozoic sedimentary rocks of the Urseren-Garvera zone from the crystalline Aar Massif and the Tavetscher Zwischen Massif to the north (Chadwick, 1968; fig J). In Lukmanier the rocks of the Massif can be divided into three different units:

(a) pre-Hercynian quartzo-feldspathic gneisses; (b) pre-Hercynian para- and mixed gneisses and (c) intrusive Hercynian granitics.

The pre-Hercynian quartzo-feldspathic gneiss (a) is characterized by K-feldspar augen and a greyish striped exterior. The name Streifengneiss is more commonly used in the area for these crystalline gneisses. Radiometric dating of zircons with the uranium-lead dating method gives ages of about 500 m.y. (Grünenfelder, 1962). This suggests emplacement of the intrusion in Cambrian or earlier times. The streifengneiss crops out mainly directly west of the Lukmanier Pass and can be followed to the west towards the Gotthard Pass (fig. 3.4).

Rocks which show a similar origin but have a different orientation are the pre-Hercynian para- and mixed gneisses (b). They occur along strike with the Gotthard Massif and consist of different zones: the Tremola zone, Borel zone and Tenelin zone. Each zone itself contains thin parallel units of para- and mixed gneisses. They are found in between the Streifengneiss west of Lukmanier Pass and are bound to the south by the Mesozoic rocks in the Valle del Lucomagno and Val Piora (Chadwick, 1968; fig 3.4). Age determination was performed by Grünenfelder and others (1964) for zircons some 20 km northwest of Lukmanier with uranium-lead dating. This resulted in ages of 514, 600 and 932 m.y. These gneisses are, like the Streifengneiss, intensely folded during the Hercynian orogenic event (Labhart, 2005).
During the Hercynian orogenic event (≈ 380 – 280 Ma) not only the older Streifengneiss and

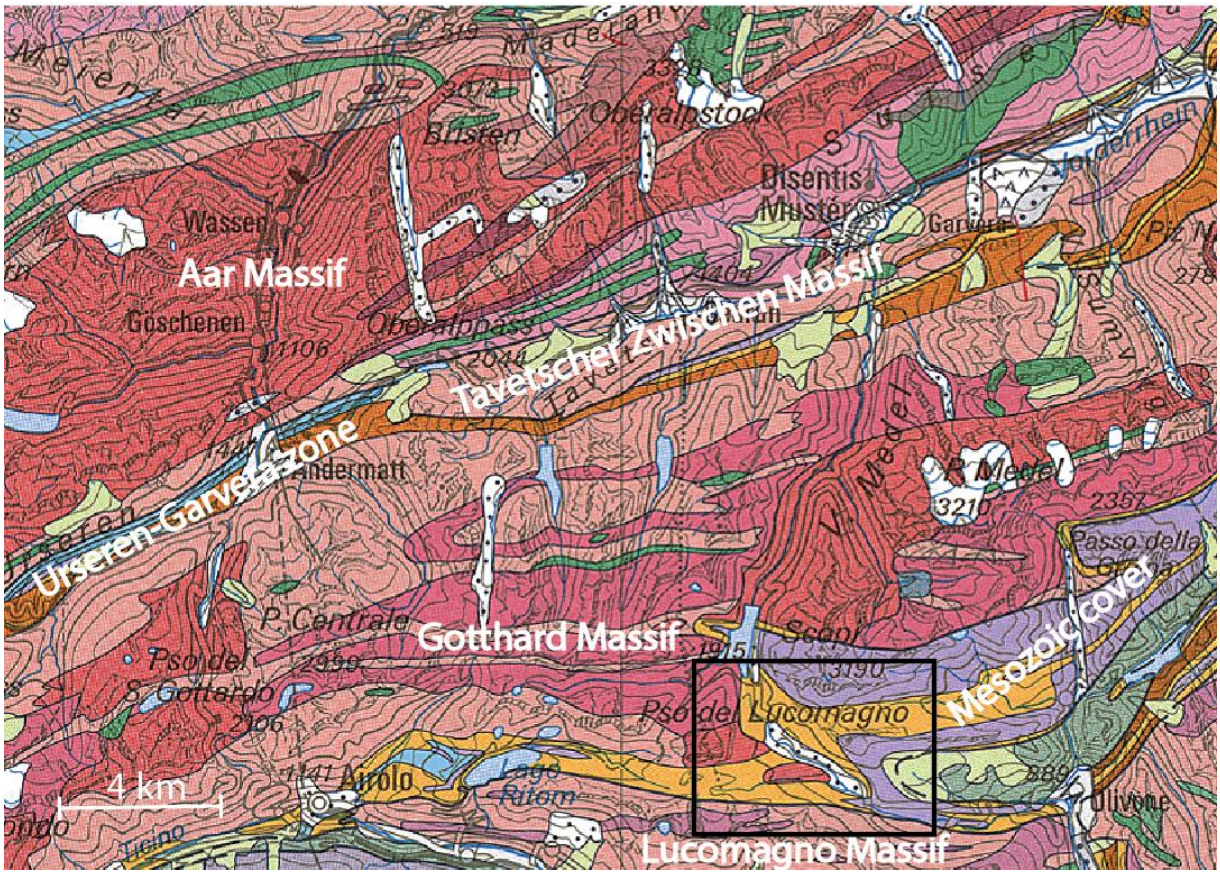

Figure 3.3. Overview of the regional geology of the Lukmanier Pass (indicated with Pso del Lucomagno). Working area is indicated as a square box. Fig 3.1. is a magnification of the box. Note the location of the different domains with the Gotthard Massif in the north-west, the Mesozoic cover in the north-east and the Lucomagno Massif in the south of the working area.

para- and mixed gneisses are heavily folded but two varieties of igneous rocks were intruded. The Cristallina granodiorite and the Medelser porphyritic granite crop out northeast of Lukmanier Pass and in the northern half of Val Piora south of the Pass. The Hercynian age has been confirmed by research of Grünenfelder (1962) who found zircon ages of 290 to 340 m.y. for the Medelser granite just north of Lukmanier Pass. Age dating of the Cristallina granodiorite at Acquacalda resulted in ages of 305 m.y. (Grünenfelder, 1962).

3.2.2 The Mesozoic cover of the Gotthard Massif

The Mesozoic rocks are originally cover rocks of the Ultrahelvetic Gotthard Massif and are bound to the south by the Pennine nappe complex, especially the rocks of the Lucomagno Massif. In the area the rocks have a sedimentary origin and have an age range from Lower Triassic (≈ 250 Ma) to Aalenian Middle Jurassic (≈ 170 Ma) (Chadwick, 1968). Most of the sedimentary cover crops out south and west of the Lukmanier Pass and is folded into synclines and anticlines by the Cenozoic Alpine deformation. Their bulk rock composition is calcareous meta-pelitic. A striking feature is the presence of many large aluminium-rich porphyroblasts like staurolite, garnet and aluminosilicates. Samples analysed for this paper contain over 30% of alumina by weight, which is confirmed by a study of Fox (1975).

The total sedimentary column is influenced by intense folding, faulting and erosion in the area. The Mesozoic cover has a thickness of roughly 1500 m in the Scopi region near the pass (Chadwick, 1968) but is less thick in other areas. An extensive description of the sedimentary column is presented by Baumer (1964) and Jung (1963). Study of the Mesozoic cover rocks was challenging during fieldwork due to the vast extent of grass, shrubs, trees and lichens. A large extent of the sedimentary rocks were covered with a 2-5 m thick soil layer which disabled further investigation of underlying Mesozoic sediment. The rocks can roughly be subdivided into five series, from which two are of Triassic - and three of Jurassic age.

The lowest unit is the Triassic Dolomite Series, which lies discordantly on top of the Gotthard Formation. Most of the rock is heavily weathered to a greyish massive rock or does contain many potholes due to dissolution via acidic rainwater. A variety of the massive dolomite is a honeycombed dolomite breccia known as rauhwacke (Chadwick, 1968). Most of the dolomites form an alteration with gypum-rich layers. Their origin is debatable but a post deformational origin is most likely due to the in situ brecciation and lack of schistosity or banding (Brückner, 1941; Leine and Egeler, 1962). The Dolomites are mostly found on the roadside from the Lukmanier Pass towards Olivone and form the core of the Val di Campo anticline. Moreover, it seems to figure as an Alpine décollement zone of the overthrusting Lucomagno nappe since it can be found adjacent to the nappe contacts in the Val Piora.

The Dolomite Series give way to an Upper Triassic formation called the Quartenschiefer, named after a village in the Helvetic nappes. These rocks consist of green micaceous schists with alternating bands of white quartzites (Chadwick, 1968). In the Valle del Lucomagno the Quartenschiefer contains nicely developed garnetiferous hornblendegarbenschiefer in which garnets have sizes up to several cm.

Conformably Lower Liassic rocks are found on top of the Triassic Series which are called Stgir Series. The Stgir has a very variable composition with alternating bands of black siliceous schists, grey quartzites and green chlorite-rich quartzites in the top of the sequence (Chadwick, 1968). The aluminium content in the rocks is concentrated in porphyroblasts of zoisite and plagioclase in the northern half near the Pass. Towards the south, where the Alpine

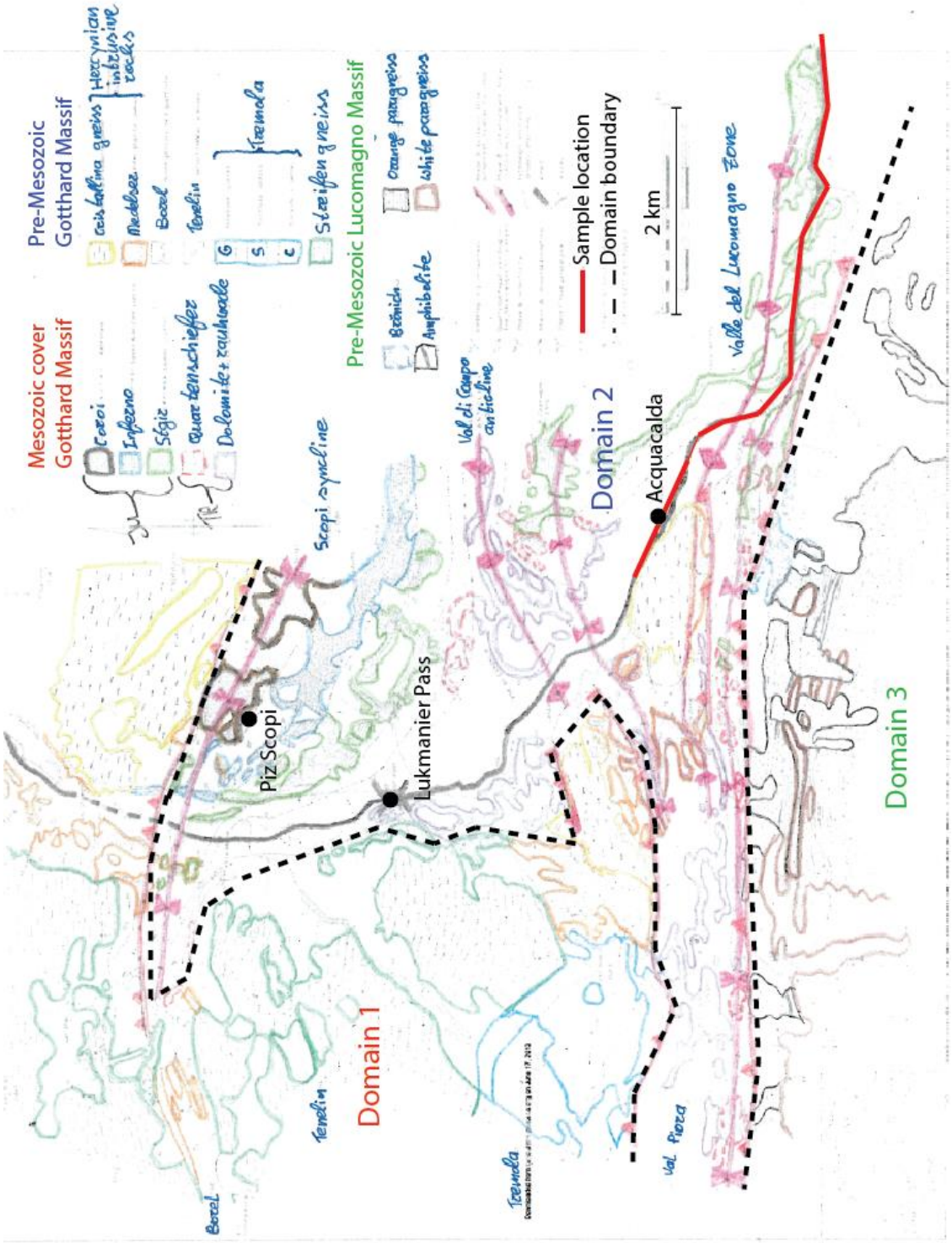

Figure 3.4. *Reconstruction of the local geology near Lukmanier Pass (indicated with the pass-sign in the centre of the figure). The colour codes of the domains correspond with the colours of the rock types at the upper right legend. Modified after Chadwick (1968).*

metamorphic grade in the area is higher, zoisite is replaced by garnet. The rocks studied in this research are mostly derived from the higher grade Stgir series around Acquacalda (fig. 3.4).

Directly on top of the Stgir Series follows the Inferno Series which have Middle to Upper Liassic (≈ 190-170 Ma) ages. These rocks are characterized by thin alternating grey limestones and black calcareous schists. Some porphyroblasts of plagioclase and zoisite are found in the lower grade rocks near Lukmanier Pass. The Inferno Series is only found in the southern flank of the Scopi synclinal zone and is eroded away in the southern half near Valle del Lucomagno and in the Val die Campo anticline (fig. 3.4).

The youngest Jurassic Series is believed to be of Aalenian age (174-170 Ma). The most common rocks are black siliceous schists. The formation itself is not very thick and only crops out in the upper half of the Scopi syncline at Piz Scopi (fig. 3.4).

3.3.3 THE LUCOMAGNO MASSIF

In the Lukmanier Pass area this Massif is mainly made of schists and gneisses which are bound to the south by the Penninic system and to the north by the Mesozoic sediments covering the Gotthard Massif. The schists and gneisses originate from sediments and igneous rocks. After field analysis of lithology they can be divided into four different groups described below.

1) The Brönich Group contains black graphitic paraschists with garnets and kyanite. Bossard (1929) suggested a Carboniferous origin due to the presence of extensive amounts of graphite.

2) The Orange Group of Gneisses occur in the eastern part of the nappe and consist mainly of garnitiferous banded paragneisses which weathers orange-brown (Chadwick, 1968).

3) Amphibolites occur in the Orange group of gneisses and contain mainly Tourmaline, biotite, epidote and quartz and

4) the White Group of Gneisses occurs in the western part of the area and contains microcline, plagioclase and micas (fig 3.4). They are compositionally similar to the Medelser granite in the Gotthard Massif, but do not contain feldspar augen Chadwick, 1968; fig 3.4).

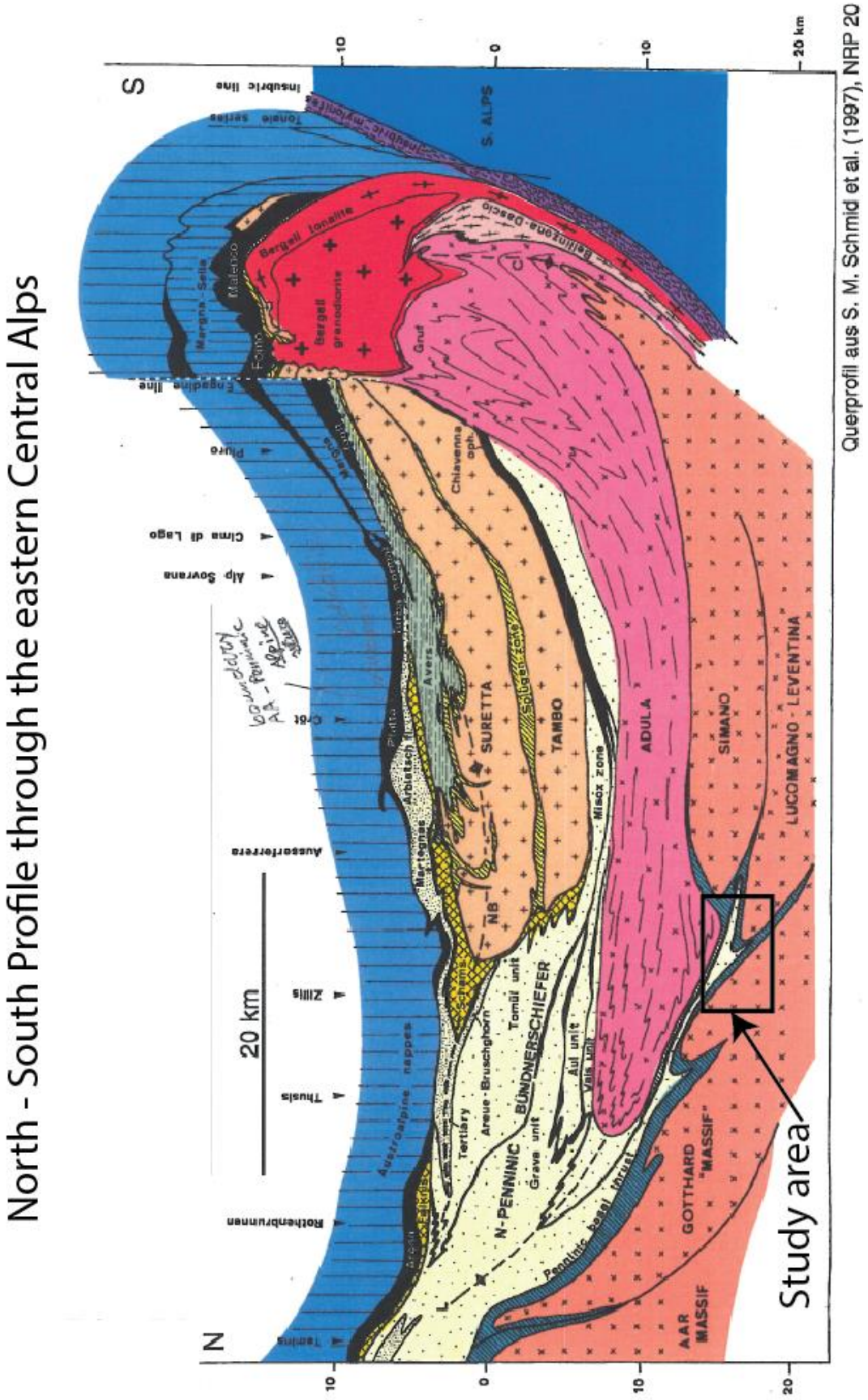

Figure 3.5 *N-S cross section through the eastern Central Alps. Black box indicates the crystalline basement rocks and overlying sediments in the Lukmanier Pass area. Crystalline basement slabs are thrusted on top of each other.*

4. Materials and methods

The following section describes the methods used in this study to acquire data. A fieldwork was combined with optical- and electron imaging by using apparatus present at the University of Utrecht. Secondly, the acquired data is analyzed by using thermodynamic-based programs in a theoretical way and on a more practical basis.

4.1 Data acquisition

4.1.1 Fieldwork Lukmanier Pass

12 samples were collected in the area near the Lukmanier Pass by me during a 4-day visit to the area in 2013. These rocks are however not used in this study, but show complementary mineral assemblages. The ones used for this study are all collected during earlier work in 2005 performed by the University Utrecht for the Utrecht Geosciences departments teaching collection. These rocks were sampled along the road crossing the Lukmanier Pass towards Campra (fig 3.1). The rock samples have volumes up to 50 cm^3 after sawing (fig. 4.1). Investigated thin sections are named P58b-5, P58b-8 (fig. 5.1.1; 5.1.2), P58b-11, P58b-12, P58b-16 and P58b-19, which are selected from a set of 22 sections. They are randomly cut sections of rock P58b with roughly the same mineralogical content and bulk rock composition. Precise location of the samples is unknown.

4.1.2 Optical microscopy

Thin sections of the samples are made for optical mineralogical and (micro)structural analysis. Rocks with a distinct mineral lineation and foliation are cut perpendicular to the foliation and parallel to the lineation. A Leica Leitz optical microscope with magnifications of the objective lens up to 63 times and 10 times magnification for the ocular was used for analysis. Pictures of minerals in plain polarized light (ppl) and cross polarized light (xpl) were made using a Leica La90PSO optical microscope.

4.1.3 Electron microscopy

A JEOL JXA8600N Superprobe is used for the determination of the major element oxides in the observed minerals in thin sections. Thin sections are coated with a carbon layer in order to disable charging. Point scans are analysed with the Energy Dispersive Spectrometry (EDS) for quick identification of minerals and Wavelength Dispersive Spectrometry (WDS) for high resolution chemical analysis of line scans. The electrons have an acceleration voltage of 15 kV and a beam current of 20 nA.

4.1.4 Scanning electron microscope (SEM)

Microstructural and chemical analysis of the samples was performed on carbon coated thin sections using a JEOL JCM-6000 NeoScope Benchtop SEM (fig. 4.2) with a thermionic electron gun. Backscattered electrons were imaged and energy dispersive X-ray analysis (EDS) was done using an accelerating voltage of 15kV. Thin sections from sample P58b were investigated using this apparatus.

4.1.5 X-ray fluorescence (XRF)

At first the samples are ground to a powder with a grainsize of <73 μm. Modified with a lithium iodine hydrate the samples are heated to temperatures above 1100^o C and cooled in a pearl-shape. Before XRF analysis, corrections for the organic matter and presence of fluids

are made. A Leco TGA701 from the Geosciences department was used for this analysis. The bulk rock composition of the samples was subsequently analyzed using an ARL 9400 WD-XRF at Utrecht University. Sample JK1-P58b was selected for this study (see section 7.1 *Bulk rock composition*).

4.2 Data analysis

4.2.1 PERPLE_X SOFTWARE

Perple_X 6.6.6 is a program package developed by Connolly (2009) at the ETH Zürich. The program is able to create and display phase diagrams. It uses the bulk rock chemical composition JK1-P58b from sample P58b and assumes chemical equilibrium throughout the sample. From a thermodynamic database (Holland and Powell, 1998) parameters are extracted for analysis. The default solution_model.dat and perplex_option.dat data files are used for calculations. Newest updates and help-files can be found on James Connolly personal website of Perple_X: http://www.perplex.ethz.ch/.

4.2.2 THERIAKDOMINO

TheriakDomino (TD) is a software package written by de Capitani (2004) and de Capitani and Petrakakis (2010) to calculate equilibrium assemblages and equilibrium phase diagrams (pseudosections). The basic assumptions of TD are not different from the Perple_X software.

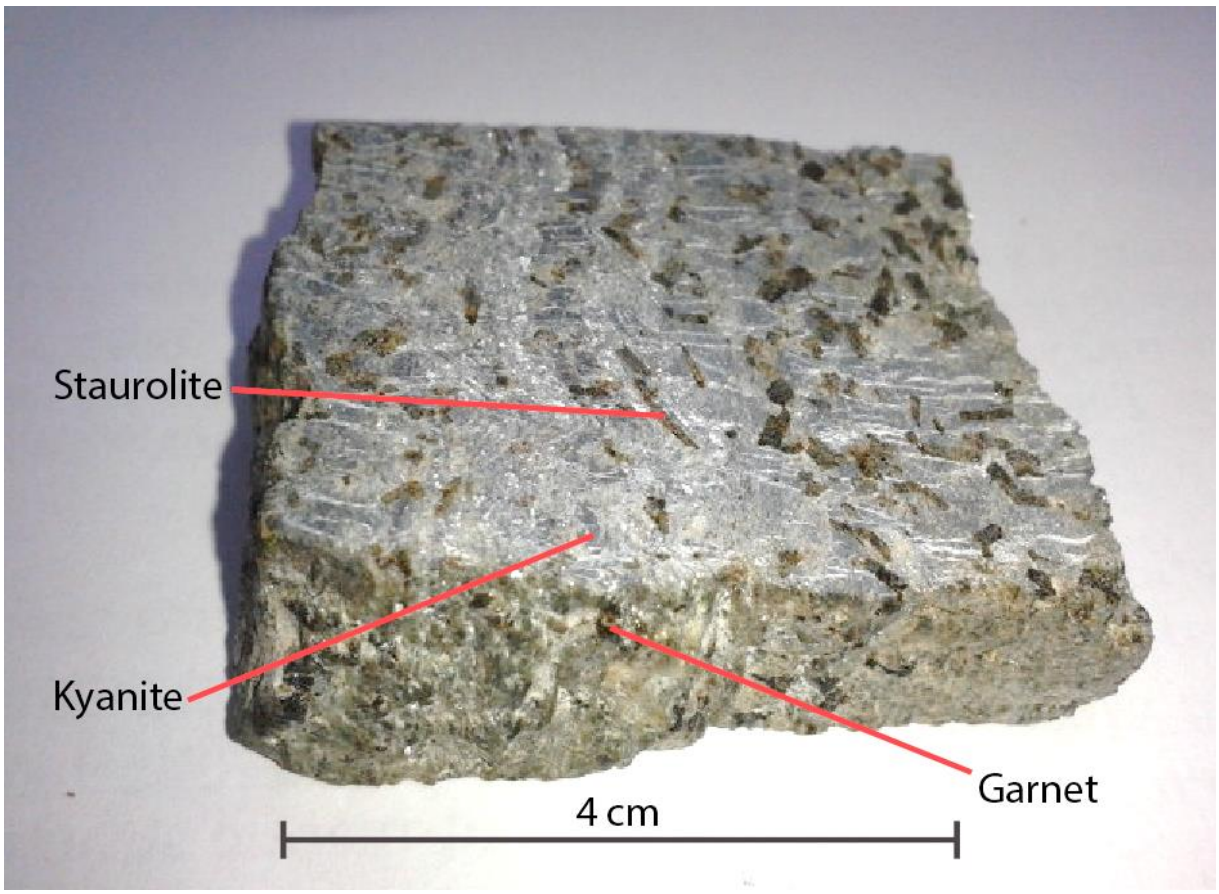

Figure 4.1. Photo of sawn hand sample P58b used for this study. Note the main porphyroblasts which can be observed and the wavy crenulation cleavage in the matrix.

There exist, however, differences in the thermodynamic data files which are used in the programmes. In this study TD is used as a brief check on the data plotted with Perple_X performed on bulk rock composition JK1-P58b.

4.2.3 GEOTHERMOBAROMETRY

Geothermometers and geobarometers are used to compare the results of the theoretical thermodynamic-based studies as Perple_X and TheriakDomino with a more classical practical method. Multiple geothermobarometers based on the minerals present in P58b are used to indicate equilibrium growth conditions of mineral assemblages in the rock. Performed analyses on the samples is indicated in chapter 7.

Figure 4.2. The JEOL JCM-6000 NeoScope Benchtop SEM used for analyses of thin sections P58b.

5. Petrological and microstructural relationships

The metapelitic schist P58b from the Lukmanier Pass area is studied with a Leica optical microscope using 30µm thick thin sections. All thin sections except for P58b-5 show a well-developed crenulation cleavage and different porphyroblasts. In the following section a description of the matrix and each porphyroblast is given and a microstructural relationship with the deformational phases is inferred.

5.1 Matrix

The 'sedimentary' groundmass of the metapelite is fairly homogeneous with a grainsize on µm-scale. Minerals that can be found in the matrix are paragonite, quartz and biotite (fig. 5.1A;B). Especially paragonite and biotite did have many nuclei to develop since they comprise up to 80% of the matrix material. Alignment of the S_0 'sedimentary' minerals under increasing metamorphic grade is the schistosity of the rock, which is first foliation observed, F_1 (fig. 5.1A;B). This first foliation F_1 is influenced by a second deformation phase that deformed the rock and developed a second foliation, F_2 (fig. 5.2). This thin section can be seen in cross polarized light (xpl) in figure 5.3. The foliation is well-developed but still

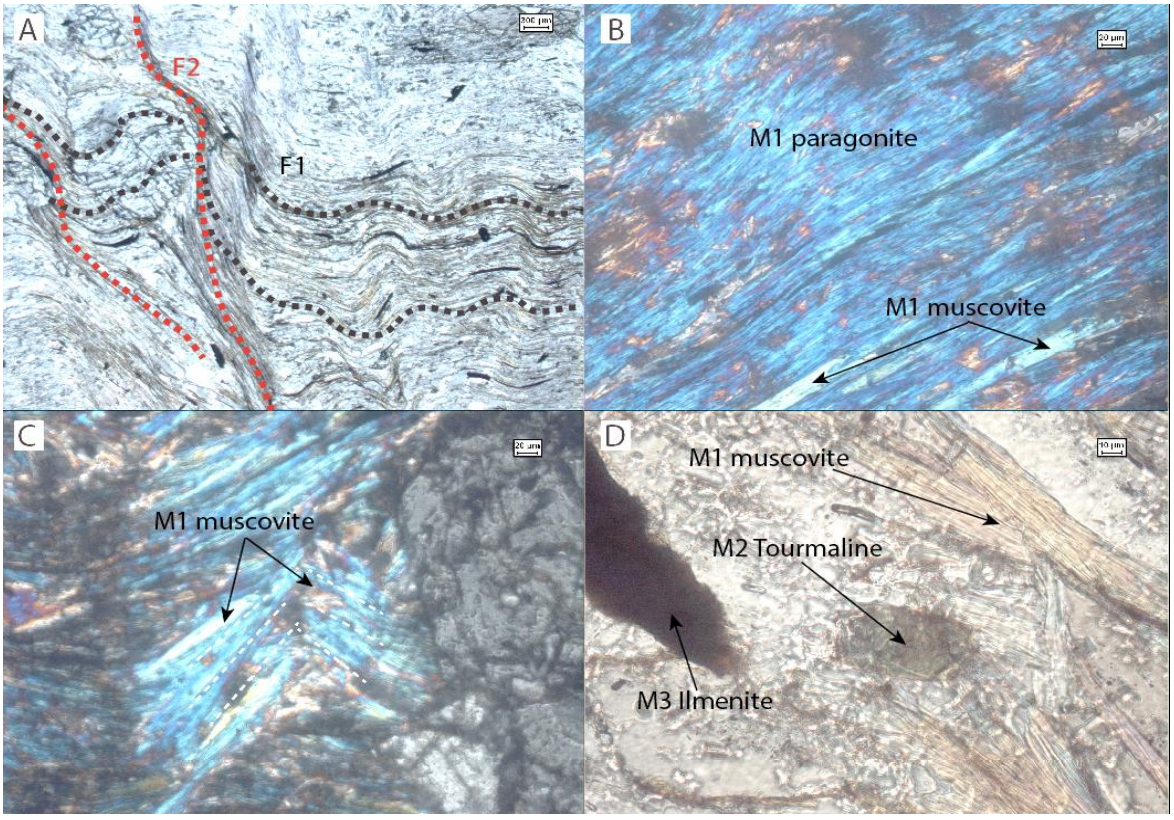

Figure 5.1. (A) *P58b-16 Matrix (ppl) showing the relationship of a garnet porphyroblast with matrix including biotite, white mica and quartz crystals. The crenulation of the former F_1 cleavage can clearly be seen, which develops into cleavage domains and microlithons, F_2.* (B) *High magnification of very fine grained M1 paragonite and M1 muscovite in matrix (xpl).* (C) *Polygonal arc structure (xpl) inside microlithons at the hinges of F_2 cleavage domains. Note that M1 micas have an oblique orientation with each other which will eventually form a new cleavage.* (D) *Tourmaline mineral inside the matrix (ppl). The crystal is parallel to matrix F_2 but unaffected by any younger deformation and/or metamorphism stages.*

incipient and not penetrative yet. The F_2 crenulation cleavage overall runs parallel to subparallel, but is not continuous throughout the observed thin sections. The matrix minerals align with each other and develop a spaced crenulation cleavage. The cleavage domains are smooth and they comprise of roughly 20-50% of the foliation. A discreet transition exists between the cleavage domains and the microlithons in which the cleavage domains have a parallel spatial relation. This relation changes to anastomosing in the presence of porphyroblasts. However, the microlithons and cleavage domains are not yet fully developed in the vicinity of porphyroblasts (fig. 5.2; fig. 5.3 and section 14.3.1-3). Therefore, porphyroblasts do not always put aside the F_2 crenulation cleavage. On occasion the cleavage domains break perpendicular to staurolite porphyroblasts which are oriented parallel to the F_1 foliation. The quartz grains are on average larger than the quartz inclusions observed in the porphyroblasts. Grains of quartz and align in the F_2 microlithons and in the strain shadows at the tails of some garnets.

Interpretation P58b matrix observations
The metamorphic field name of the rock is schist. The fine grained schistose matrix of the mineral consists of Al-rich minerals and Si-rich phases. When these phases are subjected to significant temperature and pressure the complementary phases align with each other to form F_2 cleavage domains and microlithons. The cleavage domains are in metapelitic rocks usually rich in mica and minerals as ilmenite, graphite, rutile, apatite and zircon (Passchier and Trouw, 2005). Ilmenite is another major phase that is observed in the matrix. Minor amounts of graphite and rutile are observed with the optical microscope and apatite and zircon are detected using the electron microprobe. The presence of paragonite in the matrix indicates a relative high amount of Na in the bulk rock composition.

This can for example be caused by the influence of fluids which bring salts to the rock, or the presence of acidic igneous rocks in the area. Since in the Lukmanier Pass area several pre-Alpine granitic/gneissic complexes are present, this is a valid reason. As described by Guidotti (1968b), paragonite is a stable mineral in low-grade metamorphic rocks when the bulk rock composition is aluminium-rich. This is the case in the investigated samples (fig. 9.3). Porphyroblasts which are relatively rich in Na nucleate in prograde or retrograde stages on top of paragonite crystals. The formation of this spaced crenulation cleavage can be related to several deformation phases to which the rock has been subjected. Dynamic recrystallisation during a second deformation phase, S_2, of the mica grains could have formed the F_2 crenulation cleavage.

Deformed lattice crystals of old grains are overgrown by strain-free nuclei which form the new secondary foliation on the expense of the deformed grains. Recrystallisation of minerals is related to reequilibration of the chemical composition of minerals in the rock to the metamorphic conditions of cleavage formation (e.g. Williams et al., 2001). The actual progressive formation of the spaced foliations is related to the mobility of the atoms related to stress. Durney (1972) published a mineral sequence of decreasing mobility by solution transfer: calcite > quartz > feldspar > chlorite > biotite > muscovite > opaques. Hence, under progressive increasing temperature and pressure minerals as quartz and feldspar accumulate in the fold hinges, whereas micas dissolve in the hinge and accumulates in the limbs. These phenomena can be observed by the growth of new mica grains at the limbs forming the cleavage domains. These grains will align and especially in microfolds will show a sharp contrast in angle with each other. The presence of these polygonal arcs (fig. 5.1C) of mica grains in the microlithons indicates that an increase in temperature is observed during growth and the F_1 foliation is deformed into a younger F_2 foliation (Passchier and Trouw, 2005).

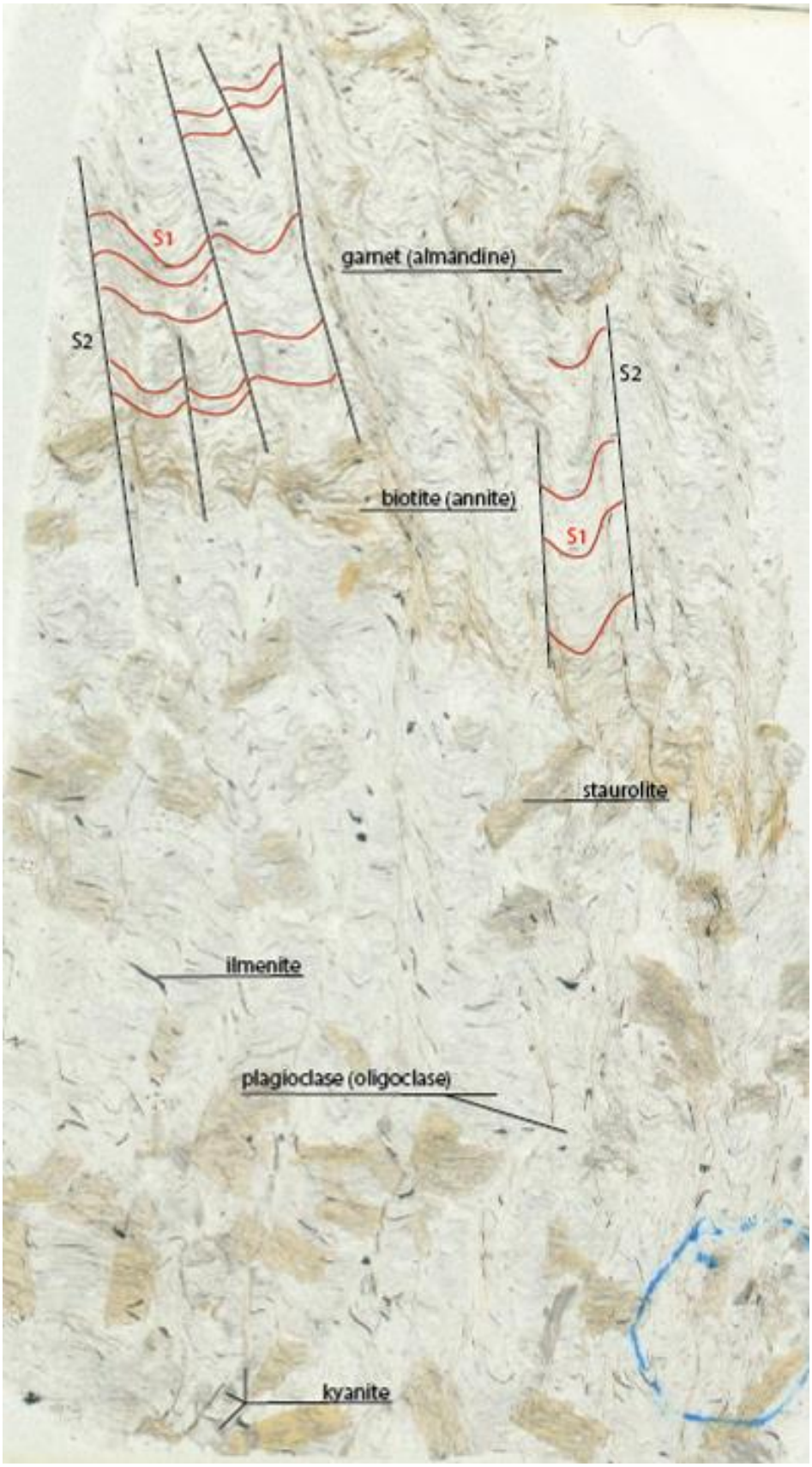

Figure 5.2. Thin section P58b-19 in plain polarized light (ppl). Note the black opaque minerals (ilmenite) and the yellow pleochroic staurolite crystals. The white minerals in the matrix are garnet crystals. Clearly visible are the microlithons and crenulation cleavage of S_2 and the previous S_1 cleavage. The colourless non-pleochroic matrix consists chiefly of quartz and white mica.

Figure 5..3 Thin section P58b-8 in cross polarized light (xpl). Note the crenulation cleavage and microlithons combined with a large volume of porphyroblasts. The large amount of rectangular cross twinned minerals are staurolite; the rounded minerals which are uniformly black are garnets; the grey irregularly shaped grey patches are plagioclase; black slivers — most clearly seen inside blasts — are ilmenite crystals. Note the apparent random orientation of the porphyroblasts compared to the crenulation cleavage S_2.

A BSE image in figure 6.1 and a line scan in figure 6.2 illustrate the boundary area between paragonite in the matrix and an oligoclase porphyroblast. A clear transition can be observed in both minerals where diffusion did not take place. This zone marks the penetration of cation exchange inside the grains between the phases. Especially the relative amount of Ca decreases in paragonite compared to oligoclase. Since Ca is highly compatible to the plagioclase series, at high temperature (where oligoclase is formed) transfer of Ca towards oligoclase can penetrate quite far into the matrix material if time and temperature are favourable.

An overview of thin sections P58b-11 (fig. 14.3.3), P58b-12 (fig. 14.3.1) and P58b-16 (fig. 14.3.2) can be found in the appendix chapter 14.3.

5.2 Porphyroblasts

5.2.1 GARNET

Garnet is one of the most common minerals in the samples. They are chiefly euhedral shaped and heterogeneously spread in the microlithons throughout the thin sections. Their size varies at the mm-scale with the largest ones up to ≈ 10 mm. Many garnets are free of inclusions but some of the garnets show straight inclusion trails and/or have rotated inclusion patterns (fig. 4A). Straight inclusion trails are formed by growth of garnet after the first S_1 deformation phase. The inclusions are predominantly material which cannot be incorporated in the crystal and therefore remains as a relict inside the crystal. When the inclusion trail is rotated, the garnet grows over the minerals/inclusions during deformation. After each increment of matrix deformation, e.g. rotation, the orientation of the relict mineral is slightly

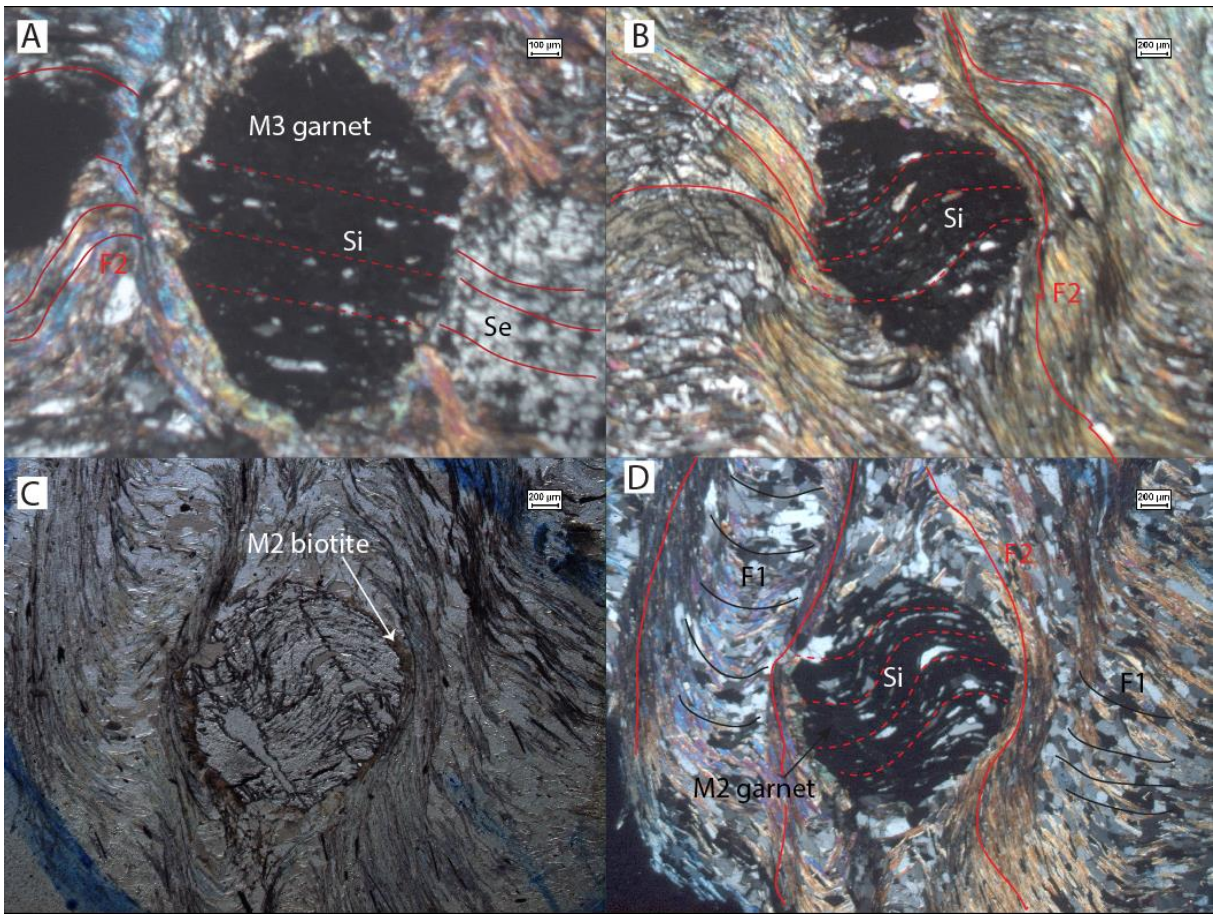

Figure 5.4. (A) P58b-11 Garnets showing a straight inclusion path and rotated inclusion paths. (B) P58b-11, sample gtA11 Note the change in orientation between the internal foliation (Si) and the external foliation (Se) in figures B, C and D. This is due to growth of the garnet after deformation has ceased. The black lines/inclusions seen in C are residual matrix material like graphite.

different from the one in the matrix which is captured subsequently in the mineral and hence unaffected by any new deformation. Hence ongoing deformation will rotate the inclusions with respect to each other.

No spatial distinction can be made between garnets having rotated, straight and an inclusion-free pattern since their distribution is random. Although their euhedral shape is mostly preserved, the garnets are heavily fractured as many randomly oriented fractures and cracks can be observed (fig. 5.5C). The F_2 matrix is pushed aside next to the garnets. This can be observed by the bended F_2 cleavage domains around the blasts without it being incorporated into the garnet itself. As the F_2 follows the outline of the mineral towards the tail sometimes strain shadows filled with material like quartz or small feldspar minerals can be observed (fig 5.5A). These features are only observed where a perfect F_2 crenulation cleavage has developed in the matrix. However, in many occasions the F_2 crenulation cleavage is incipient and not fully developed. Some of the garnet porphyroblasts are intersecting with the F_2 cleavage and the does not push the cleavage aside.

Nearly all garnets do show biotite rim (fig 5.4A; 5.4B). The observed biotite rim almost never surrounds the garnet in total; hence a transition from garnet to biotite as a reaction rim is not totally substantiated. No garnets are observed which are totally replaced by biotite. Other

minerals which are found as inclusions in garnet are quartz, white mica, ilmenite, zircon, rutile, staurolite, Tourmaline and plagioclase. Some of the ilmenite minerals observed in the garnet are only partly included and are crenulated the moment the mineral enters the matrix (fig 5.12). The presence of some of these minerals can be used as time indicators of garnet growth and for geothermobarometry (e.g. garnet-ilmenite exchange of manganese). The smallest inclusions do not show any undulatory extinction. Some of the larger inclusions (5.4B; 5.5D) are elongated parallel to $F_{i.}$ Most of the inclusions are mainly elliptically or rounded in shape, but this depends also on the composition.

Interpretation P58b garnet observations
Since the rocks are rich in aluminum, the presence of aluminum-rich phases like garnet, mica and staurolite is common. The euhedral shape of the minerals is an indication of growth under pressure and temperature well for garnet without any abrupt changes in conditions. Initial nucleation of grains is hampered by the relatively high surface energy of small grains and is therefore less stable compared to larger grains (Poirier, 1985). This surface energy can for example be overcome by small fractures or irregularities in the mineral. The reason for the relatively large amount of small garnets can be a lack of nutrients in the surrounding area. This may explain the large amount of porphyroblasts, but due to a deficit in nutrients as Al or Fe further growth is inhibited. The presence of other minerals adjacent to the garnets which are not involved in the diffusion processes can also decrease the rate of diffusion. Another reason might be a slow diffusion of 'waste' material and hence diffusion of nutrients towards the minerals is slower. Only small volumes of water can enhance the type of diffusion process already significantly. When during prograde stages fluids are released out of micas, diffusion increases and chemistries of minerals can change in relatively short time periods. Since the assumption of water oversaturation is made, diffusion happens rapidly on a geological time scale.

These factors are all dependent on the temperature of formation and the compatibility of the elements between the phases. In most cases especially in low- to medium-grade rocks as in Lukmanier, minerals which are not involved in the reactions are not removed in total but it is energetically more favourable to overgrow the remnants of former minerals. Such inclusions are called passive inclusions (Passchier and Trouw, 2005). This kind of inclusion is mainly found in the investigated rocks. There is however a certain amount of Gibbs free energy, ΔG_{chem} needed to overcome a reaction boundary to grow over the relict minerals. Hence, if temperatures are too low, any type of nucleation and growth processes is not able to initiate at all.In metapelitic systems the presence of quartz (SiO_2), zircon (ZrO_2), rutile (TiO_2) and opaque minerals in garnet can be explained by the passive inclusion theory (Passchier and Trouw, 2005). These minerals do not contain any nutrients for the garnet to grow. Mica, oligoclase and staurolite however do contain nutrients as Fe, Al and Si and are therefore rarely observed as inclusions. Carmichael (1969) proposed that the sluggishness of large Al-ions under greenschist and lower amphibolite facies conditions might however cause the formation of Al-rich phases inside a garnet. This is only possible under supersaturation conditions of these phases and hence stability inside the garnet. In metapelitic systems with bands of quartz and oligoclase adjacent to Al-rich bands of mica garnet porphyroblasts will always grow on top of the Al-rich mica phases and they have difficulties in replacing Al-poor phases like quartz.

When schist forms in a metapelitic system many nuclei are available for quartz and mica to grow in the matrix. They predominantly grow on top of 'sedimentary' quartz and mica grains. For porphyroblasts like garnet, staurolite and kyanite, which are produced in prograde

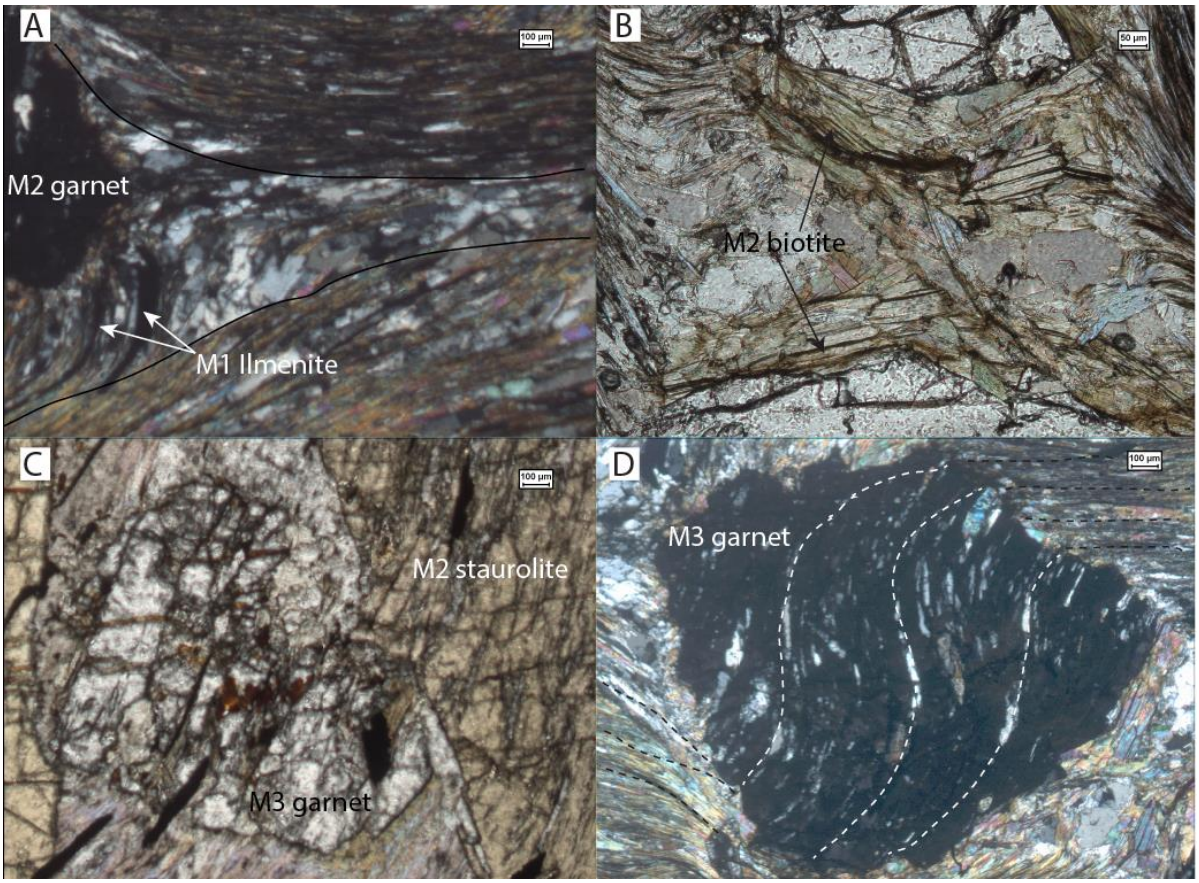

Figure 5.5 (A) P58b-11, sample GtB11 M2 garnet in xpl showing a strain shadow filled with quartz and oligoclase minerals. Note the bending of the foliation adjacent to the garnet. (B) P58b-11, sample gtA11 M2 biotite rim around garnet in ppl. The rim is common due to the instability of the garnet porphyroblasts. Note the strain-free surface of the blasts of biotite. (C) P58b-11M3 garnet in ppl showing a high amount of fractures. The black elongated grains are incorporated ilmenites; the reddish crystals are rutile crystals. (D) P58b-11, sample gtA11 rotated M3 garnet inclusion trails in which Se is continuous with Si. This microstructure indicates deformation stopped simultaneously with garnet growth (view in xpl).

reactions, only a few suitable sites (e.g. minerals) are needed for nucleation and hence their amount is small, but sufficient for growth towards larger blasts. They can only nucleate on top of the matrix minerals when temperature is high enough. Even during prograde evolution towards higher metamorphic grades the matrix minerals remain small since temperature is not high enough to nucleate and grow new porphyroblasts (Vernon, 2004).

Garnets which have straight inclusion patterns (Si) and which are oriented in a different orientation compared to the external foliation (Se) have grown after the first phase S1 of deformation, but before the second phase of deformation (S2) that reoriented the first (5.5D). Garnets showing a Si which have a spiral shaped path are syn-F2-deformation. When Se can be followed outside the garnet, deformation did not cause folding of the matrix foliation. However, when Se is disconnected from Si, deformation continued after the growth of the garnet porphyroblast has ceased (Zwart, 1960, 1962). It is however not correct to assign the second deformation phase F2 to the disconnection since multiple phases may have influenced the matrix and due to strain partitioning the garnet blast is not affected anymore. Finally the thin sections contain garnets which do not show any inclusions at all. One of the reasons

might be a formation before the first phase of deformation S1 or secondly the garnets have consumed all the matrix phases (e.g. nutrients) that they overgrew. The latter possibility might indicate a different mineral equilibrium situation compared to the garnets and porphyroblasts which have grown in a later stage with inclusions and/or supersaturation of phases. In the initial stage of garnet growth no supersaturation of Al-rich phases was present and hence everything was consumed. Subsequent deformation caused partitioning of Al-rich and Al-poor phases and garnets preferred to grow in mica rich environments. Growth on top of these sites caused supersaturation and hence inclusions of phases. Other microstructural characteristics are not observed between these opposed two groups of garnet.

The fractures observed in the garnets are formed by several deformation phases which have stressed the garnet porphyroblast. This is only possible when the garnet appears in the brittle field <15-18 km depth or in the presence of precipitation of phases out of a fluid phase. Exsolution of phases from garnet in the presence of fluids is however not observed and further research is beyond the scope of this study. According to Wiederkehr et al. (2008) the final deformation phase in the area, D4, occurred on the retrograde path of the unit towards the surface at a depth ≈ 10 km. Therefore, this deformation phase might have fractured the garnets. Since they occur randomly over the inclusion paths, the phase of deformation is probably the latest deformation in the area.

The formation of strain shadows on opposite sides of garnet minerals is caused by dissolution of the more soluble phases alongside the core object. Predominantly quartz, oligoclase and carbonate rich material precipitates in the strain shadows, whereas micas or complex chain-silicates are underrepresented in the shadows (Passchier and Trouw, 2005). The less soluble minerals accumulate perpendicular to the strain shadows on strain caps. The boundaries between the core mineral and the strain shadow are mostly gradational and do not show any features of the adjacent folded matrix material. The strain shadows tend to stabilize the porphyroblasts for further deformation, which is dependent on the size of the shadow. Strain shadows are formed pre-S_2 (fig 5.5A). Garnets which show strain shadows are only observed in parts of the rock with relatively few other porphyroblasts and a pronounced F_2 crenulation cleavage. These garnets contain a rotated Si and have mica-rich strain caps which part the Si from Se. This indicates that a stage of deformation (and hence dissolution-precipitation) occurred after the formation of garnets which overgrow at least two deformation phases, S_1 and S_2.

The formation of a biotite rim can be explained by the discontinuous reaction of staurolite to garnet + biotite + kyanite. This assemblage marks the beginning of the upper amphibolite facies. When biotite is in fact a reaction rim, it can have formed in the prograde reaction garnet + chlorite + muscovite = staurolite + biotite + quartz + water or during decompression by the net transfer reaction garnet + muscovite + water = staurolite + biotite + quartz. Discussion of possible reactions and P-T-t paths is given in chapter 12.

If the presence of mineral inclusions in garnet differs from the composition of the same minerals in the matrix via geothermobarometry on both minerals it can say something about the geodynamical evolution of the rocks over time. This is mainly applicable for the Si-content of micas, the molar fraction of Na vs. Ca in plagioclase and the composition of ilmenite inside garnet. For the ilmenite minerals, the relationship between the mineral and the matrix can be deduced with the orientation of the ilmenite crystals (5.5C). When the ilmenite crystals are partly included in the garnet, but have a different orientation outside the garnet, the matrix has developed (e.g. deformed) after the ilmenite was included in the garnet.

5.2.2 STAUROLITE

Volumetrically, staurolite is the most prominent porphyroblast in the P58b samples. They are recognized by the yellowish (light to darker) pleochroic colours in plain polarized light and the extinction as a cross shape in cross polarized light. Many crystals form a cross which is clearly visible optically. The blasts show the same mineral-inclusion relationship as observed and described above for garnet crystals. Some of the staurolite blasts do not contain any inclusions, whereas several others have straight inclusions (fig. 5.6A). Some have rotated inclusion paths (fig. 5.6B). The staurolite grains are also euhedral in shape and less fractures compared to the garnet, which could indicate a later growth phase. Various crystals show some instability features like curved grain boundaries in contact with the matrix. A microstructure that can only be seen when staurolite is in contact with plagioclase is the formation of rutile and other reddish secondary phases. The rutile appears on the plagioclase side of the grain boundary (fig. 5.7B; C). Moreover the staurolite appears to be fractured when in contact with the plagioclase, compared to straight grain boundaries of staurolite when

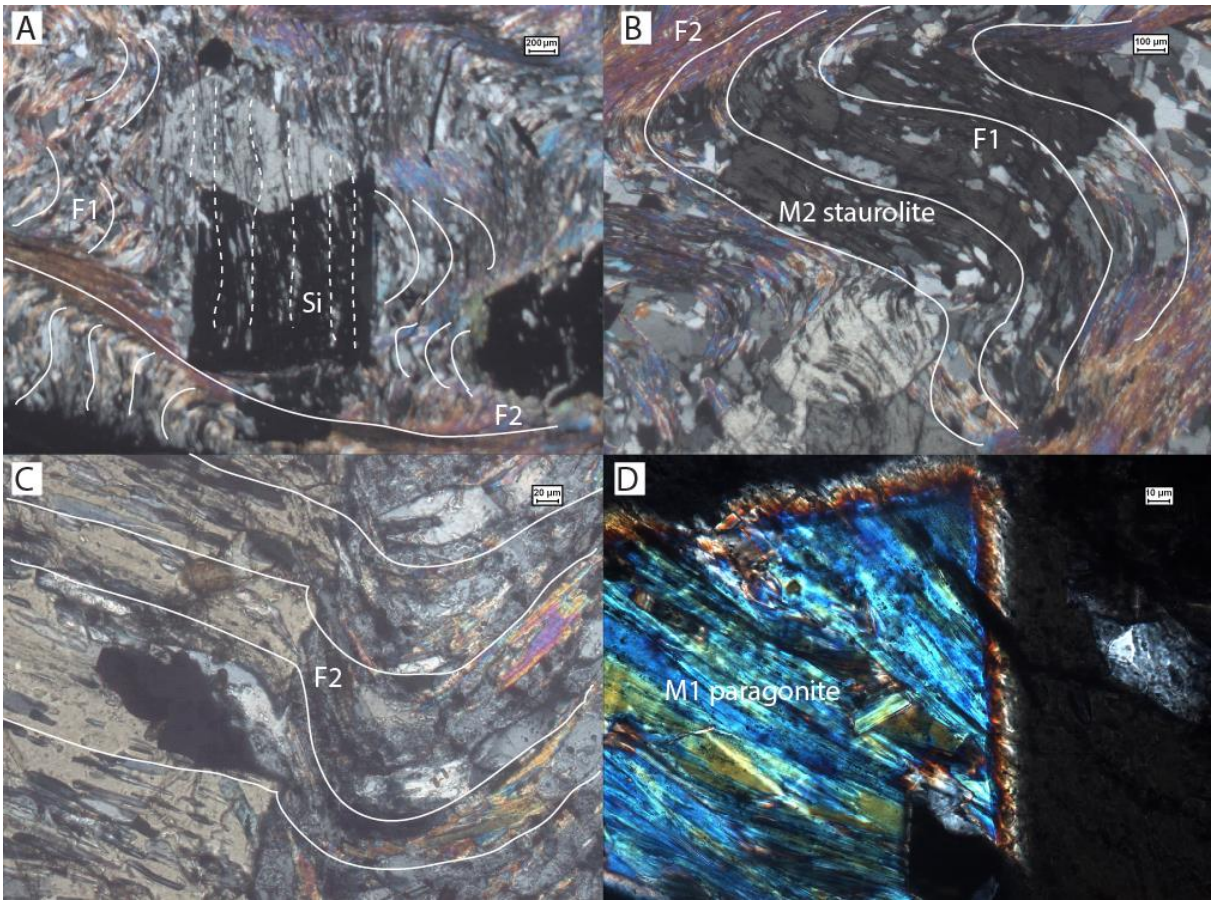

Figure 5.6. (A) *P58b-11, sample StauC11 M2 staurolite mineral in xpl containing a straight Si inclusion path. The cross-twinning characteristic for staurolite can clearly be seen in the adjacent porphyroblasts. Note the Se curves around the mineral.* (B) *P58b-11 M2 staurolite mineral in xpl with a rotated inclusion path of predominantly quartz and graphite where Si continues as Se.* (C) *P58b-11 Rim of a staurolite crystal (ppl) adjacent to the matrix. Note the shape change of the quartz grains from matrix (randomly shaped) to staurolite inclusion (elongated and smooth). Si continues as Se. Inclusions observed: M3 ilmenite (opaque); quartz; tourmaline (beige); M3 oligoclase (large 1st order birefringence clasts).* (D) *P58b-11 'reaction rim' of staurolite adjacent to the matrix (xpl) is a changing Becke line effect.*

in contact with the matrix (fig. 5.6C). Another feature is the orientation of the staurolite crystals. Most of the crystals show an orientation perpendicular to the F_2 crenulation cleavage and the cleavage does not bend around the crystal (fig 14.3.1-3). Some of the staurolite porphyroblasts do show bending of F_2 around them.

The inclusions in staurolite are mainly rounded in shape and are composed of quartz, Tourmaline, ilmenite, zircon and muscovite (fig. 5.6C). None of the grains shows any undulose extinction. Finally the staurolite crystals show a kind of 'reaction rim' when they are in contact with the matrix (fig. 5.6D).

Interpretation P58b staurolite observations
The staurolite minerals have undergone a similar evolution compared to the garnet crystals. When plagioclase grew adjacent to the staurolite minerals, rutile is formed as a reaction product. Several staurolites show curved grain boundaries which might indicate a S_2 syn-deformational growth parallel to the F_1/F_2 foliation. Another reason for this can be instability of the porphyroblast at higher temperatures when the mineral is able to exchange elements with its surrounding matrix. This process however only occurs at temperatures roughly $>650^oC$ and hence can only have occurred during a possible late stage heating event.

The porphyroblasts which developed at relatively low temperature ($<600\ ^oC$) nearly all show inclusions. But since the diffusion rate of ions is dependent on both the distance of travel and temperature, inclusions become sometimes scarcer at higher metamorphic grade. Therefore, they are moreover coarser grained. So when the temperature increases in the minerals, inclusions might disappear and the crystals itself can deform slightly (Passchier and Trouw, 2005). It can be explained by element exchange between the porphyroblast and the matrix and at temperatures high enough total diffusion can homogenize the porphyroblast again.
Since temperatures observed in these samples is relatively low (<950 K), this is however unlikely.

Most of the inclusions observed are quartz grains. They appear as rounded inclusions which are smaller compared to the adjacent quartz crystals in the strain shadows. This observation may be caused by partial diffusion or by a reaction involving the included mineral (Passchier and Trouw, 2005). Partial diffusion of silica away from the inclusions is more likely than mineral reactions since the quartz grains appear to be included and not overgrown or exsolving from another phase. Other inclusions like muscovite and ilmenite maintain their original shape and size. Tourmaline minerals appear to overgrow most of the features in the thin section. They appear as inclusions in staurolite and garnet, but maintain their euhedral shape. They seem to follow the F_2 crenulation cleavage when oriented in the matrix, so they might have grown inter-deformational between the two deformation phases S_1 and S_2 where garnet and staurolite were already both present. The staurolite porphyroblasts oriented perpendicular to the F_2 crenulation cleavage, and where the cleavage abuts at the crystal face, did not continue growing after deformation stopped. They are either post-D_2 since they contain F_2 inclusion paths or syn-D_2 simultaneously to deformation. The porphyroblasts which show a bend crenulation cleavage did grow after deformation stopped. Predominantly mica-rich cleavage domains are pushed aside and not overgrown by the staurolite crystal.

Finally the staurolite crystals show a kind of 'reaction rim' when they are in contact with the matrix (5.6D). The colours are however caused by a dipping interface of the mineral. This interface is formed by a changing Becke line. When you are focusing the mineral under the optical microscope, slightly bringing it out of focus will cause translation of the Becke line.

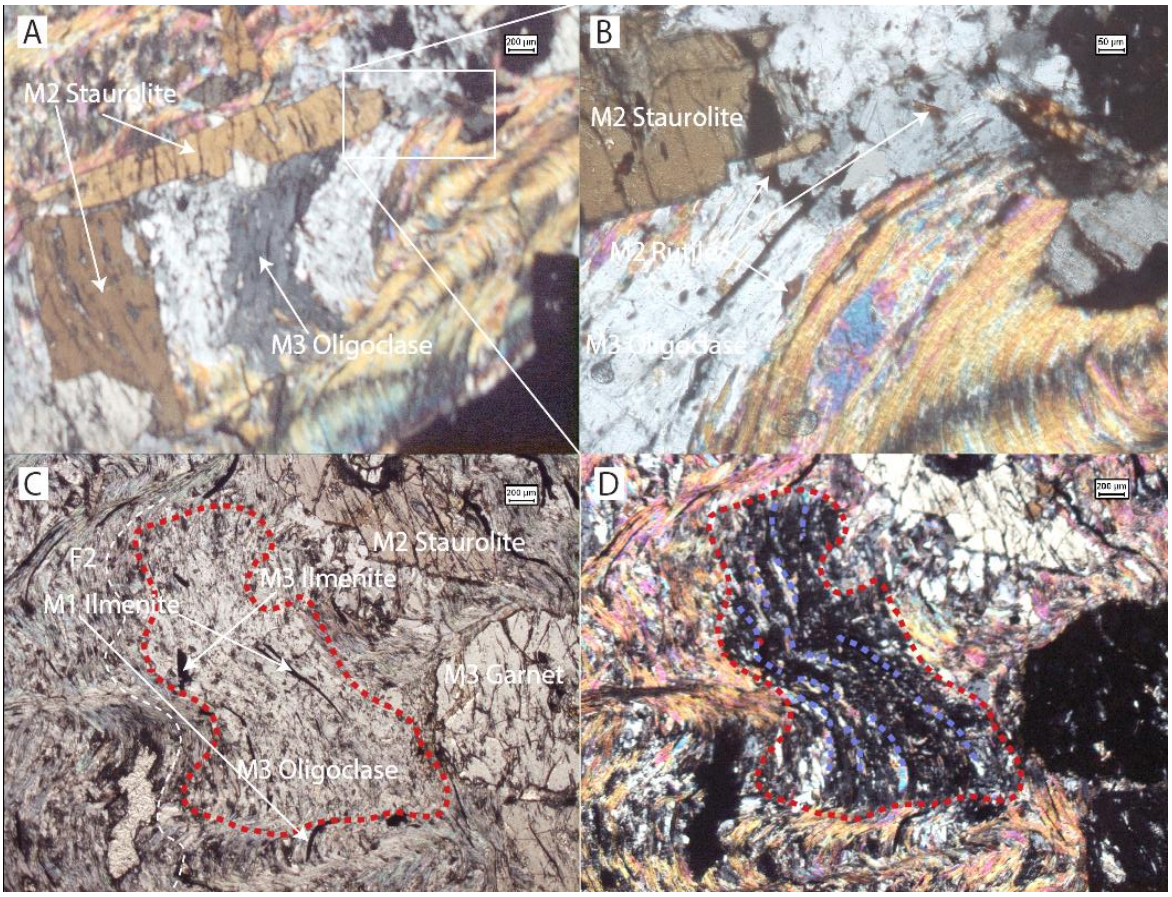

Figure 5.7. (A) *P58b-11, sample StauC11 Yellow staurolite mineral (xpl) in contact with plagioclase. Note the three-division of the single plagioclase crystal.* (B) *Magnification of photo (A). In contact with staurolite, Ti-rich phases as rutile appear in the plagioclase crystal (reddish crystals).* (C) *Plagioclase porphyroblasts (ppl) which external shape follows the crenulation cleavage in the matrix.* (D) *Same mineral as in (C) but in xpl inclusions can clearly be seen, as the orientation of the Si which follows Se.*

The Becke line appears to move into the material with the higher refractive index, e.g. the epoxy or the mineral.

The euhedral shape of the staurolite crystals can be explained by the presence of fluids alongside the grain boundaries (Vernon, 2004). When a small amount of liquid is present along the grains, nucleating porphyroblasts grow in a liquid and consequently develop their characteristic growth structures (Budworth, 1970; Sunagawa, 1974 a.o). In a dry environment adjustment boundaries develop and the minerals form concave grain boundaries with the matrix (Vernon, 2004).

Since some staurolite crystals appears inside garnet, it might indicate the breakdown of staurolite when the conditions passed the staurolite + muscovite + quartz = garnet + biotite + sillimanite + water reaction. Other reactions which formed staurolite are related with the transition to the amphibolite facies field and discussed in chapter 12.

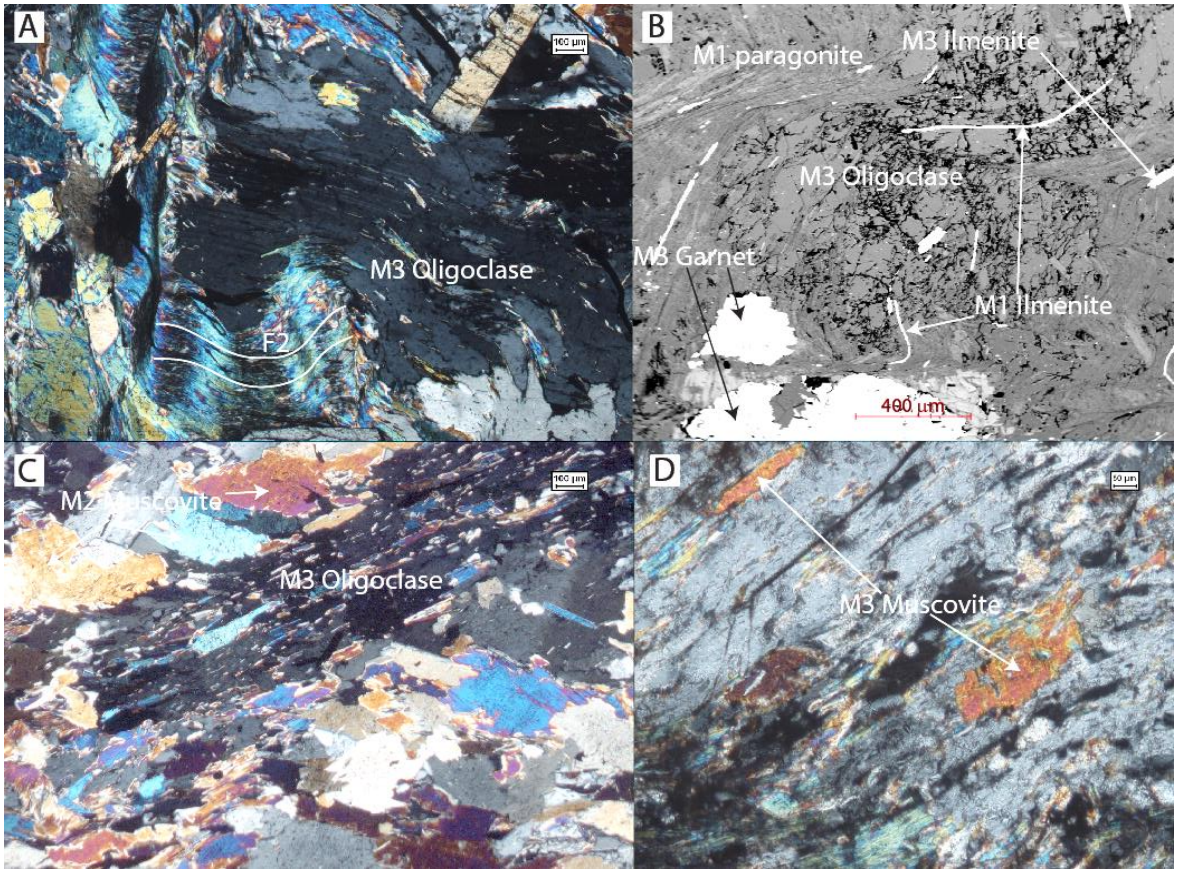

Figure 5.8. (A) *Plagioclase crystal showing deformation twinning (xpl).* (B) *Backscatter electron image (BSE) from a plagioclase crystal. Note the white elongated ilmenite grain which is surrounded by the plagioclase and follows the crenulation cleavage.* (C) *Plagioclase porphyroblast (xpl) overgrown by micas which have grown independent of the crenulation cleavage. Note the black inclusions/overgrowth of the mica flakes themselves.* (D) *Magnification of a mica overgrowth (xpl). Blast is strain free and is grown on top of the plagioclase porphyroblast.*

5.2.3 PLAGIOCLASE

The porphyroblast that at the onset of this study was still compositionally unknown, is formed by a low relief mineral which appears colourless non-pleochroic in plane polarized light (fig. 5.7C) with a first order grey interference colour. The mineral comprises roughly 10% of the rock and has a grain size between several mm up to cm-scale. A striking feature is the outline of the mineral. The shape of the crystals follows the formation of the F_2 crenulation cleavage. Hence the porphyroblasts are syn-deformational S_2 and overgrow the former minerals (fig. 5.8A). EMP analysis show they are plagioclase (oligoclase) and not restricted to the microlithons. They overgrow F_2 cleavage domains regularly and are not hampered by quartz-rich environments. The internal foliation F_i observed by alignment of inclusions follows the external foliation F_2 without any offset (fig. 5.7D).

The plagioclase porphyroblast microstructure is also characterized by a high amount of inclusions (fig. 5.8C) Elongated ilmenite grains seem unaffected by the overgrowth, as the tourmaline minerals which remain stable. Overgrown mica grains maintain their original orientation related to the crenulation cleavage (5.8C; D). Some of the micas have

recrystallised on top of the plagioclase mineral. The mineral inclusions are elongated and show curved grain boundaries. Next to that, the inclusions appear smaller compared to the minerals outside the plagioclase blast. Quartz inclusions are however larger compared to the crystals in the matrix.Several of the plagioclase porphyroblasts contain deformation twins (5.8A). This in combination with undulose extinction of some of the plagioclases indicates formation related to deformational processes and possible changing P-T conditions. Deformation could however have occurred without changing conditions, since the observed oligoclase minerals are homogeneous. In contact with staurolite, plagioclase porphyroblasts contains secondary phases like rutile and seem to influence the crystal structure of the staurolite since the latter mineral appears broken.

Interpretation P58b plagioclase observations
With the aid of the EMP the chemical composition of the unknown mineral was determined. The EMP analyses are listed in table D of section 14.1. The plagioclase had an An_{15}-An_{40} composition with wt% of K <5%. In the plagioclase solid solution diagram (fig. 6.12) the chemical composition is that of oligoclase. This has important consequences for the timing of formation. Since the amount of Ca is quite significant the porphyroblasts are most likely grown under amphibolite facies conditions under medium-grade pressures. The porphyroblasts are formed during a deformation phase since the grain boundaries follow the F_2 external foliation and F_i is connected with F_e. Growth is >600 ^oC since the chemical composition indicates the amphibolite field, i.e. the molar fraction of calcium is > 20 wt%. Undulose extinction in the plagioclase indicates the influence of at least another deformation phase since dislocations start to align in kink walls due to deformation of the crystal structure.

The plagioclase minerals do not show any preference in growing over the microlithon ore cleavage domains. The porphyroblasts follow the crenulation cleavage outline and grow without preference over cleavage domains and microlithons. Since the cleavage domains are Al-rich, it would be a logical assumption to initiate plagioclase growth there on top of unstable micas. Nutrients as Na and Ca can be found in Na-rich micas like paragonite or calc-silicates which are present in minor amounts. Quartz rich inclusions are remnants of microlithons and the mica inclusions are still present since there existed probably supersaturation of Al- and Si-atoms and hence the inclusions remained stable. Since there is no offset seen following the inclusion trails into Se, deformation ceased at least before the plagioclase minerals stopped growing. This is confirmed by the orientation of the stable ilmenite minerals (fig. 5.8B). When some of the ilmenites are deformed this is due to earlier deformation of the matrix.

After the formation of the plagioclase porphyroblasts there appears to be some overgrowths of mica along the boundaries of the oligoclase crystal. These overgrowths can be related to late growth. Since the mica flakes are chemically similar (table A in chapter 14.1) with each other the P-T situation does not change significantly. The flakes are however undeformed and do not contain any inclusions or dislocations so they seem to be post-deformation (fig. 5.8C; D).

Deformation twinning of the plagioclase minerals develops when minerals are objected to a certain amount of stress and formation of new orientations within the grain develop. They tend to cluster near sites of large strains, like grain boundaries. The deformation twins propagate by moving the tip of the twin through the grain or by moving the twin boundary through the untwined crystal (Passchier and Trouw, 2005). They can be recognized by multiple twins who are roughly uniform in width across a single grain. The presence of deformation twinning is another indicator of increased stresses during formation and hence

late stage deformation. According to Vurnon (2004) plagioclase shows deformation twinning in combination with undulose extinction at medium-grade conditions between 450 ^{o}C – 600 ^{o}C.

5.2.4 KYANITE

The high amount of aluminium present in the bulk rock composition allows the formation of an Al_2SiO_5-phase (see bulk rock composition, chapter 7.1). Throughout the P58b thin section kyanite is the only observed aluminium-silicate pseudomorph, e.g. no sillimanite and/or andalusite are observed. The kyanites can be roughly divided into two groups. The first group consists of tabular kyanites which show clear undulatory extinction and are in particular located inside the F_2 cleavage domains (fig. 5.9A; B). They can appear in groups together with other kyanites or as singular blasts. The second group of porphyroblasts (fig. 5.9C; D) has a euhedral shape and shows a parallel cleavage. This set of kyanites dominantly occurs outside the F_2 cleavage domains in the microlithons, but is mainly observed in the cleavage domains. They overgrow all the S_2 deformational features in the rock and seem to be undisturbed by any later deformation if present.

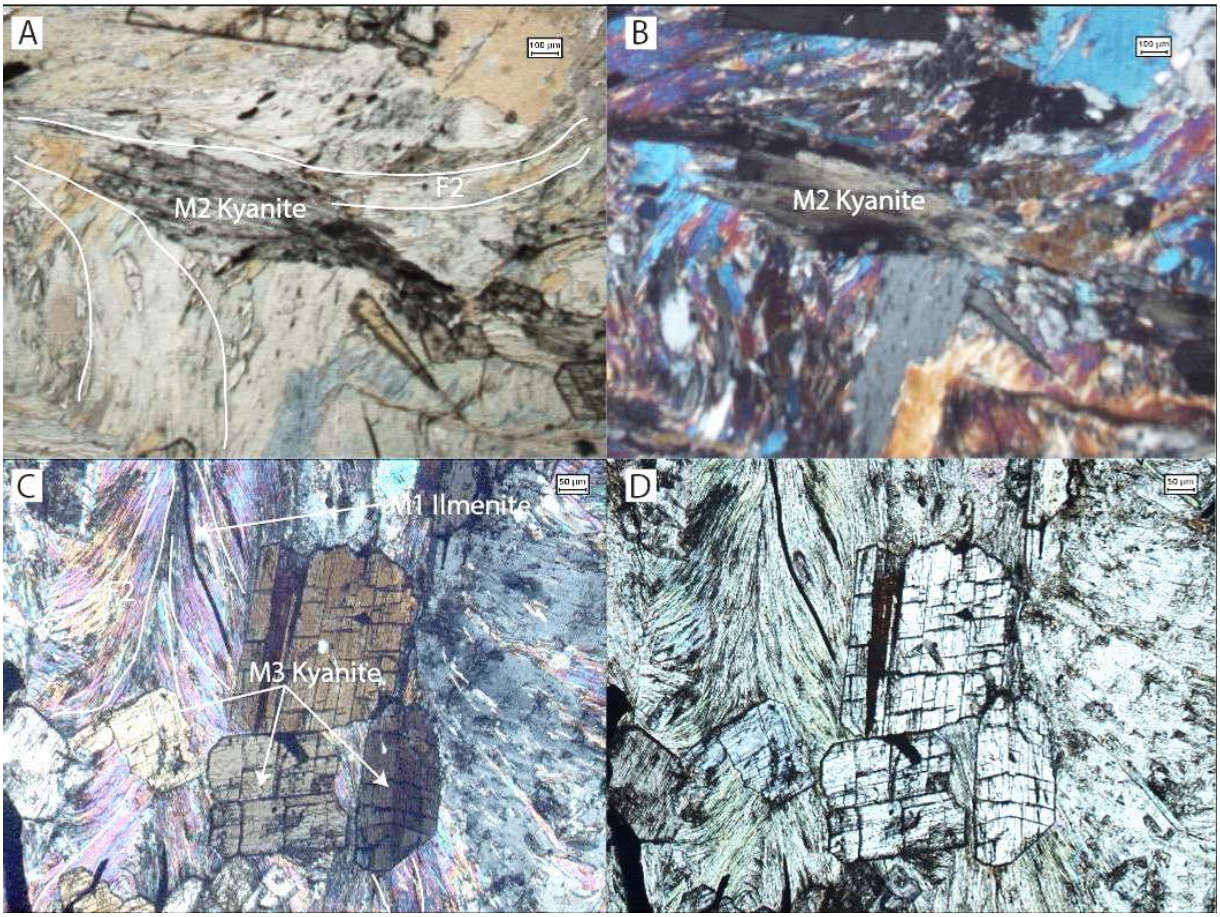

Figure 5.9. (A) *P58b-12, sample KyC12 'Elongated' kyanite crystal (ppl) located in a cleavage domain.* (B) *Kyanite of (A) in xpl, showing clear subgrains.* (C) *P58b-16, sample Ky16C Kyanite crystal (xpl) with a blocky shape. Note the clear cleavage in the mineral and the lack of internal inclusions.* (D) *Kyanite of (C) in ppl. Note the high relief and overgrowth of all the older phases. The mineral seems unaffected by later phases of deformation and/or metamorphism.*

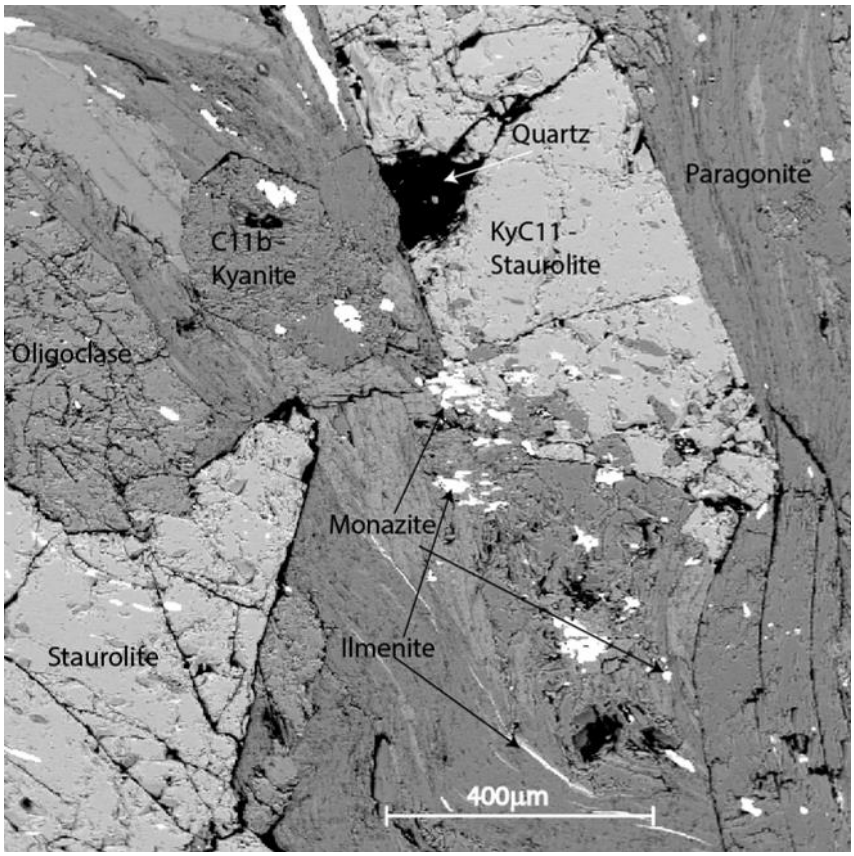

Figure 5.10. P58b-11, sample KyC11 BSE image of a kyanite crystal growing over F_2 crenulation cleavage. Note the blocky shape of the crystal.

Both groups of kyanites do not have any inclusions. Reaction rims are also uncommon around the kyanite. As is the case with plagioclase and staurolite crystals, in the vicinity of kyanite secondary oxides and rutile are present in contact with quartz and oligoclase.

Interpretation P58b kyanite observations

Late-kyanite formation is an indication of a late stage heating event. The porphyroblasts are compositionally not different from each other but seem to have formed at different times. The kyanites that show undulose extinction and are elongated have formed, at least, before the final observed D_2 deformation phase. They are called M2. Elongation of the blasts can be explained either by the high temperatures and breakdown of kyanite by diffusional processes. The kyanites which do not show any relation to deformation and appear to grow over all other phases are most likely grown after the last phase of deformation, but have still grown in the vicinity of peak temperature conditions. This explains the blocky shape of the kyanites which has allowed time to develop (fig. 5.10). They are referred to as M3.

As can be seen with the plagioclase porphyroblasts, when kyanite is in contact to feldspar or quartz minerals secondary oxides and rutile are present as separate phases. The reactions which are involved cannot be explained clearly. Exsolution of a Fe-/Mg-rich phase in the presence of Na-/K-rich minerals seems to occur to balance the whole system, where the Fe-/Mg-phases can neither be incorporated into the Al-rich phase, nor in the Na-/K-rich phase (e.g oligoclase, muscovite). The reactions are occurring during a late stage, since the Fe-/Mg-

rich phase is only present in the vicinity of kyanite, which is a late growing mineral in the samples.

5.2.5 BROWN MICA

The weakly brownish pleochroic minerals present in my thin sections are biotite. They occur mainly in the crenulated cleavage domains and as a reaction product of garnet porphyroblasts. This type of biotite is called M1. Most of the crystals are in a scale of 0.1-0.5 mm; only a few biotite flakes have grown to sizes of mm-scale. The biotite rims around garnet are not affected by any deformation of the matrix. This type of biotite will be referred to as M2.

Interpretation P58b brown mica observations

The presence of B1 biotite in the matrix can be explained by the reaction of white mica with an iron-rich phase like chlorite or chloritoid which is subsequently completely degraded and disappeared from the hand samples in the early stages of low grade metamorphism. The disappearance of chlorite and chloritoid from the samples could be valid if the formation of biotite took place on the prograde path (fig. 5.11A). Hence, the biotite would be formed before the peak metamorphic pressure and hence still be able to fold within the F_2 crenulation cleavage. The biotite crystals in the matrix are rich in Fe and hence are referred to as annite in the biotite solid solution series.

The formation of B2 biotite which surrounds the garnet porphyroblasts is described above in the garnet porphyroblast subsection 5.2.1 (fig. 5.11B).

5.2.6 ILMENITE

This porphyroblasts comprise only a few percent of all the hand samples but is a mineral in which Ti is most compatible in metapelitic rocks. Ilmenite occurs as elongated crystals and can be found as irregularly shaped blasts on a 0.1-0.5 mm scale (fig. 5.12B). This group is called M1. A second group of ilmenite crystals, hereafter called M3 is more prismatic shaped and seems to overgrow all other phases (fig. 5.12A). The mineral is opaque and hence no optical observations can be made regarding internal deformation features. In all the thin sections ilmenite is overgrown by many porphyroblasts and does not show any chemical reaction with one of them. Some of the minerals are totally included inside a porphyroblast of e.g. staurolite or garnet, others are only partly included and a change in orientation is sometimes observed when the mineral leaves the porphyroblast.

There are no optical signs of any chemical instability of the ilmenite porphyroblasts.

Interpretation P58b ilmenite observations

All the elongated ilmenite grains are deformed by the crenulation cleavage, which means they are formed prior to the second deformation phase S_2. Since they seem to be aligned parallel to the first formed foliation F_1, the M1 could be formed as one of the first metamorphic porphyroblasts of the sample. This is plausible since ilmenite is the only phase in which titanium is compatible. M2 seems to overgrow all the matrix material and porphyroblasts. By using the stability fields in the pseudosections created with Perple_X a late ilmenite phase can be present above 500 ^{o}C and below 13 kbar. There are two different phases of ilmenite growth present in these rocks. The latter M3 phase has not been affected by any further deformation or metamorphism.

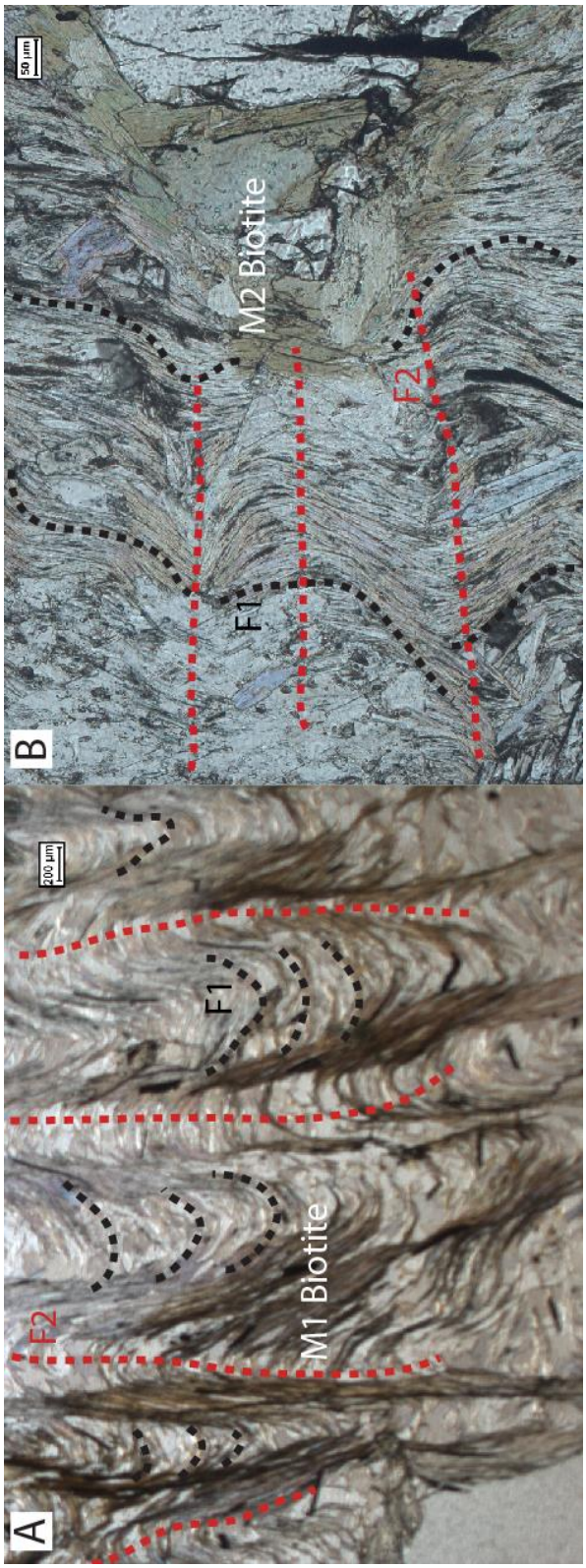

Figure 5.11. (A) *P58b-16 B1 M1 biotite flakes (ppl) present as S_0 in the matrix in the F_2 crenulation cleavage. The crystals are aligned in the F_2 cleavage domains.* (B) *P58b-12, sample PlC12-2 B2 M2 biotite crystals (ppl) as a rim, surrounding a M2 garnet.*

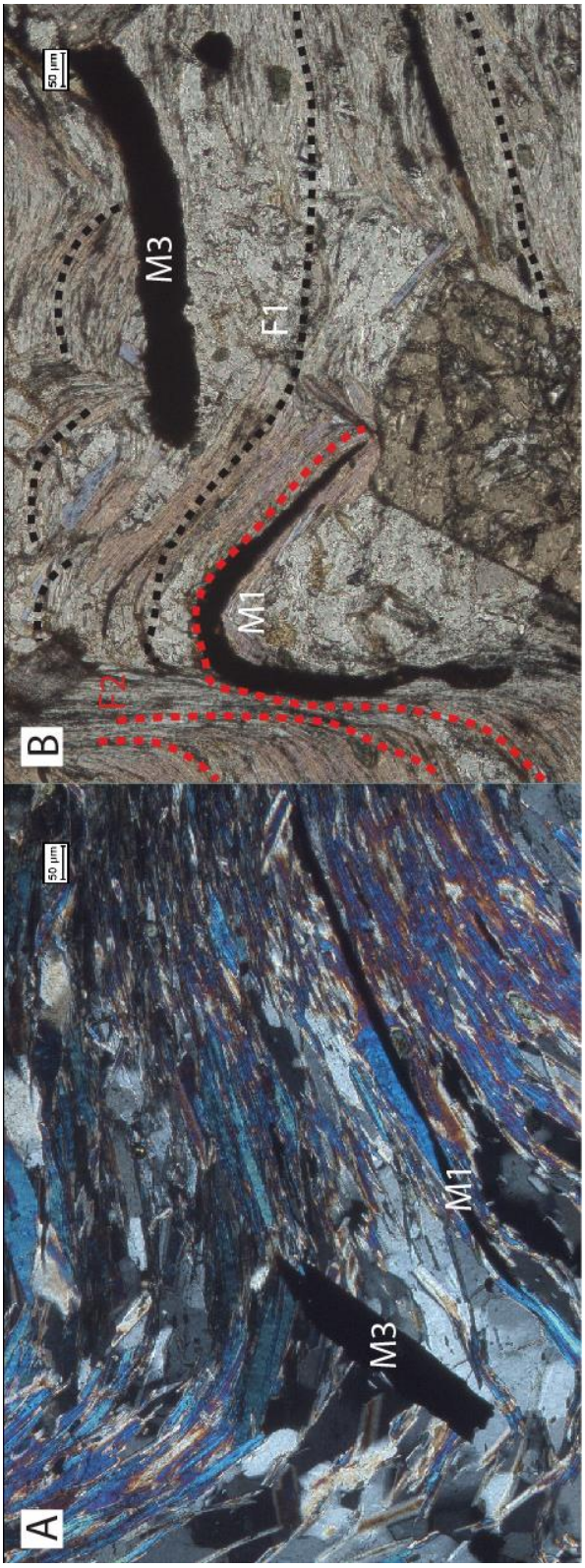

Figure 5.12. (A) *P58b-16 I2 Ilmenite porphyroblast (xpl) overgrowing the matrix material in a random orientation.* (B) *P58b-16 ilmenite crystals (ppl) whereas the left one (M1) is crenulated by the F2 crenulation cleavage and the right one (M3) overgrows the matrix in a random orienttation. Two different stages of ilmenite growth are observed.*

The included ilmenite crystals are used for geothermobarometry in combination with garnet to calculate the equilibrium conditions porphyroblasts. EMP analyses of ilmenite are listed in table E of chapter 14.1.

5.2.7 WHITE MICA

There are multiple classes of white mica observed in the thin sections. The first class M1 comprises a large amount in the matrix of the samples. These are very small, 0.1 mm-scale, flakes of white mica. These micas are included in most of the porphyroblasts which have grown during the first deformational phases on the prograde path. Micas which have undergone multiple deformation phases show in the hinges of F_2 microlithons polygonal arc structures (Passchier and Trouw, 2005). Most of these micas are consumed by the growth of new porphyroblasts. The second class of white mica grains are muscovite porphyroblasts, hereafter called M2. The blasts are on an mm-scale and are mainly nucleated inside the matrix. Some of the micas show undulatory extinction. Most of M2 micas however show a particular feature in which F_1 oriented needles on a microscale are formed on top of the M2 porphyroblasts. The last group of micas which is observed grows over plagioclase crystals, called M3. These are flakes on a mm-scale and are compositionally similar to the M2 porphyroblasts observed in the matrix. They show no undulatory extinction however in comparison to the blasts in the matrix. one formed (fig 5.13A; B) (Vernon, 2004). These M2 also contain small needles of rutile which align with each other. Further analysis of this type of mica is given in the Appendix, chapter 14.4.

White mica M3 flakes inside the oligoclase blasts are undeformed and do not show any undulose extinction, which means that they have grown after the formation of plagioclase and after the last phase of S_2 deformation inside the stability field of muscovite. These M3 flakes are compositionally similar to M2 but are unaffected by any later deformation or metamorphic events.

5.3 Secondary minerals

Other minerals present in only small volume amounts (<1%) are described briefly below.

5.3.1 RUTILE

It is formed as a side product in reactions with staurolite, oligoclase, kyanite and M1. Additional Ti can be found in rutile needles on top of late muscovite M2 grains. The needles align parallel to with the long crystal faces of the muscovite (fig. 5.8).

5.3.2 TOURMALINE

They are weakly pleochroic, greenish to colourless on a µm-scale size. Tourmaline grains occur throughout the whole section, especially in the matrix. It appears as a euhedral mineral and does not react with any matrix material or porphyroblasts (fig. 5.1D; fig 5.14). The mineral is overgrown by most porphyroblasts and tends to follow the F_2 crenulation cleavage when located inside the matrix. Since the minerals show no signs of any S_1 deformation, they have grown post-S_1, pre-S_2 inter-deformational (fig 5.14).

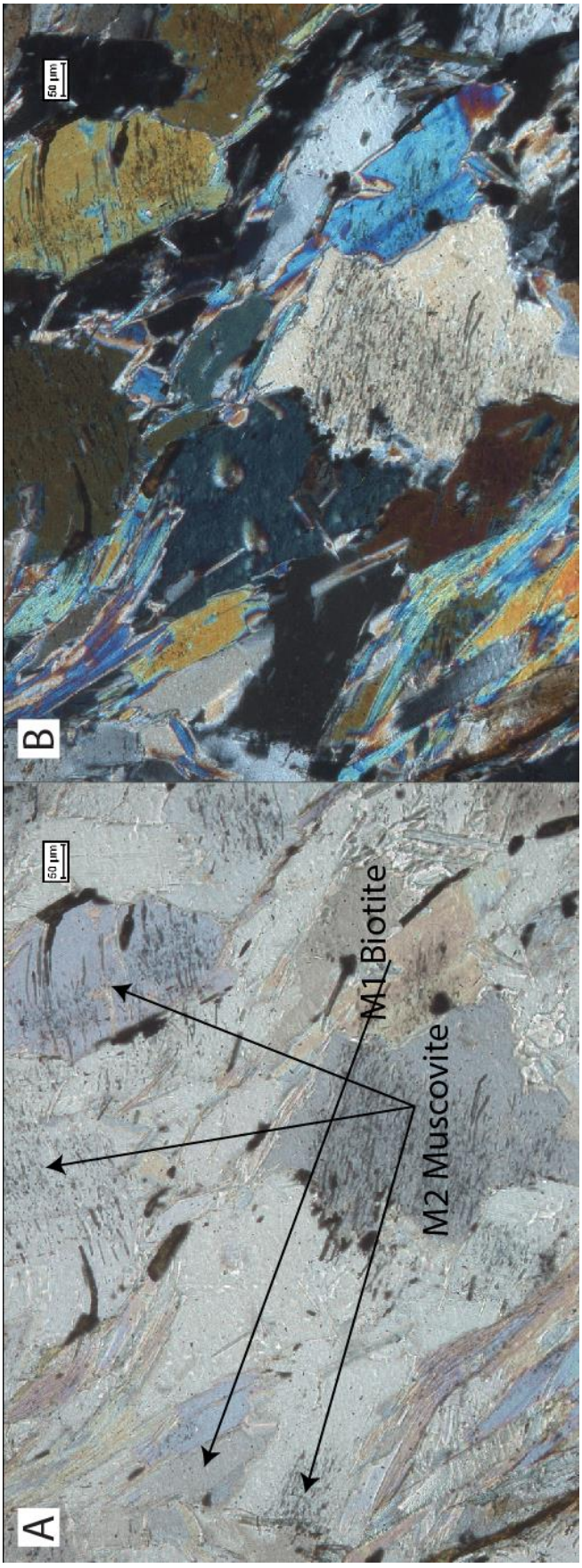

Figure 5.13. (A) *P58b-12 dark grey M2 muscovite blasts (ppl) which have grown post-tectonically (post F_2) and brownish M1 biotite porphyroblasts. Note their random orientation compared to the older crenulation cleavage F_2. The inclusions observed are dark grey rutile needles.* (B) *Picture (A) in xpl*

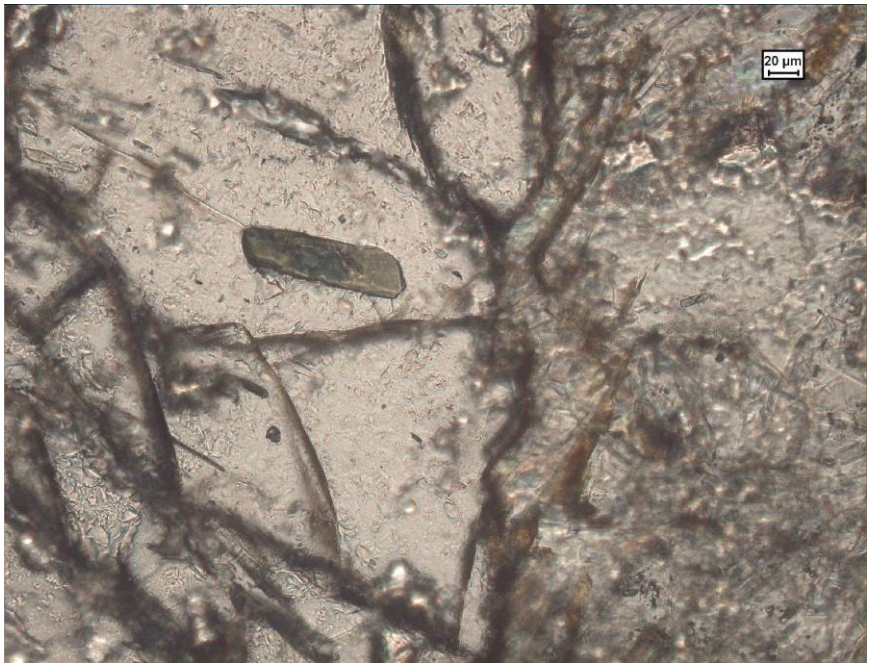

Figure 5.14. P58b-16 Tourmaline mineral as a porphyroblast inside garnet. Note their elongated shape is caused by an optical orientation perpendicular on the c-axis. Tourmaline minerals that appear hexagonal have an optical orientation parallel to the c-axis.

5.4 Mineral growth – time diagram

Table 1. Paragenetic grid of P58b. H_2O is present throughout the whole rock, whereas the amount of CO_2 is assumed to be zero. Minor amounts of minerals as magnetite are not included in this diagram. M1, M2 and M3 correspond to the stable mineral assemblages and S1 and S2 are two observed deformation phases. Reference to the figures, 9.1 and 9.2. Dashed lines indicate stability transition or uncertainty and solid lines indicate stability.

	S_0	S_1 (schistosity F_1)		S_2 (crenulation cleavage F_2)	
	M1		**M2**		**M3**
Staurolite			--------	----------	----------
Garnet		-- -- -- -- ----------	-- ----------	----------	----------
Oligoclase				----------	----------
Kyanite		-- -- -- -- ----------	----------	----------	----------
Biotite	----------	-- -- -- -- ----------	----------	----------	----------
Ilmenite	-- -- ---------	----------		-- -- --	-- -- --------
Rutile		-- -- -- -- ----------	----------	----------	-- --
Muscovite	----------	----------	----------	----------	----------
Paragonite	----------	----------	----------	---------- -- --	-- --
Tourmaline		---------	----------	----------	
Quartz	----------	----------	----------	----------	----------

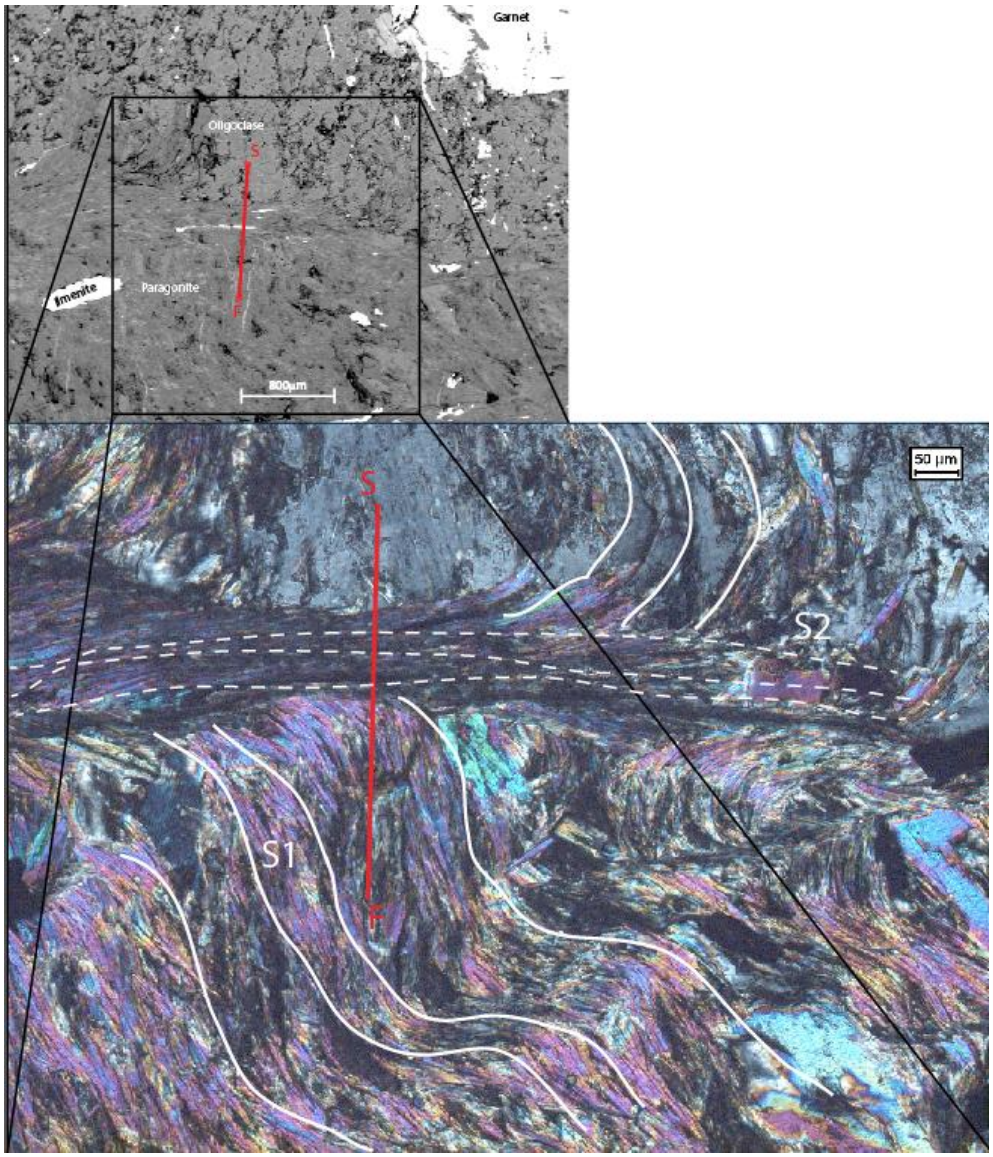

Figure 6..1 BSE image (above) and optical image (below) of thin section P58b-16, section Overview A16-2 (indicated in the thin section overview in the Appendix). Minerals observed are indicated in the BSE image.

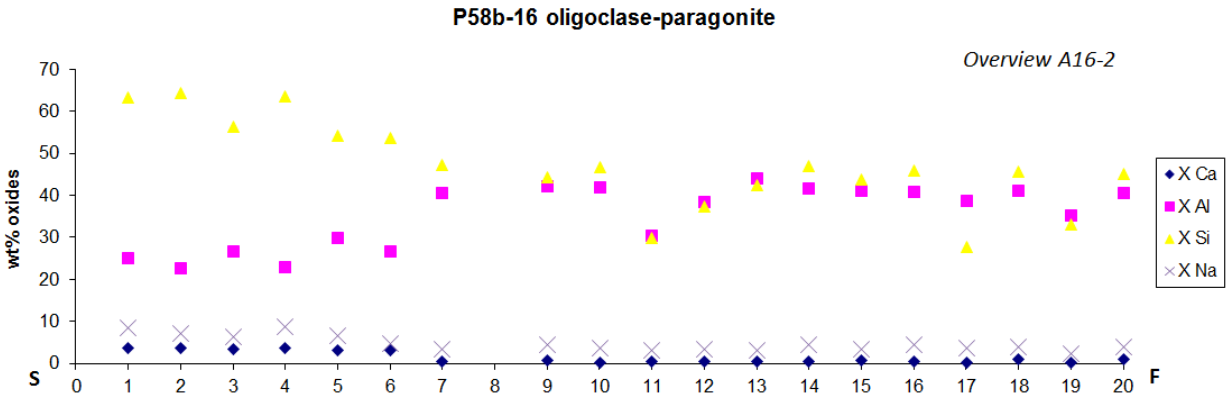

Figure 6.2. Line scan of 20 points whereas point 0 corresponds to point S in figure 5.1.3. Distance between the points is 35µm. Between point 6 and 7 the transition between the oligoclase (left) and paragonite (right) can be recognized.

6. EMP analysis and mineral chemistry

The M2 garnets observed in the samples of this study are in equilibrium with porphyroblasts of plagioclase, biotite, staurolite and kyanite. However the M2 biotite crystals outside the garnet crystals seem to have grown as a reaction rim around it. Indistinctly, it would not form part of the stable mineral assemblage with the M2 garnet. This is caused by changing PT conditions (fig. 6.3; 5.4). Due to these changing P-T conditions, it is worthwhile investigating the chemical heterogeneity of the garnet porphyroblasts. EMP and SEM analyses performed on porphyroblasts and matrix should reveal a chemical heterogeneity and zonation in the P58b samples.

6.1 Matrix

The minerals present in the matrix have been part of the stable 'sedimentary' mineral assemblage S_0 (table 1 section 5.4). It predominantly consists of Na-rich white mica, M1 paragonite (listed in table B, chapter 1.41). EMP elemental analysis on the matrix minerals is plotted in the appendix, section 14.3. A line scan has been drawn in P58b-16, sample Overview A16-2 (fig. 6.2). As can be seen in figure 6.2, the composition changes when the boundary to the matrix is crossed. Matrix chemical analysis were also performed with the scanning electron microprobe (SEM). Analysis 015 and 016 show the matrix composition (table 2). This composition is comparable to the chemical compositions in table B of the appendix.

Table 2 *SEM analysis of M1 paragonite in P58b-7.*

cations	015	016
Al	3.500	3.515
Si	3.175	3.160
Na	0.675	0.805
K	0.135	-

Minerals which are less common in the S_0 'sedimentary' matrix are M1 ilmenite, M1 muscovite and M1 biotite. The chemical composition of the ilmenite porphyroblasts is listed in table E in chapter 14.1. They are compositionally not different from the M3 ilmenite blasts. EMP elemental analysis on ilmenite is plotted in the appendix, section 14.3.

M1 muscovite grains (fig. 5.1C) relatively small compared to M2 and M3 grains (fig. 5.13A; B). Chemically they are comparable with each other (table A in chapter 14.1; table H in section 14.4). Due to the small size (mostly <3µm) no line scans are made on M1 muscovite. The line scans which are performed on the matrix show the paragonite composition since it composes roughly 90% of the matrix. M1 muscovite flakes themselves compose roughly 5% of the matrix. After progressive deformation, the amount of newly formed M1 muscovite grains increases and their contribution to the matrix increases.

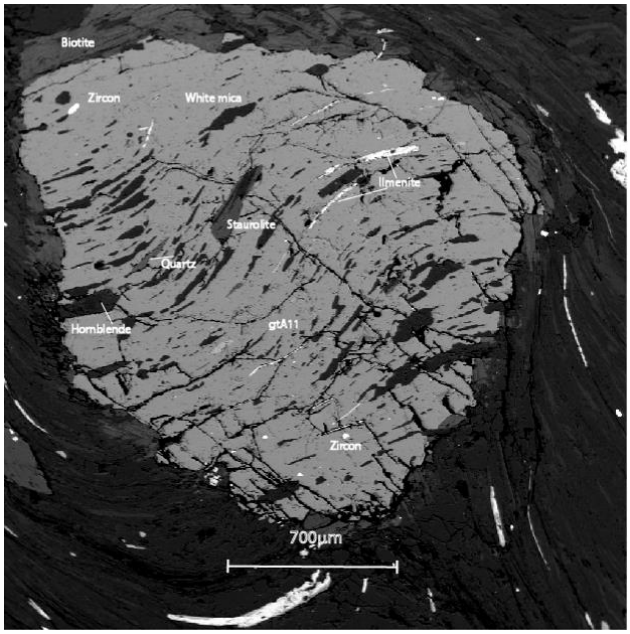

Figure 6.3. P58b-11, sample gtA11Garnet with rotated inclusions showing a biotite rim and a broad scale of inclusions which defines a curved internal fabric (Si).

Chemical analysis of the M1 biotite is listed in table C of the appendix 14.1. The M1 biotite is not homogeneously spread throughout the P58b samples. Especially in regions without large porphyroblasts of garnet, staurolite and kyanite, M1 biotite is observed as matrix material. As with muscovite, it probably represents 5% of the matrix.

6.2 Porphyroblasts

The following section describes the porphyroblasts and their mineralogical relationship with the surrounding matrix.

6.2.1 GARNET

Several EMP linescans were performed on garnet crystals (fig. 6.4; 6.6; 6.7). Over a distance of 300- 450 µm with a distance of 15 µm between two points, WDS point scans showed the composition of the garnets rim section. Analyses with a total compound <96 wt% or >104 wt% were discarded from further use (chapter 14.1). Proper elemental x-ray maps are not performed for this study, since zonation of minerals is not the main aim of research.

As can be seen in figure 6.4, when plotting the weight fraction of Fe versus the distance, there is indeed a small increase of Fe towards the rim of the garnets. The zonation is however small (<2 wt%) and with an factor of error of 1.5% per element analysis for the wavelength dispersive spectrometer (WDS) taken into account, calculations with a presumed zonation might be debatable. Table 3 and figure 6.5 show also a small zonation regarding Fe, Mg and Ca composition. The rims are ‘enriched’ in Fe and slightly depleted in Mg and vice versa for the core compositions. Garnets become more almandine rich towards higher temperature and pressure. Since the garnets are formed in the prograde stages and are unstable in the more retrograde part of the path where the matrix is more Fe-enriched, the zonation might actually represent diffusion with matrix minerals.

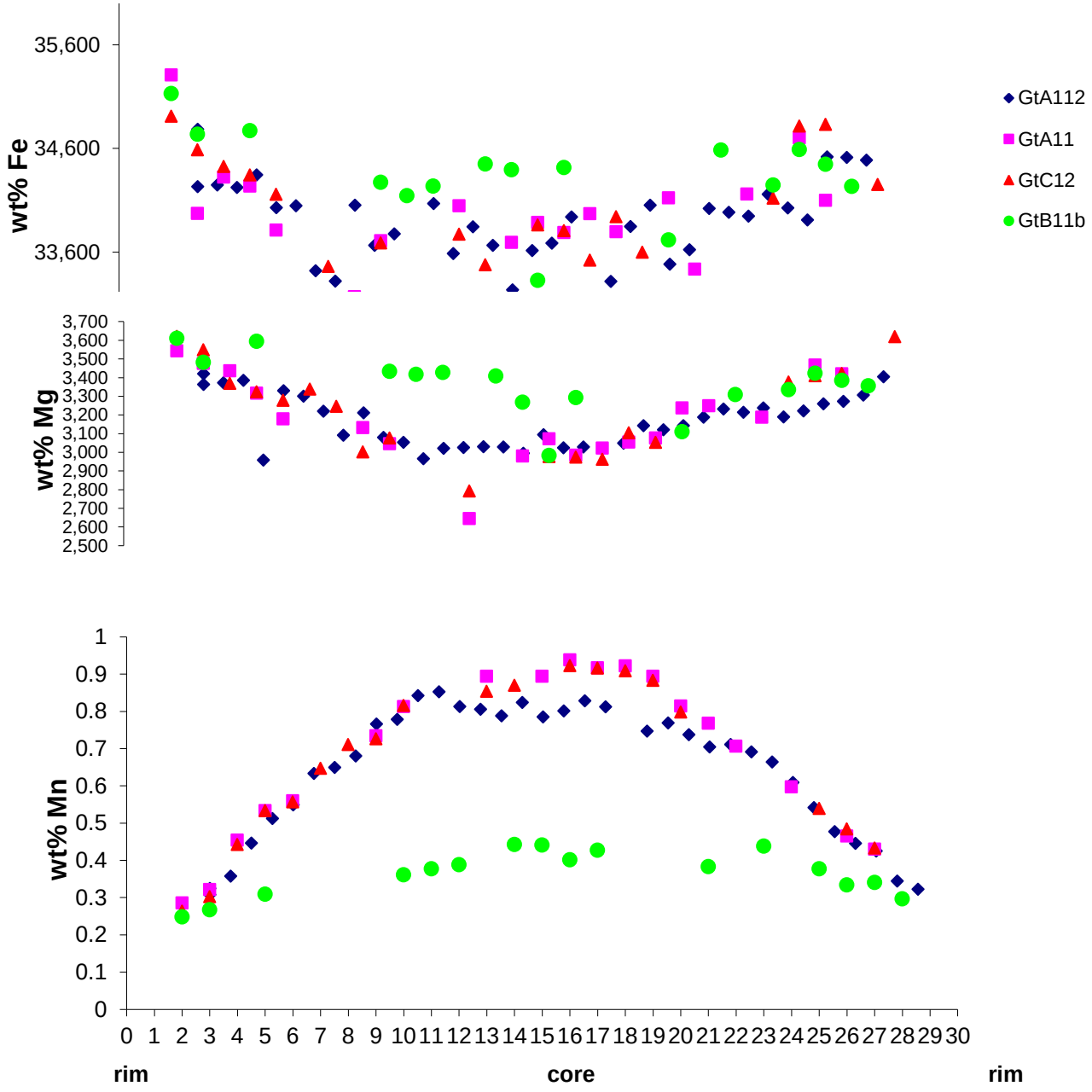

Figure 6.4. Weight fraction of almandine, pyrope and spessartine are plotted against points in line scan. Distance between points is 15μm. EMP line scans across garnets show that a chemical zonation in the elements Mg, Fe and Mn can be observed.

Table 3. See figure 6.4 for an optical overview of line scan Gt16-D2. NA means not available.

cations	GtA112	GtA11	GtC12	GtB11b	GtA12	Gnt16	Gt16D2	Gnt16-2	16A1-2	GtB12
core										
Fe	2,277	2,265	2,262	2,3	2,273	2,274	2,338	2,196	2,283	2,163
Mg	0,379	0,379	0,377	0,402	0,403	0,366	0,407	0,423	0,401	0,405
Ca	0,311	0,306	0,302	0,268	0,055	0,331	0,242	0,213	0,284	0,336
sum	**2,967**	**2,95**	**2,941**	**2,97**	**2,731**	**2,971**	**2,987**	**2,832**	**2,968**	**2,904**
Xfe	0,767	0,768	0,769	0,774	0,832	0,765	0,783	0,775	0,769	0,745
Xmg	0,128	0,128	0,128	0,135	0,148	0,123	0,136	0,149	0,135	0,139
Xca	0,105	0,104	0,103	0,090	0,020	0,111	0,081	0,075	0,096	0,116
rim	R	R	R	R	NA	NA	R	R	NA	NA
Fe	2,322	2,374	2,329	2,364			2,415	2,343		
Mg	0,407	0,424	0,430	0,422			0,417	0,422		
Ca	0,268	0,232	0,218	0,251			0,265	0,221		
sum	**2,997**	**3,030**	**2,977**	**3,037**			**3,097**	**2,986**		
Xfe	0,775	0,783	0,782	0,778			0,780	0,785		
Xmg	0,136	0,140	0,144	0,139			0,135	0,141		
Xca	0,089	0,077	0,073	0,083			0,086	0,074		
sum	1,000	1,000	1,000	1,000			1,000	1,000		

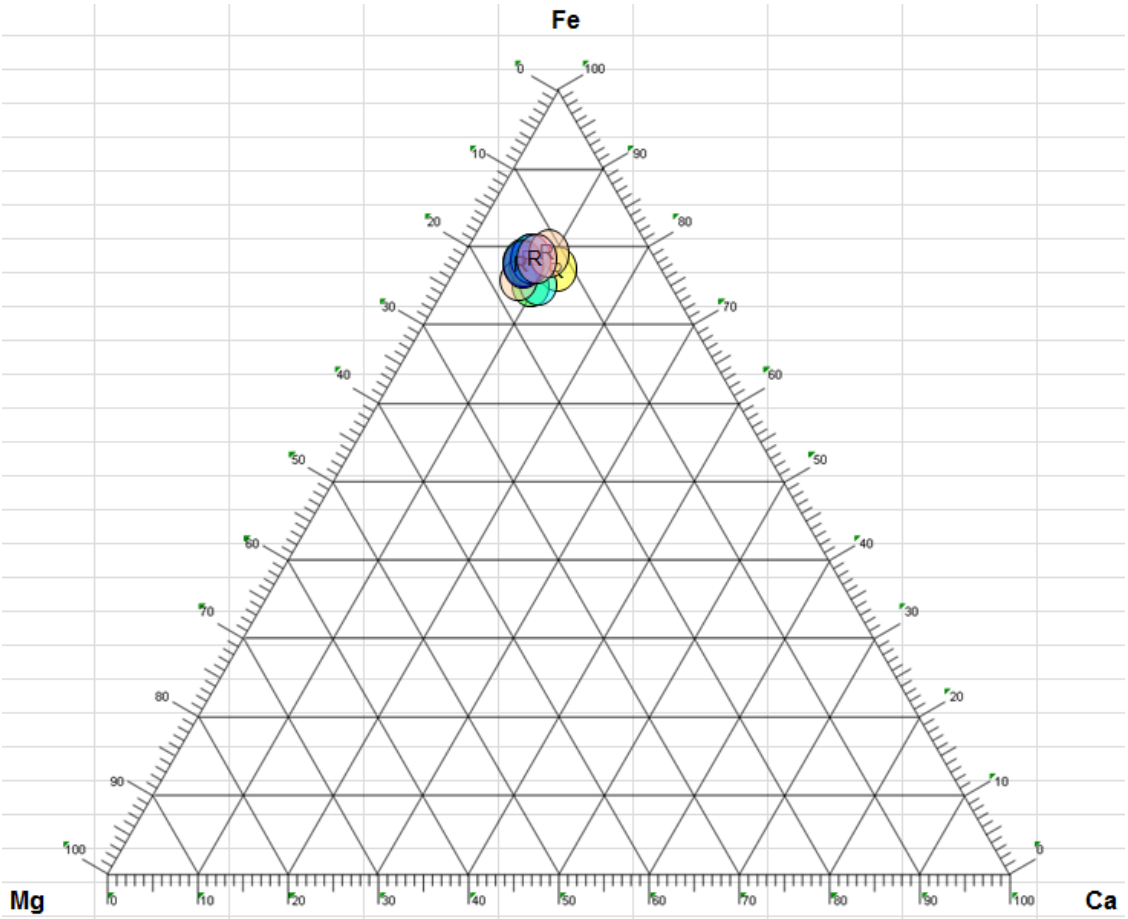

Figure 6.5. Ternary end member diagram of garnet fractions of pyrope (Mg), grossular (Ca) and almandine (Fe+ Mn) are plotted. Colours correspond to colours in table 1. Circles with an R indicate rim compositions.

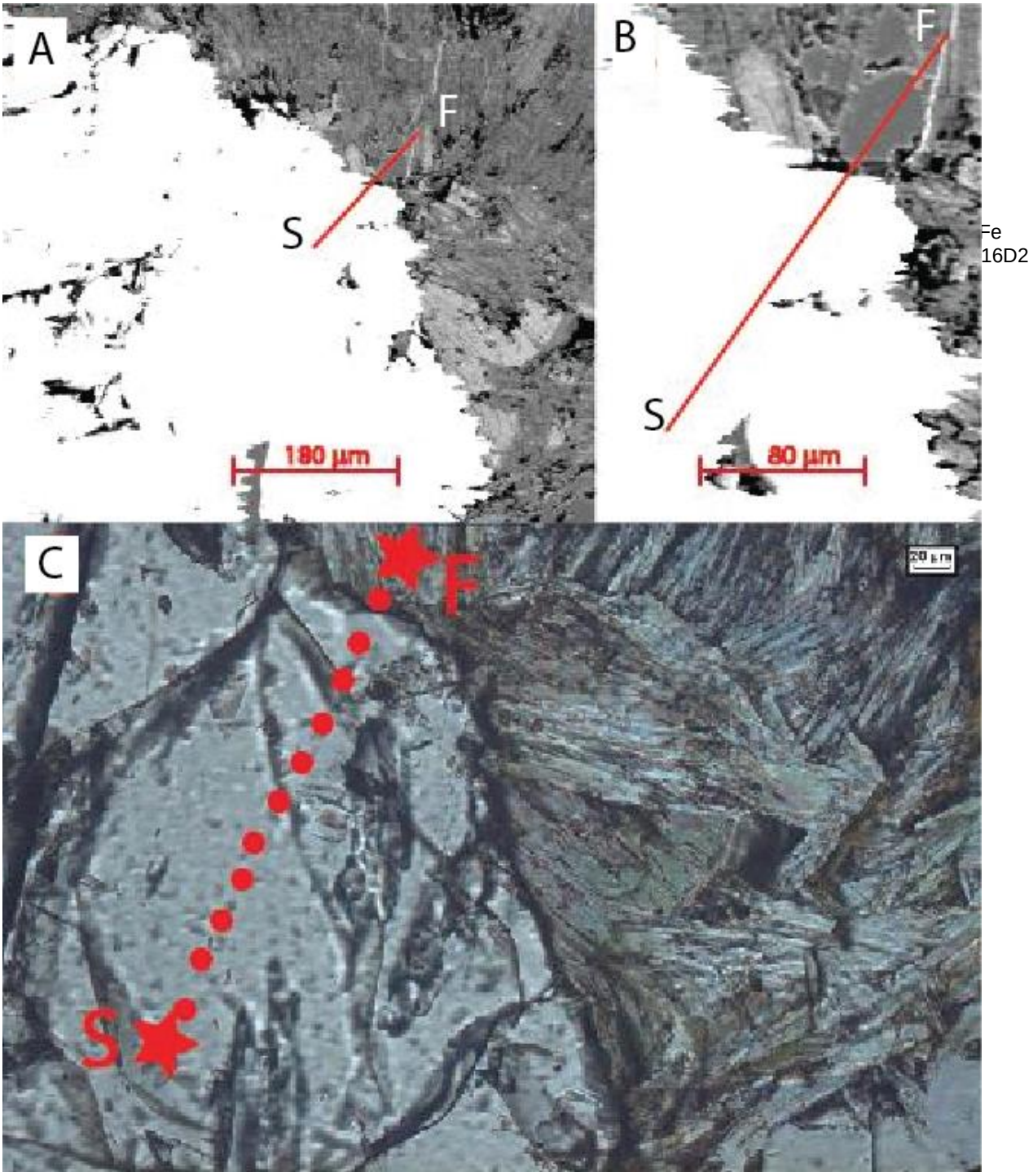

Figure 6..6 (A) BSE image of garnet P58b-16, sample Gt16D-2. The line segment SF indicates the location of the line scan of 15 points. (B) Magnification of picture (A). (C) Light microscope picture of the same blast with the 'S' indicating the first point of the line section and 'F' the final point. The points in between are the remaining line scan points. Line scan results are indicated in appendix chapter 14.3.

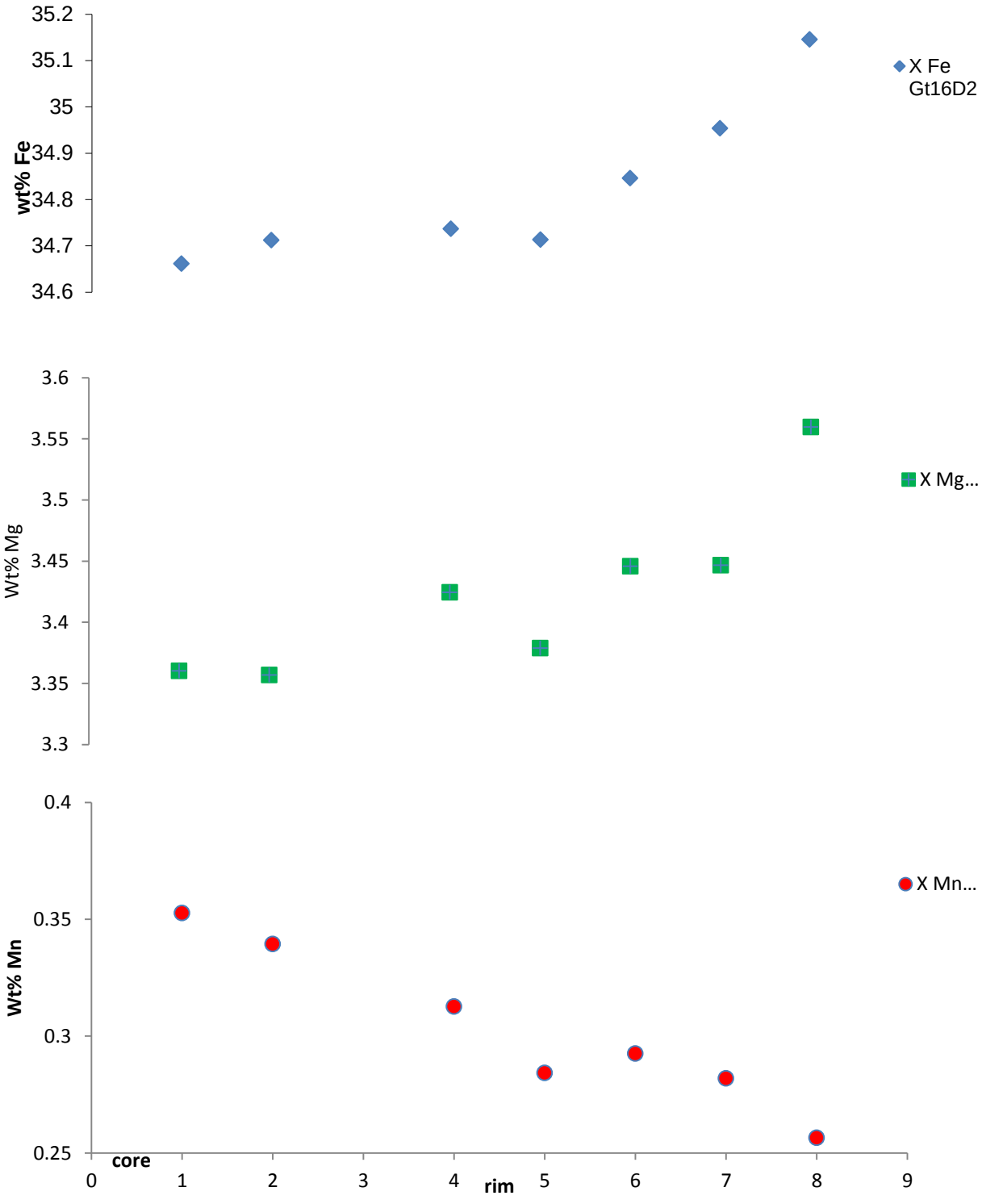

Figure 6.7. P58b-16, sample Gt16D-2 weight fraction of almandine, pyrope and spessartine are plotted against points in line scan. Distance between points is 15µm. EMP line scans across garnets show that a chemical zonation in the elements Mg, Fe and Mn can be observed. Core is related to point S and rim to point F.

Garnet Zonation

The type of zonation present in the porphyroblasts is called diffusion zoning (Spear, 1995), which is basically a modification of the preexisting garnet composition without the addition of later grown garnet. The driving force for this type of diffusion is a change in pressure and temperature. It is however mineral dependent at which speed diffusion happens, where diffusion of similar charged en sized species is quicker. For example, manganese diffusion in garnet is faster than iron diffusion because the 8-fold size in garnet is large and Mn atoms are bigger. Spear (1995) composed a hierarchy of diffusivities for metamorphic minerals:

$$D_{K-Na}^{Micas} >> D_{Fe-Mg}^{Biotite} > D_{Fe-Mg}^{Staurolite} > D_{Fe-Mg}^{Garnet} > D_{Ca}^{Garnet} >> D_{CaAlNaSi}^{Plagioclase}$$

This implies that over geological time micas are homogenized relatively quickly compared to garnet and plagioclase porphyroblasts. This is indeed observed in the P58b thin sections, where biotite and white mica don't show a zonation pattern and garnet does. There are however several assumptions and factors which influence the diffusion of elements. One of the major factors is temperature. Diffusion of cations like Ca, Fe, Mg and Mn in garnet slows down to almost zero (µm-scale) at temperatures between 400 and 500 ^{o}C (Spear, 1995). At higher temperatures, cation exchange increases. The actual amount of diffusion is dependent on the size of the garnet crystals, s total homogenization can only take place if temperature is above >500 ^{o}C long enough to homogenize the whole blast. Another factor is the cooling rate (e.g. exhumation rate) of the rocks. Rocks which cool relatively quickly will tend to record higher temperatures compared to rocks which cool relatively slowly (Spear, 1995).

Since only the outer rim of the garnet crystals is affected by diffusion (fig. 6.7), we assume the temperature has not been significantly high to homogenize the whole sample. Therefore, the core composition reflects the composition and temperature of formation whereas the rim composition will show the temperature at which garnet exchanged cations with biotite and/or matrix. The difference between core and rim compositions remains relatively small due to this small amount of diffusion, before temperature dropped below 500 ^{o}C and diffusion of garnet stopped.

6.2.2 STAUROLITE

Staurolite minerals do not show any zoning (fig 6.8; 6.9). Their composition is relatively Fe-rich, as observed in the garnet porphyroblasts. EMP compositional line scan data are listed in table F in the appendix chapter 14.1. Staurolite M2 porphyroblasts have grown after D_1 and before or during D_2 according to their straight and slightly rotated inclusion paths (fig 5.6). It is the most common porphyroblast in the thin sections, volumetrically.

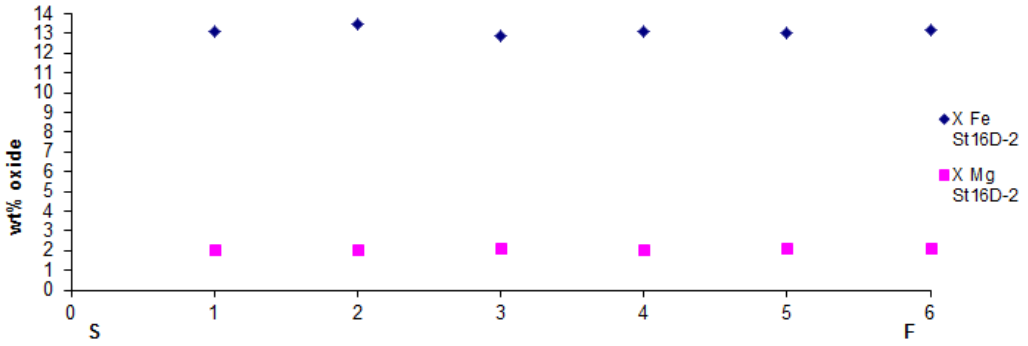

Figure 6.8. EMP chemical line scan of the six points corresponding to the BSE image of M2 staurolite in figure 6.9. Note the homogeneity of the staurolite towards the rim.

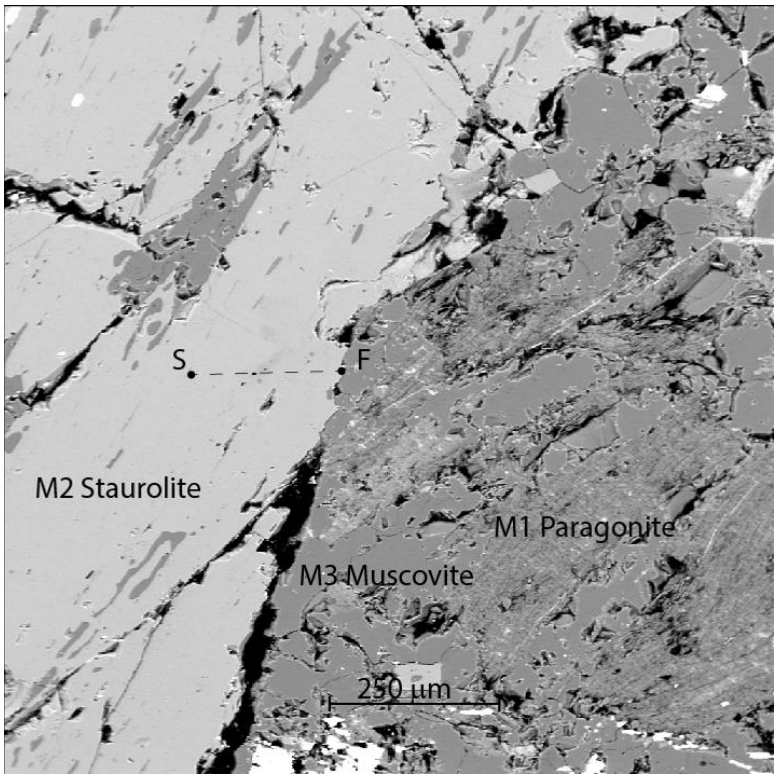

Figure 6.9. P58b-16, sample St16D-2 BSE image M2 staurolite in contact with M1 paragonite in matrix and M3 muscovite minerals. Distance between the points is 30 µm.

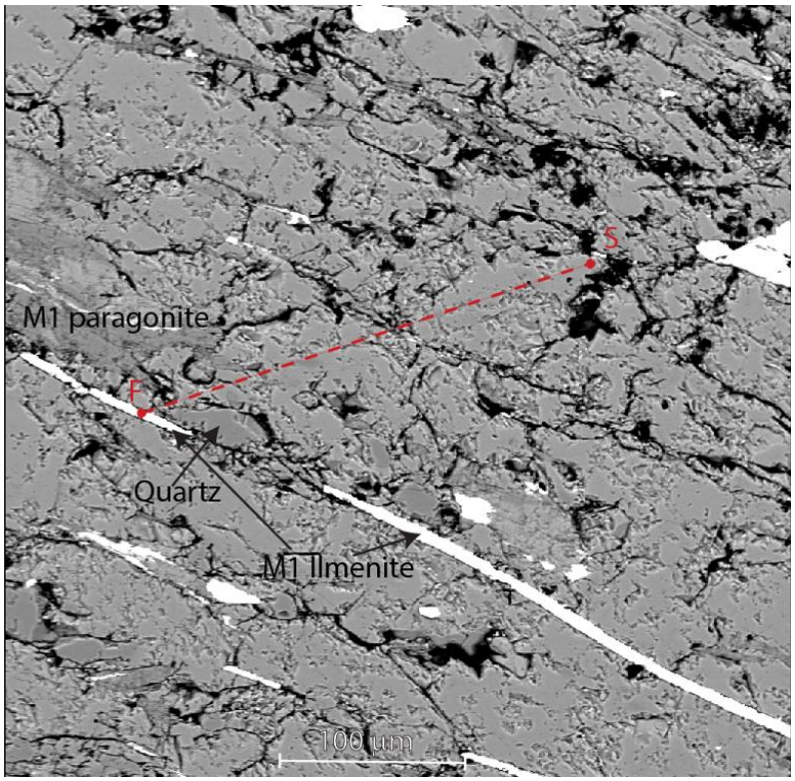

Figure 6.10. P58b-11, sample C11-a BSE image M3 oligoclase porphyroblast. Line scan performed on crystal starts at 'S' and finishes at 'F'.

6.2.3 OLIGOCLASE

Several line scans are performed on oligoclase porphyroblasts. They are compositionally all similar to each other, which inidcates similar P-T conditions of growth. One example, P58b-11 C11-a is shown in figure 6.10. Line scan data of this sample are listed in table 4. Figure 6.11 indicates the presence of Na, K and Ca on the A-site of plagioclase ($AB_{2/3}C_{2/3}O_8$). The majority of the samples plots in the area 10-30 An% and therefore the mineral is oligoclase.

The porphyroblasts are fairly homogeneous. Irregularities are caused by inclusions of other minerals, like quartz and ilmenite (fig. 6.10). Porphyroblasts follow the F_2 outline of the cleavage domains. Since the inclusions in the blasts also follow the F_2 outline the minerals are syn-D_2. Minerals of this phase are named M3.

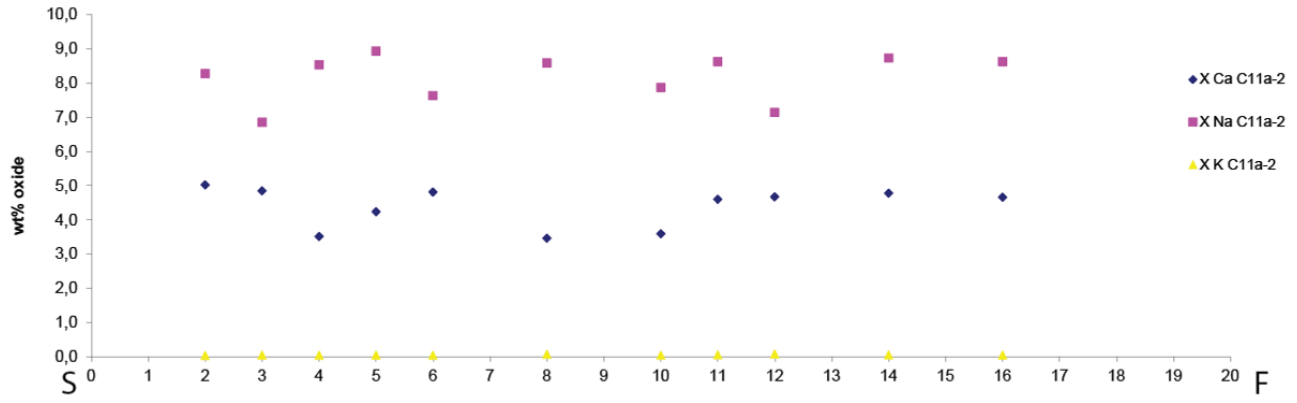

Figure 6.11. P58b-11, sample C11a line scan analysis. Note the absence of K in the sample.

Table 4. EMP line scan P58b-11, sample C11-a point analysis corresponding to figure 6.11 line scan.

POINT	Si	Al	Fe	Mn	Mg	Ca	K	Na	Ti	Cr	Total	
	Wt% oxide	Wt% oxide	Wt% oxide	Wt% oxide	Wt% oxide	Wt% oxide	Wt% oxide	Wt% oxide	Wt% oxide	Wt% oxide		
1 - S	54,736	18,698	0,222	0,000	0,004	3,117	0,055	8,292	0,009	0,000	85,1	discarded
2	63,304	23,609	0,000	0,000	0,000	5,020	0,037	8,271	0,000	0,011	100,3	
3	65,926	25,501	0,056	0,023	0,003	4,846	0,046	6,852	0,006	0,000	103,3	
4	65,415	22,303	0,052	0,018	0,005	3,513	0,043	8,531	0,000	0,005	99,9	
5	61,670	22,914	0,042	0,018	0,003	4,239	0,048	8,927	0,003	0,000	97,9	
6	62,082	25,023	0,001	0,000	0,006	4,812	0,046	7,632	0,000	0,000	99,6	
7	59,164	23,511	0,000	0,000	0,000	4,861	0,057	8,247	0,024	0,008	95,9	discarded
8	66,557	24,448	0,199	0,000	0,013	3,462	0,069	8,581	0,009	0,000	103,3	
9	58,006	26,461	0,064	0,036	0,019	4,067	0,058	6,876	0,010	0,000	95,6	discarded
10	63,089	23,655	0,033	0,045	0,000	3,594	0,042	7,867	0,000	0,000	98,3	
11	62,540	23,262	0,016	0,000	0,005	4,598	0,058	8,621	0,000	0,008	99,1	
12	63,018	24,234	0,052	0,000	0,000	4,669	0,083	7,139	0,000	0,000	99,2	
13	52,930	21,723	0,108	0,000	0,015	3,413	0,060	6,601	0,008	0,000	84,9	discarded
14	62,883	23,677	0,006	0,000	0,000	4,776	0,052	8,732	0,000	0,007	100,1	
15	33,688	12,313	0,046	0,000	0,005	4,158	0,052	5,905	0,000	0,000	56,2	quartz
16	63,079	23,503	0,070	0,002	0,000	4,659	0,047	8,620	0,027	0,000	100,0	
17	44,879	20,295	0,000	0,007	0,000	3,444	0,041	4,695	0,023	0,000	73,4	discarded
18	61,395	32,206	0,199	0,000	0,006	3,615	0,061	10,217	0,019	0,014	107,7	discarded
19	56,271	23,032	0,166	0,000	0,007	4,291	0,065	6,503	0,072	0,007	90,4	discarded
20 - F	1,130	0,788	44,535	0,085	0,480	0,148	0,000	0,076	50,852	0,039	98,1	Ilmenite
	63,597	**23,830**	**0,048**	**0,010**	**0,003**	**4,381**	**0,052**	**8,161**	**0,004**	**0,003**	**100,1**	

Table 5. Plagioclase porphyroblast composition on A-site. Ratio between Ca, Na and K is indicated in ternary end member diagram below.

cations	PlC12	Pl16A	16A2	C11a	OverviewA16-2	GtB11inc3	B12matrix1
Na	0.821	0.623	0.706	0.786	0.709	0.763	0.681
K	0	0.181	0.003	0	0.004	0	0.002
Ca	0.17	0.002	0.164	0.169	0.174	0.197	0.217
sum	**0.99**	**0.81**	**0.87**	**0.96**	**0.89**	**0.96**	**0.90**
Xna	0.83	0.77	0.81	0.82	0.80	0.80	0.76
Xk	0.00	0.22	0.00	0.00	0.00	0.00	0.00
Xca	0.17	0.00	0.19	0.18	0.20	0.20	0.24
sum	**1.00**	**1.00**	**1.00**	**1.00**	**1.00**	**1.00**	**1.00**

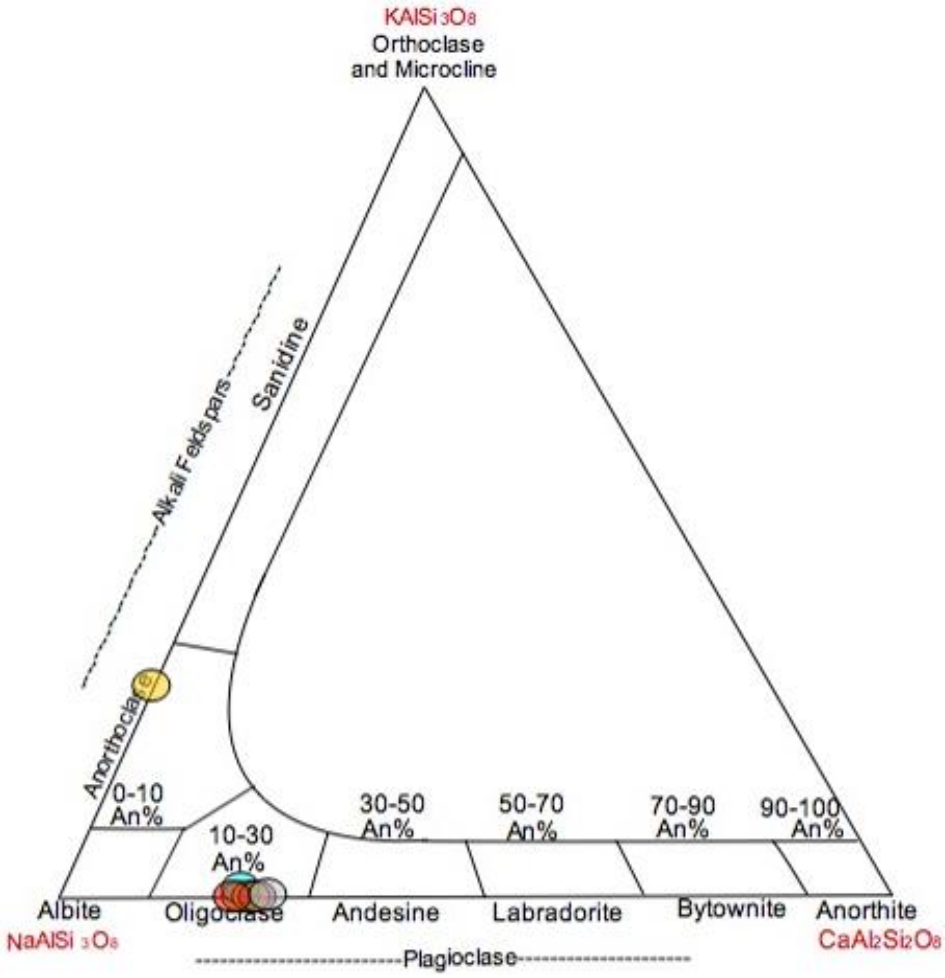

Figure 6.12. Composition of plagioclase porphyroblasts plotted in a ternary end member diagram. All samples plot in the oligoclase field except for Pl16A. The latter is alkali feldspar.

6.2.4 KYANITE

Kyanite porphyroblasts can be subdivided into two groups. The first group of porphyroblasts shows undulatory extinction, which is an indication of pre- or syn-deformational growth. Therefore, this first group are M2 kyanite porphyroblasts. The second group of kyanites grows over the cleavage domains (fig. 6.13) and shows no deformational features. They have a blocky shape and grow predominantly over cleavage domains.

The minerals are homogeneous and do not show any other elements on their sites. An X-ray energy spectrum is shown in figure 6.14. No other aluminium-oxide phases as sillimanite or andalusite are observed.

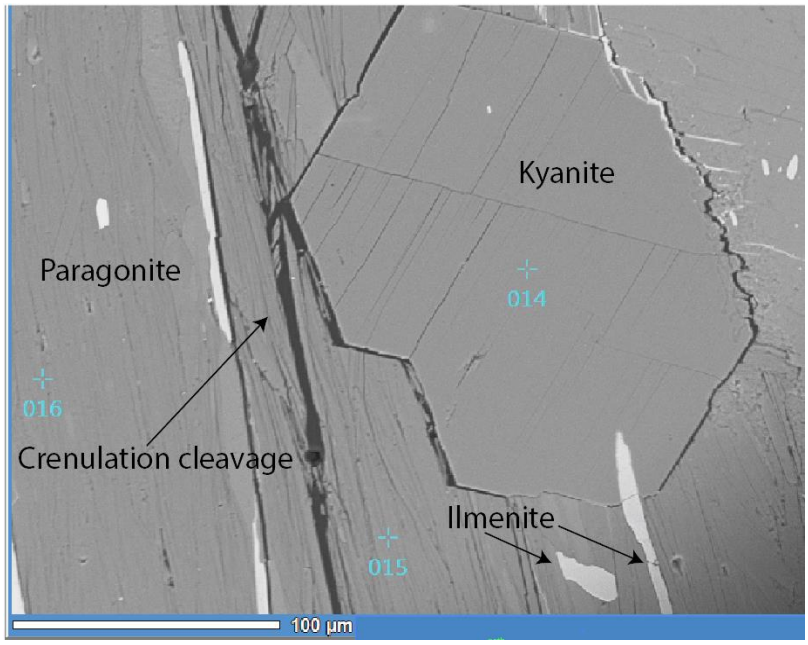

Figure 6.13. P58b-7, sample 014 BSE image of M3 kyanite porphyroblast together with M1 and M3 ilmenite and M1 paragonite.

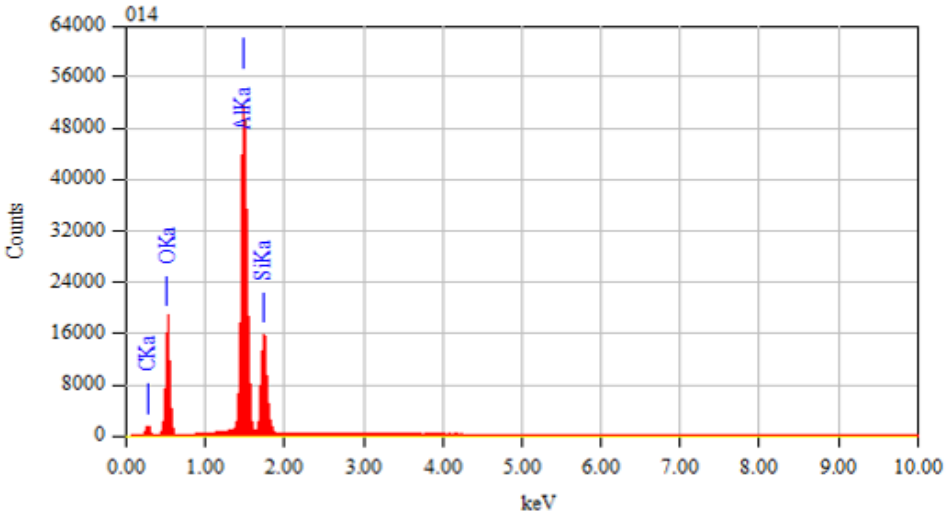

Figure 6.14. X-ray energy spectrum of sample 014 in figure 6.13.

6.2.5 BROWN MICA

Brown mica porphyroblasts can be subdivided into M1 minerals. This type of biotite was present at S_0 and is part of the mica-rich crenulated cleavage domains. The second type of biotite has grown adjacent to garnet as a reaction product and is marked as M2. EMP chemical analysis of the biotite porphyroblasts is listed in table C of appendix, chapter 14.1. An X-ray energy spectrum of the elements is plotted in chapter 14.3 in the appendix. As can be seen in figure 6.15, both types of biotite have a similar composition. The mineral contains quite similar weights of Fe, Al and Mg and hence the mineral is named biotite.

SEM chemical analysis of some porphyroblasts is also performed on M2 biotite flakes (fig. 6.16). Chemical compositions are listed in table 6 and figure 6.17 and show an X-ray energy spectrum of the SEM spot analysis. This analysis indicates a slightly more magnesium-enriched endmember of biotite (fig. 6.15).

Table 6. P58b-7 sample 013 chemical analysis Fe assumed to be all Fe^{2+}; calculations based on 24 oxygen.

elements	cations
Mg	3.52
Al	3.67
Si	5.82
K	2.06
Fe	2.30
sum	17.38

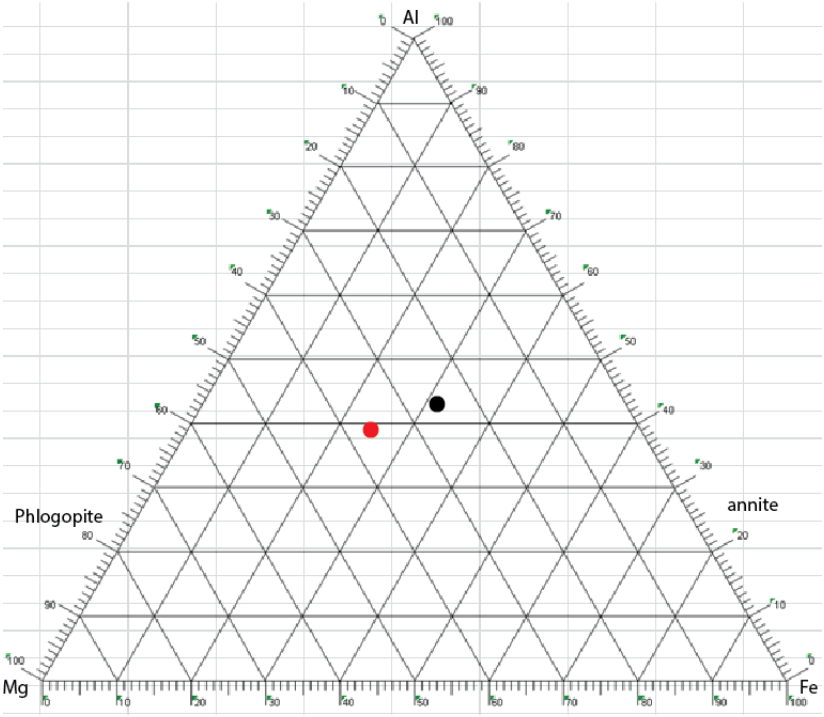

Figure 6.15. Ternary phase diagram of EMP analysis P48b M1 and M2 biotite samples, indicated by the black dot. SEM analysis of P58b-7 sample 013 indicated by the red dot.

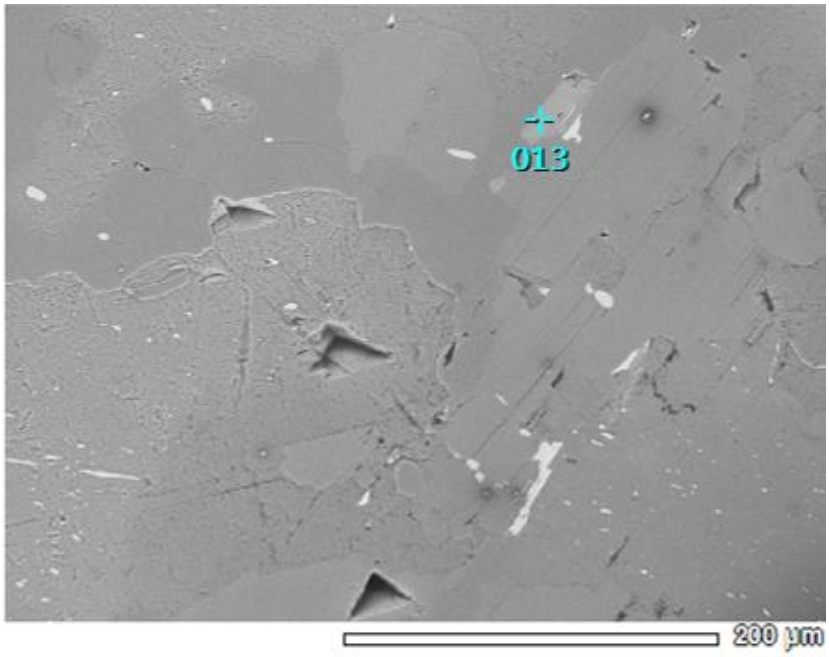

Figure 6.16. ***P58b-7, sample 13, BSE image of M2 biotite porphyroblast.***

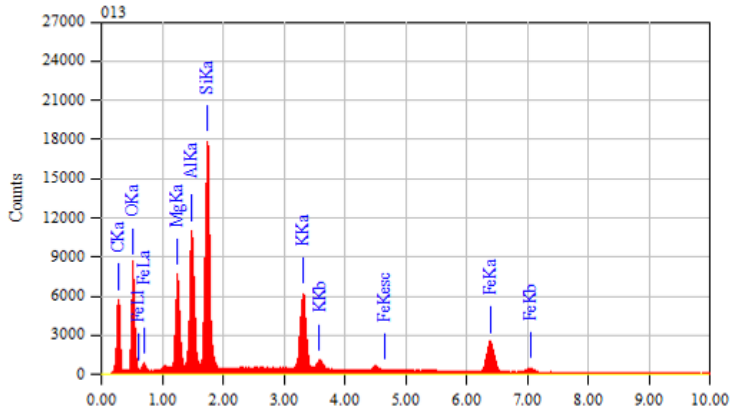

Figure 6.17 X-ray energy spectrum of M2 biotite SEM point analysis.

6.2.6 ILMENITE

The porphyroblasts of ilmenite are the only major phases that contain titanium. EMP chemical analysis performed on the porphyroblasts is listed in table E of 14.1 in the appendix. A spot analysis is indicated in 14.1 in the appendix. The ratio of Fe/Ti is roughly 1 in all the analysed ilmenite porphyroblasts. Hence, there exist no significant chemical changes between the M1 and M3 types. Ilmenite can form a solid solution with pyrophanite (Mg-component) and commonly contains a proportion of giekelite ($MgTiO_3$). This is however, not commonly observed in the P58b metapelite.

6.2.7 WHITE MICA

The group of white mica can be subdivided into three different stages of growth. M1 is part of S_0 and included in both deformation phases S_1 and S_2 (fig. 5.1C). M2 has grown syn- to post-

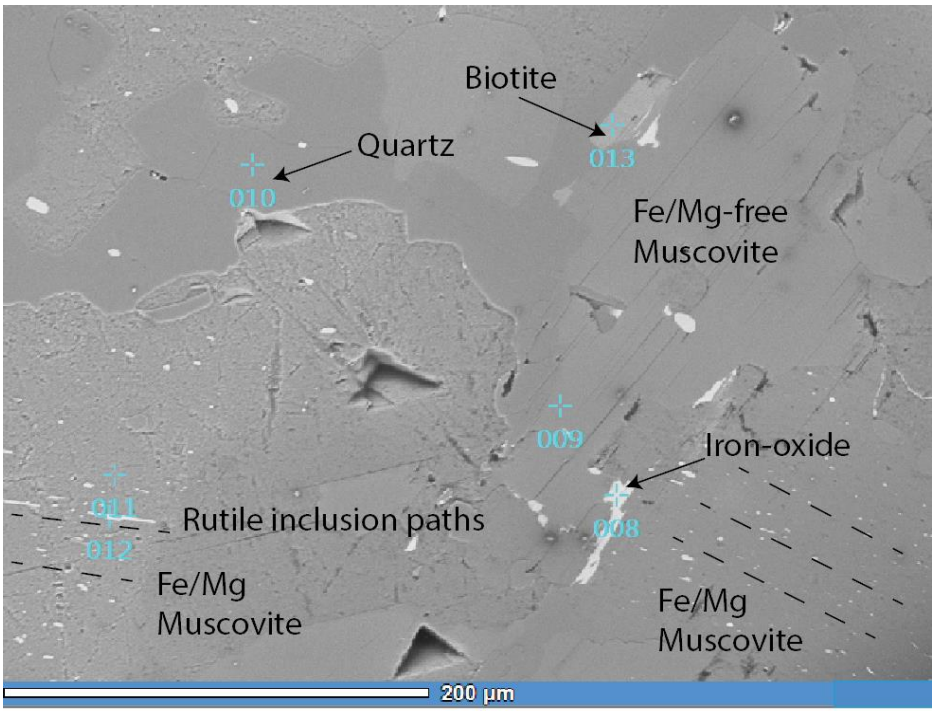

Figure 6.18 P58b-7 BSE image of M2 muscovite flakes with rutile inclusions. Black dashed lines indicate rutile inclusion path orientation.

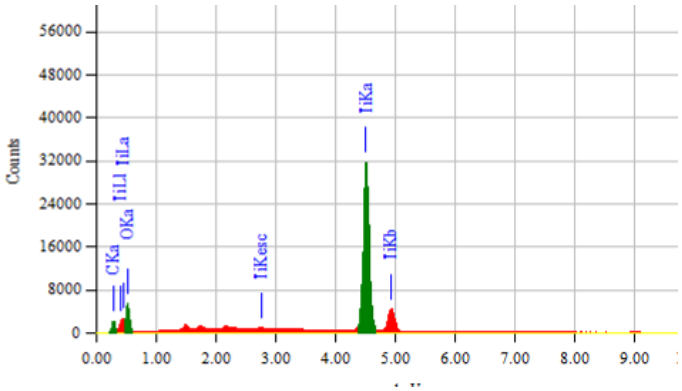

Figure 6.19. SEM X-ray energy spectrum of P58b-7, sample 004.

D_2 and contains exsolved rutile needles on top (fig. 5.13A; 14.5 in appendixes). M3 has grown post-D2 and forms recrystallised muscovite flakes on top of oligoclase porphyroblasts (fig 5.8D). Despite their different stages of growth, the porphyroblasts do not differ majorly on a chemical basis. EMP chemical analyses are listed in table A of chapter 14.1 in the appendix. X-ray energy spectrum of EMP point analyses is included in chapter 14.2 in the appendix. No proper EMP line scan analyses are performed on M2, M3 muscovite crystals.

SEM chemical analysis performed on sample P58b-7 M2 muscovite porphyroblasts is listed in table 7; fig 6.18. The observed inclusions are aligned inside the muscovite porphyroblasts. They follow the F_1 foliation.

Table 7. ***SEM analysis of M2 muscovite in P58b-7.*** *Fe assumed to be all Fe^{2+}; calculations based on 24 oxygen.*

cations	**001**	**003**	**006**	**007**	**009**	**011**
Al	6.29	6.36	6.17	6.43	6.37	6.28
Si	6.69	5.70	6.65	6.64	6.66	6.59
K	1.65	-	1.58	1.62	1.78	1.59
Na	0.44	0.61	0.42	0.55	0.48	0.42
Fe	0.14	0.64	0.13	-	-	0.12
Mg	-	2.11	0.31	-	-	0.27
sum	15.21	15.42	15.26	15.23	15.28	15.28
inclusions?	yes	yes	yes	no	no	yes

Table 8. SEM analysis of inclusions in M2 muscovite in P58b-7.

004	Rutile
012	Rutile

The inclusions which are observed in sample 011 and 003 are samples 012 and 004 respectively (table 8). The inclusions observed are μm-scale rutile needles (TiO_2). An X-ray energy spectrum of the needles is plotted in figure 6.19. Following the grain boundaries, grains which include rutile inclusions can be distinguished from grains which do not contain inclusions. As can be seen in table 7, the rutile needles only exist in mica when any amount of Fe or Mg is present. For example sample 009 in figure 6.18 does not contain any Fe and Mg and hence no aligned TiO_2 inclusions, whereas the adjacent grain 011 is not that different but contains needles of TiO_2.

7. Thermodynamics

When computer-based programs are used in order to create pseudosections out of a bulk rock composition, thermodynamic data are important. A pseudosection is a phase diagram that shows the assemblage in a system of specified bulk rock composition as a function of two variables (P and T in our case). Information regarding the entropy, enthalpy and Gibbs free energy of minerals is essential to predict which minerals are stable at certain PT conditions. There are multiple databases with thermodynamic data. This study uses that of Holland and Powell (1998). Creating PT sections is possible with a theoretical method and in a practical approach. Both methods need bulk rock chemical data to predict mineral stability. The bulk rock composition is described in the first section.

This study uses Perple_X (Connolly, 2005) to calculate PT pseudosections. These pseudosections are compared with pseudosections created with another thermodynamic database in TheriakDomino (de Capitani, 1994). Secondly, geothermobarometry is used as a practical approach. Stable mineral assemblages should indicate PT conditions of growth. A combination of these three methods should give good constraints on the PT path of metapelite P58b in the Lukmanier Pass area.

7.1 Bulk rock composition

X-ray fluorescence (XRF) analysis is performed on hand sample P58b (table 9). All P58b thin sections used in this study (chapter 14.3 in appendix) have therefore the same bulk rock composition (BRC). This BRC is used as input data in the theoretical and practical studies of Perple_X, TheriakDomino (TD) and geothermobarometry.

To create a P-T-(t) path you have to choose a bulk rock chemical system first. The minerals present in the investigated metapelitic rocks from this study would require a chemical system with the components SiO_2, Al_2O_3, MgO, CaO, FeO, K_2O, Na_2O, TiO_2, MnO included. The amount of P_2O_5 is 0.13 wt% and hence discarded from further use. Since there is a significant amount of Na_2O present in the rocks and a relatively small amount of MgO the K (= K_2O) N (= Na_2O) F (= FeO + MgO) A (= Al_2O_3) S (= SiO_2) H (= H_2O) system is used to plot the stabilities of the metamorphic minerals. The KNFASH system assumes quartz and H_2O saturation which is reasonable for these rocks. A lot of water is released from micaceous minerals along the prograde path and staurolite contains also some water which causes a permanent saturation of the rocks when released. Quartz saturation is reasonable to assume due to the high amount in the bulk rock composition (48.32 wt%) and the fact that it is a felsic metapelitic schist. The amount of CO_2 is set to 0 since hardly any carbonaceous matter is observed in the rocks.

Table 9. Bulk rock chemical composition of hand sample P58b. Trace elements are unused in this study. P58b is LOI corrected for orogenic material using a Leco TGA701.

Monster	SiO_2	Al_2O_3	TiO_2	FeO	MnO	CaO	MgO	Na_2O	K_2O	P_2O_5	Sum
	%	%	%	%	%	%	%	%	%	%	%
JK1-P58b	48.32	36.33	1.67	6.09	0.02	0.98	0.81	4.41	1.24	0.13	100

7.2 Perple_X

In the following section the Perple_X software is explained and how it is used to create PT pseudosections for certain bulk rock compositions. Since the software is fairly new and still under development by their creators, a first-approach for calculation is attached in chapter 14.6 in the appendix. The second part of this chapter shows some of the PT pseudosections and isopleths created. Isopleth maps are created for garnets where the ratio of pyrope (Mg), almandine (Fe) and andradite (Ca) are plotted against each other. The obtained EMP ratio between the elements can be observed in the graph and this indicates a stable assemblage at the time of growth.

7.2.1 Calculation method

The main aim of this study is to derive the P-T path of the rocks from the Lukmanier Pass area. In order to do so, a P-T pseudosection was calculated using Perple_X and coherent packages. The range of pressure and temperature range conditions are set to 0 - 20 kbar and 500 – 1000 K. In addition, isopleths of end members of different minerals were added to the PT diagram (fig. 8.3). Examples are the Si content in white mica and the modal parameters like weight fractions of almandine (Fe), grossular (Ca) and pyrope (Mg) in garnet.

For the calculations in Perple_X the thermodynamic data set of Holland and Powell (1998), with their specific model CORK (Holland and Powell, 1990) was used. Since the thermodynamic data set of Holland and Powell was used, most of the used solid-solution models were compatible to the data set of Holland and Powell (1998). In the solid-solution model from Perple_X the following solid-solutions were chosen: San and Kf for alkali feldspars, Pl(h) for plagioclase, TiBio(HP) for biotite, Carp for carpholite, Chl(HP) for chlorite, Ctd(HP) for chloritoid, IlGkPy for ilmenite, Pheng(HP) for potassic white mica with a maximum content of 30 mol% paragonite, MaPa for white mica with a higher paragonite content of 30 mol%, St(HP) for staurolite and Gt(HP) for garnet. Phases which do not play a part regarding the stability of the solution-models above and do not have a relation with metapelitic rocks were excluded (fig. 7.1).

The pseudosection was calculated for the SiO_2-TiO_2-Al_2O_3-MgO-MnO-FeO-CaO-Na_2O-K_2O-O_2 system. H_2O was taken as an (over)saturated phase, $P_{H2O} \geq 1$, since the metapelitic rocks contain a significant amount of hydrous minerals (e.g. micas, tourmaline) and CO_2 was neglected since there are hardly any carbonate-rich rocks present in the environment.

7.2.2 Results: PT pseudosections and isopleths

Hand sample P58b was used to calculate the pseudosection illustrated in figure 7.2. The large amount of different fields can be explained by the high amount of stable assemblages and incorporated phases. Water is stable throughout the whole P-T range shown here and assumed to be $P_{H2O} \geq 1$ throughout the evolution of the rock. Note that only the most important fields are highlighted and smaller fields are ignored in order to maintain an overview. The grey tones of the P-T fields are related to the variance [degree of freedom; f = C (components) + 2 (T and P) – φ (number of phases)] of the corresponding mineral assemblage. This means, the darker the field, the greater the variance is.

The following aspects are here of importance in analyzing the pseudosection. Chloritoid, lawsonite and carpholite are unstable above respectively 850 K, 780 K and 740 K. Chlorite appears below 850 K and is moreover only stable below 22 kbar. K-rich mica phengite is stable throughout nearly the whole section, except for temperatures above 800 K coupled with

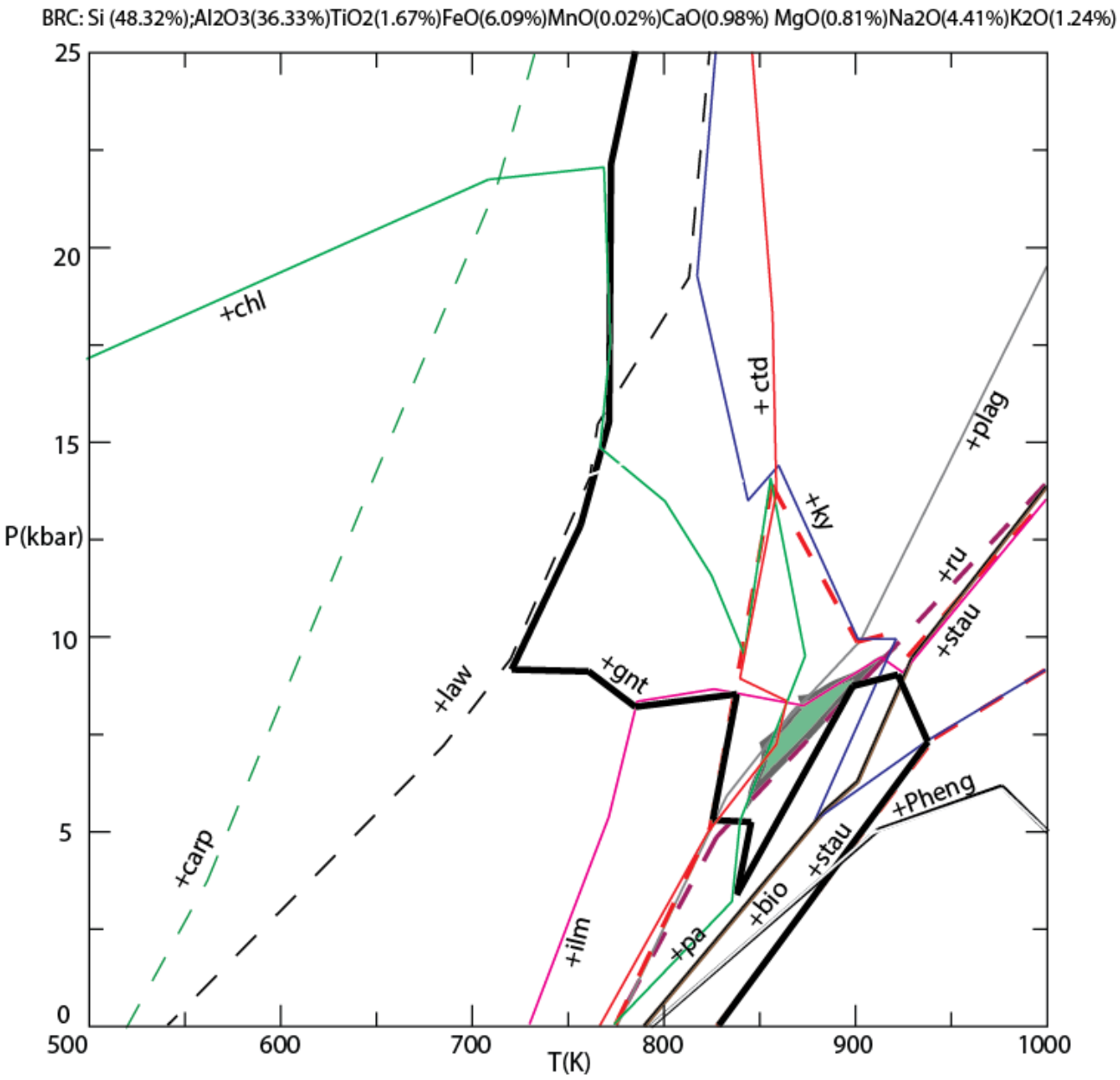

Figure 7.1. Pseudosection created with BRC of P58b in Perple_X. Outlined is the stability field of the assemblage rutile + M3 plagioclase + M2 staurolite + M 2 muscovite. Phase boundary lines indicate stability fields of separate phases present in a metapelitic system. Quartz + water are stable throughout the whole section.

pressures below 8 kbar. The Na-rich mica paragonite is stable in similar fields as phengite, but is unstable at temperatures of > 800 K coupled with pressures below 13 kbar. The same is true for rutile and quartz which are unstable phases in P-T fields > 780 K and 18 kbar.

Interesting for the present study is the PT stability field of the main porphyroblasts and/or matrix minerals in a P-T diagram. Kyanite is stable at high-pressure conditions above 800 K and is transformed into sillimanite below 8 kbar at 1000 K following the generally accepted phase diagram of the Al-Si-O phases. Ilmenite and biotite appear at temperatures above 730 K and 780 K respectively. Both minerals are bound by upper pressures of 12 kbar. Oligoclase (10-30 An%) appears at temperatures above 750 K. Compositional differences in plagioclase

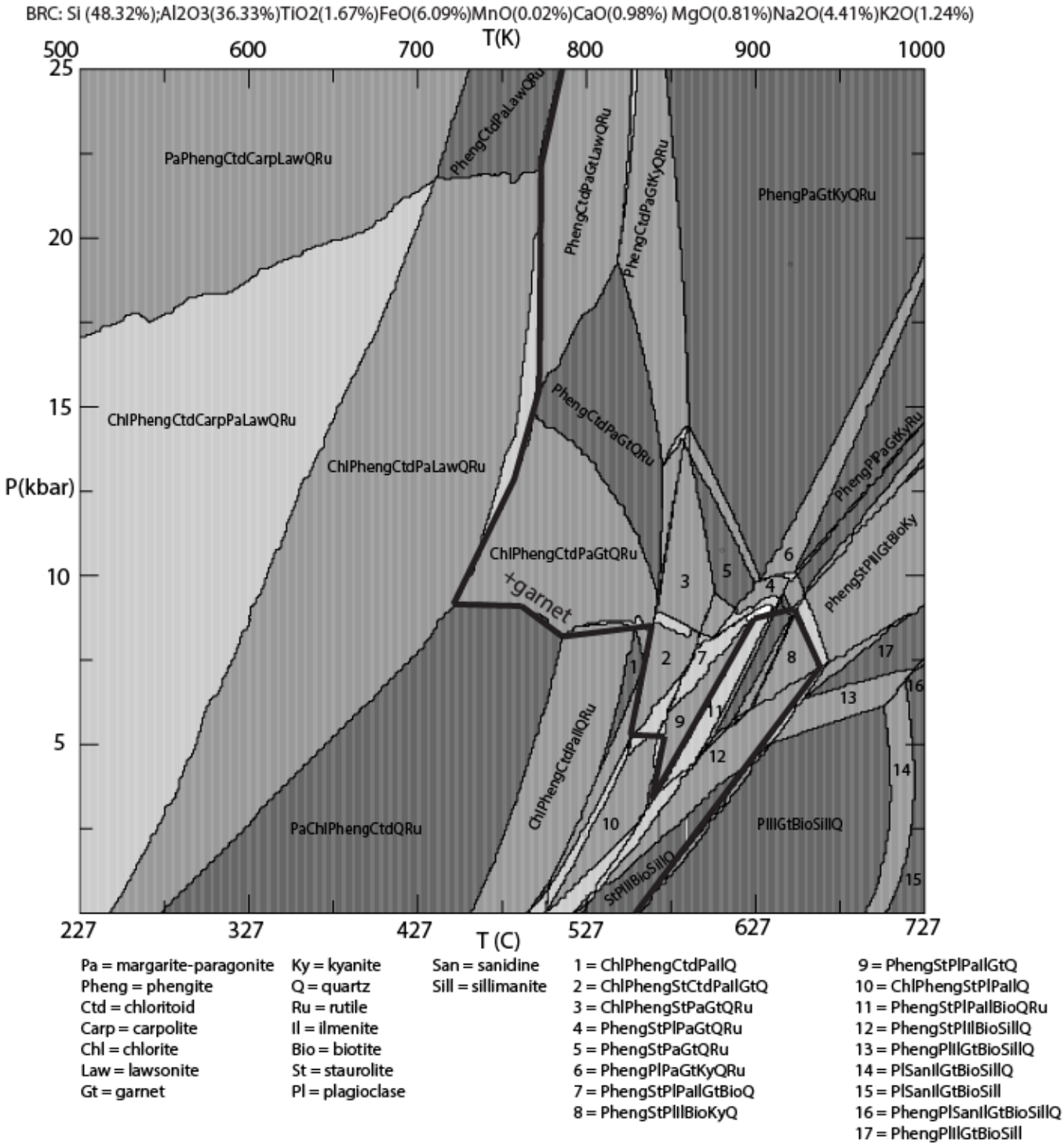

Figure 7.2. Pseudosection illustrating fields of the stable mineral assemblage as indicated. Quartz + water are stable throughout the whole section.

will indicate a more albite to anorthite rich phase, which has consequences for the stability of the plagioclase phase in a P-T diagram.

Staurolite is stable in P-T space above 780 K and has an upper stability limit of 13 kbar. Porphyroblasts are unstable in a field above 830 K and below 7 kbar. Depending on the molar fractions of iron and magnesium staurolite is stable at a certain range of pressure and temperature.

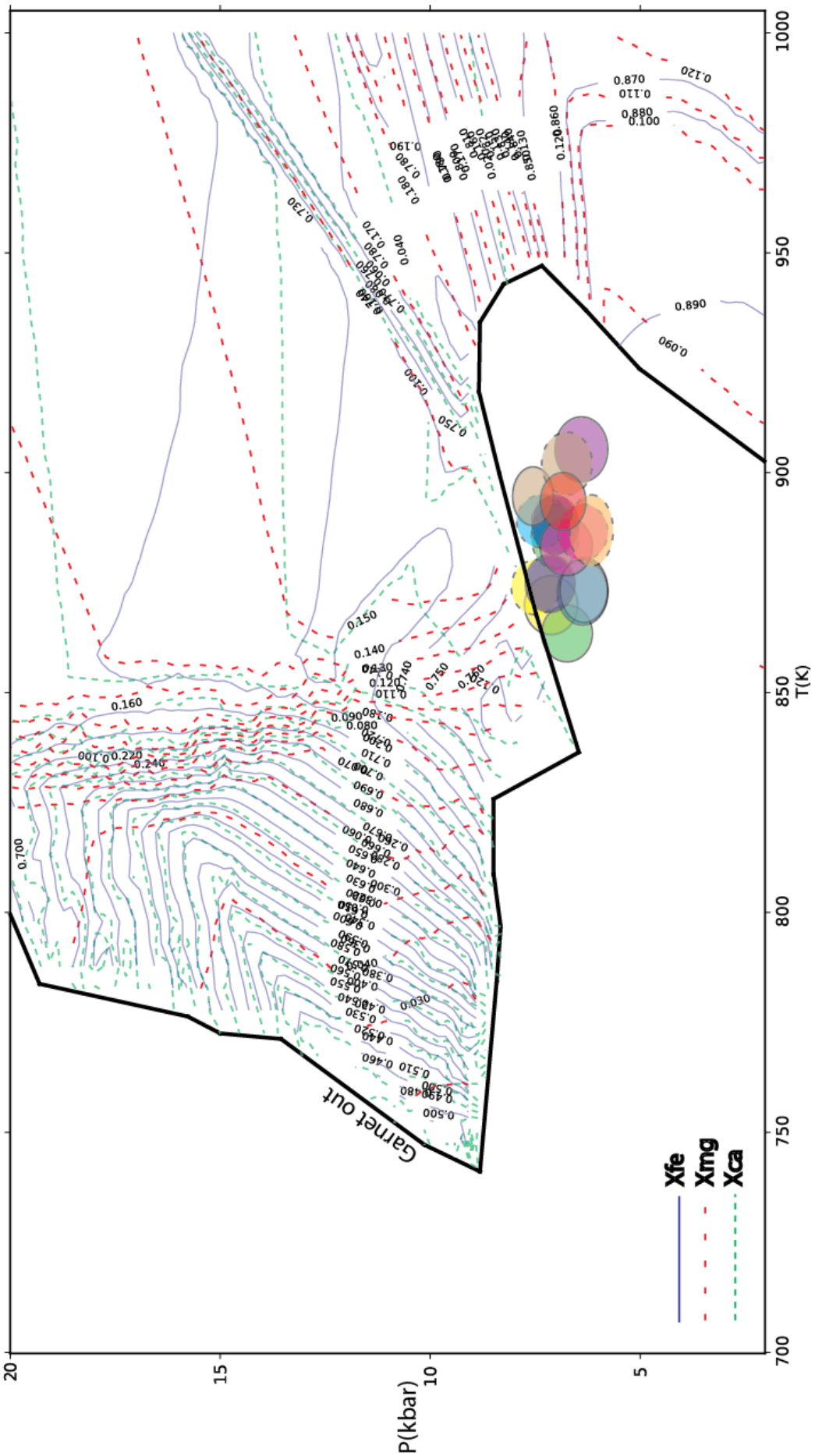

Figure 7.3. *Fractions of Ca, Mg and Fe in garnet (e.g. Xfe = [Fe/(Fe+Mg+CaO)]. Note the metastable position of the garnets outside the stability field. Core compositions show a solid outer rim compared to a dotted outer rim for the rim compositions. Compositions plotted via extrapolation of isopleths. Colours correspond to garnets in Table 3 in chapter 6.2.1*

Garnet is stable at temperatures above 720 K and has no direct pressure limits. Molar fractions of the different end member solid solutions in garnet specify the stable conditions per phase. Garnet was of particular interest since the molar fractions of grossular (X_{ca}), pyrope (X_{mg}) and almandine (X_{fe}) act as geothermobarometers. The P-T field of garnet was contoured by these isopleths (fig. 7.3). As can be seen in the figure, the contents of almandine increase towards higher P and T. The same is true for pyrope, which has a peak composition around 10 kbar and 900 – 1000 K. The grossular component however increases with decreasing temperature. Isopleths are also plotted for the Si content of M2 and M3 potassic white mica (e.g. muscovite) minerals (see chapter 7.4.4). These isopleths act as geobarometers and have a range between 3.040 and 3.360 whereas the higher Si contents are observed at higher pressure.

Equilibrium PT conditions can be deduced by comparing the element oxide weight percentages of minerals, measured with the electron microprobe, with the isopleths calculated in Perple_X using the bulk rock composition of the same rock in which the EMP analyses were done. This can be seen in figure 7.3, where the molar fractions of grossular, pyrope and almandine are compared with each other. Due to the minor heterogeneity in the core and the rim components of garnets, both core and rim compositions are treated separately. However, when we plot the garnet endmember compositions the various isopleths intersect below the garnet-in phase boundary line. The garnets are still observed in the optical microscope, but using the P58b bulk rock composition in their current configuration the garnets are metastable. Rim compositions are slightly enriched in Fe and hence plot slightly more to higher temperatures. This metastability of garnet implies that exchange with other phases progressed during the retrogressive stage of the rock. Metamorphic reactions of garnet together with other phases as plagioclase ± biotite ± muscovite took significant time and were not completed by the time of outcropping. This can be explained by the relative low temperatures and hence slow diffusion of large Na, K atoms and 2+ covalent cations between the phases (see chapter 7.4). A factor which can also explain the slow retrogression is an event of late stage heating which caused re-stability of garnet at higher temperatures. Therefore, the time for garnet to decay after this phase of late stage heating was even less and with high exhumation rates garnet was still present at the surface.

There are many reasons why the observed and predicted compositions do not coincide. First and foremost are the errors in the thermodynamic data and solution models. Thermodynamic data are mostly calculated and estimated data which are acquired from lab results which brings with itself several assumptions and simplicities. Secondly the errors in the determination of bulk and mineral compositions, followed by errors in assumptions, e.g., that your rock records a bulk equilibrium condition. This has to do with the accuracy of the XRF analyser and the assumption that no external forces have been present to influence the chemical composition of the rock. Since we assume an open system for this bulk rock composition, it is difficult to assign the label equilibrium to sets of minerals. If material is removed or incorporated during throughout the progressive or retrogressive stages, comparison with each other is strictly not allowed anymore. A further view on the stability of garnet is given in chapter 6.2.1.

7.3 TheriakDomino

In order to get a good understanding of the stable mineral assemblages, a different software package is used to plot the pseudosections. TheriakDomino (TD) is based on similar

assumptions as Perple_X. Theriak calculates phase compositions and mineral assemblages given a bulk rock composition at specified PT conditions. Subsequently, with Domino, PT pseudosections and phase isopleths (e.g. spessartine, almandine and andradite in garnet) can be obtained. TD is relatively quickly in calculations by making use of Gibbs free energy minimization instead of complex equations (Peters, 2010).

TD is in this study only used to compare the results of Perple_X with another thermodynamic data based software package. Therefore, thorough explanation and results are not present in this study.

7.3.1 CALCULATION METHOD

The following section is a summary of a brief user's manual from Peters (2010).

Many similarities exist in the usage of the software package compared to Perple_X. First of all you have to define the mineral assemblage of your rock, e.g. use the bulk rock composition that is calculated using the XRF. The more complex the chosen system is to calculate your pseudosection, the more precise the stable mineral assemblages will be. Secondly, you choose a thermodynamic database where the calculations are based on. In this section it is important to choose the minerals and/or endmembers which should be included. For example, if titanite is present in ilmenite but also in biotite, you should use a database which is calibrated for the incorporation of Ti in both phases. These considerations should be made for each individual mineral and the possible solid solutions.

Thereafter, all the Fe present in the rock will be considered to be Fe^{2+}. If this is incorrectly for your samples, recalculate the wt% of FeO to Fe_2O_3.

Decide next the amount of water that should be added to the system. Almost all systems have an excess of water, but this depends on the minerals present in your rock. Minerals of biotite and hornblende can include several wt% of water which influences the stability of phases present in the rock. Finally, you can use isopleths to distinguish between the different stages in the metamorphic evolution of the rocks. Hence, you can differentiate between core and rim compositions if your minerals show any zonation. With help of isopleths, you are able to find an equilibrium point/area that corresponds to a certain part of the PT path.

In order for clear representation of your chosen system, use a chemical notation of a system like: TiCNKFMASH (if Ti, Ca, N, K, Fe, Mg, Al, Si and H are included).

7.3.2 RESULTS: PT PSEUDOSECTIONS

Figure 7.4 is a pseudosection plotted for the bulk rock composition of P58b. The points mentioned in table 10 correspond to the points in fig. 7.4. These points indicate stable mineral assemblages important for the evolution of the PT path. The thermodynamic database used in TD is tcdb55c2d, which is based on Holland and Powell (1998). The minerals which have been included in the calculations are comparable with the Perple_X calculations. Composition of the points can be compared with the stability of minerals in Perple_X (table 10; fig. 9.1 and fig. 9.2).

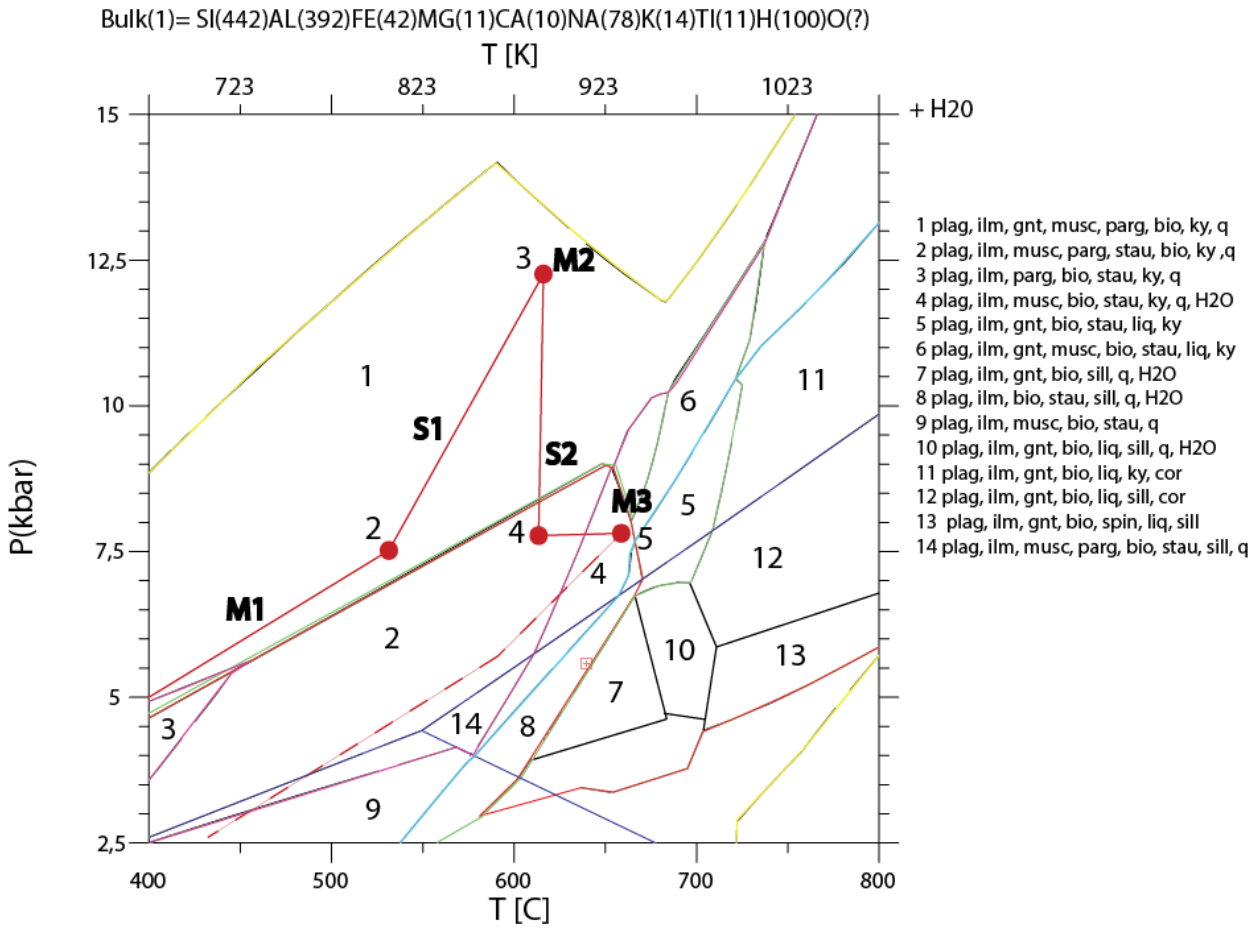

Figure 7.4 Pseudosection of major stability fields from the metapelitic bulk rock composition. Note the large variation in the fields compared to the Perple_X plot (fig. 9.1). The red line and points highlight the PT path of the rock. Bulk rock composition in cations and Fe = Fe^{2+}.

In the input file for TheriakDomino, the notation O(?) is used in the bulk rock composition, which means that the amount of oxygen is not given, but the programme will use the amount of oxygen that is required to charge balance the oxides that are incorporated in the calculation, assuming that $Fe_{total} = Fe^{2+}$.

The point analyses are chosen in a way to represent the stable mineral assemblages which can be compared to the Perple_X calculations (M1, M2 and M3). A brief comparison is also done with the experimental based petrogenetic grids of Bucher and Frey (1994). The proposed P58b PT path based on the Perple_X results is plotted in a KNFASH diagram (fig. 7.5). The

Table 10. Stable solid phases at the point locations important for the P-T path. Wt% of minerals inside brackets.

Point 2	**Point 3**	**Point 4**	**Point 5**
Oligoclase An_{13} (23)	Oligoclase An_{16} (24)	Oligoclase An_{15} (31)	Oligoclase An_{11} (42)
Ilmenite (3)	Ilmenite (3)	Ilmenite (3)	Ilmenite (3)
Almandine (10)	Almandine (9)	Muscovite (6)	Annite (5)
Muscovite (7)	Muscovite (6)	Paragonite (16)	Staurolite (20)
Paragonite (25)	Paragonite (26)	Annite (5)	Kyanite (21)
Annite (3)	Annite (4)	Staurolite (21)	Quartz (3)
Kyanite (25)	Kyanite (25)	Kyanite (14)	Muscovite (6)
Quartz (4)	Quartz (4)	Quartz (5)	

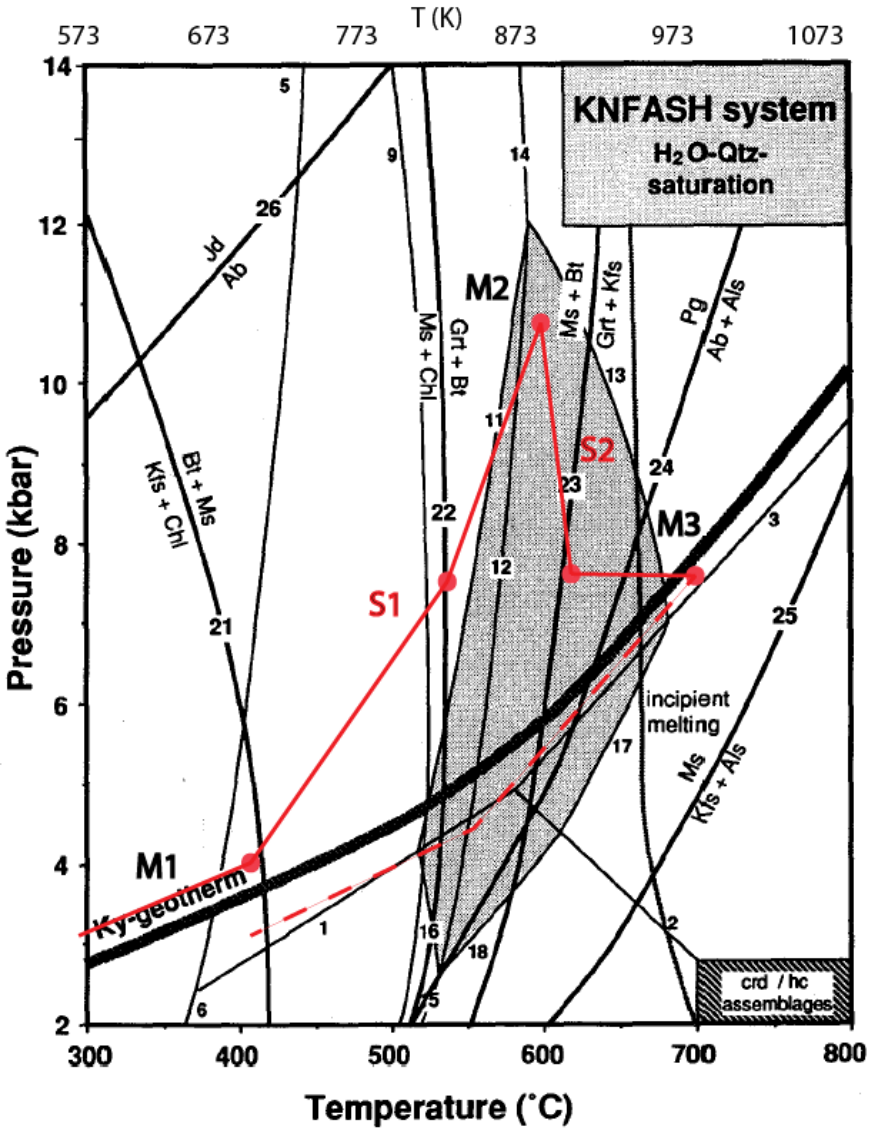

Reactions in the KNFASH-system

(1) And = Ky
(2) And = Sil
(3) Sil = Ky
(4) Kln + 2 Qtz = Prl + H_2O
(5) Prl = Ky + 3 Qtz + H_2O
(6) Prl = And + 3 Qtz + H_2O

Reactions with excess quartz + H_2O

(7) Chl + 4 Prl = 5 Cld + 2 Qtz + 3 H_2O
(8) Chl + 4 Hem = Cld + 4 Mag + 2 Qtz + 3 H_2O
(9) Chl + Cld + 2 Qtz = 2 Alm + 5 H_2O
(10) 3 Chl = 3 Alm + 2 Mag + 12 H_2O (+ QFM)
(11) 8 Cld + 10 Ky = 2 St + 3 Qtz + 4 H_2O
(12) 23 Cld + 7 Qtz = 2 St + 5 Alm + 19 H_2O
(13) 75 St + 312 Qtz = 100 Alm + 575 Ky + 150 H_2O
(14) 3 Cld + 2 Qtz = Alm + 2 Ky + 3 H_2O
(15) 3 Cld + 2 Qtz = Alm + 2 And + 3 H_2O
(16) 8 Cld + 10 And = 2 St + 3 Qtz + 4 H_2O
(17) 75 St + 312 Qtz = 100 Alm + 575 Sil + 150 H_2O
(18) 75 St + 312 Qtz = 100 Alm + 575 And + 150 H_2O
(21) 3 Chl + 8 Kfs = 5 Ann + 3 Ms + 9 Qtz + 4 H_2O
(22) 1 Ms + 3 Chl + 3 Qtz = 4 Alm + 1 Ann + 12 H_2O
(23) 1 Ms + 1 Ann + 3 Qtz = 1 Alm + 2 Kfs + 2 H_2O
(24) Pa + Qtz = Ab + Als + H_2O
(25) Ms + Qtz = Kfs + Als + H_2O
(26) Jd + Qtz = Ab

Figure 7.5. Petrogenetic grid for the KNFASH system including mineral reactions as indicated in the left table. Shaded field is the coexistence of staurolite + quartz. The red line indicates the proposed PT path of P58b where S1 and S2 correspond to deformation phases 1 and 2. Modified Bucher and Frey, 1994

experimental analyses and mineral reactions of Bucher and Frey (1994) are used to explain the mineral reactions that took place in our Perple_X analysis.

7.4 Geothermobarometry

Another way to calculate PT conditions during which stable mineral assemblages in rocks formed can be performed using a technique called geothermobarometry (Spear, 1995). Geothermometers are subvertical reaction curves in PT space and reflect mineral reactions involving large ΔS and ΔH and small ΔV. Geobarometers are subvertical reaction curves in PT space. Such mineral reactions involve large changes in ΔV and small changes in ΔS and ΔH.

The technique of geothermobarometry implies that geothermometer and geobarometer were formed at the same time in PT space, which is the basic assumption of a stable mineral assemblage. In practice this means that the two reaction curves in PT space intersect each other. The intersection point in PT space (provided equilibrium) reflects the metamorphic conditions at which the stable mineral assemblage was formed.

By combining different generations of mineral assemblages (see M1, M2 and M3 in the paragenetic grid, table 1 in chapter 5.4) the PT path can be reconstructed provided the assemblages were formed during the same PT conditions.

Input data for geothermobarometry are the mineral chemistries of the assemblage analyzed by EMP. The latter data is summarized in chapter 14.1 in the appendix. Multiple geobarometers and geothermometers are used to analyze the stable mineral assemblages.

Geothermo- and -geobarometers used in this study:

1) Plagioclase-biotite-garnet-muscovite assemblage
2) Gartnet-ilmenite Fe-Mn exchange
3) Garnet-rutile-ilmenite-aluminumsilicate-quartz assemblage
4) Phengite Si content pfu
5) Garnet-plagioclase-kyanite-aluminumsilicate assemblage

Results will be described in the following section.

7.4.1 PLAGIOCLASE-BIOTITE-GARNET-MUSCOVITE

Theory

The mineral assemblage plagioclase-biotite-garnet-muscovite is widely present in most metapelitic rocks from garnet zone to lower sillimanite zone (Ghent and Stout, 1981). Since the rocks of our study are part of this range of metamorphic zones, this geothermobarometer is of great use to calculate the stable mineral assemblage PT conditions.

Equilibria between the minerals exist with the following minerals:

(1) $Mg_3Al_2Si_3O_{12} + Ca_3Al_2Si_3O_{12} + KAl_2(AlSi_3O_{10})(OH)_2 = CaAlSi_2O_8 + KMg_3(AlSi_3O_{10})(OH)_2$

garnet + garnet + white mica = plag. + brown mica I

(2) $Fe_3Al_2Si_3O_{12} + Ca_3Al_2Si_3O_{12} + KAl_2(AlSi_3O_{10})(OH)_2 = CaAlSi_2O_8 + KFe_3(AlSi_3O_{10})(OH)_2$

garnet + garnet + white mica = plag. + brown mica II

These equilibria can be expressed with the solid activity products:

$$K_s(1) = \frac{[X_{an}^{pl}]^3[X_{phl}^{bi}]^3}{([X_{K}^{mu}]*[X_{Al^{vi}}^{mu}]^2)[X_{pyr}^{ga}]^3[X_{gr}^{ga}]^3}$$

$$K_s(2) = \frac{[X_{an}^{pl}]^3[X_{ann}^{bi}]^3}{([X_{K}^{mu}]*[X_{Al^{vi}}^{mu}]^2)[X_{alm}^{ga}]^3[X_{gr}^{ga}]^3}$$

Where X indicates the activity and the superscripts refer to phases and the subscripts refer to components. Abbreviations are: K_s = solids activity product; pl = plagioclase; an = anorthite; bi = biotite; ann = annite; mu = muscovite; K = potassium; Al^{vi} = octahedral aluminium; ga = garnet; alm = almandine; gr = grossular, pyr = pyrope; phl = phlogopite.

The thermochemical properties of the minerals involved in these equilibria like enthalpy, entropy, Gibbs free energy and heat capacity are estimated by Zen and Rosenboom (1972), Helgeson and others (1978) and Robie and others (1978). Ghent and Stout (1981) made use of an empirical way to derive their equilibrium constant equations. Thompson (1976) showed that these equations could be derived by using natural assemblages where ln K_s could be measured and pressure and temperature estimated from other equilibria. Hence, he was able to check his equilibrium constant equations and apply it to magnesium-iron exchange between biotite and garnet. Work done by Ferry and Spear (1978) on magnesium-iron exchange verified his method.

The mineral reactions K_s (1) and K_s (2) above could be rewritten as

(A) $0 = -8888.4 – 16.675\ T + 1.738\ P + RT \ln K_s(1)$
(B) $0 = 4124.4 – 22.061\ T + 1.802\ P + RT \ln K_s(2)$

Where T is in K ; P in bar and R in cal/mol/K. Pressures which are estimated from formulae (A) and (B) have generally a standard deviation of ± 800 bar (Ghent et al., 1979). Another factor which has to be taken into account is the assumption of pure ideal compositions. E.g. for plagioclase we assume a maximum An_{20} for samples and for the composition of garnet pure endmember compositions as grossular, pyrope and almandine are used.

From (A) and (B) it will be clear that when $RT\ln K_s$ is known, a line can be constructed in PT space. For (A) two different values for T and for (B) two different values for P can be chosen (fig. 7.6) and the two lines intersect at the stable mineral assemblage conditions.

Many uncertainties that develop in pressures are due to uncertainties in the temperature measurements. Ghent and Stout (1981) have calculated that an uncertainty of ± 50 ^oC would already produce an uncertainty of roughly ± 1 kbar. Ferry and Spear (1978) indicate the influence of atoms on the same octahedral site in garnet as Fe and Mg, e.g. Mn and Ca. When the amount of these components goes up to 0.2 ± 0.02 the samples should be discarded from further use. The same is true for biotite in which the Al^{vi} and Ti presence on the mixing site of Fe and Mg should not increase above 0.15 ± 0.02. In muscovite solid solutions, the octahedral Al substitution for Mg and Fe is necessary and becomes more important at lower metamorphic grade where the content of phengite is higher. Uncertainties in the estimated thermodynamic data can influence the pressure and temperature up to a factor of 70 ^oC and 0.7 kbar according to Anderson (1977).

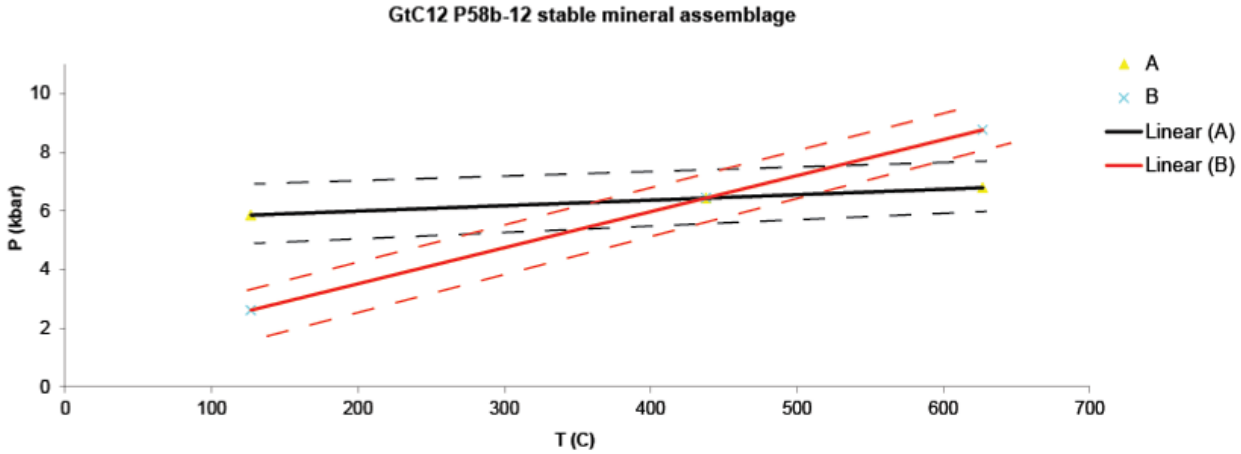

Figure 7.6. PT diagram showing the linear least square equations A and B of the two equilibrium constants Ks_1 and Ks_2. The intersection point indicates the PT conditions in the mineral assemblage assuming equilibrium. Note that the intersection angle of the geothermometers is small implying that the calculated PT conditions for the intersection point are very variable.

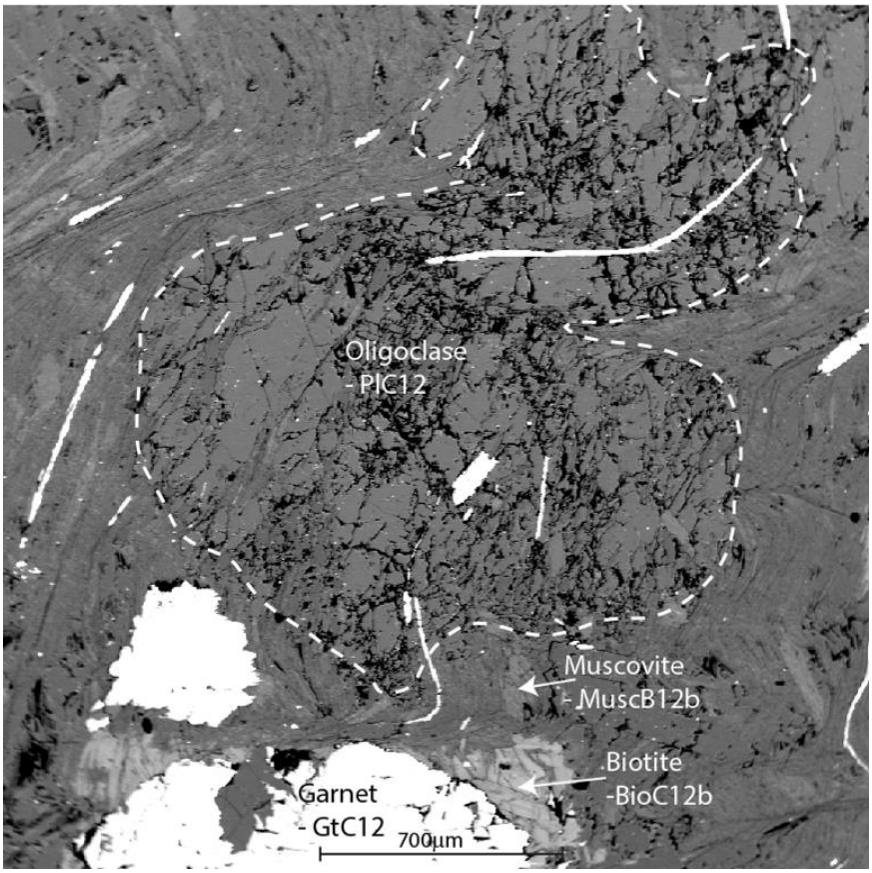

Figure 7.7. P58b-12, sample GtC12 Minerals used for the Ghent and Stout (1981) geothermobarometric calculations. Minerals named for the geothermobarometric calculation are indicated in the figure. EMP analyses listed in tables A-G in chapter 14.1 in the appendix. Note white porphyroblasts at bottom are overexposed garnets.

Results

This specific geothermobarometer is applied to sample GtC12 in P58b-12 (fig. 7.7). Chemical compositions of the minerals can be found in the chapter 14.1 in the Appendix. As can be seen in figure 7.6, equilibrium between the phases exists at a temperature ≈ 700 ± 70 K and a pressure of ≈ 6 ± 0.8 kbar.

7.4.2 GARNET-ILMENITE FE-MN

Theory

A widely used geothermometer for medium grade metamorphic rocks is the element exchange reaction based on diffusion between iron and manganese in garnet and ilmenite (Pownceby et al., 1987). The basis for these geothermometers is the strong fractionation of a particular element in a phase (e.g. Mn in garnet). In metapelitic systems, manganese is strongly compatible in garnet over other coexisting phases (Hollister, 1966). The ration Mn/(Mn+Fe) decreases in the order Gar > Ilm >> Sta > Crd > Bio. This seems applicable to the rocks of this study, as can be seen when the proportions of manganese in the minerals is compared (tables in 14.1 in the appendix). The mineral ilmenite ($FeTiO_3$) can incorporate minor fractions of cations with similar size like Mn. Hence, ilmenite can be regarded as a solid solution with pyrophanite ($MnTiO_3$) and/or giekelite ($MgTiO_3$). Since metapelitic rocks also contain a significant amount of aluminous-rich phases like garnet, kyanite, staurolite, ilmenite can be used in medium grade metamorphic rocks containing the assemblage garnet-ilmenite. It can be used for geothermometry (at certain PT conditions). A geothermometer with the diffusional exchange of Mn with a cation of similar size like Fe, Mg or Ca can be used.

An advantage from garnet-ilmenite over geothermometers like garnet-biotite, garnet-olivine and garnet-orthopyroxene is the simplicity of the mineral structure. Hence a more precise calculation should enable the possibility to compare obtained results with other thermometers which are more vulnerable to factors like fractional diffusion and/or additional solid solution effects (Pownceby et al., 1987). The best way to use the geothermometer is on ilmenite inclusions in garnet, as in this case the ilmenite solid solution composition remains unaffected by diffusional exchange reactions with matrix material below the closure temperature of garnet. The exchange of Fe and Mn atoms between garnet and ilmenite is restricted to the mineral growth conditions (T <600 ^oC and ilmenite-garnet 700-800 ^oC) and the closure temperatures of Mn and Fe in ilmenite (T<600^oC; Rollinson, 1980) and garnet (≈ 700 – 800 ^oC; Lasaga, 1983). When ilmenite is situated in the matrix, additional diffusion reactions with ferromanganese phases like chlorite or biotite at conditions below the closure temperature of garnet, but above that of ilmenite, yield erroneously high apparent temperatures (Pownceby et al., 1987). Apart from the simple structural formula, the garnet-ilmenite geothermometer is independent of pressure which increases the reliability of the geothermometer to natural rock systems (since less factors and hence uncertainty is involved).

The following exchange reaction represents the portions of iron and manganese between a stable garnet and ilmenite:

(1) $$\tfrac{1}{3}Fe_3Al_2Si_3O_{12} + MnTiO_3 = \tfrac{1}{3}Mn_3Al_2Si_3O_{12} + FeTiO_3$$

almandine (garnet)	pyrophanite (ilmenite)	spessartine (garnet)	ilmenite (ilmenite)

If we assume that the minerals are in ideal solid solution with each other, the activity can be written as:

$$(2) \qquad K_d = \frac{(X_{Mn}^{gnt})(X_{Fe}^{ilm})}{(X_{Fe}^{gnt})(X_{Mn}^{ilm})} = K_{D_{Fe-Mn}}^{gnt-ilm}$$

Where X_{Fe}^{gnt} is the mole fraction of Fe^{2+} in garnet and X_{Fe}^{ilm} the mole fraction of Fe^{2+} in ilmenite. The rock samples do not contain significant amounts of Fe^{3+} (EMP data in chapter 14.1 of appendix).

Ideal solid solution is however not always plausible between the different phases. Since natural garnets often contain at least molar portions of Ca, Mn, Fe or Mg in many amphibolites, peraluminous rocks and/or granulites, the effects of the additional solid solution mixings should be taken into account (Pownceby, 1991). This was not done during the development of the original gnt-ilm geothermometer (Kretz, 1959). Subsequent variations in measured K_d can influence the measured P and T and hence influence the temperature calculated with the geothermometer. In a study published by Pownceby et al., (1991) the solid solution of the additional grossular component in garnet is taken into account. This study reveals an influence of the grossular component, ($Ca_3Al_2Si_3O_{12}$) on the partitioning of Fe-Mn between coexisting garnet and ilmenite. The range of this influence is dependent on the pressure and temperature conditions during equilibrium combined with the molar fraction of calcium in garnet.

Despite the addition of, X_{Ca}^{gnt} component into the garnet solid solution series, the resulting influence remains marginal on the Fe-Mn partitioning in a range between 650 and 1000 ^{o}C. In order to be of significance, the grossular component in garnet should be ≥ 0.35 (Pownceby et al., 1991). The reformulation of the upgraded geothermometer developed by Pownceby, (1987), thus incorporates the molar fraction of grossular in garnet. The mathematical expression of this upgraded thermometer is:

$$(3) \qquad T(^{o}C) = \left[\frac{14918 - 2200(2X_{Mn}^{ilm} - 1) + 620(X_{Mn}^{gnt} - X_{Fe}^{gnt}) - 972X_{Ca}^{gnt}}{R\ln K_D + 4.38} \right] - 273.15 \qquad \text{(new)}$$

where R is in mol/cal/Kelvin. The mathematical expression of the original thermometer by Pownceby (1987) to garnet-ilmenite bearing mineral assemblages remains valid since $X_{Ca}^{gnt} << 0.35$ (table 11; table 12). The geothermometer expresses temperature (^{o}C) in terms of the mineral phase composition analyzed by the EMP:

$$(4) \qquad T(^{o}C) = \left[\frac{-4089 + 420(2X_{Mn}^{ilm} - 1) - 77(2X_{Mn}^{gar} - 1)}{-R\ln K_D - 1.44} \right] - 273.15 \qquad \text{(old)}$$

The upgraded geothermometer (3) has a margin of T ± 30 K, which corresponds to margins of 0.01 in X_{ilm}, X_{pyr}, X_{alm}, X_{spss} when propagated through the equilibrium exchange reaction for K_d. When the fractions of X_{Mn} and X_{Fe} are low in the minerals, the errors in K_d will increase (Pownceby et al., 1987). This error margin is based on the weight fractions of the solid solutions. Moreover, the compositions of the phases should be known and solution models should be available to measure the activity of end-member components in the minerals in case the mineral contains small amounts of other cations.

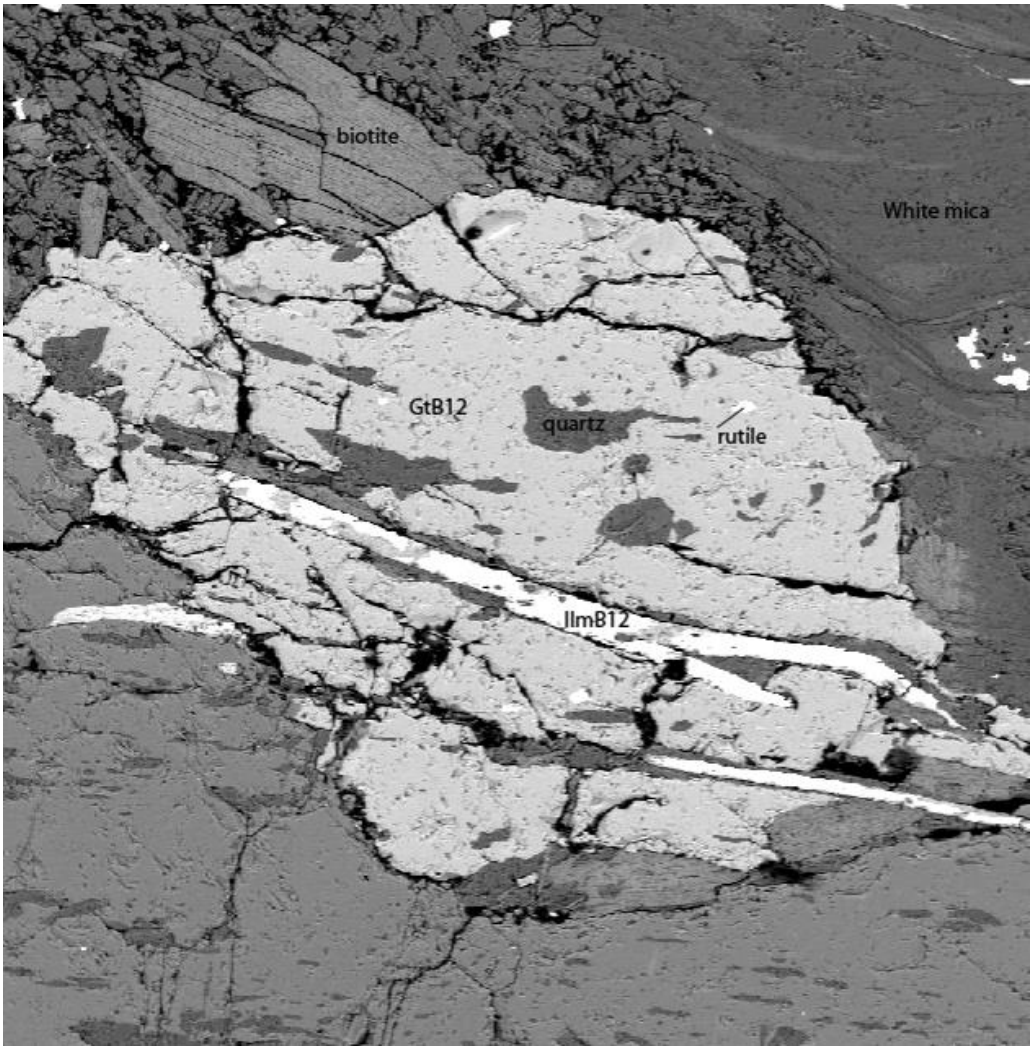

Figure 7.8. P58b-12, sample GtB12/IlmB12 BSE image showing several rutile crystals and M1 ilmenite porphyroblasts included by M3 garnet. The garnet-ilmenite Fe-Mn exchange geothermometer was applied to this equilibrium assemblage. A core-ilmenite and rim-ilmenite analysis were taken in order to be able to mutually compare the obtained PT results (table 11).

Ilmenite can form a solid solution with pyrophanite (Mg-component) and commonly contains a proportion of giekelite ($MgTiO_3$). When the fraction of these components combined is less than 10 mol%, any errors in the calibrated components will not affect the temperature of the geothermometer (Pownceby et al., 1987). The same is true for garnet solid solution series. As stated before, metapelitic rocks of low- to medium-metamorphic grade contain a high almandine component. A solid solution series with significant amounts of pyrope, andradite and grossular can influence the Fe-Mn partitioning however. Hence the upgraded geothermometer can be safely used when the fractions of these components are less than 10-30 mol% combined.

Results

The original geothermometer (4) is used on several different garnet compositions in Perple_X. GtB12 (table 11) and GtC12 (table 12) showed most reliable values but garnetA11 (table 4.1) showed some deviation. The variation in composition of ilmenite and garnet as described above indicates that the geothermometer can be used for analysis. Figure 7.8 shows mineral assemblage GtB12 and IlmB12 used for this geothermometer. EMP analyses are

Table 11. M3 garnet core and rim compositions in sample GtB1. Fe assumed to be all Fe^{2+}; P.f.u. calculations based on 12 oxygen assuming stoichiometry. Compositions of other minerals involved in the Gt-Ilm reaction can be found in chapter 14.1 in the appendix.

	Sample GtB12						
	rim		Cations p.f.u.		core		Cations p.f.u.
Wt% oxide				Wt% oxide			
SiO_2	37.86	Si	3.02	SiO_2	37.97	Si	3.01
Al_2O_3	20.97	Al	1.97	Al_2O_3	21.37	Al	1.99
FeO	34.91	Fe	2.33	FeO	33.60	Fe	2.22
MnO	0.26	Mn	0.02	MnO	0.80	Mn	0.05
MgO	3.62	Mg	0.43	MgO	3.05	Mg	0.36
CaO	2.56	Ca	0.22	CaO	4.13	Ca	0.35
Na_2O	0.03	Na	0.00	Na_2O	0.02	Na	0.00
TiO_2	0.03	Ti	0.00	TiO_2	0.07	Ti	0.00
Cr_2O_3	0.00	Cr	0.00	Cr_2O_3	0.01	Cr	0.00
NiO	0.01	Ni	0.00	NiO	0.03	Ni	0.00
total	100.25		7.99		101.05		7.98

listed in table 11. Since M1 ilmenite already became included in the prograde path of the rock, the core of the M3 garnet should reflect the PT conditions of incorporation of the M1 ilmenite apparently (chapter 6.2.1), whereas the rim reflects the more retrograde stages in which the garnet composition is metastable.

The difference in calculated temperatures between the core (433 ^oC and 600 ^oC) and rim (837 ^oC) is caused by changing P-T conditions over time. Due to a number of assumptions an error margin of ± 50 ^oC should be taken into account. Results obtained are discussed in chapter 9.

7.4.3 GARNET-RUTILE-ILMENITE-ALUMINOSILICATE-QUARTZ

Theory

This barometer is based on the assemblage ilmenite-garnet-Al_2SiO_5-quartz-rutile (hereafter called GRAIL) and is widely used in rocks of metapelitic composition. The large fraction of the almandine component in garnet is mostly observed in metapelitic rocks which makes the barometer useful:

$3\ FeTiO_3 + Al_2O_5 + 2\ SiO_2 = Fe_3Al_2Si_3O_{12} + 3\ TiO_2$
3 ilmenite + aluminosilicate + 2 quartz = almandine + 3 rutile

In the GRAIL geobarometer (Bohlen et al., 1981) available volume data (Robie et al., 1966), thermal expansion and compressibility values (Skinner, 1966) are combined to calculate the equilibrium constant K_d:

$$(1) \qquad K_d = \frac{(a_{ilm}^3)(a_{Al_2SiO_5})(a_{qtz}^2)}{(a_{alm})(a_{ru}^3)}$$

Table 12 Geothermometer results obtained by using thermometer (4). EMP analyses of table 11.

GtB12-IlmB12	CORE				
	Ilm	Gnt	Kd	T (C)	T (K)
Xmn	0.002	0.024	2.434	433	**706**
Xfe	0.998	0.977			
	RIM				
	Ilm	Gnt	Kd	T (C)	T (K)
Xmn	0.002	0.008	1.285	837	**1110**
Xfe	0.998	0.992			
GtC12-IlmC12	CORE				
	Ilm	Gnt	Kd	T (C)	T (K)
Xmn	0.005	0.033	1.831	600	**873**
Xfe	0.995	0.967			
Fe^{3+} + Mg Ilmenite	0.027				
Pyrope + grossular components	0.085				
GarnetA11-garnetA11inc2	CORE				
	Ilm	Gnt	Kd	T (C)	T (K)
Xmn	0.001	0.030	3.455	261	**534**
Xfe	0.999	0.856			
Fe^{3+} + Mg Ilmenite	0.052				
Pyrope + grossular components	0.089				

Where (a_{phase}) are the activities of the phases present in the system. Phases with a reasonable constant composition like quartz (SiO_2), rutile (TiO_2) and Al_2SiO_5 are considered to have a unit activity (a_{phase} = 1). Their activity differs only slightly (<5%) from those of end-member components. When there are other cations p.f.u. present on the same crystal site in the mineral other than Fe and Ti, in ilmenite, solid solutions are taken into account and the unit activity value changes.

The experimentally derived values for log K_d equilibrium values of reaction (1) are plotted in figure 7.9 (after Bohlen et al., 1981). It can be seen in fig 7.9 that the K_d equilibrium values (expanded at 0.1-0.9) systematically vary with P and T. This relationship is therefore a good geobarometer since the slope dP/dT of the $\log_{10}K$ curves is very shallow. Important assumptions which have to be taken into account using this geobarometer are (1) equilibrium between the assemblage, (2) composition of the (impure) phases and (3) appropriate solution models for the end-member components (Bohlen et al., 1981). If for example the sum of the secondary elements like Mg, Ti, Cr in rutile exceeds 5 wt% this is of importance for the error margin in your calculations. In order to use the geobarometer as a reliable metamorphic pressure indicator, a reasonable estimate of the metamorphic temperature should be known.

The same is true for the fractions of hematite (Fe_2O_3) and pyrophanite ($MgTiO_3$) in ilmenite. Hematite-rich ilmenite is not stable in combination with almandine-rich garnets (Bohlen et al.,

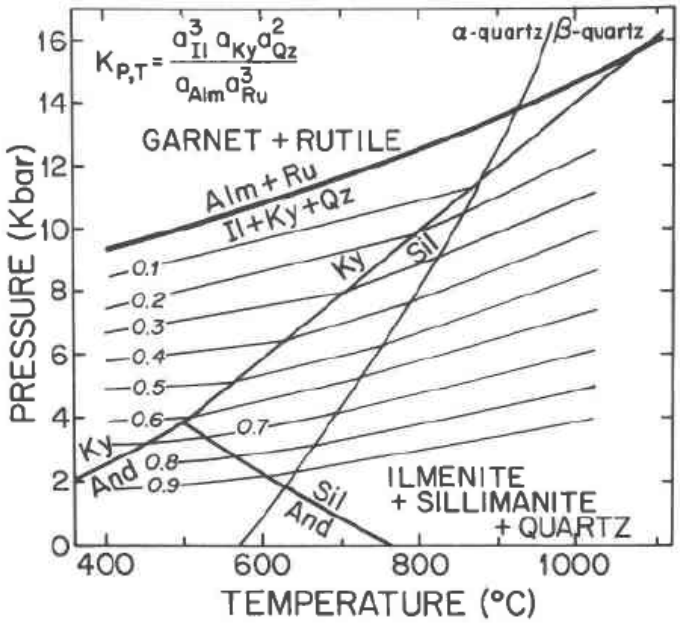

Figure 7.9. Pressure-temperature-log K diagram for the ilmenite-Al_2SiO_5-quartz-almandine-rutile geobarometer which is experimentally calculated. Al_2SiO_5 phase reactions are derived from Holdaway (1971). Note that the K_d equilibrium values (0.1-0.9) systematically vary with P and T. This allows it to be used dominantly as a barometer.

1981). Moreover, significant amounts of Fe^{3+} might be formed during retrograde alteration of ilmenite. In order to maintain proper solid solution series, the amount of hematite and pyrophanite should be less than 15 mol%.

Bohlen et al. (1981) suggest that the GRAIL geobarometer is in particular useful in Barrovian-style metamorphic terranes. This is mainly because all the phases, except garnet, do not depart far from ideal end-member components. This heterogeneous composition of garnet is especially useful in analysing the retrograde evolution of rocks. If garnets are zoned and the rims are enriched in Mn and Fe compared to the internal parts this is chiefly caused by diffusion with matrix during retrograde processes related to exhumation. Pressures are than calculated when equilibrium of this garnet rim with the matrix is assumed and hence leads to smaller log K_d values (Bohlen et al., 1981). Note: the calculations made using this geobarometer can subsequently be compared with the pseudosections calculated with Perple_X (chapter 7.2).

Results

The following results are obtained when using formula (1). For the activities of kyanite and quartz, a = 1. The activity of rutile is 0.945 as calculated with the composition of the rutile crystal analysed in P58b-12, sample GtC12inc1 (fig. 7.10; table 13). Table 14 shows the results obtained. The calculated K_d values vary between 0.30 and 0.45, which corresponds to pressures of 5.5–7 kbar. Dependent on the temperature and the stability fields of the corresponding minerals a fairly good estimate can be made regarding the P-T conditions of stability.

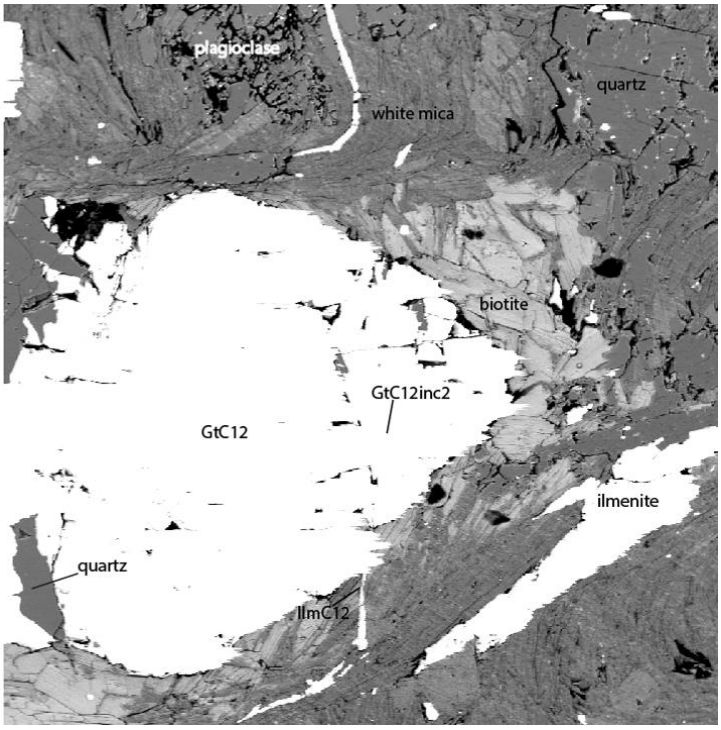

Figure 7.10. P58b-12, sample GtC12 BSE image showing the mineral assemblage used for GRAIL analysis 4 (EMP data in tables A-G in the Appendix). Minerals are preferably in contact with each other for good ion exchange reactions. Note however that microstructural instability of zoned minerals during retrograde circumstances can modify the mineral chemistries and hence can influence the calculated K_d and hence the final P-T conditions. Note that sample GtC12 is also used in calculations using the plag-bio-muscovite-gnt assemblage in chapter 7.4.1. Overexposed garnet causes rutile inclusion to be invisible.

Table 13. Rutile composition. All Fe assumed to be Fe^{2+}; P.f.u. calculations based on 2 oxygen assuming stoichiometry. Compositions of the other minerals involved in the GRAIL reaction can be found in tables A - G in chapter 14.1 in the Appendix.

	Sample GtC12inc1
Wt% oxide	
SiO_2	1.39
TiO_2	94.25
Al_2O_3	1.30
FeO	0.08
MgO	0.00
CaO	0.24
K_2O	0.00
Na_2O	0.29
MnO	0.00
Cr_2O_3	0.30
NiO	0.17
total	98.02
	p.f.u
Ti	0.945

Table 14. Calculated results for the equilibrium value (Kd) of reaction (1).

Analysis	K_d	*ln Kd*	*Minerals involved*
1	1.58	0.45	GtB12 – IlmB12-GtC12inc1
2	1.51	0.41	GtB12-GtB12inc4-GtC12inc1
3	1.43	0.36	GtB11b-IlmA11-GtC12inc1
4	1.49	0.30	GtC12-IlmC12-GtC12inc1

When the $\ln K_d$ values (table 14) are plotted in figure 7.9 for an assumed temperature range below 700 ^oC this will result in primary values in the order of 5-7 kbar. In other words, in combination with a good thermometer GRAIL can be used to calculate PT condition of mineral equilibrium assemblages in nature. This will be discussed in chapter 9.

7.4.4 PHENGITE

Theory

The phengite barometer was experimentally derived and calibrated by Massonne (1991), which is a modified version of their initial calibration (Massonne and Schreyer, 1987; Rötzler et al., 1999: modified version). It can be used to calculate a minimum pressure value in the Si-content of white micas containing a phengite component ($K(Al,Mg)_2(OH)_2(Si,Al)_4O_{10}$). Results from his study are plotted in fig 7.11 which shows the Si-isopleths for phengite with pressures up to 24 kbar.

The barometer is based on the muscovite-celadonite solid solution series: $KAl_2[AlSi_3O_{10}](OH)_2$-$K(Mg,Fe^{2+})(Fe^{3+},Al)[Si_4O_{10}](OH)_2$. The miscibility between the different phases increases towards celadonite with increasing pressure or decreasing temperature and is therefore of great value for geothermobarometry (Velde, 1965). It is mainly used in KMASH systems, which is therefore applicable to this study. When a phengite decomposes under changing P-T conditions it forms K-feldspar, phlogopite, quartz, a Si-poorer phengite and small amounts of water. Phengite occurs mainly in low-temperature metamorphic rocks compared to muscovite which grows at higher metamorphic temperatures (Ernst, 1963).

Important assumptions concerning the BRC need to be taken into account in order to apply the Si geobarometer. A maximum Si content in phengite can only be attained when the mineral coexists together with K-feldspar, quartz and a trioctahedral mica like biotite, muscovite or phlogopite. Massone and Schreyer (1987) examined the stability of the mentioned phases, which ranges roughly between 3 to 24 kbar and 350 to 700^oC. This stability range is however strongly dependent on the composition of the coexisting phases (e.g. bulk rock composition). When a Si-rich phengite is in equilibrium with a more Na-rich paragonite, the Si content of phengite is reduced due to the presence of Na for K in the interlayer, compared to other phengite (Massone and Schreyer, 1987).

The theoretical data by Velde (1965) and Massone and Schreyer (1987) were only based on experiments. In nature, the application of the phengite geobarometer is a lot more complicated due to several additional factors. Mostly, phengite in metamorphic rocks is not equilibrated with the surrounding matrix or even with other phengite crystals in the rock. This is mainly due to the very slow diffusion rates of elements in mica (Massone and Schreyer, 1987).

Frequently phengite is chemically zoned, and some rocks show phengite with different Si contents in the same rock. Even within geological times, homogenization and equilibration of phengite is sluggish. On the contrary to these disadvantages, an advantage of this slow homogenization and reequilibration is the possibility to investigate earlier stages of the metamorphic history of the rocks. So when several different Si contents are observed, this might reflect different stages formed during the rock history (PT path).

Results

The pressures obtained from this geobarometer are significantly lower compared to the GRAIL geobarometer. A valid reason for the misfit of these data is the disequilibria of the white micas in the rock. As stated in chapter 5.2.7, most of the white micas are matrix material or late-deformational grown and hence not stable with minerals like staurolite and garnet. Secondly, this geobarometer only gives minimum pressures when one of the components k-feldspar, phlogopite, quartz, or a Si-poorer phengite is not formed as a reaction product. Since some k-feldspar is observed (chapter 6.2.3) in the rocks, pressures can be combined with geothermometers to find equilibrium mineral assemblage growth conditions.

As can be seen in figure 7.11, the calculated pressures are in the order of 2-0.5 kbar. Table 15 indicates the muscovite flakes on which the barometer is performed. The calculated pressures are moreover influenced by the presence of Na-rich paragonite. The more K and Na are present, the lower the obtained pressures will be. Hence, these pressures might be an underestimate of the real pressure (Massone and Schreyer, 1987). The authors also indicate that even in the same rock micas can show different Si contents. There is however no zoning observed in the M1, M2 and M3 micas which complicate the application of this geothermometer.

The late grown M3 muscovite flakes formed late at high T analysed using the SEM (chapter 6.2.7; chapter 14.4) show a Si p.f.u. around 3.30. This is in sharp contrast with the lower values obtained for the M1 matrix muscovites (table 15). Assuming overall equilibrium of one assemblage, it makes sense that different generations of white mica show variable values. Another fair reason for this might be the sluggish homogenization since the M3 muscovite flakes have late grown at high T and the matrix material have grown at earlier stages at lower T conditions.

Table 15. Si p.f.u. for white mica and paragonite. Calculations based on EMP analysis listed in chapter 14.1 of the appendix.

sample	Si p.f.u.
MuscB12b (M1)	3.07
BioC11 (M1)	3.03
MuscC11 (M2)	2.95
AlbC11 (M1 par)	3.08
OverviewA16-2 (M1 par)	2.94
BioC11-2 (M1)	3.13

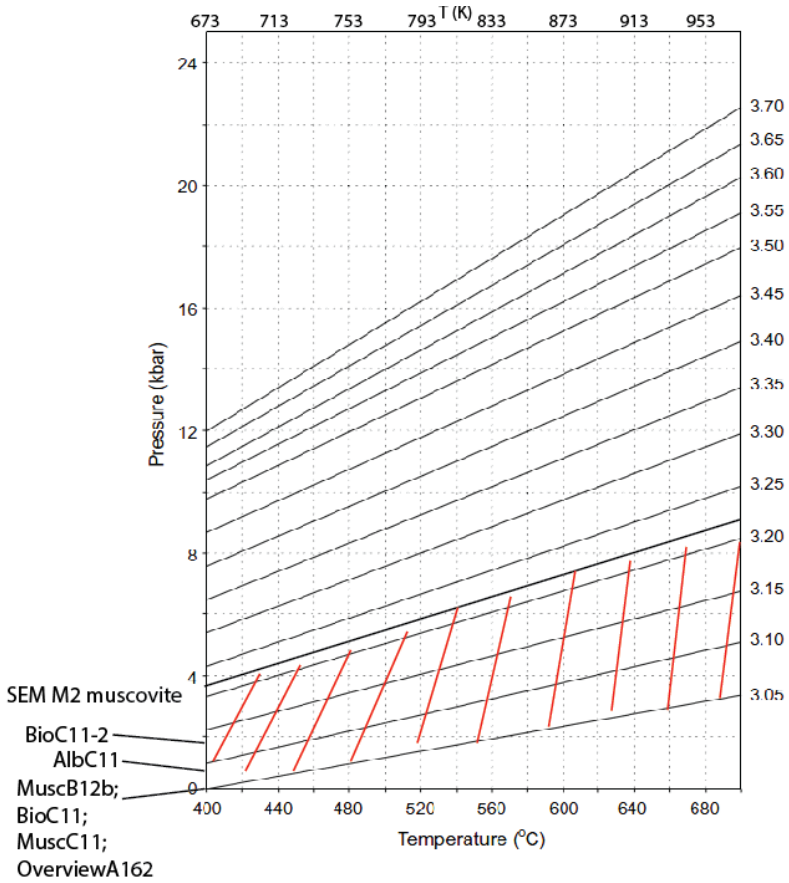

Figure 7.11. Si-isopleths experimentally derived for phengite, Interpolated after Massonne (1991). The isopleths are Si atoms per formula unit (p.f.u.) calculated on the basis of 11 oxygen assuming stoichiometry.The obtained results are indicated with the red striped area. More information becomes available when the barometer is combined with the geothermometers.

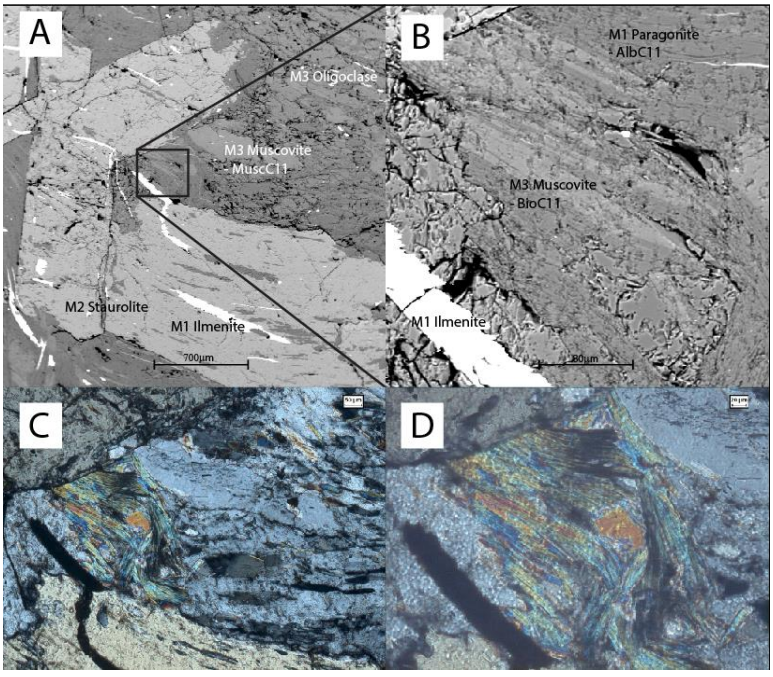

Figure 7.12. P58b-11, sample MuscC11 (A and B) BSE images show the minerals in equilibrium with each other. Si p.f.u calculations to calculate the phengite component are performed on the assemblage. (C and D) are magnifications of (A). Note the inclusion pattern on the late grown M3 muscovite mineral in C and D.

7.4.5 GARNET-PLAGIOCLASE-KYANITE-QUARTZ

Theory

This geobarometer has been used by many studies regarding metapelitic systems and has been updated several times throughout the years (Ghent et al., 1979; Newton and Haselton, 1981; Hodges and Spear, 1982). According to Wu and Cheng (2006) a good garnet-plagioclase-kyanite-quartz barometer (hereafter called GASP) should meet the following criteria: (1) the samples should plot in the correct Al_2SiO_5 polymorph stability field, (2) rocks without any post-metamorphic deformation should show no pressure diversity, (3) rocks in equilibrium with each other within a limited contact area should be metamorphosed at constant pressure and (4) only samples with X_{ca}> 0.03 in garnet and X_{ca}> 0.17 in plagioclase should be considered. As far as these criteria are concerned to the samples of our study area, it does apply to these criteria. EMP mineral chemistries can be found in tables A-G in 14.1 in the Appendix.

The mathematical expression of the GASP geobarometer is formulated as:

(1) $7635 - 19.66T + 0.7963(P-1) + 3T\ln(\frac{X_{pl}^{an}}{X_{gnt}^{gr}}) = 0$ which uses the end-member component reaction:

3 $CaAlSiO_8$ = $Ca_3Al_2Si_3O_{12}$ + 2 Al_2SiO_5 + SiO_2
3 anorthite grossular + 2 aluminosilicate + quartz

If the weight fraction of the grossular component in garnet is used and the total iron content in garnet is treated as ferrous (Fe^{2+}) a maximum estimate of the grossular component can be calculated from EMP analyses. Idem ditto with the anorthite activity in plagioclase (Ghent et al., 1979). Obtained values (table 7) can then be filled in in equation (1). Consequently, for a particular value of T P can be calculated. A fair standard deviation of the pressure is taken to be ±1.6 kbar (Ghent et al., 1979).

Results

For the geobarometric calculations only equilibrium mineral compositions are used which means the minerals are in contact with each other (table 16). Since kyanite and quartz have a unit activity, the activity of their minerals is taken as 1.

Three of the four analysis performed show geobarometers which can be correlated to the kyanite-sillimanite-phyllosilicates (table 16; fig. 7.13). Sample 16A1-2 plots off this curve due to an X_{ca} of 0.002 which is too low for proper analysis, and is therefore discarded. The remaining analyses are in accordance with data from Wu and Cheng (2006). With the error range taken into account the barometer is quite powerful in the stability fields of kyanite and

Table 16. P58b mineral assemblages used for the GASP geobarometer.

Locations	Samples used	ln(K)	X_{ca} gt	X_{ca} pl
P58b-12, sample GtC12	GtC12 + PlC12	0.528	0.101	0.172
P58b-16, sample 16A1-2	16A1-2 + Pl16A	-3.641	0.094	0.002
P58b-11, sample GtB11	GtB11b + GtB11inc3	0.828	0.089	0.205
P58b-12, sample GtB12	GtB12 + B12matrix1	0.757	0.113	0.241

garnet with plagioclase. It should be noted that for the analysed samples used in this MSc thesis the stability of garnet growing together with kyanite and plagioclase is debatable, hence the absolute correctness of the geobarometric calculations is debatable.

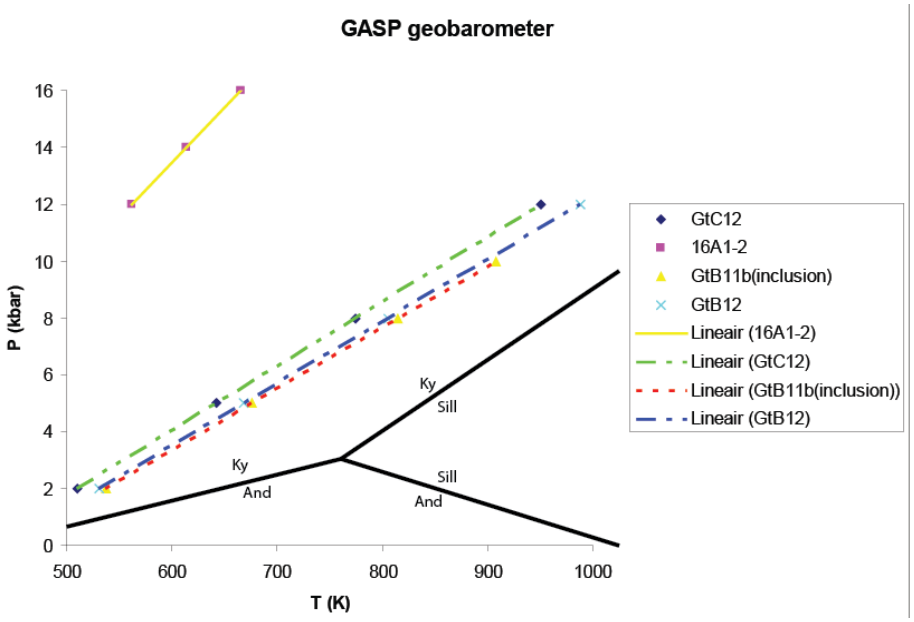

Figure 7.13. PT results after application of the GASP geobarometer (1) plotted in PT space. Note that the barometers are parallel with the kyanite-sillimanite stability field, but all results plot inside the kyanite field.

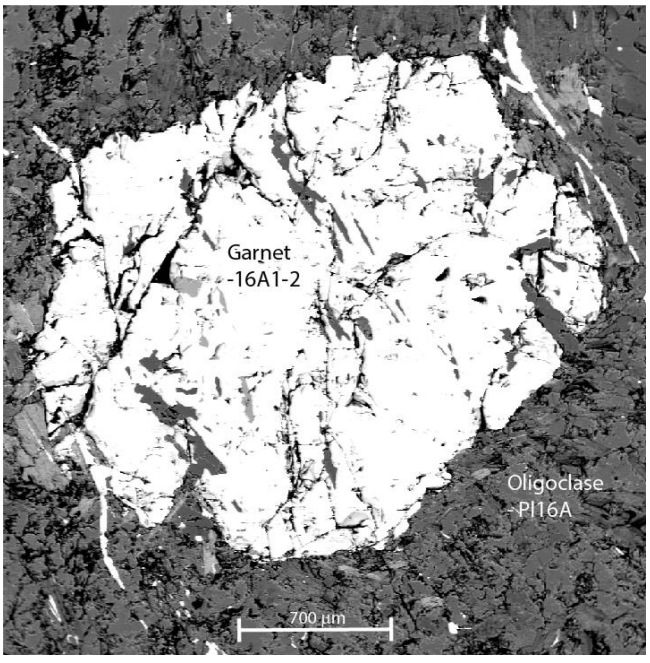

Figure 7.14. P58b-16 M3 Garnet 16A1-2 in contact with M3 plagioclase Pl16A (oligoclase composition) as illustration of equilibrium and contact between the phases. Note that a rim of biotite lacks around this garnet which makes diffusion of calcium between garnet and plagioclase more precise.

7.5 Discussion on calculation methods

7.5.1 PERPLE_X AND THERIAK-DOMINO

In general, the outline of the thermodynamic based programs TheriakDomino and Perple_X is comparable, but the data should be analyzed taken into account that it is really dependent on the software what the exact outcome of the pseudosection is and hence your P-T path will be. This is quite important since research will be dependent on man-made software. If the software results are not consistent, it is more difficult to solve geological problems since the margin of error increases a lot. Another reason can be the understanding of the program itself (e.g. Perple_X) which can be insufficient in this case and therefore errors are incorporated which could have been avoided otherwise. Important differences are the pressure and temperature conditions at which various mineral phases are stable. For example, kyanite is in Perple_X only stable at T > 580 ^{o}C, whereas in TD it is stable above the aluminum silicate intersection point. This has profound consequences for the interpretation of the data. Kyanite is not the stable Al-phase at temperatures below 400 ^{o}C; this is pyrophyllite. But according to TD, kyanite is present with quite a large mass (table 10). The same is true for the presence of biotite, which is according to Perple_X restricted to high temperatures and relatively low pressures, whereas according to TD biotite is stable throughout most of the pseudosection.

Data that is consistent in both programs are the outline of the stability fields of important porphyroblasts like garnet, staurolite, paragonite and muscovite. If temperature is increased, paragonite disappears from the composition, staurolite is introduced, the fraction of calcite in oligoclase is increased and muscovite is growing on top of unstable paragonite. Compared with the KNFASH-system of Bucher and Frey (1994) the stability field of staurolite has a comparable shape, but temperatures of stability are dissimilar (fig. 7.5). A reason for these differences can be found in the updated thermodynamic data over the years and the simplification of the system. E.g. in TD a TiCNKFMASH system is plotted, as is used in Perple_X. Bucher and Frey experimented with a KNFASH system.

Secondly, the database with end members and solution models is decisive for the calculation of stable phases. Simplification of a complex system can influence the reliability of the results calculated with the thermodynamic software. E.g. when a database does not include the Mn-end member component for garnet (spessartine), Mn will be incorporated in other minerals. But if your garnets do contain significant amounts of Mn, the data will be influenced incorrectly. Another example is the presence of Ti in the bulk rock composition. The software might put all Ti in titanite and ignores that this element can also be present in biotite and/or ilmenite. Again, if the amount of Ti in other minerals is low, this is no problem. The results are restricted by the database you choose. Since the endmember components and some of the minerals are not included in both models, the area of the stable mineral assemblage can significantly be influenced.

As stated above, a striking difference is the stability field of some minerals. Take kyanite for example. As can be seen in TD, kyanite is stable almost throughout the whole P-T diagram, whereas kyanite is only stable in a restricted field in the Perple_X model (fig. 7.1). In Perple_X, carpholite, lawsonite, chlorite and chloritoid are included in the modeling whether our TD model does not and only includes cordierite (which is not included in Perple_X). Therefore, most of the aluminum in the bulk rock composition will be compatible to LT phases as carpholite, lawsonite, chlorite and chloritoid and hence Perple_X does not indicate a stable kyanite phase until some of these phases have disappeared. Kyanite will only be a

stable phase above 800 K. In contrast to TD, since none of the LT phases are present, it assumes aluminum is directly stable in kyanite above the kyanite-in stability-line. This is an important difference and could be solved by using input data which are more compatible to each other. The same argument can be used for biotite.

Moreover, the amount of water added to the system plays an important role. Most of the times, an oversaturation of water is added to ensure proper formation of water-rich minerals like biotite, tourmaline and white micas. A varying amount of water between the programs will change the stability fields of both hydrous and anhydrous minerals in the stable mineral assemblage. Since in both models a water oversaturation is assumed, this should not lead to significant variation in the pseudosections.

If the composition of point 1 calculated with Perple_X is compared with a calculation from TheriakDomino (TD) the results are not immediately comparable. The stable minerals according to TD around 350 ^{o}C (≈ 625 K) and 3 kbar are oligoclase (An_{12}), ilmenite, muscovite, paragonite, annite, staurolite, kyanite and quartz, whereas the total water content is 1.62 wt%. Especially the stability of Al-rich phases as kyanite and staurolite at low temperatures is disputed since chloritoid and pyrophyllite should be the stable Al phases. The presence of oligoclase and early muscovite can be related to the 'sedimentary origin' of the shale. This can either be due to the lack of phases included into the model, or due to the use of a different thermodynamic data file (in Perple_X: Holland and Powell, 1998). The calculated composition at point 2 (540 ^{o}C and 7.5 kbar) show a first stability of almandine rich garnet ($Alm_{76}Py_{14}Gr_{10}$). These data show a significant amount of pyrope and grossular which affect the stability of garnet by placing it at lower temperatures. Other stable minerals at 813 K; 7.5 kbar are oligoclase (An_{13}), ilmenite, muscovite, paragonite, annite, kyanite and quartz and water which is comparable to the results from Perple_X.

The stable assemblage at 883 K and 11 kbar, located on the isothermal retrogressive part of the PT path, calculated with TD gives an assemblage of oligoclase (An_{16}), almandine ($Al_{79}Py_{15}Gr_{6}$), muscovite, paragonite, biotite, kyanite ± quartz, ± ilmenite. This indicates an increase in Fe in garnet on the prograde path which is also observed in Perple_X (fig. 7.3).

The stable mineral assemblage around point 4 at 883 K; 7.5 kbar is composed of: ilmenite, muscovite, paragonite, annite, staurolite, kyanite and quartz. This composition also indicates unstable garnet compositions. The amount of paragonite (16 wt%) is decreasing compared to the peak metamorphic equilibrium (25%) due to the transitional reaction to plagioclase. Ilmenite is again a stable phase after decreasing pressure along the retrograde path.

The peak temperature conditions at point 5 in table 10 in the late stage heating event show a stable mineral composition with increased amounts of plagioclase (42 wt% compared to 31 wt% at point 4), total consumption of paragonite and an increase in the amount of kyanite (13 wt% to 21 wt%). However, also a significant amount of staurolite is observed in the rocks (20 wt%), which would indicate a continues stability of this phase. In the TD plot, this is however possible to temperatures of 980 K before staurolite breaks down to form garnet and an aluminum-phase.

7.5.2 GEOTHERMOBAROMETRY

The second part of this section was oriented on the use of geothermobarometry. One of the differences between the theoretical and practical application of both methods is they are based

on different mineral equilibria. In the geothermobarometric applications, only one group of minerals together in the same thin section of the same mineral assemblage is used. For the thermodynamic calculations with Perple_X and TD, the whole bulk rock composition is analysed. This could partly explain the differences in estimated temperatures and pressures.

A major advantage of using geothermobarometers in PT calculations is the determination of the input values. EMP analyses (table A-G in chapter 14.1) are used as input values, providing a way to distinguish between prograde-, peak- and/or retrograde conditions. This is however not possible to determine by using only the bulk rock chemical composition. Programs as TD and Perple_X are therefore very powerful to apply to homogeneous rocks. However, if a rock is layered and hence has a different BRC throughout the sample, thermodynamic software is not able to calculate pseudosections for several compositions at once.

Results

As can be seen in figure 7.15, three fields can be assigned in which the barometers intersect with the thermometers and hence form a stable composition with each other. However, some of the intersections do not plot inside the stability field of the minerals according to Perple_X figure 7.2 (e.g. the most left grey box). This box is an intersection of the garnet GtC12 core composition used in the plag-bio-gnt-musc barometer by Ghent et al. and of the GtB12 and IlmB12 Fe-Mn exchange. It might be possible that some relict garnet composition with increased amounts of calcium and manganese relative to magnesium and iron was starting to grow around 450 ^{o}C (table 11, chapter 7.4.2). This garnet core would then be preserved through PT conditions since temperature was never high enough to homogenize the whole garnet and hence show zonation. The most likely explanation of the intersection point outside the stability field is that minerals have grown during different phases and hence are not stable with each other.

The shaded field around 10 kbar and 870 K is also performed on the M3 GtC12 garnet porphyroblast composition. However, these are rim compositions which are homogenized through time. The gnt-ilm thermometer (GtC12-Ilmc12) combined with the Si p.f.u. in phengite (M2 muscovite in chapter 14.3 appendix) and GASP barometer (GtC12-PlC12-Ky-qz) intersects in the stability field of the used minerals. The stable conditions show (near peak) metamorphic pressures. M2 phengite (muscovite), M2 garnet and M3 kyanite are stable whereas M3 ilmenite and M3 plagioclase are starting to grow.

Finally, the lower left shaded field which reflects the P-T conditions before the initiation of the Buchan-type late stage heating event. The area coincides with the intersection of the Gt-Ilm (GtC12-IlmC12) thermometer and the GRAIL (GtC12-IlmC12-GtC12inc1) barometer. M3 Garnet is still stable at this stage and the M3 ilmenite stability field is reached hence a proper equilibrium assemblage can be plotted (fig. 9.1B). The GRAIL barometer is moreover dependent on rutile and an aluminum-silicate phase. The shaded area plots in the rutile stability field (fig. 9.4).

As indicated before, PT calculations should only be performed on stable mineral assemblages (eg. M1, M2, M3). If minerals show a stable composition throughout time (e.g. ilmenite and rutile), M1 ilmenite blasts can be combined with M3 garnet porphyroblasts, for instance. A combination of geothermobarometry, Perple_X, mineral composition isopleths and TheriakDomino will prove more efficient compared to a singular use of one of them.

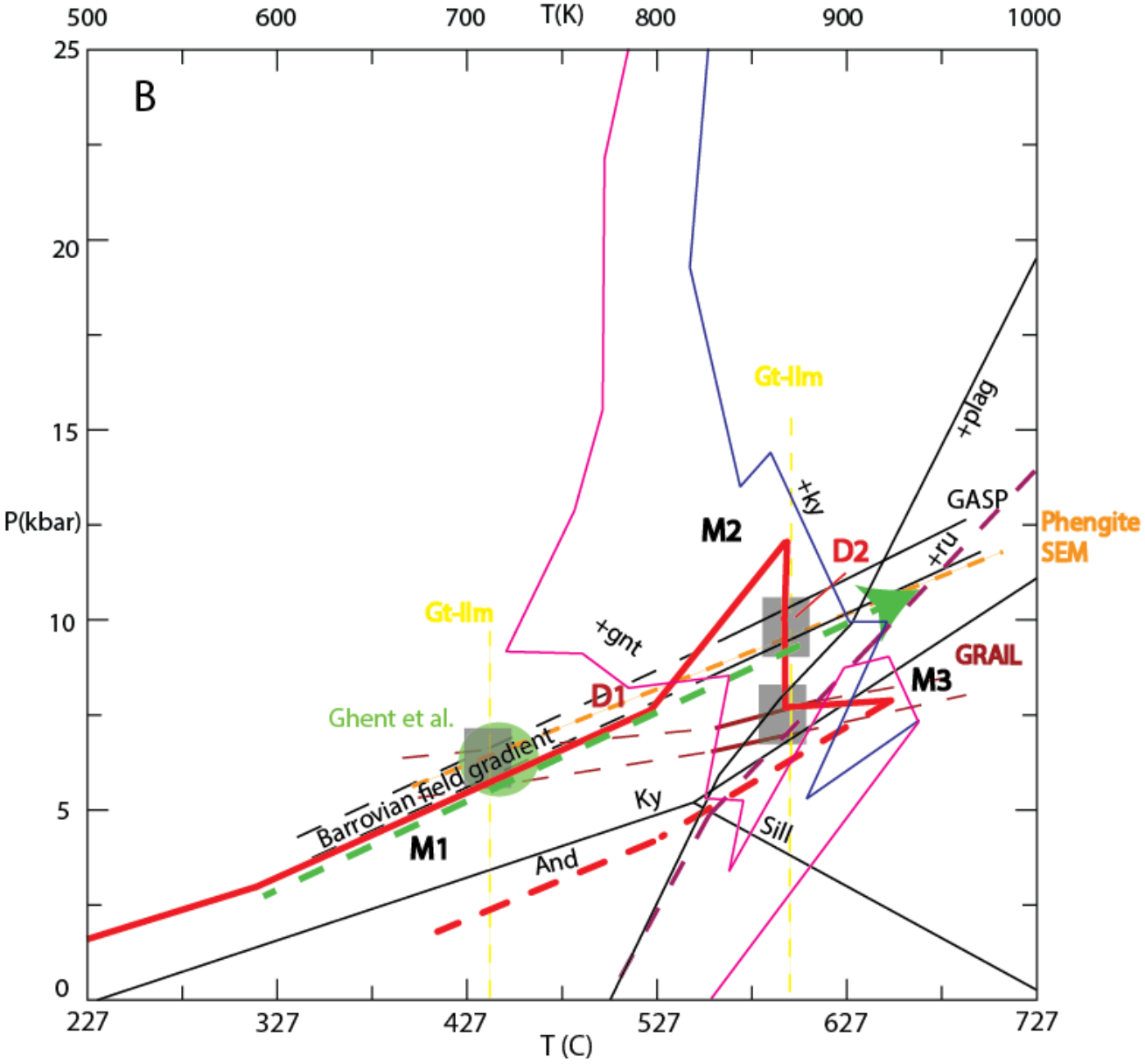

Figure 7.15. Geothermobarometric analyses based on the Pl58-b EMP analyses. Three fields can be assigned in which barometers intersect thermometers. Dashed parts are instable and solid lines indicate a stable position inside mineral stability fields of the geothermobarometers.

8. Comparison with other studies

Several studies are performed in the area from and in the vicinity of Lukmanier Pass. The following section compares our Perple_X and TD modeling results with previous research. This is done on metabasic eclogite bodies in the Northern Adula nappe and on units in the north-eastern margin of the Lepontine Dome (fig. 8.1).

8.1 Eclogite Northern Adula nappe

To derive regional PT paths in the central Penninic domain, the occurrences of eclogitic rocks is often used (CNR, 1990; Pognante, 1991; dal Piaz et al., 1993 e.o.). Fresh eclogite-facies rocks contain significant information regarding early (prograde) stages of orogenic processes as well as peak 'eclogite-facies' metamorphic conditions. To reconstruct the retrograde exhumation path, eclogite facies rocks of Alpine age within the wide axial belt are used (fig 8.2). The ophiolites are intercalated between the Penninic frontal thrust and the Peradriatic line (Spalla et al., 1996; fig. 3.2). These paths can subsequently be compared with the data results from the PT path created with the thermodynamic software and geothermobarometry. Resulting differences in the trace of the PT path can then be used to say something about whether or not a late crustal heating event has taken place in P58b.

The eclogite rocks which are formed in the Alps are found within the axial belt of the Alps where ophiolitic sheets occur (Spalla et al., 1996). They form the BRC of the eclogites. Eclogite formation is related to the subduction of the Adrian micro-continent during Eoalpine

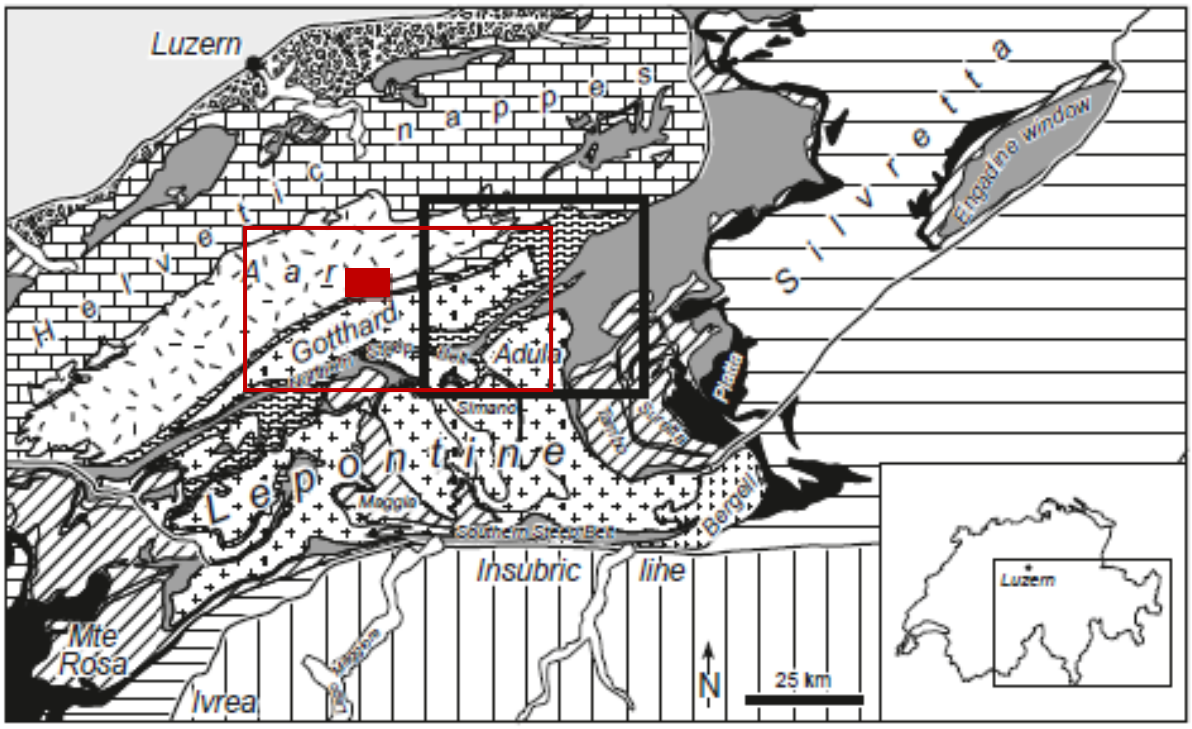

Figure 8.1.Overview of area adjacent to the Lepontine Dome. Red box indicates our study area in the north-eastern part of the Lepontine Dome. Red frame indicates the eclogite rocks in the eastern Central Alps of Spalla et al., (1996). Large black frame represents the study area of Wiederkehr et al., (2008).

(Cretaceous-Paleocene) time, although this is still debatable (Hunziker, 1974 a.o). Pre-collisional models reflect subduction of the oceanic lithosphere of the European plate which carried several micro-continents (Platt, 1986) or small crustal fragments (Polino et al., 1990 a.o.). Collision thickened the crust by underplating (Platt, 1987). Several different theories about the mechanism of exhumation from depth exist in literature. A combination of mechanisms as buoyancy (Ernst, 1971), wedge extension (Platt, 1986, 1987), post-thickening (Mancktelow, 1992), slab detachment (Ballevre and Merle, 1993 a.o.), extensional tectonics or externally applied forces (Polino et al., 1990) probably form the most reliable model.

Spalla et al. (1996) compare the retrograde exhumation paths in different locations of the Alps (fig. 8.2). Each PTt path of the eclogites is subsequently compared to the initial steady state geotherm (stable geotherm = SG) and to the maximally relaxed geotherm (= RG) of an experimentally produced thickened continental crust (England and Thompson, 1984). A subduction zone starts at PT conditions below the SG (fig. 8.2), through time the PTt track evolves in PTt space from peak eclogite conditions to lower grade conditions. During subduction and subsequent continental collision (Alpine-Himalayan type) crustal thickening is assumed and followed by extensional collapse (Dewey, 1988). The latter process causes upwelling of heat and hence an evolution towards the newly developed RG line.

As such eclogites in the vicinity of the Lukmanier Pass area are of interest for this study. The sample which is most closely related is the Zerfreila sample (point 5 in fig. 8.2), which is located in the Northern Adula nappe. Zerfreila is located 12-16 km east of Lukmanier (fig 8.3). The protolith of the eclogite is metabasic and peak pressure and temperature conditions observed are 1.2-1.5 GPa and 470 – 540 ^{o}C. According to Löw (1986) the metamorphic age is eo-Alpine (>50-60 Ma). Note that the retrograde PT path of the Zerfreila eclogite is characterized by isothermal decompression.

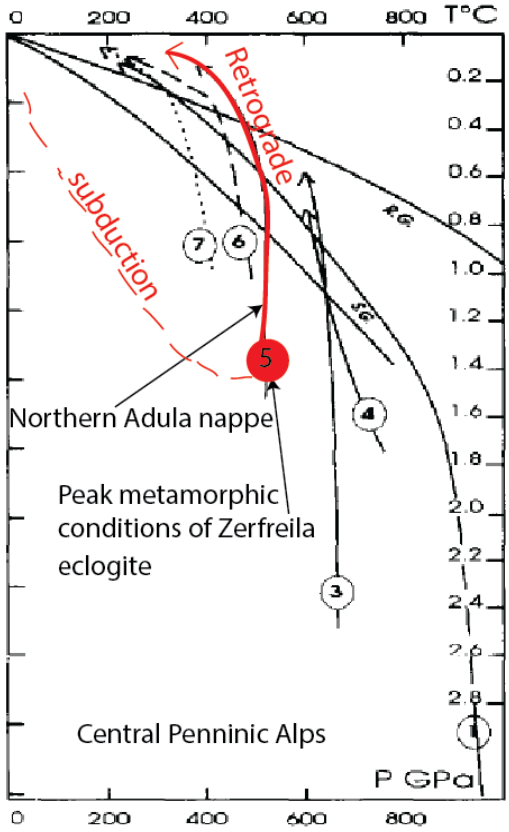

Figure 8.2. P-peak conditions of Alpine eclogites and HP related rocks of the Penninic domain in the Central Alps. Exhumation path 5 represents the Zerfreila Northern Adula nappe and is relevant for comparison with our study. Modified after Spalla et al. (1996).

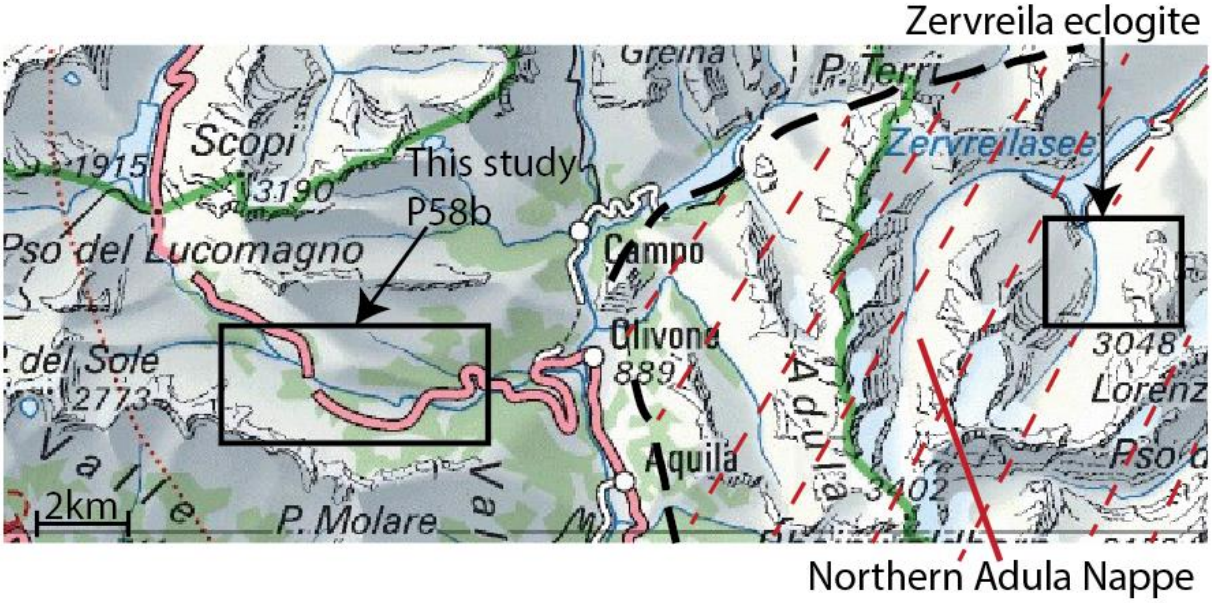

Figure 8.3. Zervreila eclogite locations in the Northern Adula nappe 12-16 km east of Lukmanier Pass area P58b samples from this study. Centre of Lepontine Dome located towards the SSW.

The opposed P-T-t paths observed in figure 8.2 depend mainly on the paleogeographic location and hence stacking order. The deeper the structural levels in the chain, the higher the original temperature conditions were. The eclogites in the Northern Adula nappe have been exhumed under isothermal circumstances (≈ 500 - 550^{o}C). At pressure conditions of circa 3-4 kbar (± 10-14 km depth) the eclogites cross the R.G. line and start cooling down. The observed cooling happens less rapidly compared to the relaxed geotherm. A reason for this can be a late stage heating event which caused regional heating. Such a regional late heating event is observed in the Dora-Maira eclogites in the Western Alps and is related to slab detachment processes (Davies and von Blanckenburg, 1995) or late-orogenic collapse extension of the Alpine belt (Malavieille et al., 1990). The Northern Adula nappe eclogites are placed into a group called low-T eclogites (Newton, 1986 a.o.). This means that the eclogites were uplifted under low-T (<650^{o}C) conditions. For this study it is important to mention that no heating during decompression is demonstrated for the Zerfreila eclogites (fig. 8.2).

A comparison of the PT path of the Zerfreila eclogites and the metapelitic rocks from this study will be made in the next chapter.

8.2 Thermal overprint in the north-eastern Lepontine Dome

In 2008 Michael Wiederkehr and colleagues performed a tectono-metamorphic study on orogen-parallel metasediments in eastern Central Alps in Grisons (fig 8.4). The area stretches from the north-eastern part of the Lepontine Dome near the Lukmanier Pass in the west to the Safiental area in the east. Their primary aim was to document the transition from HP/LT conditions in the east towards more LP/HT conditions further west. This change from blueschist-grade to Barrow-type amphibolite facies investigation should have occurred either simultaneously or during consecutive stages in the evolution of the Alpine orogen. Their subsequent aim of research was to answer the question whether the Barrow-type overprint is associated with a second and discrete heating pulse (Engi et al., 2001 a.o), or just a late stage isothermal decompression event (Nagel et al., 2002; Keller et al., 2005). Finally they propose a heat source for the late stage heating event observed in the north-eastern Lepontine Dome (fig 8.4).

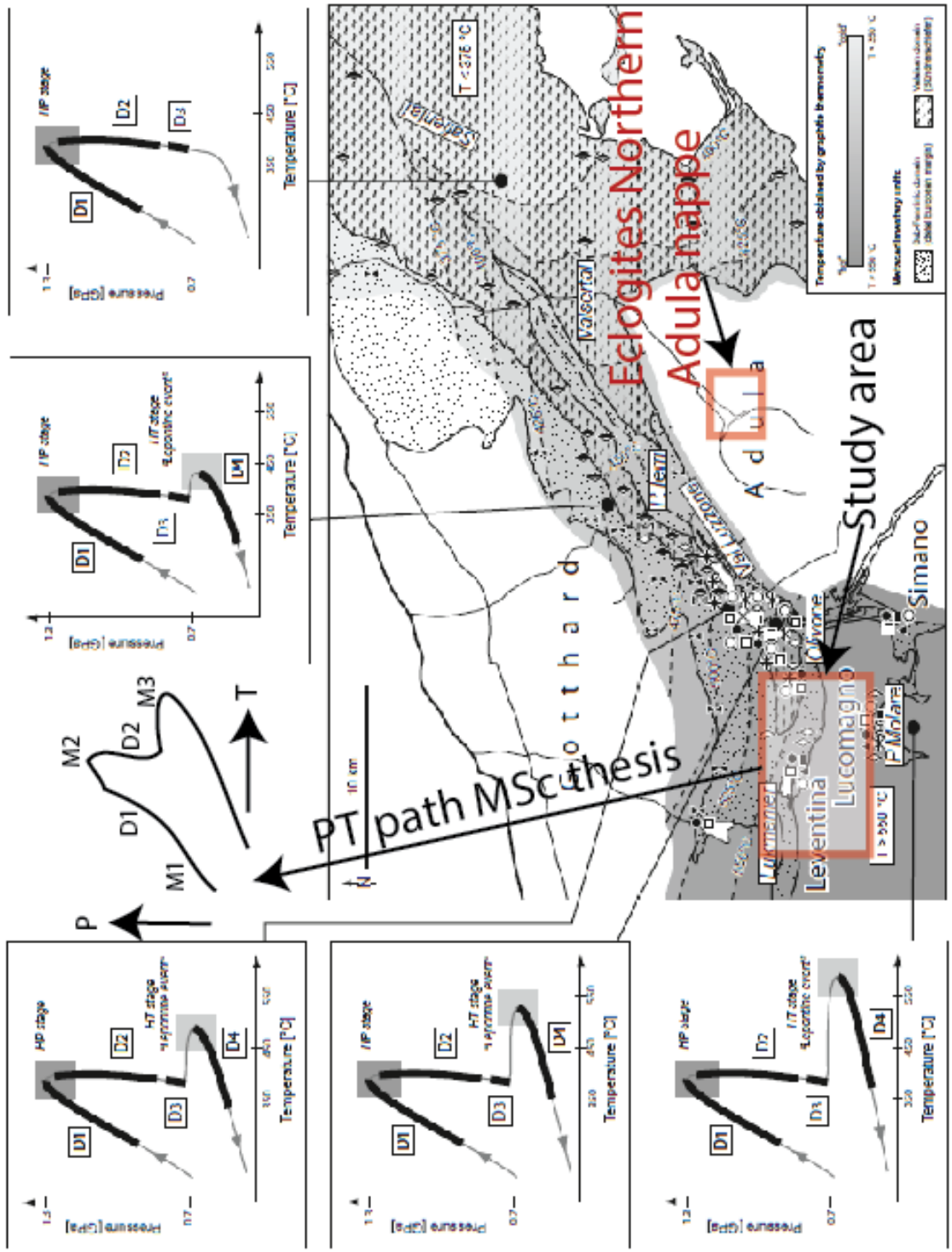

Figure 8.4. Proposed P-T diagrams north-east of the Lepontine dome. These diagrams illustrate the tectono-metamorphic evolution of the meta-sedimentary units at the north-eastern rim of the Lepontine Dome. Modified after Wiederkehr et al. (2008).

Deformation phases D1 and D2 from our study can be linked to deformational events described in other papers. This study D1 can be parallelized with the Safien phase of Wiederkehr et al. (2008) and the D1a of Weh & Froitzheim (2001) based on tectono-sedimentary research. Timing of this stage of sediment-accretion is placed in the Late Eocene (between 40 – 30 Ma; Berger & Bousquet, 2008). Our D2 can be linked with the Ferrera phase of Wiederkehr et al., 2008, the Ferrera by Schmid et al. (1996) and the D1b by Weh & Froitzheim (2001). D2 lasted probably until some 30 Ma ago, but can be separated by D1 by different mineral assemblages present (table 1 in chapter 5.4). Before the onset of the late stage heating event, a deformation phase which caused nappe re-folding, known as the Domleschg phase (Wiederkehr et al., 2008) influenced the large scale structure of the area. No real indications are observed of this phase in the P58b thin sections (chapter 5). Timing is associated with back thrusting along the Insubric mylonite belt, i.e. 30 - 25 Ma (Schmid et al., 1987 a.o.). The Barrow thermal pulse occurred in a phase without any deformation, as can be seen in the undeformed late grown porphyroblasts in P58b. Therefore, it post-dates D3 and was likely active around 20 - 18 Ma (Janots et al., 2007; Allaz et al., 2007).

According to tectono-metamorphic research, an absolute time can be coupled to the relative time of the metamorphic and deformational events. Wiederkehr et al. (2008) highlights important arguments for a Barrovian P-T evolution followed by a Buchan late stage heating event. (1) Two individual sets of metamorphic minerals exist which are separated through time by deformation. Where the HP event at M2 was estimated to have started ca. 40 Ma ago (Lihou and Allen, 1996), the late stage heating (M3) overprints the F_2 crenulation cleavage event and was younger than 20 Ma (obtained on micas; Allaz et al., 2007 and Janots et al., 2007). (2) D_2 nappe stacking decompression was isothermal and did not cause an increase in temperature in the rocks. (3) The Buchan-type heating took place under static conditions after deformation. These arguments are in agreement with microtextures in P58b. Since our study did not incorporate any absolute age analyzes, only relative ages could be made about regarding the stable mineral assemblages.

Wiederkehr et al. (2008) also suppose their own scenario for the tectonic-metamorphic evolution of the area. Basically this comprises of the following five stages:

1) Subduction and sediment-accretion stage (D1; our D1)
2) Nappe stacking and decompression (D2; our D2)
3) Nappe re-folding (D3)
4) Barrow-type thermal overprint
5) Back-folding in the Northern Steep Belt (D4)

Finally the authors make a qualitative analysis of potential heat sources suggested by previous research. Any arguments for or against possible theories are further discussed in the discussion of the P-T path heat source in chapter 9.6. They propose a combination of radiogenic heat production by accretion of continental material in an accretionary wedge, associated with rising isotherms by late back-thrusting and nappe-refolding. The accretions of massive basement nappes in the accretionary wedge form the Lepontine Dome in the area.

There is therefore tectono-metamorphic evidence for a late stage heating event in the north-eastern part of the Lepontine Dome. The next chapter discusses the results of this MSc thesis and relates them to previous research and possible heat sources for a late stage-heating event.

9. Discussion of the P-T path for the metapelite in rock sample P58b collected at Lukmanier Pass

The following section will give a more thorough analysis of the presumed P-T path for sample P58b. This is mainly done by integrating the petrographic microstructural relationships, EMP data and thermodynamic studies. Subsequently the factor time is introduced by comparing this study with studies regarding the eclogites in the Northern Adula nappe and the north-eastern Lepontine Dome (chapter 8).

The dominant minerals observed in the thin sections are staurolite, garnet, kyanite and oligoclase. A petrogenetic grid for metapelitic rocks is illustrated in table 1 in section 5.4. From this diagram it can be seen that rock P58b shows a metamorphic evolution. The transition from the Chlorite and Biotite Zone into the Almandine (garnet) Zone marks the upper boundary of the greenschist facies. The Staurolite and Kyanite Zone indicates low to medium grade amphibolite facies conditions and the Sillimanite Zone is the first indication of the higher grade upper amphibolite to granulite facies. In addition the results of thermodynamic calculations, based on geothermobarometry (chapter 7.4) are indicated in figure 7.15. Clearly, from this diagram it can be seen that the samples in this study show a Barrovian metamorphic field gradient in the Kyanite and Staurolite Zones. Minerals that are related to pelitic rocks in the greenschist facies are (Chemeketa, 2012):

white mica-chlorite-chloritoid-quartz-albite-magnetite-biotite-epidote-garnet-pyrophyllite

whereas stable minerals when crossing into the amphibolite facies are:

white mica-chlorite-biotite-quartz-oligoclase-garnet-magnetite-staurolite-ilmenite-kyanite-(± sillimanite

The porphyroblasts observed in this study show most affinity with the (upper) greenschist and lower to middle amphibolite facies and have no affection with the granulite facies since no late growing k-feldspar and sillimanite are present (fig. 9.3). In the following part of the discussion I discuss a P-T-t path for P58b (fig. 9.1). The description of the stability and P-T conditions starts at the lowest grade and follows the P-T path through time. Some references are made to earlier shown figures and tables in chapter 5. The paragenetic grid which describes the relation between the observed metamorphic and deformational events is given in table 1 in chapter 5.4.

9.1 PT conditions M1 stable mineral assemblage

	S_0	S_1 (schistosity F_1)		S_2 (crenulation cleavage F_2)	
	M1		M2		M3
Staurolite					
Garnet					
Oligoclase					
Kyanite					
Biotite					
Ilmenite					
Rutile					
Muscovite					
Paragonite					
Tourmaline					
Quartz					

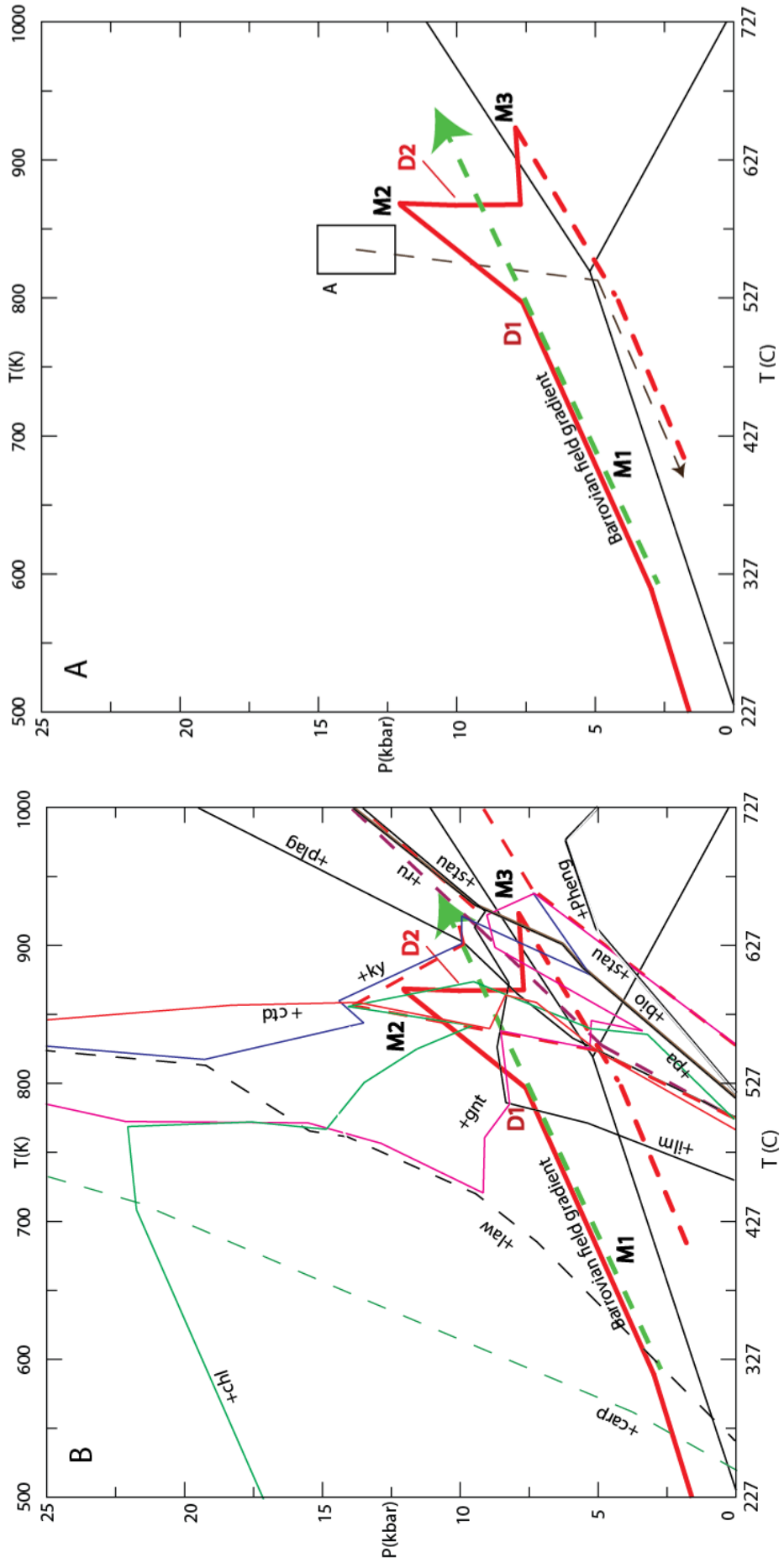

Figure 9.1. (A) *P-T-t path for P58b metapelite. Note the Northern Adula nappe exhumation path indicated with A. Barrovian metamorphic gradient is indicated as reference. Exhumation path is not preserved in the rock, hence showed as a dashed line.* (B) *Figure (A) with stability fields of metapelitic minerals. Figures created with Perple_X software.*

The initial 'sedimentary' mineral assemblages S_0 cannot be seen in the samples of this study anymore. Tables A-G in appendix 14.1 show the low grade shales contain modally abundant amounts of quartz, chlorite and pyrophyllite. M1 paragonite is the main white mica phase present at this stage. A striking feature is the enrichment in Al in the bulk rock composition (fig. 9.3). This means that in the initial S_0 composition pyrophyllite is the main Al-bearing mineral. Temperature of this composition does not exceed 400 ^oC where pyrophyllite reaches its uppers stability level in the presence of a pure fluid (Bucher and Frey, 1994; 7.5). However, according to the PT diagram created with Perple_X, no pyrophyllite is observed at temperatures of 400 ^oC. Already at temperatures below 250 ^oC pyrophyllite and chlorite are replaced by chloritoid by the reaction chlorite + 4 pyrophyllite = 5 chloritoid + 2 quartz + 3 H_2O. The stable mineral assemblage is pyrophyllite + chloritoid which is only stable in Al-rich rocks as P58b. Since the minerals are not observed in thin sections of P58b, they are not included in the paragenetic diagram. Next to chlorite there exists another iron-rich phase, magnetite. Around 300 ^oC chlorite reacts with hematite to form chloritoid and magnetite (Bucher and Frey, 1994). One of the M2 staurolite minerals (StaubB11) contains an inclusion of magnetite (StauB11inc2). The magnetite minerals were still stable during staurolite growth and were already formed when M2 staurolite overgrew them. The 'sedimentary' mineral assemblage described is represented by M1 in the P-T field of figure 9.1.

As described by Wiederkehr et al. (2008) the first lower greenschist facies LP/LT observed can be correlated with a mineral assemblage which is retrogressive from a blueschist facies HP/LT stage related to subduction of the Sub-penninic meta-sediments. This HP/LT assemblage consisted of carpholite-chlorite-phengite-quartz ± chloritoid. Peak conditions were calculated to be 1.2-1.4 GPa and 350-400 ^oC. The subsequent greenschist facies minerals, phengite-paragonite-chlorite-quartz, are common in the Stgir and Coroi Series of the Gotthard-Mesozoic cover found in the area (chapter 3.2). The formation of these minerals can be linked with the breakdown of carpholite at higher temperature: carpholite = chloritoid + quartz + 2 H_2O (Bucher and Frey, 1994). Since no carpholite is observed in the thin sections, the equilibrium temperature should be > 280 ^oC. The formation of chlorite and paragonite indicates a cold decompression path after the HP/LT metamorphic stage (Gillet and Goffé, 1988).

9.2 PT conditions S1 stable mineral assemblage

	S_0	S_1 (schistosity F_1)		S_2 (crenulation cleavage F_2)	
	M1		**M2**		**M3**
Staurolite					
Garnet					
Oligoclase					
Kyanite					
Biotite					
Ilmenite					
Rutile					
Muscovite					
Paragonite					
Tourmaline					
Quartz					

With increasing temperature, a deformation phase developed schistosity in the rock (D1=S1). The D1 deformation phase can be linked to subduction and sediment accretion as described in chapter 8.2. This schistosity is simultaneously formed with the replacement of pyrophyllite by

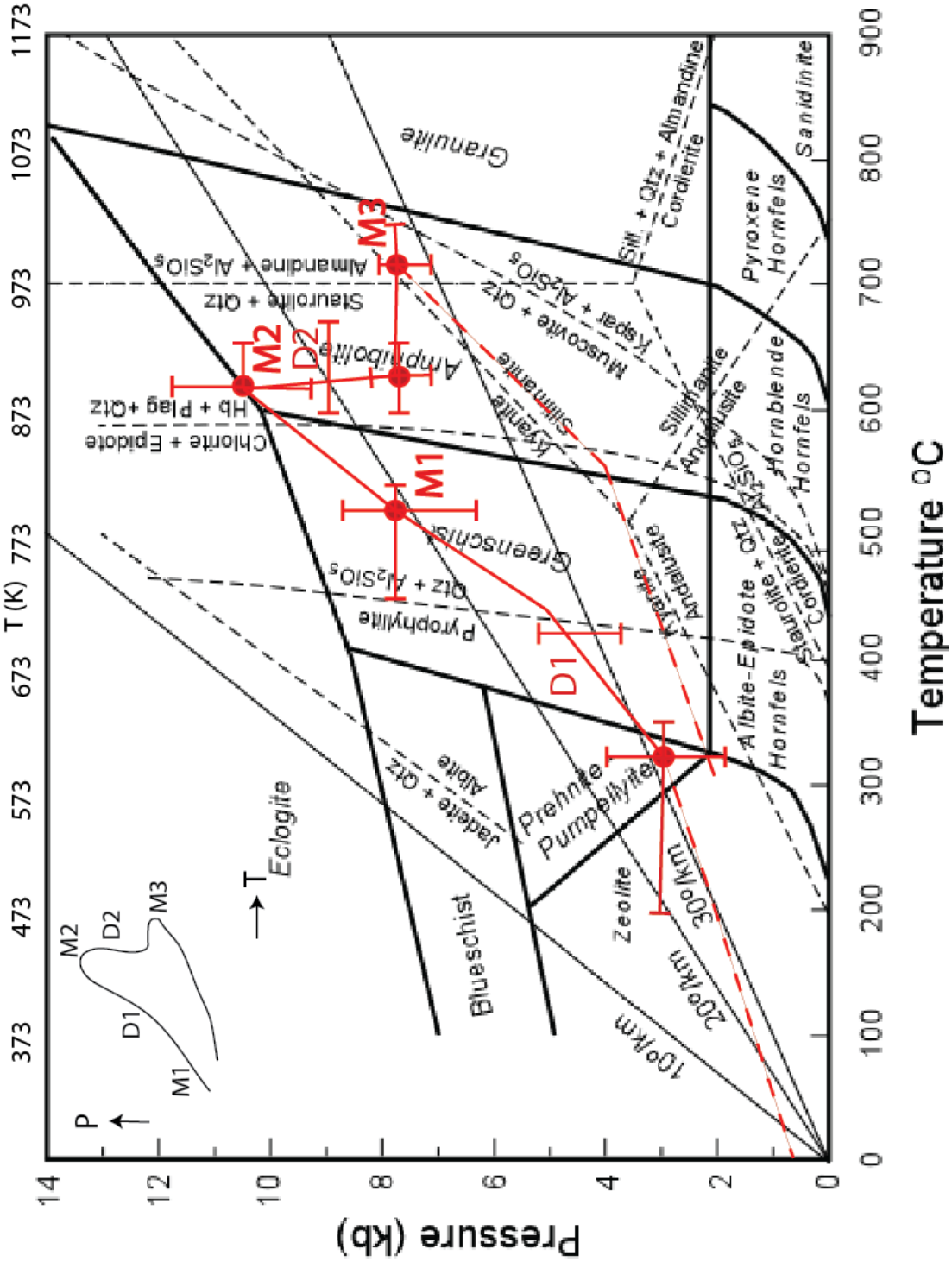

Figure 9.2. Petrogenetic grid for a pelitic bulk rock composition. In addition, the PT results determined for the M1-M2-M3 assemblages are added to this diagram. A clear PT-path can be deciphered through the mineral assemblages Note the error bars that indicate the upper and lower boundaries of the path. D1 and D2 correspond to the observed deformation phases described in chapter 6. Overview of PT path indicated in the upper left corner

kyanite and quartz around 370 ^{o}C. Now, M2 kyanite and chloritoid are the main minerals observed in the rock. Since the composition is rich in M1 ilmenite (which is folded in D1=S1), the assemblage is situated within the ilmenite stability field (fig. 9.1B). The reaction 3 chlorite + 8 k-feldspar = 5 annite (biotite) + 3 muscovite + 9 quartz + 4 H_2O replaces any 'sedimentary' minerals left by M1 Fe-rich biotite and M1 muscovite. The pressure and temperature conditions under which this exchange happens depends on the molar fraction of Fe present in the rocks. Since our rocks are highly enriched in Fe and lack significant Mg (see bulk rock composition, chapter 7.1) the reaction happened roughly around 420 ^{o}C and 3.5 kbar (Bucher and Frey, 1994). The formation of M2 kyanite and the replacement of pyrophyllite is possibly also observed in the samples. The heavily deformed M2 kyanite crystals which show undulatory extinction and are located mainly on top of the cleavage domains have formed during this reaction. M1 paragonite is the stable phyllosilicate phase observed in the matrix, although some M1 muscovite minerals are formed in combination with M1 biotite according to the reaction described above.

Around 510 ^{o}C M2 almandine garnet is formed by the reaction of chlorite + chloritoid + 2 quartz = 2 almandine + 5 H_2O. Chlorite is fully replaced around the same temperatures by the reactions with M1 muscovite to M2 garnet and M2 biotite (muscovite + 3 chlorite + 3 quartz = 4 almandine + annite + 12 H_2O). The precise temperature conditions of this reaction are dependent on the fractions of Mn and Ca present in garnet, but since these are almost negligible compared to Fe and Mg, the reaction is placed around 500 ^{o}C (table G chapter 14.1). The stable aluminum assemblage at this stage is M2 garnet + chloritoid + M2 biotite that marks the transition from the greenschist to the amphibolite facies (fig 9.3). This disputes the interpretation of the reaction rim of biotite around garnet (chapter 5.2.1). Inside the matrix the stable mineral assemblage remains M1 paragonite, M1 biotite and M1 muscovite. The first M2 rutile crystals are observed in the vicinity of growing M2 garnets and chloritoid. According to the Perple_X diagram in figure 12.1B, S2 does not plot in the stability field of garnet but due to the wide transition zone the first garnets are formed.

As a minor phase tourmaline is formed. The tourmaline minerals align with the F2 crenulation cleavage and are formed during increasing metamorphic grade in metapelitic systems.

This progressive heating is linked to the formation of an accretionary wedge by the subduction of the Valais Ocean and parts of the European margin beneath the Briançonnais micro-continent with scraping of the upper layers of sediments into an accretionary wedge (Schmid et al., 2004). This wedge could have reached a thickness of ca. 20 km (Hitz and Pfiffner, 1997). Dependent on the depth of the rocks in the accretionary wedge, some of them reached blueschist facies up to 1.2-1.4 GPa. Minerals associated with the blueschist facies like lawsonite and carpholite are not observed in our samples, hence I assume the rocks went less deep into the accretionary prism into the subduction zone. This is also indicated by the peak metamorphic pressure at 10-11 kbar. A majority of the present research performed is in agreement that accretionary prism formation and subduction are the main mechanisms for the pressure increase (Lihou and Allen, 1996; Schmid et al., 1987).

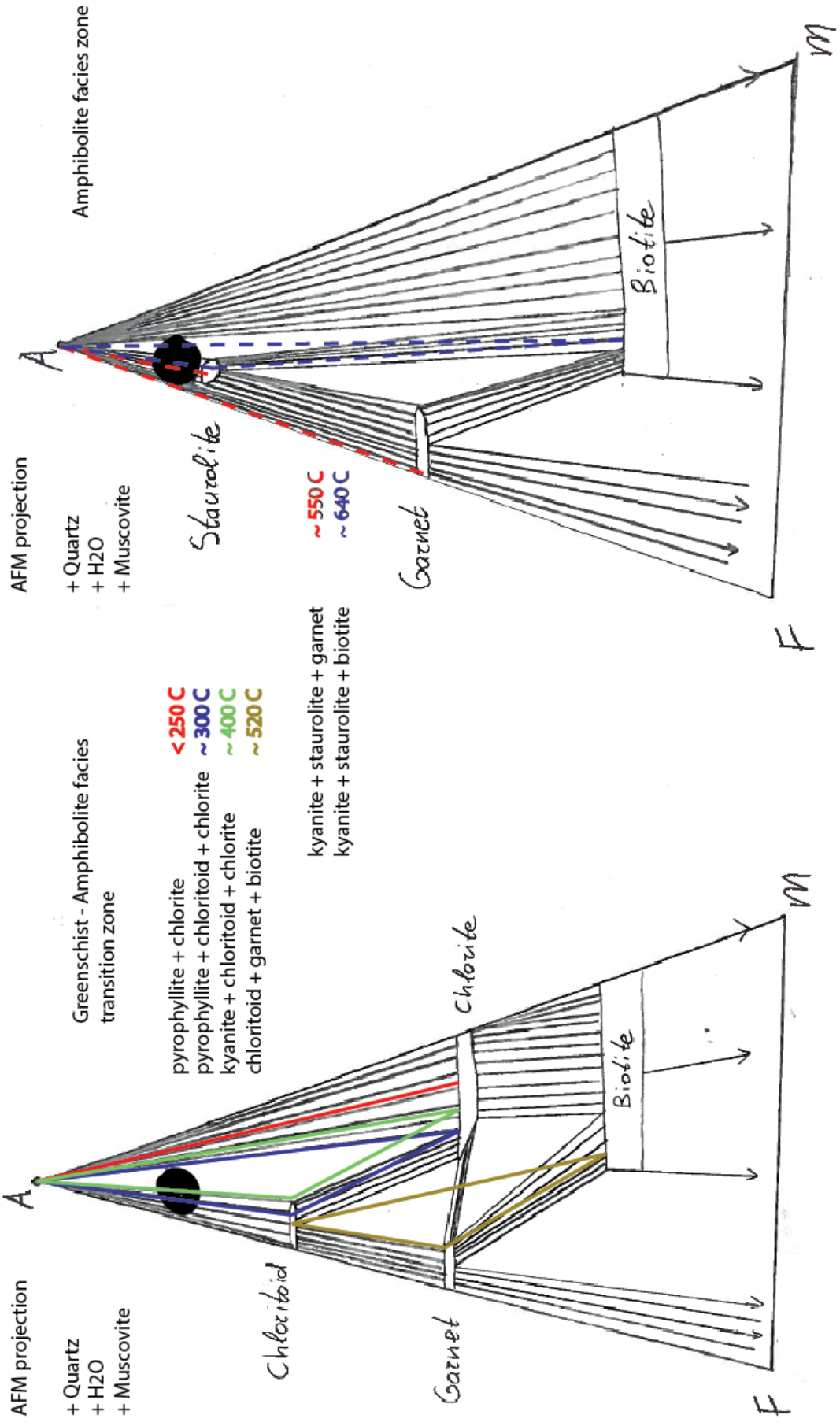

Figure 9.3. AFM projections of stable mineral assemblages in the KFMASH system during progressive metamorphism. Note the absence of the N-phase which represents the amount of Na in the KNFASH system, hence '+Muscovite' comprises muscovite + paragonite. The bulk rock composition of P58b is indicated with the black dot.

9.3 PT conditions M2 stable mineral assemblage

	S_0	S_1 (schistosity F_1)		S_2 (crenulation cleavage F_2)	
	M1		M2		**M3**
Staurolite					
Garnet					
Oligoclase					
Kyanite					
Biotite					
Ilmenite					
Rutile					
Muscovite					
Paragonite					
Tourmaline					
Quartz					

M2 represents the peak metamorphic pressure in the P58b samples. Fe-rich M2 staurolite, M2 almandine and M2 kyanite are the stable porphyroblasts observed. M1 Ilmenite is not growing anymore at this stage and the matrix did not change compositionally compared to the D1 assemblage. The first staurolite starts to grow at the expense of chloritoid and M2 kyanite: 8 chloritoid + 10 kyanite = 2 staurolite + 3 quartz + 4 H_2O. This reaction marks the Staurolite Zone in the lower amphibolite facies (Chemeketa, 2012). Since there is no chloritoid observed at peak pressure conditions, the stable mineral assemblage has crossed the chloritoid-out isograd, which is situated in the amphibolite field. The last chloritoid minerals decompose in a continuous reaction of 23 chloritoid + 7 quartz = 2 staurolite + 5 almandine + 19 H_2O around 550 ^oC.

Since M2 staurolite is observed, the PT path crosses the stability field of the staurolite between 2.5 kbar < staurolite < 12 kbar of the KNFASH system of Bucher and Frey (fig. 7.5). Peak metamorphic conditions hence are not greater than 12 kbar. I assume peak pressure conditions around 10–11 kbar. According to Perple_X, at these conditions chlorite and chloritoid are instable, staurolite and garnet are stable and kyanite is metastable. At higher pressures, M2 kyanite is the most significant Al-phase and forms a stable assemblage with M2 garnet and M2 staurolite.

The retrograde decompression path of P58b can be compared with the retrograde PT path from the eclogites of the Northern Adula Nappe (chapter 8.1). This path, indicated in figure 8.2, shows however decompression at temperatures roughly 30-50 ^oC colder. The different temperatures can be related to a variable depth of burial and exhumation. The Northern Adula nappe shows peak pressures of 12 – 14 kbar (Spalla et al., 1996). However, no late stage heating event is observed in the eclogites. This can be correlated with the distance between the source of the heat (e.g. Lepontine dome) and the geographical nappe position. Whereas the Lukmanier rocks do show a late heating stage since they are located more in the vicinity of the source, the nappe itself does not show any late heating effect (fig. 8.2).

The decompression and D2 formation is related to a phase of nappe stacking of the peak metamorphic units (Wiederkehr et al., 2008). Since the Adula nappe comprises of European continental basement rocks, not only the outer margins of the continent but also the more felsic parts did partly subduct during the early phases. This nappe stacking is the precursor of the Lepontine Dome structure.

9.4 PT conditions S2 stable mineral assemblage

	S_0	S_1 (schistosity F_1)		S_2 (crenulation cleavage F_2)	
	M1		**M2**		**M3**
Staurolite					
Garnet					
Oligoclase					
Kyanite					
Biotite					
Ilmenite					
Rutile					
Muscovite					
Paragonite					
Tourmaline					
Quartz					

A second deformation phase (D2) causes deformation of the schistosity and the formation of crenulation cleavage domains and microlithons. All the matrix minerals are affected by this crenulation cleavage, just like the S1 tourmaline minerals formed at a previous stage. As isothermal exhumation progresses, various mineral isograds are crossed. The retrograde temperature remains below 670 ^{o}C in the staurolite-stability field since there is no sign of a reaction between staurolite and quartz to form almandine and kyanite via: 75 staurolite + 312 quartz = 100 almandine + 2 kyanite + 3 water (fig. 9.2).

The ‘sedimentary’ Na-rich white mica paragonite breaks down in the presence of quartz at temperatures at about 620 ^{o}C via the reaction: paragonite + quartz = albite + Al-silicate + H_2O. This implies that M1 paragonite is present in large portions of the staurolite + quartz stability field. Schists containing staurolite-kyanite-paragonite are classical metamorphic rocks of the mid-amphibolite facies zone in the Central Alps (Bucher and Frey, 1994). The Perple_X diagram of figure 9.1B shows stability fields (e.g. 6, 7, 9, 10, 11) in which both paragonite and plagioclase are stable. The observed mineral assemblage of S2 is located inside the stability field of plagioclase since it starts growing late syn- to post-deformational (where D2 is the deformation phase). M1 paragonite starts to decay and M3 oligoclase minerals are formed. M2 muscovite flakes start overgrowing the matrix material. The same is true for M2 rutile crystals. The formation of rutile needles on top of M2 muscovite flakes is restricted to a small stability field indicated in fig. 9.4 where rutile is stable in combination with M2 muscovite and M3 plagioclase. The needles appear to be aligned inside the M2 muscovite flakes, which could indicate growth on a specific plane of the muscovite crystals (chapter 6.2.7). Analysis of this alignment is however beyond the scope of this work. New M3 ilmenite growth is initiated by intersection of the PT path with the ilmenite-in isograd and M2 staurolite remains stable, although slightly more enriched in iron according to the TD calculations (chapter 7.3.2).

Garnet porphyroblasts have been analyzed in zonation using EMP line scan analyses. As can be seen in figure 7.3, the observed garnet core and garnet rim compositions plot around 875 K and 890 K respectively. The rim compositions are slightly more enriched in Fe which is a result of ongoing matrix diffusion. This element diffusion requires temperatures above at least 800 K. However, the garnet compositions are unstable according to the plot in Perple_X. This means that the original compositions are influenced by metamorphism or deformation. Since garnet has been stable on the prograde path, the proposed PT path should cross the metastable garnet composition PT conditions (fig. 7.3) during a late stage heating event.

This D2 deformation phase can be linked with the D2 deformation as described in Wiederkehr et al. (2008). The relative timing compared to D3 and the late stage heating event cannot be correlated properly, since no signs of D3 deformation are observed in P58b.

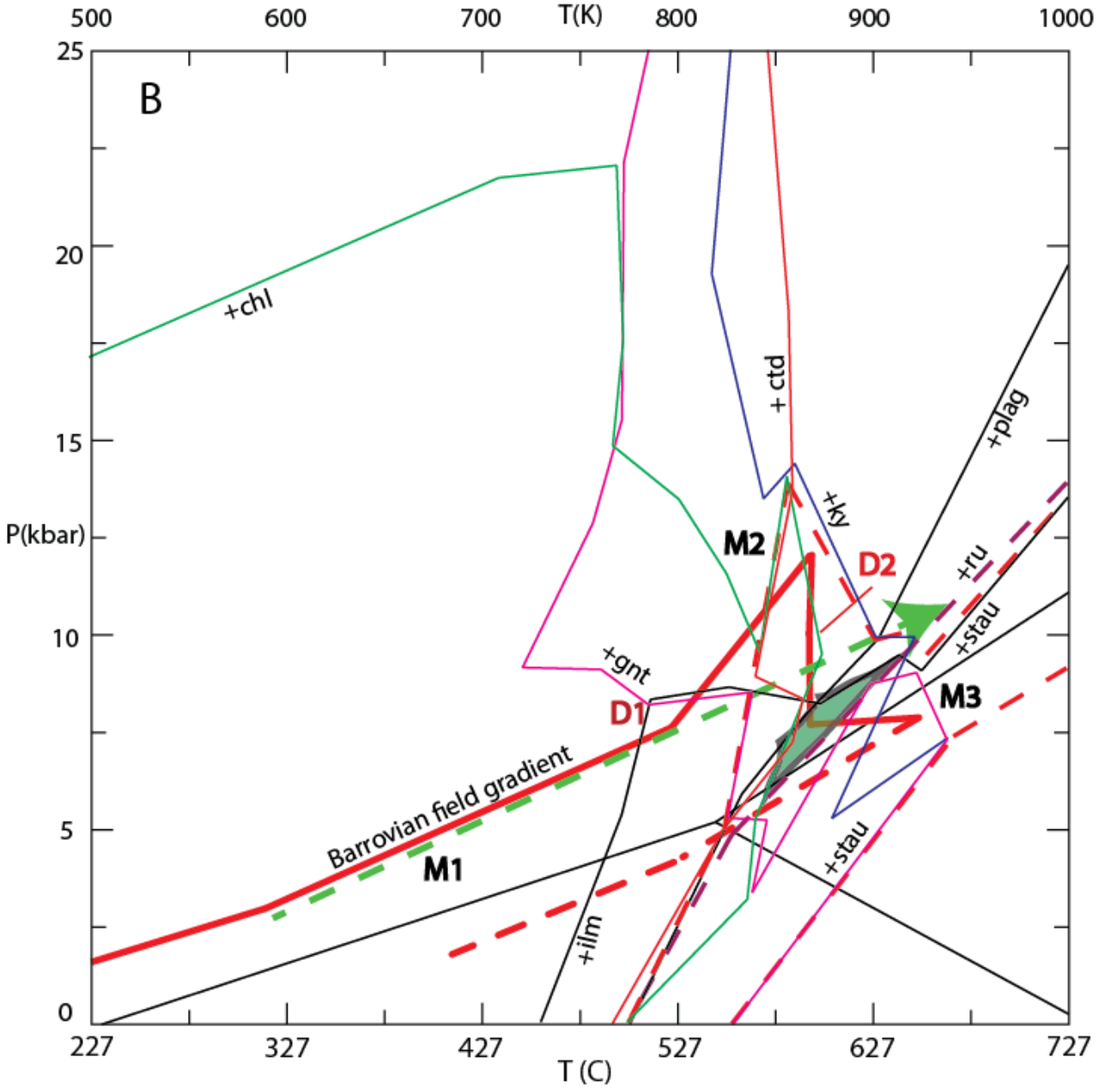

Figure 9.4. Mineral stability field of M2 rutile in combination with M2 muscovite, M3 ilmenite and M3 plagioclase, but limited by the presence of M1 paragonite, chlorite and chloritoid.

9.5 PT conditions M3 stable mineral assemblage

	S_0	S_1 (schistosity F_1)		S_2 (crenulation cleavage F_2)	
	M1		M2		M3
Staurolite					
Garnet					
Oligoclase					
Kyanite					
Biotite					
Ilmenite					
Rutile					
Muscovite					
Paragonite					
Tourmaline					
Quartz					

The P-T path is influenced by a Buchan-type late stage heating event. Undeformed, euhedral shaped porphyroblasts are formed and form the M3 stable mineral assemblage (chapter 5.2). The M3 formed minerals do not show a shape preferred orientation related to earlier deformation phases and have therefore grown post-D2. These minerals are M3 kyanite, M3 biotite, M3 oligoclase, M3 ilmenite, M2-3 rutile and M2-3 muscovite. The M3 kyanite porphyroblasts have grown at prograde temperatures just inside the kyanite-in isograd. No exsolution of a new sillimanite phase is observed, despite entering the sillimanite-in field. Therefore the M3 kyanite blasts remain metastable. Secondly, oligoclase grows at increasing temperature. The porphyroblasts grow on top of M1 paragonite and show rotated inclusion trails indicating a syn-/post-D2 growth. The undeformed M3 ilmenite started to grow late syn-D2 (fig. 9.1B). The M3 muscovite flakes observed are starting to grow at the expense of paragonite and plagioclase and grow randomly over the minerals. They remain stable at peak temperature conditions, since no back reaction of muscovite + quartz to k-feldspar + aluminosilicates + water is observed (fig 9.1B; 7.5 reaction 25). The growth of new muscovite flakes indicates the presence of a free fluid phase which is incorporated into the minerals. Hence stable mineral assemblage M3 crosses the metastable kyanite field (in the sillimanite stability field) at temperatures around 920 K and 7.5 kbar and subsequently follows a retrograde path as observed in the Northern Adula nappe eclogites (fig. 9.1A). This is the peak temperature observed in P58b. Any possible causes for a late stage heating event will be discussed in a later stage.

9.6 Late stage heating event

Debate is ongoing regarding the conditions along the P-T path obtained. Relationships between metamorphism and deformation are important indicators whether or not the PT evolution appeared in one stage or subsequent phases. According to this MSc thesis and the study by Wiederkehr et al. (2008), there is evidence for a late stage heating event on top of a Barrovian metamorphic field gradient.

This Buchan-type thermal overprint can probably best be explained by a combination of several proposed models in literature. Since the heating event happened under static conditions, a model without crustal deformation is most likely. The combination between slab break-off, which induces flow of hot asthenosphere to lower depths and causes reheating of previously formed sediments and structures, and a nappe stacking event, which induces accretion of crustal material and therefore radioactive elements, can possibly explain why late reheating influenced the area. Slab break-off would have occurred at depths of maximum

30 km depth (Brouwer et al., 2004). This depth is however disputable since temperatures are probably not high enough to break a slab at depths around 30 km depth. The presence of garnet peridotite bodies in the area (Olker et al., 2003) cannot be explained by this theory. Since convection of material is relatively quickly compared to conduction timing should not be problematic if slab break-off is placed at a higher depth. This flow of hot material into the crust would result in a temperature increase of at least 200 ^{o}C in only a few million years (Brouwer et al., 2004).

Conductive heating of continental material by radioactive decay is a process which is relatively slow compared to flow of hot asthenosphere into the crust. Jamieson et al. (1998) suggests that radiogenic heating of crustal material which has accreted at middle crustal depths could provide enough heat to increase temperature. This accretion can be coupled with the nappe stacking of crustal material during collisional and post-collisional stages in the Alps (the Lepontine metamorphic event). The Lepontine Dome itself consists of massive accretions of granitoid basement units derived from the European margin (Milnes, 1974; Schmid et al., 2004). Temperature increase would be significantly less compared to convection of material, but a rise of about 50-70 ^{o}C is plausible according to the tectonically accreted radiogenic material (TARM) model of Jamieson (1998). If the formation of an accretionary wedge at the subduction through started 70 Ma (and our P58b pelitic rocks are incorporated in it), time would be sufficient to reheat the Barrovian-type metamorphism (Jamieson, 1998). Note however that observations can be very local due to the heterogeneity of the Alpine Orogen.

Other models supposed include assumptions which are unlikely or debatable regarding the Alpine Orogen. The shear heating model by Burg & Gerya (2005) would only work if rapid tectonic convergence would have taken place to cause heating of the adjacent sediments when nappes slide over each other. Since the Barrow-type overprint occurs at a very late stage in the Alpine evolution, shear heating is an unlikely cause (as convergence is very slow). Advective heat transfer from plutons formed out of the upwelling asthenosphere, like the 32-30 Ma Bergell intrusion; do contribute to the heat aureole around Lepontine Dome. However, most of these intrusions occur along the Southern Steep Belt which is located in the southern part of the Lepontine Dome, hence these effects can be ignored in the north-eastern part of the belt at our study area.

A combination between slab break-off at higher depth and accretion of continental material in a sedimentary wedge as the Lepontine Dome can increase temperatures in relatively short amounts of time. This heating event might be sufficient to show a local Buchan-type overprint over a Barrovian metamorphic field gradient.

Multiple assumptions and parameters are observed throughout modeling and interpreting and study of the evolution of the Alpine orogeny will be ongoing in the upcoming years.

10. Conclusion

The metapelitic rocks of P58b are strikingly rich in Al with increased amounts of Na and Fe. The amounts of Ca, Mn and Mg are relatively small compared to standard metapelitic systems observed. This Al enrichment is possibly caused by the changing pressure-temperature conditions and the initial 'sedimentary' S_0 composition. The system has to be regarded as an open system where phases and fluids are able to transfer elements in and out of the bulk rock composition. A possible late stage heating event can cause metasomatic fluids to transfer soluble elements through the system.

As can be seen in the TiCNKFMASH system used for this study, P58b gets progressively enriched in K and depleted in Na (muscovite and biotite grow; paragonite breaks down). Moreover, Fe increases at higher temperature (ilmenite and rutile growth) and Al is distributed amidst different aluminium-silicate phases and Al-rich porphyroblasts, which indicate element diffusion transfer. Regarding the growth of porphyroblasts, fluids are an important factor. CO_2 concentration is negligible and discarded since hardly any Ca-rich rocks are present and fluids are assumed to be almost pure H_2O. The fluids cause growth of porphyroblasts and transfer of nutrients and waste material away from the growth sites. P_{fluid} = 1 is assumed throughout the PT path, since many water-rich phases are present.

The stable mineral assemblages can be subdivided in three compositions: M1, M2 and M3. M1 represents the 'sedimentary composition'. In the Barrovian-type prograde part greenschist facies minerals like paragonite, chlorite, pyrophyllite, ilmenite, biotite, chloritoid and magnetite are formed. Matrix material is represented by these minerals and hardly any porphyroblasts are formed due to low pressure and temperature conditions. After a first phase of deformation (D1 ≈ 40-30 Ma) where F_1 schistosity develops in the samples, at increasing temperature and pressure conditions kyanite, garnet, staurolite, rutile and tourmaline form porphyroblasts on a mm-scale. At peak metamorphic pressures of ≈ 10-12 kbar, this stable mineral assemblage M2 contains mainly amphibolite facies minerals. An isothermal retrograde path exhumes the rocks by nappe stacking and thrusting (phase D2 ≈ 35-30 Ma) of HP units on top of LP units (Wiederkehr et al., 2008) to final pressures of 6-7 kbar. During this exhumation a new deformation phase develops F_2 spaced crenulation cleavage in the rocks. A Buchan-type LP/HT thermal overprint causes a temperature increase of ≈ 100 ^{o}C in the region. This is observed by post-deformational (or late-syn) growth of M3 minerals like oligoclase, kyanite, muscovite and ilmenite. These blasts do not show any signs of deformation and have grown over all previously formed deformational and metamorphic structures.

The kyanite porphyroblasts have grown in two stages, both outside the initial S_0 mineral assemblage. The first phase is formed pre-D2 and shows undulatory extinction and deformation on cleavage domains. The second group of kyanites is undeformed and blocky in shape due to growth during the late stage heating event.

In the vicinity of the Lukmanier Pass, data regarding exhumation paths of deep subducted eclogite bodies in the Northern Adula nappe is compared to the exhumation path of this study (fig. 8.2; fig. 9.1A). It shows a similar isothermal exhumation, but the temperature at which exhumation takes place is lower and the path does not show a late stage heating event. This highlights the heterogeneity of the Alpine Orogeny and the regional influences which

overprint the main phases of deformation. The Buchan-type late stage overprint is not recorded in the eclogites (fig 8.2). The tectono-metamorphic study by Wiederkehr et al. (2008) on metasediments in the area does show a late stage heating event in the area of the Lukmanier Pass. The temperature increase does however diminish further away from the Lepontine Dome, which is the source of heating.

To assign a geodynamic model which explains the evolution in the area is difficult, due to the heterogeneity of the Alps itself. As indicated in previous research, there are several reasons which can explain a late stage heating event. The most likely method is a combination of slab break-off at depth and uplift of accreted crustal nappes which cause a regional heat pulse. The slab break-off induces upwelling of hot asthenosphere and radiogenic material in accreted granitic basement nappes would heat up the units. The Barrovian metamorphic field gradient observed is therefore overprinted by a late stage impulse of heat. This is however dependent on the location with respect to the source of heating.

Many studies have been performed on Penninic units in the Central Alps. Each study raises more questions itself and the real metamorphic and deformational evolution will probably never be exactly understood. Future technical developments and more precise dating methods should however give more opportunities for solid research regarding the geology in the Lukmanier Pass area.

11. Future works

More knowledge should be gained about regional heterogeneities regarding the geology of the Alps which cause all sorts of problems. More studies on a regional scale should improve this lack of knowledge, and when this is bundled in an open access database people can view and review work more often. For example, the study of Spalla et al. (1996) on eclogite bodies in the central Alps could be checked with new developed techniques whether or not a late stage heating event has taken place in the Northern Adula nappe. According to this thesis and study of Wiederkehr et al. (2008) there should be a late stage heating event. Secondly, research regarding the overall evolution of the Alps should be continued. There is still a large variety of ideas about the cause of, e.g. a thermal overprint, and other phenomena observed in the Alpine orogeny. Improving techniques, smaller error margins and more money would enhance research and probably reach a break-through at some point.

Finally, calculations with modeling programs like TheriakDomino, Perple_X and Thermocalc still show significant differences in results when inserting the same bulk rock composition. Further research and/or experience in the use of them and knowledge in thermodynamics of elements is important to get more precise results and hence a better understanding of the metamorphic evolution.

12. Acknowledgements

I would like to thank my supervisors Martyn Drury, Herman van Roermund and Oliver Plümper for their assistance and advice regarding the aim of this study and related programs like Perple_X and the use of geothermobarometry. In addition, I would like to thank Otto Stiekema for perfect thin section preparation and assistance with the pearl preparation for the XRF analysis. Tilly Bouten assisted helpfully during my work at the electron microprobe, which is really appreciated and e-mail correspondence with James Connolly regarding his Perple_X software helped me to understand the program sufficiently to interpretate my results. Finally I would like to thank Kalijn Peters for her time and effort to assist when she created pseudosections with TheriakDomino and explained the basic assumptions and knowledge of the software. Last but not least I would like to mention my roommates at the university, Jorien van der Wal, Karin Los, Adriana Currin, Marianne Robijn, Marc Breddels, Niels Olfert and Giel van der Grind who made the work environment enjoyable and relaxed, even in times of particular stress from my side.

January 2013, Joep Kiers

13. References

Allaz, J., Janots, E., Engi, M., Berger, A. and Villa, I.M., Understanding Tertiary metamorphic ages in the northern Central Alps, 2007, Geophysical Research Abstracts 9, EGU2007-A-07684

Anderson, D.E., Olimpio, J.C., Progressive homogenization of metamorphic garnets, South Morar, Scotland: evidence for volume diffusion, 1977, Canadian Mineralogist, v. 15, p. 205-216

Ballevre, M., Merle, O., The Combin fault: compressional reactivation of a Late Cretaceous-Early Tertiary detachment fault in the Western Alps, 1993, Schweizer Mineralogical und Petrological Mitteilungen, v. 73, p. 205-228

Baumer, A., Geologie der gotthardmassivisch-penninischen Grenzregion im oberen Bleniotal: Geologie der Blenio-Kraftwerke, 1964, Beiträge zur Geologie der Schweiz, Geotechnische Serie, v. 39, p 105

Berger, A., and Bousquet, R., Subduction related metamorphism in the Alps: Review of isotopic ages based on petrology and their geodynamic consequences. In: Siegesmund, S. et al. (Eds): Tectonic Aspects of the Alps-Dinarides-Carpathians system., 2008, Geological Society Special Publications, v. 298, p. 357-382

Bohlen, S.R., Boettcher, A.L., Experimental investigation and geological applications of orthopyroxene-olivine-quartz geobarometry., 1981, American Mineralogist, v. 66, p. 951-965

Bossard, L., Zur Petrographie der unterpenninischen Decken im Gebit der Tessiner Kulmination,1929,Schweizerische Mineralogische und Petrographische Mitteilungen,v.9, p. 47-107

Brouwer, F.M., Zedde, van de, D.M.A., Wortel, M.J.R., Vissers, R.L.M., Late-orogenic heating during exhumation: Alpine PTt trajectories and thermomechanical models, 2004, Earth and Planetary Science Letters,v.220, p.185-199

Brückner, W., Uber die Entstehung der Rauhwacken und Zellendolomite, 1941, Eclogae, Geol. Helveticae, v.34, p.117-134

Bucher, K. and Frey, M., Petrogenesis of Metamorphic Rocks, 1994, Springer-Verlag, Berlin, 6th edition, 318 p.

Budworth, D.W., The selection of grain-growth control additives for the sintering of ceramics, 1970, Mineralogical Magazine, v. 37, p. 833-838

Capitani, de C., Gleichgewichts-Phasendiagramme: Theorie und Software, 1994, Beihefte zum European Journal of Mineralogy, 72. Jahrestagung der Deutschen Mineralogischen Gesellschaft, v. 6, p. 48

Capitani, de, C. and Petrakakis, K., The computation of equilibrium assemblage diagrams with Theriak/Domino software, 2010, American Mineralogist v. 95, p. 1006-1016

Carmichael, D.M., On the mechanism of prograde metamorphic reactions in quartz-bearing pelitic rocks, 1969, Contributions to Mineral Petrology, v. 20, p. 244-267

Chadwick, B., Deformation and Metamorphism in the Lukmanier Region, Central Switserland, 1968, Geological Society of America Bulletin, v. 79, p. 1123-1150.

Channell, J.E.T., Brander, R., Spieler, A., Smathers, N.P., Mesozoic paleogeography of the Northern Calcareous Alps-Evidence from paleomagnetism and facies analysis, 1990, Geology, v. 18, p. 828-831

Chemeketa Community College, Barrovian Facies Series, website visited: 27/11/2013, http://faculty.chemeketa.edu/afrank1/rocks/metamorphic/regional.htm

CNR, Structural Model of Italy at 1:500 000, sheets 1 and 2, 1990, S.E.L.C.A.-Florance

Connolly, J.A.D., Computation of phase equilibria by linear programming: a tool for geodynamic modelling and its application to subduction zone decarbonation, 2005, Earth and Planetary Science Letters, v. 236, p. 524-541

Dal Piaz, G.V., Gosso, G., Pennacchioni, G. and Spalla, M.I., Geology of eclogites and related rocks in the Alps, 1993, Italian Eclogites and Related Rocks (Morten, L. eds.), v. 13, Rome, scritti e documenti, p. 17 - 58

Davies, J.H. and von Blanckenburg, F., Slab breakoff: a model of lithosphere detachment and its test in the magmatism and deformation of collisional orogens, 1995, Earth Planetary Science Letters, v. 129, p. 85-102

Dewey, J.F., Helma, M.L., Turco, E., Hutton, D.H.W., Knott, S.D., Kinematics of the western Mediterranean, 1989, in: Alpine Tectonics, edited by Coward, M.P., Dietrich, D., Park, R.G., Geological Society Special Publications, v. 45, p. 265-283

Durney, D.W., Solution transfer, an important geological deformation mechanism, 1972, Nature, v. 235, p. 315-317

Engi, M., Todd, C.S. and Schmatz, D.R., Tertiary metamorphic conditions in the eastern Lepontine Alps, 1995, Schweizerische Mineralogische und Petrographische Mitteilungen, v. 75, p. 347-369

Ernst, W.G., Significance of phengitic micas from low-grade schists, 1963, American Mineralogist, v. 48, p. 1357-1373

Ernst, W.G., Metamorphic zonations on presumably subducted lithospheric plates from Japan, Galifornia and the Alps, 1971, Contributions to Mineralogical Petrology, v. 34, p. 43-59

Ferry, J.M., Spear, F.S., Experimental calibration of the partitioning of Fe and Mg between biotite and garnet. Contributions of Mineral Petrology, v. 66, p. 113-117

Fox, J.S., Three-dimensional isograds from the Lukmanier Pass, Switzerland, and their tectonic significance, 1975, Geological Magazine, v. 112, art. 6, p. 547-626

Ghent, E.D., Robbins, D.B., Stout, M.Z., Geothermometry, geobarometry and fluid compositions of metamorphosed calc-silicates and pelites, Mica Creek, British Columbia, 1979, American Mineralogist, v. 64, p. 874-885

Ghent, E.D., Stout, M.Z., Geobarometry and geothermometry of plagioclase-biotite-garnet-muscovite assemblages, 1981, Contributions to Mineralogical Petrology, v. 76, p. 92-97

Gillet, P. and Goffé, B., on the significance or aragonite occurrence in the Western Alps, 1988, Contributions to Mineralogy and Petrology, v. 99, p. 70-81

Grünenfelder, M. and Hafner, S.T., Uber das Alter und die Entstehung des Rotondogranites, 1962, Schweiz. Mineral. Petrogr. Mitt., v. 42, p. 169-208

Guidotti, C.V., On the relative scarcity of paragonite, 1968b, American Mineralogist, v. 53, p. 963-974

Hauck, J., Paleomagnetic research on chosen Profils from the Cretaceous in the Rhenodanubic Flysch-Zone, Ph.D. thesis, Inst. Geophys. Ludwig-Maximilians-University, Munic, Germany, 1998

Helgeson, H.C., Delany, J.M., Nesbitt, H.W., Bird, D.K., Summary and critique of the thermodynamic properties of rock-forming minerals, 1978, American Journal of Science, v. 278A, p. 1-299

Hesse, R., Flysch-Gault und Falknis-Tasn-Gault (Unterkreide): Kontinuierlicher Ubergang von der distalen zur proximalen Flyschfazies auf einer penninischen Trogebene der Alpen, 1973, Geol. Palaeontol., v.2, p. 1-90

Hesse, R., Long-distance continuity of turbidites: Possible evidence for an Early Cretaceous trench-abyssal plain in the East Alps, 1974, Geological Society America Bulletin, v.85, p. 859-870

Hitz., L and Pfiffner, O.A., Geologic interpretation of the seismic profiles of the Eastern Traverse (lines

E1-E3, E7-E9): eastern Swiss Alps. In: Pfiffner et al. (eds.): Deep structure of the Swiss Alps - Results of NRP 20, 1997, Birkhäuser, Basel, p.73-100

Hodges, K.V., Spear, F.S., Geothermometry, geobarometry and the Al2SiO5 triple point at Mt. Moosilauke, New Hampshire, 1982, American Mineralogist, v. 67, p. 1118-1134

Holdaway, M.J., Stability of andalusite and the aluminium silicate phase diagram, 1971, American Journal of Science, v. 271, p. 97-131

Holland, T.J.B, and Powell, R., An enlarged and updated internally consistent thermodynamic dataset with uncertainties and correlations: the system K2O-Na2O-CaO-MgOMnO-FeO-Fe2O3-Al2O3-TiO2- SiO2-C-H2-O2, 1990, Journal of Metamorphic Geology, v. 8, p. 89-124

Holland, T. J. B. and Powell, R., An internally-consistent thermodynamic dataset for phases of petrological interest, 1998, Journal of Metamorphic Geology, v. 16, p. 309-344

Hollister, L.S., Garnet zoning: an interpretation based on the Rayleigh fractionation model, 1966, Science, v. 154, p.1647-1651

Hunziker, J.C., Rb/Sr and K/Ar age determination and the Alpine tectonic history of the Western Alps, 1974, Mem. 1st. Geol. Min. University Padova, v. 31, p. 1-55

Jamieson, R.A., Beaumont, C., Fullsack, P., Lee, B., Barrovian metamorphism : Wher's the heat ? in: Treloar, P.J., O'Brien, P.J. (Eds.), What Drives Metamorphism and Metamorphic Reactions?, 1998, Geological Society Londen Special Publications,v.138,p.23-51

Janots, E., Engi, M., Berger, A., Rubatto, D. and Gregory, C., Texture, chemistry and age of monazite and allanite in the northern Central Alps, 2007, Geophysical Research Abstracts 9, EGU2007-A-08582

Jung, W., Die mesozoischen Sedimente am Südostrand des Gotthard-Massivs (zwischen Plaun la Greina und Versam), 1963, Eclogae geologicae Helveticae, v. 56, p. 653-754

Keller, L.M., Hess, M., Fügenschuh, B., Schmid, S.M., Structural and metamorphic evolution of the Camughera – Moncucco, Antrona and Monte Rosa units southwest of the Simplon line, Western Alps, 2005, Eclogae geologicae Helvetiae,v.98,p.19-49

Kretz, R., Chemical study of garnet, biotite and hornblende from gneisses of S.W. Quebec, with emphasis on distribution of elements in coexisting minerals, 1959, J. Geol., v. 67, p. 371-402

Labhart, T.P., Geologie der Schweiz, 2005, Haupt Verlag, Bern, 7th edition, p. 215

Lasaga, A.C., Geospeedometry: an extension of geothermometry. In: Saxena SK (ed) Kinetics and equilibrium in mineral reactions, 1983, Springer, Berlin-Heidelberg New York, p. 81-115

Leine, L., Egeler, C.G.,Preliminary note on the origin of the so-called "Konglomeratische Mergel" and associated "Rauhwackes", in the region of Menas de Serón, Sierra de los Filabres(SE Spain): Geologie en mijnbouw, 1962, jr.41,v.7, p.305-341

Lihou, J.C. and Allen, P.A., Importance of inherited rift margin structures in the early North Alpine Foreland Basin, Switzerland. Basin Research, 1996, v. 8, p. 425–442.

Löw, S., Ein tektono-metamorphes Entwicklungsmodell der nördlischen Adula-Decke, 1986, Schweizer Mineralogische und Petrologische Mitteilungen, v. 66, p. 129-134

Malavieille, J., Guihot, P., Costa, S., Lardeaux, J.M., Gardien, V., Collapse of the thickened Variscan crust in the French Massif Central : Mont Pilat extensional shear zone and the St. Etienne Late Carboniferous basin, 1990, Tectonophysics, v. 177, p. 139-149

Mancktelow, N.S., Neogene lateral extension during convergence in the Central Alps: evidence from interrelated faulting and backfolding around the Simplonpass (Switerland), 1992, Tectonophysics, v. 215, p. 295-317

Massonne, H.J., Schreyer, W., Phengite geobarometry based on limiting assemblage with K-feldspar, phlogopite and quartz, 1987, Contributions to Mineral Petrology, v. 96, p. 212-224

Massonne, H.J., High-pressure, low-temperature metamorphism of pelitic and other protoliths based on experiments in the system K2O-Mgo-Al2O3-SiO2-H2O, 1990, [Unpublished Post-Doc thesis], Bochum, University of Bochum

Maxelon, M., Mancktelow, N.S., Three-dimensional geometry and tectonostratigraphy of the Pennine zone, Central Alps, Switzerland and Northern Italy, 2005, Earth-Science Reviews, v.71, p. 171-227

Milnes, A.G., Structure of the Pennine Zone (Central Alps): a new working hypothesis, 1974b, Geological Society of America Bulletin, v.85, p. 1727-1732

Nagel, T., de Capitani, C., Frey, M., Froitzheim, N., Stünitz, H., Schmid, S.M., Structural and metamorphic evolution during rapid exhumation in the Lepontine dome (southern Simano and Adula nappes, Central Alps, Switzerland), 2002, Eclogae geologicae Helvetiae, v. 95, p. 301-321

Newton, R.C., Metamorphic temperatures and pressures of group B and C eclogites, 1986, Geological Society of America Memoires, v. 164, p. 17-30

Newton, R.C., Haselton, H.T., Thermodynamics of the garnet-plagioclase-Al2SiO5-quartz geobaromter. In: Newton, R.C., (ed) Thermodynamics of Minerals and Melts, 1981, Springer-Verlag, New York, p. 131-147

Olker, B., Altherr, R., Paquin, J., Fast exhumation of the ultrahigh-pressure Alpe Arami garnet peridotite (Central Alps, Switzerland): constraints from geospeedometry and thermal modeling, 2003, Journal of Metamorphic Geology, v. 21, iss. 4, p. 395-402

Passchier, C.W., Trouw, R.A.J., Microtectonics, 2005, Springer-Verlag, Berlin, 2nd edition, 366 p.

Peters, K., Metamorphic evolution of the Hirkadag and Kirsehir massifs, Central Turkey, 2010, MSc thesis, University Utrecht.

Pfiffner, A., Geology der Alpen, 2010, Haupt Verlag, Berlin, 2nd edition, p. 20-23

Platt, J.P., Dynamics of orogenic wedges and the uplift of high-pressure metamorphic rocks, 1986, Geological Society America Bulletin, v. 97, p.1037-1053

Platt, J.P., The uplift of high-pressure low-temperature metamorphic rocks, 1987, Phil. Trans. R. Soc. London, p. 87-103

Poirier, J.P., Creep of crystals: high-temperature deformation processes in metals, ceramics and minerals, 1985, Cambridge University Press, Cambridge

Pognante, U., Petrological constraints on the eclogite- and blueschist-facies metamorphism and P-T-t paths in the Western Alps, 1991, J. metamorphic Geology, v. 9, p. 5-17

Polino, R., Dal Piaz, G.V., Gosso, G., Tectonic erosion at the Adria margin and accretionary processes for the Cretaceous orogeny of the Alps, 1990, Memoires Society Geology France, p. 156

Pownceby, M.I., Wall, V.J., O'Niel, H.S.C., Fe-Mn partitioning between garnet and ilmenite: experimental calibration and applications (correction), 1987, Contribution to Mineralogical Petrology, v. 97, p. 539

Pownceby M.L., Wall V.J. and O'Neill H.S.C., An experimental study of effect of Ca upon garnet-ilmenite Fe-Mn exchange equilibria, 1991, American Mineralogist v. 76, p. 1580-1588

Robie, R.A., Bethke, P.M., Toulmin, M.S. and Edwards, J.L., X-ray crystallographic data, densities and molar volumes of minerals, 1966, In: Clark, S.P. Jr., Handbook of Physical Constants,

Geological Society of America Memoir, v. 97, p. 27-74

Robie, R.A., Hemingway, B.S., Fisher, J.R., Thermodynamic properties of minerals and related substances at 298.15 K and 1 bar (10^5 pascals) pressure and at higher temperatures, 1978, US Geological Survey Bulletin, p. 1452-1456

Rodgers, J., Fourth time slice: mid-Devonian to Permian synthesis, 1988, Geologica Society Special Publications, v. 38, 6. 621-626

Rollinson, H.R., Iron-titanium oxides as an indicator of the role of the fluid phase during the cooling of granites metamorphosed to granulite grade, 1980, Mineralogical Magazine, v. 43, p. 623-631

Rötzler, J., Carswell, D.A., Gerstenberger, H. And Haase, G. Transitional blueschist-epidote amphibolite facies metamorphism in the Frankenberg massif, Germany, and geotectonic implications, 1999, Journal of Metamorphic Geology, v. 17, p. 109-125

Rubatto, D., Gebauer, D., The Bonze unite (Sesia-Lanzo zone, western Alps): a gabbroic Early Carboniferous intrusion that recorded Hercynian and Alpine metamorphism, 1997, Abstract Volume of the 3rd workshop on Alpine Geological Studies, Milan, v. 4, p. 317-325

Schmid, S., Geologie ddes Umbrailgebietes, 1973, Eclogae Geol. Helv., v.66, p. 101-210

Schmid, S.M., Zingg, A., Handy, M., The kinematics of movements along the Insubric line and the emplacement of the Ivrea zone, 1987, Tectonophysics, v. 135, p. 47-66

Schmid, S.M., Fügenschuh, B., Kissling, E., Schuster, R., Tectonic map and overall architecture of the Alpine orogen, 2004, Ecl. geologicae Helvetiae,v.97, p.93-117

Skinner, B.J., Thermal expansion, 1966, In: Clark, S.P. Jr., Handbook of Physical Constants, Geological Society of America Memoir, v. 97, p. 75-96

Spalla, M.I., Lardeaux, J.M., Dal Piaz, G.V., Gosso, G., Messiga, B., Tectonic significance of Alpine eclogites, 1996, Journal of Geodynamics, v. 21, n.3, p.257-285

Spear, F. S., Metamorphic phase equilibria and Pressure-Temperature-Time Paths, 1995, Mineralogical Society of America, 2nd edition, 799 p.

Sunagawa, I., Growth of crystals in nature, 1974, in: Mineral Genesis, Sofia: Bulgarian Academy of Sciences Geological Institute, p. 79-90

Tesauro, M., Hollenstein, Ch., Egli, R., Geiger, A., Kahle, H.-G., Continuous GPS and broad-scale deformation across the Rhine Graben and the Alps, 2005, Int. J. Earth Sci. v. 94 (4), p. 525–537.

Thompson, A.B., Mineral reactions in pelitic rocks: II. Calculation of some P-T-X(Fe-Mg) phase relations, 1976, American Journal of Science, v. 276, p. 425-454

Trümpy, R., Ostalpen und Westalpen-Verbindendes und Trennendes, 1992, Jahrb. Geol. Bundesanst. Austria, v. 135, p. 875-882

Velde, B. Phengite micas: Synthesis, stability and natural occurrence, 1965, American Journal of Science, v. 263, p. 886-913

Vernon, R. H., A practical guide to rock microstructure, 2008, Cambridge University Press, 2nd edition, 594 p.

Weh, M. and Froitzheim, N., Penninic cover nappes in the Prättigau half-window (Eastern Switzerland): Structure and Tectonic evolution, 2001, Eclogae geologicae Helvetiae, v. 94, p. 237-252

Wiederkehr, M., Bousquet, R., Schmid, S. M., Berger, A., From subduction to collison: thermal overprint of HP/LT meta-sediments in the north-eastern Lepontine Dome (Swiss Alps) and consequences regarding the tectono-metamorphic evolution of the Alpine orogenic wedge, 2008, Swiss Journal of Geosciences, v. 101, p. 127-155

Williams, M.L., Scheltema, K.E., Jercinovic, M.J., High-resolution compositional mapping of matrix phases: implications for mass transfer during crenulation cleavage development in the Moretown Formation, western Massachusetts, 2001, Journal of Structural Geology, v. 23, p. 923-939

Wortel, M.J.R., Spakman. W., Subduction and slab detachment in the Mediterranean-Carpathian region, 2000, Science, v. 290, p. 1910-1916; Erratum: Science, v. 291, p. 437

Wortmann, U. G., Weissert, H., Funk, Hp, Hauck, J., Alpine plate kinematics revisited: The Adria Problem, 2001, Tectonics v.20 n.1, p. 134-147

Wu, C.M., Cheng, B.H., Valid garnet-biotite (GB) geothermometry and garnet-aluminum silicate-plagioclase-quartz (GASP0 geobarometry in metapelitic rocks, 2006, Lithos, v. 89, p. 1-23

Zedde, van de, D.M.A., Wortel, M.J.R., Shallow slab detachment as a transient source of heat at mid-lithospheric depths, 2001, Tectonics, v. 20, p. 868-882

Zen, E. and Rosenboom, E.H., Some topologic relationships in multisystems of n+3 phases, II. Unary and binary metastable sequences, 1972, American Journal of Science, v. 265, p. 871-897

Zwart, H.J., The chronological succession of folding and metamorphism in the central Pyrenees, 1960, Geologische Rundschau, v. 50, p. 203-218

Zwart, H.J., On the determination of polymetamorphic mineral associations, and its application to the Bosost area (central Pyrenees), 1962, Geologische Rundschau, v. 52, p. 38-65

14. Appendix

14.1 EMP mineral chemistry

Table A Sample chemical composition M1 = M2 = M3 muscovite (white mica)

	(M1) *MuscB12b*	(M1) *BioC11*	(M3) *MuscB12*	(M1) *BioC11-2*	(M3 inclusion) *Plinc3*	(M2) *MuscC11*
Wt% oxide						
SiO_2	47.20	47.77	47.77	47.16	48.82	47.65
TiO_2	0.65	0.35	0.62	0.34	0.51	0.54
Al_2O_3	36.74	37.89	37.31	36.30	38.14	37.01
Cr_2O_3	0.11	0.12	0.00	0.03	0.025	0.00
FeO	0.79	0.73	0.45	0.71	0.84	0.69
MnO	0.00	0.06	0.06	0.00	0.01	0.08
MgO	0.71	0.56	0.61	0.61	0.58	0.54
CaO	0.00	0.08	0.05	0.18	0.08	0.07
Na_2O	1.94	2.16	1.89	1.78	1.98	2.28
K_2O	7.91	7.85	7.73	5.46	7.84	8.05
H_2O	4.61	4.63	4,65	4.52	4.80	4.65
Total	100.65	101.20	101,14	97.09	103.63	101.55
Si	3.070	3.028	3.080	3.126	3.047	3.075
Al	2.817	2.892	2.836	2.836	2.880	2.816
Al^{vi}	1.888	1.920	1.916	1.962	1.928	1.891
Na	0.245	0.272	0.236	0.229	0.239	0.284
K	0.656	0.648	0.636	0.462	0.624	0.663
Ca	0	0.006	0.003	0.013	0.005	0.005

Fe assumed to be all Fe^{2+}; calculations based on 11 oxygen

Table B Sample chemical composition M1 paragonite (white mica)

	(M1) *PlA12*	(M1) *PlC12b*	(M1) *OverviewA16-2*	(M1) *AlbC11*	(M1) *C11a-2inc1*
Wt% oxide					
SiO_2	50.94	45.06	45.42	46.64	48.09
TiO_2	0.00	0.58	0.13	0.13	0.11
Al_2O_3	37.39	40.14	41.61	40.97	42.39
Cr_2O_3	0.00	0.00	0.03	0.00	0.02
FeO	0.44	0.36	0.35	0.27	0.21
MnO	0.00	0.09	0.00	0.02	0.00
MgO	0.00	0.00	0.09	0.00	0.10
CaO	3.17	0.58	0.70	0.69	1.00
Na_2O	6.73	5.60	3.92	6.44	2.74
K_2O	0.13	1.43	0.91	1.05	0.70
H_2O	4.86	4.61	4.64	4.74	4.53
Total	98.8	98.43	97.80	100.95	99.87
Si	3.141	2.928	2.935	2.951	2.911
Al	2.719	3.075	3.171	3.057	3.012
Al^{vi}	1.860	2.002	2.106	2.008	2.001
Na	0.804	0.706	0.492	0.790	0.561
K	0.010	0.119	0.075	0.085	0.072
Ca	0.209	0.040	0.048	0.047	0.078

Fe assumed to be all Fe^{2+}; calculations based on 11 oxygen

Table C Sample chemical composition M1, M2 = M3, biotite (brown mica)

	(M2) *BtB12*	(M2) *BtC12b*	(M1) *B12matrix4*
Wt% oxide			
SiO_2	38.49	38.21	37.70
TiO_2	0.66	0.61	0.07
Al_2O_3	20.92	21.08	19.42
Cr_2O_3	0.00	0.00	0.08
FeO	14.65	15.27	15
MnO	0.00	0.00	0
MgO	13.79	13.84	13.14
CaO	0.00	0.07	0.28
Na_2O	0.42	0.53	0.26
K_2O	9.03	8.81	7.33
H_2O	4.20	4.20	4.12
Total	102.15	102.61	101.42
K	0.823	0.801	0.698
Na	0.059	0.073	0.038
Mg	1.469	1.471	1.462
Fe	0.875	0.911	0.937

Fe assumed to be all Fe^{2+}; calculations based on 11 oxygen

Table D Sample chemical composition M3 oligoclase (plagioclase)

	(M3) *PlC12*	(M3) *Pl16A*	(M3) *16A2*	(M3) *C11a*	(M3) *OverviewA16-2*	(M3 inclusion) *GtB11inc3*	(M3) *B12matrix1*
Wt% oxide							
SiO_2	65.63	62.16	64.26	65.35	63.78	64.10	63.49
TiO_2	0.01	0	0	0.30	0	0.02	0
Al_2O_3	23.28	23.84	22.24	23.48	23.61	24.42	23.61
Cr_2O_3	0.19	0	0	0.10	0	0	0.02
FeO	0.04	0.05	0.03	0.02	0.01	0.54	0.03
NiO	0.07	0	0	0.32	0	0.36	0
MgO	0	0	0	0	0.01	0	0
CaO	3.68	3.69	3.43	3.68	3.69	4.28	4.59
Na_2O	9.86	7.14	8.17	9.43	8.29	9.12	7.97
K_2O	0	0.04	0.06	0	0.07	0	0.03
Total	102.77	96.94	98.18	102.73	99.46	103.01	99.79
Na	0.821	1.870	0.706	0.786	0.709	2.29	0.681
K	0	0.543	0.003	0	0.004	0	0.002
Ca	0.169	0.006	0.164	0.169	0.174	0.59	0.217

Fe assumed to be all Fe^{2+}; calculations based on 8 oxygen

Table E Sample chemical composition M1, M3 Ilmenite

	(M1) *IlmB12*	(M1) *IlmA11*	(M1 inclusion) *GtB12inc4*	(M1 inclusion) *garnetA11inc2*	(M3) *Ilm C12*	(M3 inclusion) *StauC11inc2*	(M3 inclusion) *StauC11inc3*
Wt% oxide							
SiO_2	0.19	0.16	0.27	0.33	0.13	0.21	0.277
TiO_2	53.94	54.44	52.05	53.30	54.03	52.61	53.22
Al_2O_3	0.26	0	0.10	0.34	0.06	0.15	1.09
Cr_2O_3	0	0	0.13	0.01	0	0.18	0.25
FeO	45.60	46.59	43.70	44.30	46.10	44.90	45.22
Fe_2O_3	0	0	3.25	3.64	2.14	2.61	0.88
MnO	0.24	0.51	0.234	0.059	0.11	0	0.20
MgO	0.41	0.377	0.72	0.73	0.38	0.27	0.57
CaO	0	0	0	0.13	0.01	0.09	0
Na_2O	0.44	0.271	0.42	0.53	0.36	0.43	0.39
K_2O	0.04	0	0	0	0.05	0	0
Total	101.10	102.35	100.57	103.37	103.362	101.12	102.10
Fe	0.940	0.955	0.906	0.932	0.935	0.975	0.938
Ti	1.001	1.003	0.980	0.958	0.986	0.981	0.976
Mn	0.005	0.011	0.005	0.001	0.002	0	0.004
% R*	1	1	5	2	3	1	1

*Calculations based on 3 oxygen; * percentage hematite + pyrophanite*

Table F Sample chemical composition M2 Staurolite

	(M2) *StauB12*	(M2) *KyC12*	(M2) *StA11*	(M2) *GtB11stau*	(M2) *St16D-2*	(M2) *KyC11*
Wt% oxide						
SiO_2	28.62	28.38	29.16	28.98	27.92	28.82
TiO_2	0.59	0.56	0.45	0.51	0.59	0.44
Al_2O_3	54.99	55.54	55.01	55.29	54.13	55.14
Cr_2O_3	0.09	0.07	0.58	0.23	0.04	0.31
FeO	13.24	14.24	13.43	13.82	13.33	12.33
MnO	0.05	0	0.20	0	0.03	0
MgO	2.12	2.24	2.56	1.98	2.13	2.35
CaO	0.02	0.03	0.05	0.05	0	0.03
Na_2O	0.19	0.20	0.30	0.17	0.01	.025
K_2O	0.02	0	0	0.05	0	0
Total	100.03	101.24	101.22	101.07	98.18	99.66
Fe	1.564	1.668	1.572	1.617	1.604	1.454
Mg	0.446	0.467	0.533	0.413	0.457	0.494
# Mg	0.222	0.219	0.253	0.203	0.222	0.254

Fe assumed to be all Fe^{2+}; calculations based on 24 oxygen

Table G Sample chemical composition M2, M3 almandine (Garnet)

	(M2) *GtA112*	(M2) *GtA11*	(M3) *GtC12*	(M3) *GtB11b*	(M3) *GtA12*	(M2) *Gnt16*	(M3) *Gt16-D2*	(M2) *Gnt16-2*	(M3) *16A1-2*	(M3) *GtB12*
Wt% oxide										
SiO_2	37.52	37.63	37.72	37.47	38.18	36.79	37.47	37.08	37.37	37.14
TiO_2	0.063	0.06	0.05	0.05	0.02	0.05	0.06	0.07	0.06	0.17
Al_2O_3	20.81	21.22	21.32	21.19	21.77	20.72	20.97	22.38	21.09	21.69
Cr_2O_3	0.02	0.01	0.01	0.01	0.07	0.01	0.02	0.02	0.02	0.19
FeO	33.91	33.96	33.98	34.36	33.78	33.45	34.86	32.69	34.02	32.97
MnO	0.64	0.68	0.64	0.36	0.12	0.88	0.31	0.27	0.50	1.01
MgO	3.17	3.19	3.18	3.37	3.36	3.02	3.41	3.53	3.35	3.46
CaO	3.62	3.58	3.54	3.13	0.64	3.80	2.82	2.48	3.30	4.00
Na_2O	0.01	0.02	0.02	0.01	0.13	0	0.01	0.06	0.01	0.55
Total	99.77	100.35	100.46	99.96	98.07	98.72	99.93	98.58	99.72	101.56
Fe	2.277	2.265	2.262	2.300	2.273	2.274	2.338	2.196	2.283	2.163
Mg	0.379	0.379	0.377	0.402	0.403	0.366	0.407	0.423	0.401	0.405
Mn	0.044	0.046	0.043	0.024	0.008	0.061	0.021	0.018	0.034	0.067
Ca	0.311	0.306	0.302	0.268	0.055	0.331	0.242	0.213	0.284	0.336

Fe assumed to be all Fe^{2+}; calculations based on 12 oxygen

14.2 EMP X-ray energy spectra

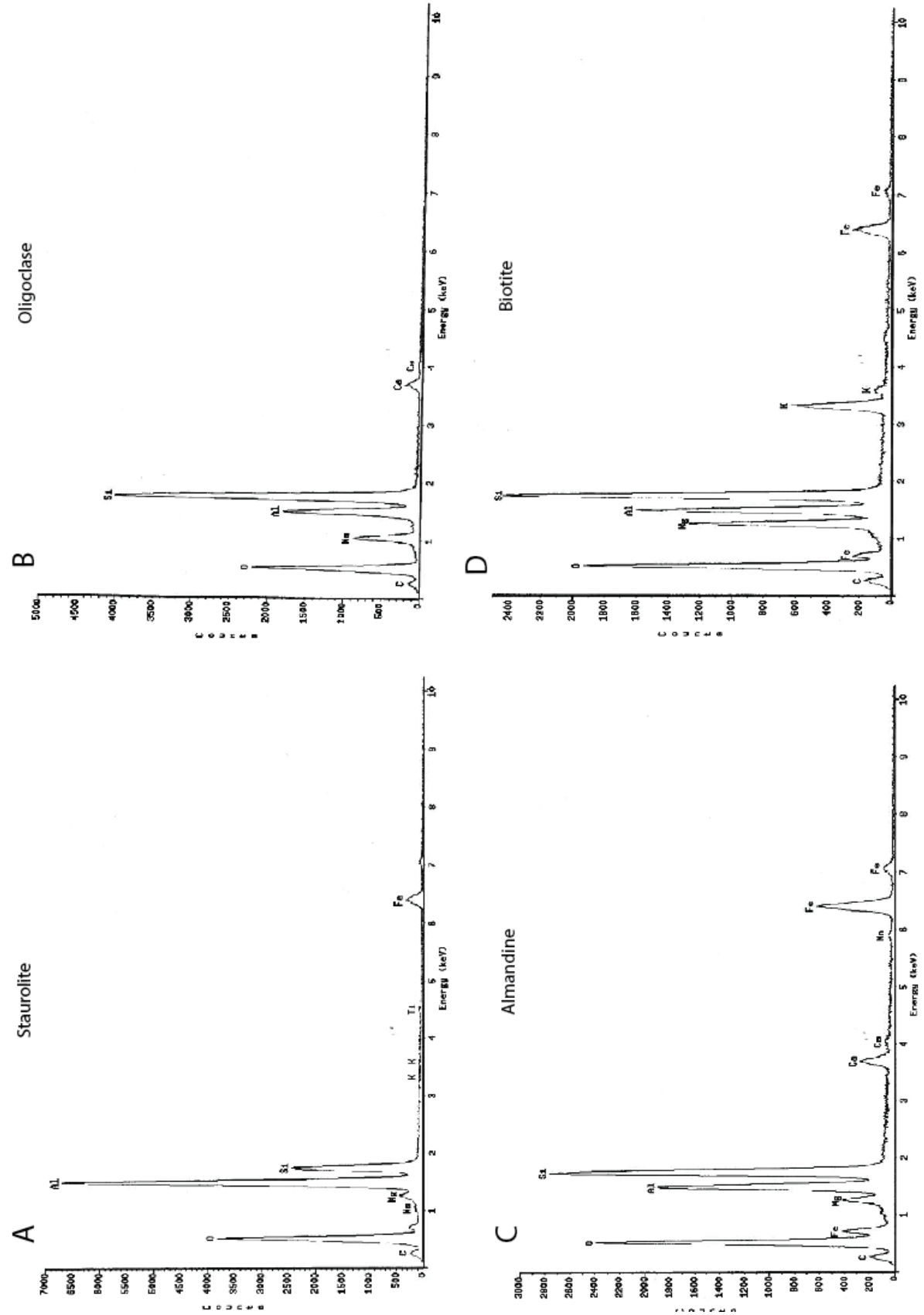

Figure 14.1 *EMP X-ray energy spectra for porphyroblasts observed in P58b. (A) Staurolite, (B) oligoclase, (C), almandine and (D) biotite*

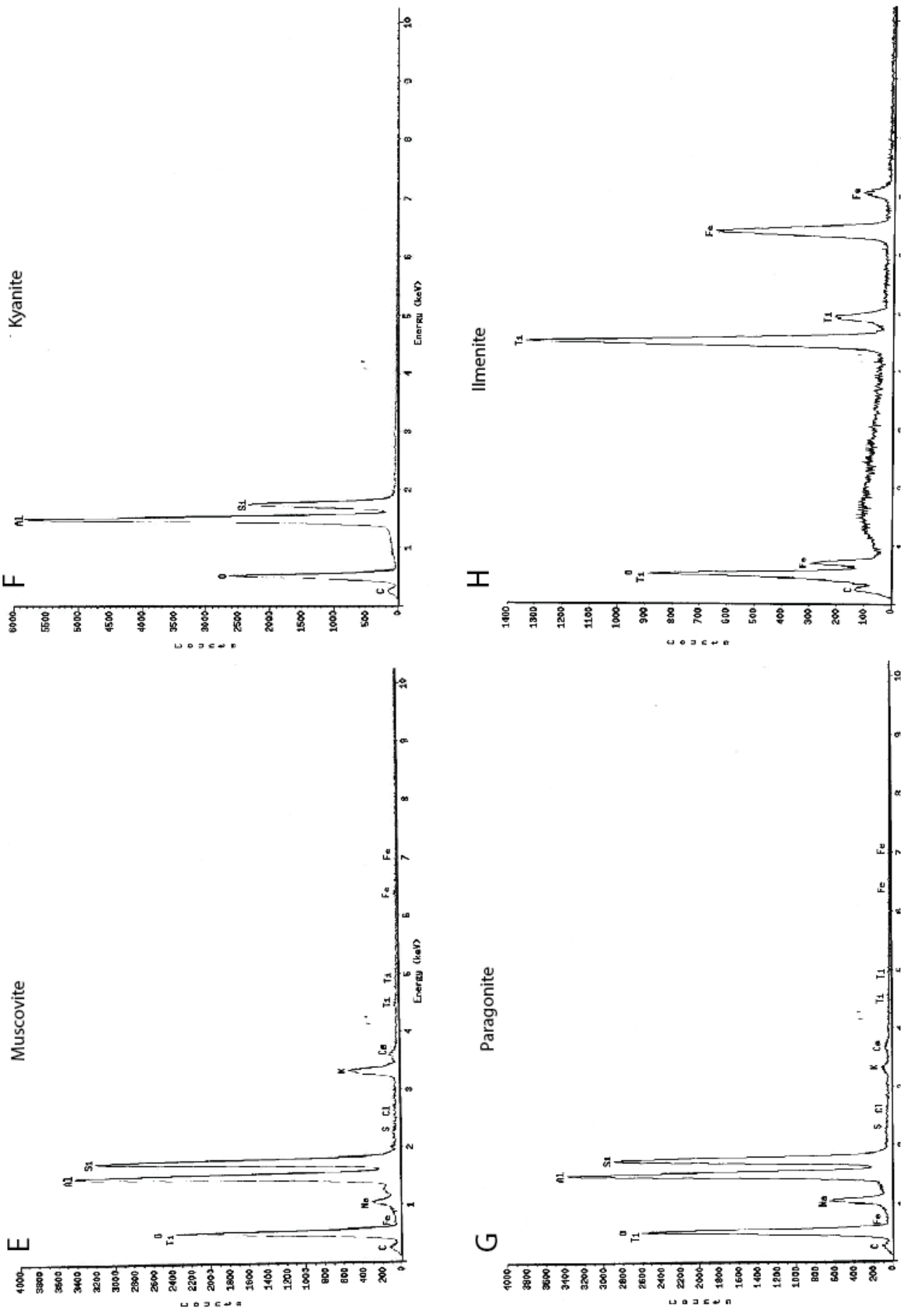

Figure 14.1 continued (E) *Muscovite,* ***(F)*** *kyanite,* ***(G)****, paragonite and* ***(H)*** *ilmenite*

14.3 P58b Thin section numbering system

Thin section P58b-12	Numbering system in thin section									
	KyC12	***OverviewC12-3***	***OverviewC12***	***PlC12***	***B12matrix1-m***	***OverviewC122***	***OverviewB12***	***OverviewA12***		
Sample name →	KyC12	OverviewC12	GtC12	PlC12-2	B12matrix1-2m	KyB12	B12matrix	GtA12		
	KyC12inc1	Bt12Cb	GtC12inc1	PlC12-3	B12matrix1-1m	KyB12b	B12matrix1	PlA12		
	KyC12inc2	PlC12b	IlmC12		B12matrix1-2n	MuscB12b	B12matrix2			
			BtC12		B12matrix1-2	StB12	B12matrix3			
						IlmB12	B12matrix4			
						BtB12				
						GtB12				
						GtB12inc1				
						GtB12inc2				
Thin section P58b-16	*area*					GtB12inc3				
	Overview16C	***Gnt16***	***16A1-2***			GtB12inc4				
Sample name →	Pl16C	Gnt16-2	St16A			GtB12inc5				
	Mica16C		Pl16A			StauB12				
	Ky16C		16A-2			PlB12				
	Pl16C2		Bt16A			MuscB12				
Thin section P58b-11	*area*									
	KyC11	***StauC11***	***StauB11***	***PlB11***	***GtB11***	***gtA11***	***StA11***	***C11a***		
Sample name →	KyC11	C11a	GtB11stau-2	Plinc1	GtB11inc1	A11	StA11	C11a-2inc1		
	KyC11inc1	MuscC11inc1	GtB11stau-2inc1	Plinc2	GtB11inc2	A11inc4	Stinc1	C11a-2		
	C11b	AlbC11	GtB11stau-2inc2	Plinc3	GtB11inc3	A11d	Stinc2			
	KyC11inc2	BioC11	StauB11inc2	Plinc4	GtB11b	A11b	Stinc3			
		StauC11inc1	StauB11inc1	Plinc5		A11c				
		StauC11inc2	StauB11inc2	Plinc6		Allinc1				
		StauC11inc3	StauB11inc3			Allinc2				
		StauC11inc4				Allinc3				
		MuscC11				Allinc4				
		BioC11-2				Allinc6				
						GtA112				
						btA12				

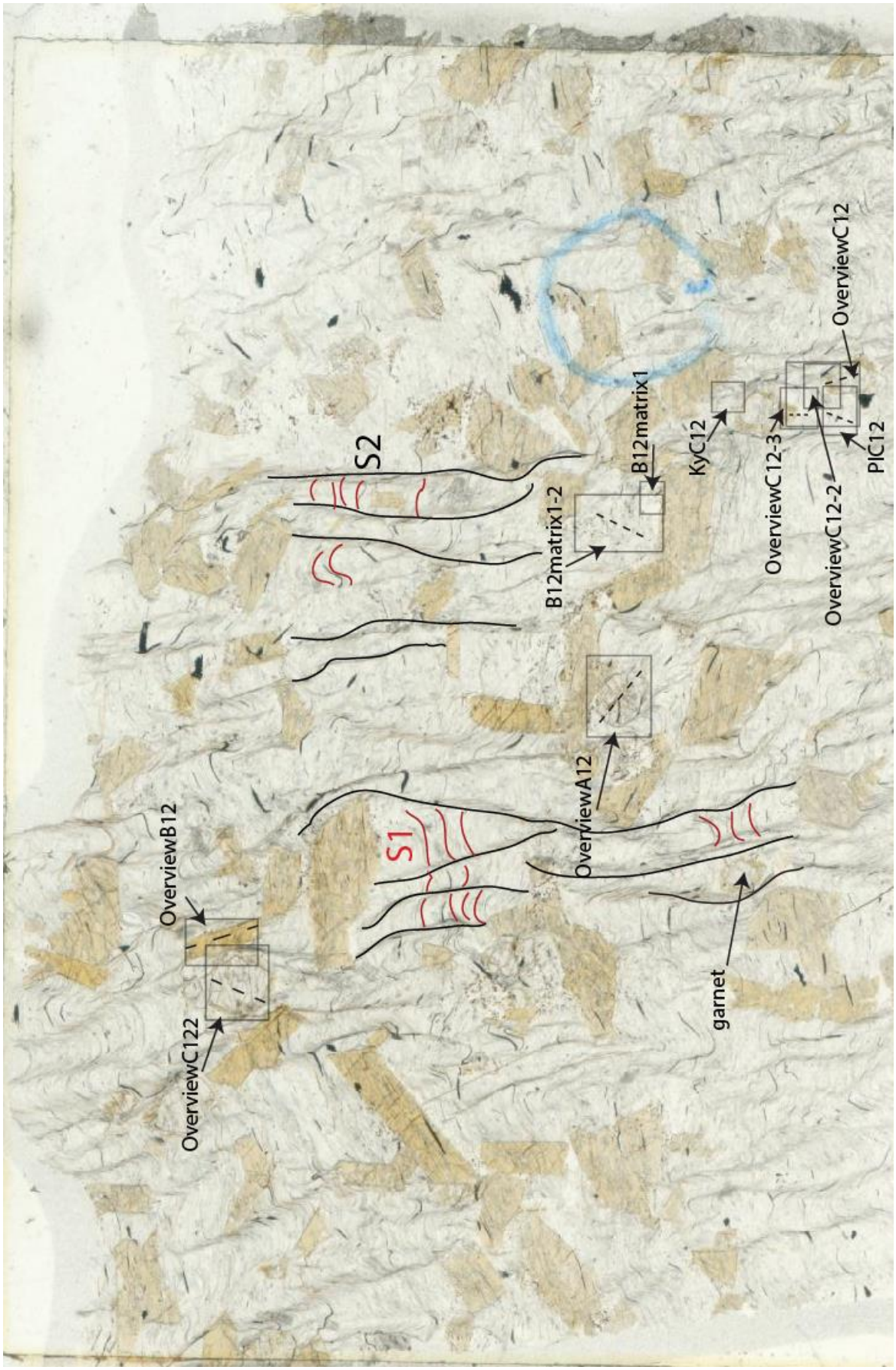

.

Figure 14.2*Plane polarized light overview of thin section P58b-12. Line scans indicated as dotted lines. Description of microstructure in chapter 6.1*

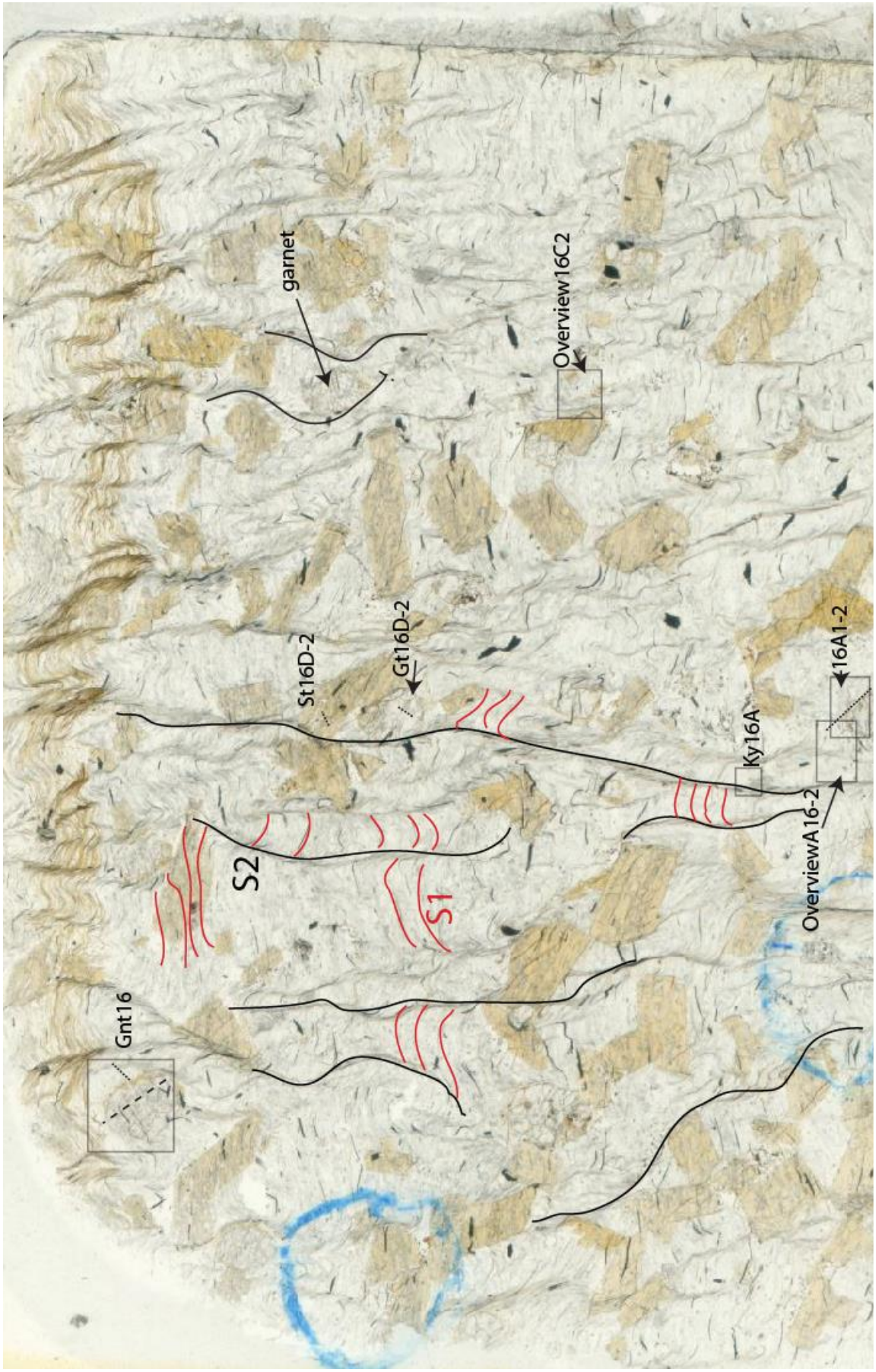

Figure 14.3 *Plane polarized light overview of thin section P58b-16. Line scans indicated as dotted lines. Description of microstructure in chapter 6.1*

.

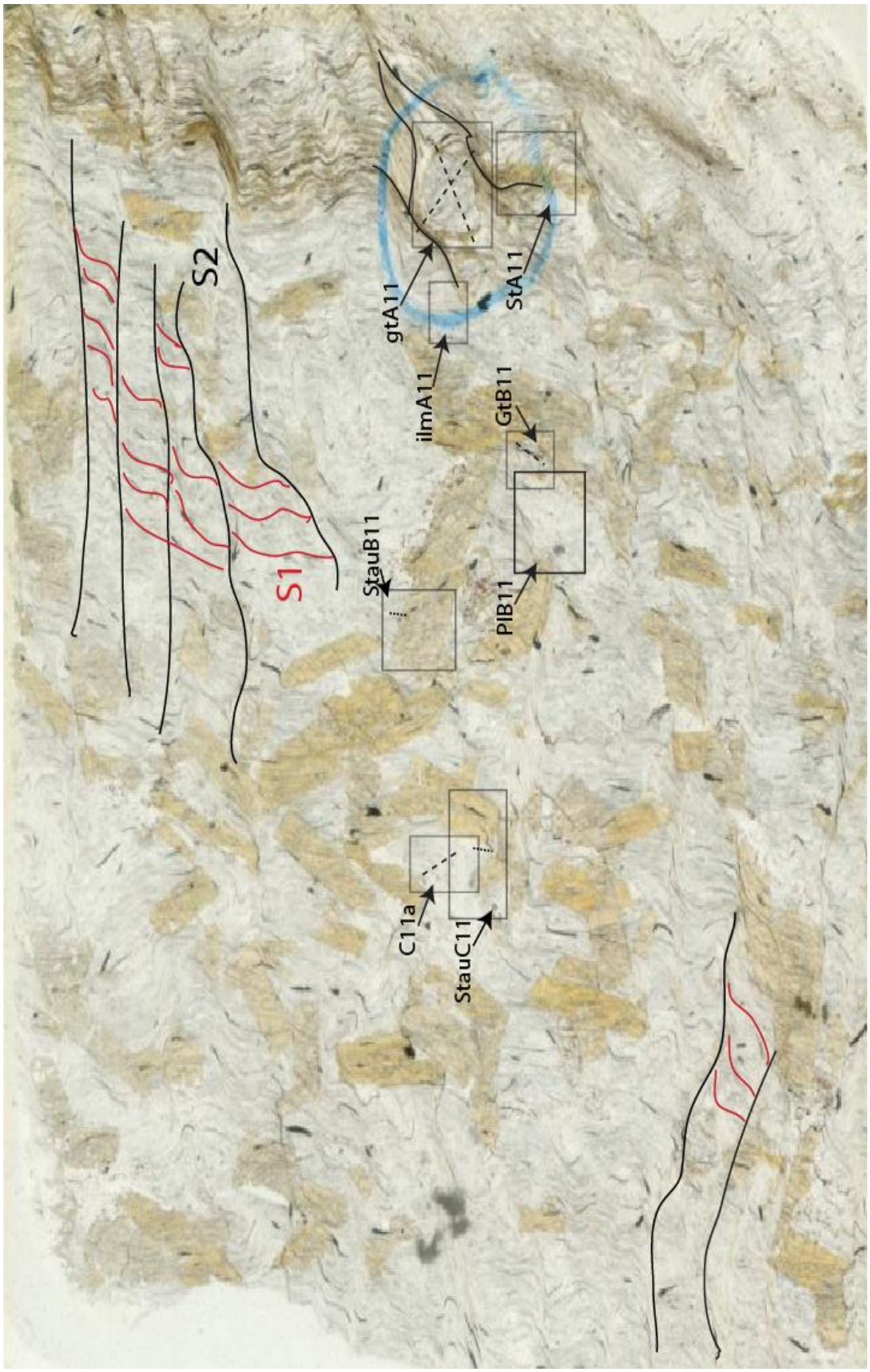

Figure 14.4 *Plane polarized light overview of thin section P58b-11. Line scans indicated as dotted lines. Description of microstructure in chapter 6.1*

14.4 Additional SEM analysis M2 muscovite

The JEOL JCM-6000 NeoScope Benchtop SEM was used to investigate the composition of the optical opaque inclusions inside the M2 muscovite porphyroblasts. P58b-7 was polished since this sample contained the best micas showing the inclusions. This analysis is performed using backscatter electrons shot on P58b-7 with an acceleration voltage of 15 kV. Multiple minerals and inclusions are measured (table H) in order to get an idea of the composition and relationship of the inclusions with the muscovites.

Table H *SEM analysis of M2 white micas in P58b-7. Figure 14.5 shows some of the analysed minerals.*

Muscovite	*sample*				
cations	**001**	**006**	**007**	**009**	**011**
Al	3.145	3.085	3.215	3.185	3.140
Si	3.345	3.325	3.320	3.330	3.295
K	0.825	0.790		0.890	0.795
Na	0.220	0.210	0.275	0.240	0.605
Fe	0.070	0.065			0.060
Mg		1.055			0.135
inclusions?	yes	yes	no	no	yes

Paragonite	*sample*	
cations	**015**	**016**
Al	3.500	3.515
Si	3.175	3.160
Na	0.675	0.805
K	0.135	

Inclusions	
sample	*mineral*
002	Rutile
008	Iron-oxide
012	Rutile

Fe assumed to be all Fe^{2+}; calculations based on 11 oxygen

The inclusions observed are μm-scale rutile needles. They appear in a similar orientation dependent on the mineral orientation (fig. 14.5). Following the grain boundaries, grains which include rutile inclusions can be distinguished from grains which do not contain the inclusions. As can be seen in table 1, the rutile needles only exist in a mineral when a certain amount of Fe or Mg is present in the sample. For example sample 009 in figure 7.1 does not contain any Fe and Mg and hence no aligned rutile inclusions, whereas adjacent lying grain 011 is not that different but contains needles of rutile.

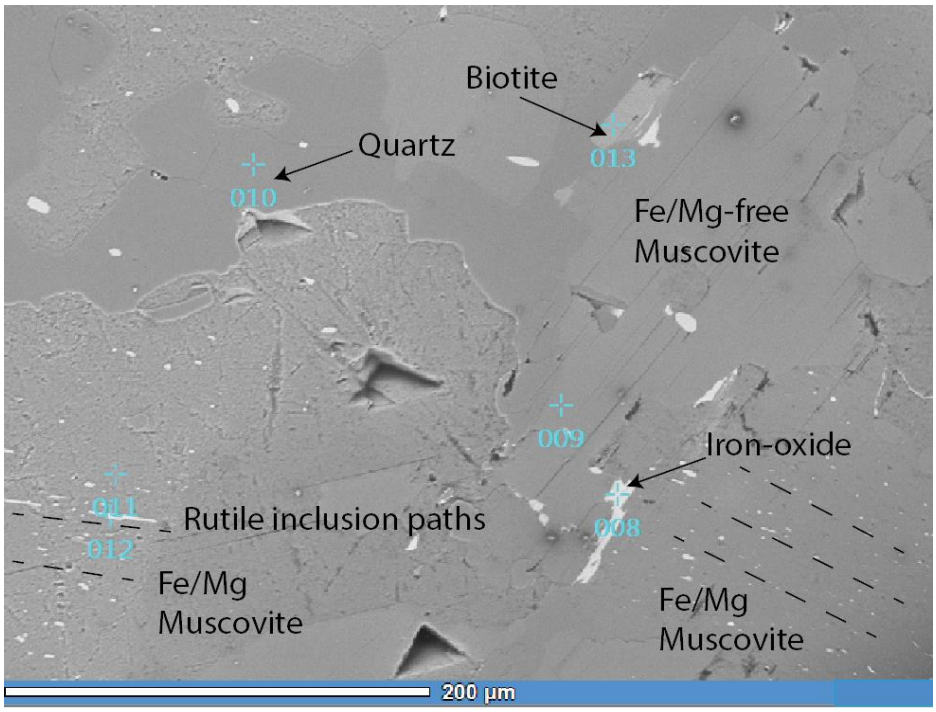

Figure 14.5 *BSE image of muscovite flakes with rutile inclusions.*

Interpretation

The needles are elongated in one direction and have a smooth surface which shows stability between the host and inclusion (Vurnon, 2004). Equilibrium between a Ti-rich phase as rutile and muscovite is not uncommon, especially at low P; high T conditions (fig. 12.1A). When the temperature is increased in a late heating event you cross the rutile stability field and rutile starts to exsolve from muscovite porphyroblasts which are slightly enriched in Fe and Mg. Blasts which do not show any Fe or Mg are not affected and do not show any exsolution.

As can be seen in the figure, exsolution of these phases is an indication of high temperature circumstances. Ilmenite is observed as a stable phase in combination with these white mica flakes in optical and petrogenetic analysis. Together with late growing plagioclase which is stable at high temperature, an equilibrium P-T field which is bounded by the stability of the minerals can be drawn (see chapter 9).

A last group of minerals was observed with the SEM regarding the matrix composition in combination with kyanite crystals (fig. 14.6). The mineral compositions indicate in the figure can be found in table 1. The kyanite crystal overgrows the crenulation cleavage but does not seem to be affected by this deformation phase. The two elongated ilmenite grains are folded into the crenulation cleavage which indicates their presence prior to the cleavage formation. Some of the ilmenite grains are however prismatic in shape and do not align with the matrix. The composition of the matrix minerals is highly enriched in Na compared to K and Ca, hence the initial matrix was paragonite-rich. There is no significant chemical difference in undeformed matrix white mica compared to crenulated white mica.

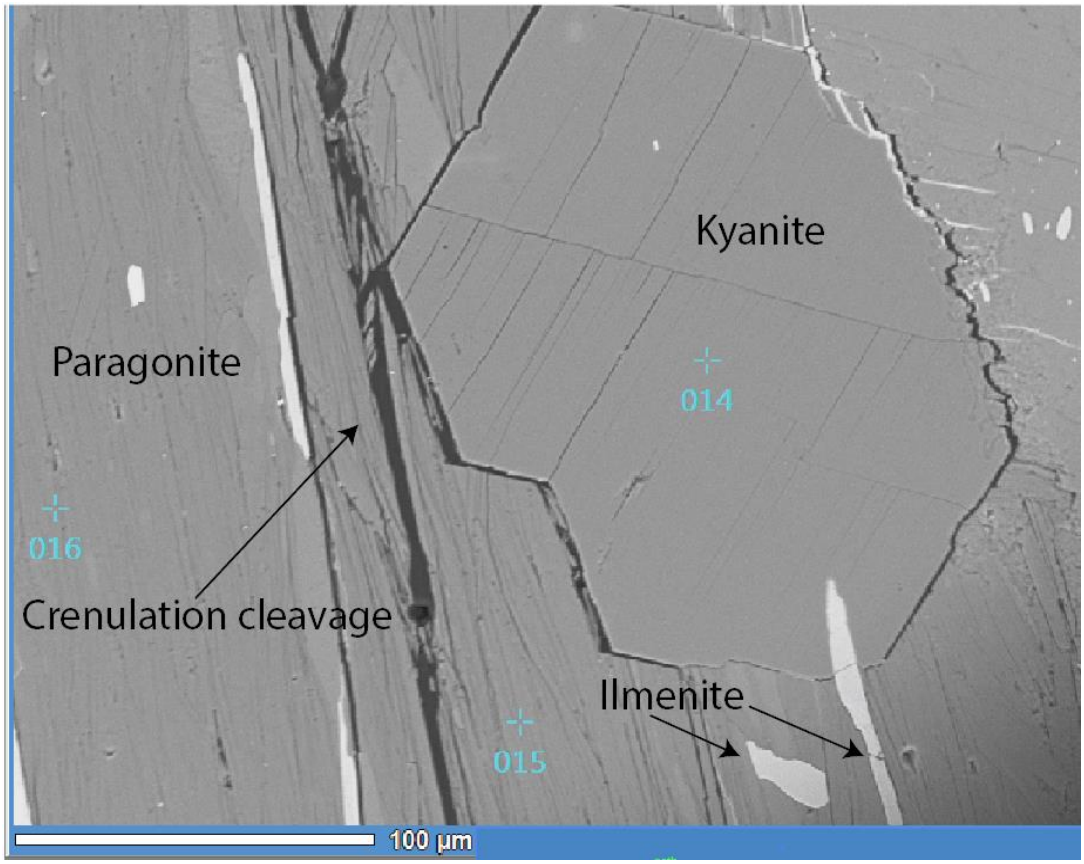

Figure 14.6 *BSE image of an undeformed kyanite crystal overgrowing the matrix.*

Interpretation

The undeformed kyanite minerals have grown post-deformational on top of the crenulation cleavage domains. The Al-content of the domains acts as a nucleation point for the kyanite crystals. Since the grains were highly deformed and hence rich in dislocations many nucleations points were available compared to the more-Si rich matrix. As with the kyanites, ilmenite minerals have grown post-deformational over the matrix. However, the paragonite minerals are overgrown by muscovite and plagioclase which indicates an instable situation somewhere along the retrograde (or prograde late heating) path. The transition of the stability fields of paragonite to plagioclase is a diffuse boundary in these metapelitic rocks. Minerals which are most likely involved in the reaction are plagioclase, paragonite, white mica, kyanite and garnet which become unstable at higher T.

14.5 How to use Perple_X to create pseudosections?

A way of modeling phase diagrams, phase equilibria and thermodynamic data is by using software like THERMOCALC (KTH, Stockholm, Sweden), THERIAKDOMINO (De Capitani, Basel, Switzerland) and Perple_X (Connolly, Zurich, Switzerland). These programs can be freely downloaded from the internet on the following places:

THERIAKDOMINO: http://titan.minpet.unibas.ch/minpet/theriak/theruser.html

THERMOCALC: http://www.thermocalc.se/Software.htm

Perple_X: http://www.Perple_X.ethz.ch/

Each of these programs has his advantages and disadvantages over each other, but for the main purpose of creating phase equilibria diagrams (e.g. pseudosections) they are similar in usage. Their outcomes are different due to the differences in thermodynamic database which is used.
This hand-out will be focused on the use of Perple_X 6.6.6 software developed by James Connoly and colleagues at the ETH Zürich. The main reason for writing this handout is the lack of up-t-date handouts on the Perple_X website. The outline of this handout will follow the outline of the tutorial, but is applied to a petrological problem. On this website there exists a tutorial, but this one is mainly focused on geophysical applications like wave speeds in the mantle. All the other examples are created for older versions of Perple_X and are obsolete for the current software.

On the main page of the Perple_X website you will find all the options, examples, tutorial, README files, and possible bugs (in newer versions) and updates. I advise to go through them and follow the tutorial step by step. Although it is not a petrological example, it is wise to get familiar with the different programs included in the Perple_X package.

How to create a pseudosection with Perple_X?

The most important assumption of Perple_X is they assume equilibrium between the phases. This assumption is mostly highly doubtful, but without making it there is no way to start.

The calculation and interpretation of a phase diagram consists of five steps: the problem definition (using Build); the phase diagram section computation (using Vertex); computational assessment (using Vertex); digital interpretation (using Werami); and graphical interpretation (using Pssect, PyWerami). Each step involves different programs that are described in the following sections (see table below). For the following case we use this bulk rock chemical composition*:

monster	SiO2 %	Al2O3 %	TiO2 %	Fe2O3 %	MnO %	CaO %	MgO %	Na2O %	K2O %	P2O5 %	som %
X	46,16	34,71	1,60	5,82	0,02	0.94	0,77	4,21	1,18	0,12	95,53
NORMALIZED	48,32	36,33	1,67	6,09	0,02	0.98	0,81	4,41	1,24	0,13	100,00

Bulk rock chemical composition used as input in *Build*

***** This is a major element bulk rock analysis. Fe_2O_3 cannot be dealt with by Perple_X so you always insert the wt% Fe_2O_3 as FeO. Don't forget to normalize everything to 100%.

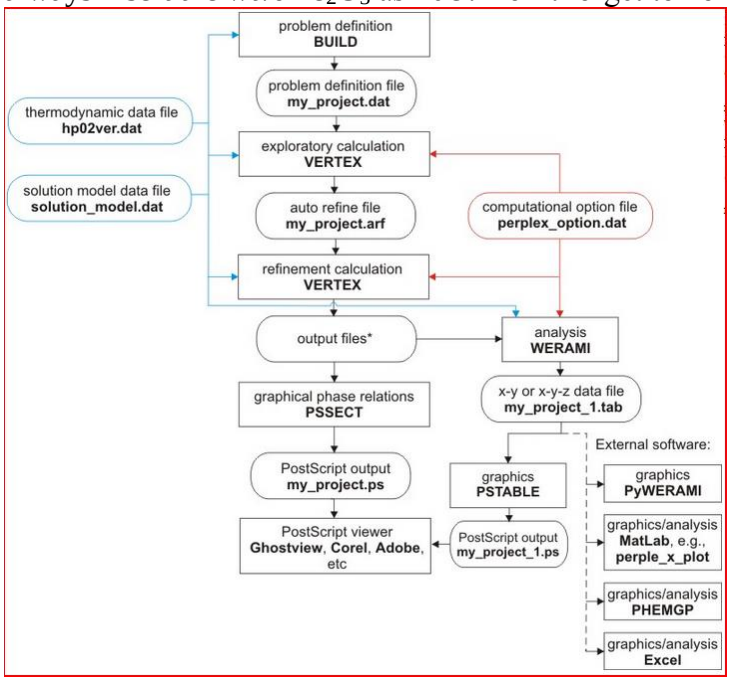

Running Build

The following dialog details the prompts from the program BUILD (normal font) and user responses (**bold font**). Explanatory comments are written in red. If there are more ambiguities you can also go to the Build prompts page (http://www.Perple_X.ethz.ch/Perple_X_66_build_prompts.html) and go through it step by step. Here also reasons of error notifications are analysed.

Enter a name for this project (the name will be used as the root for all output file names) [default = my_project]:
test

Enter thermodynamic data file name, left justified, [default = hp02ver.dat]:
hp02ver.dat

hp02ver.dat is the standard database created by Holland and Powell (1998). The hp02ver.dat file is suitable for calculations to pressures approaching 12 GPa. It can however depend on what kind of system you have what thermodynamic database you prefer to use. Commonly used thermodynamic files can be viewed at *http://www.Perple_X.ethz.ch/Perple_X_thermodynamic_data_file.html#Commonly_Used_Thermodynamic_files*.
Extra note: each database contains a list of mineral abbreviations. The abbreviations can differ per database so you can always open the database-file (e.g. open hp02ver.dat in notepad) and check which abbreviations are used.

Enter the computational option file name, left justified, default = Perple_X_option.dat]:
See: www.Perple_X.ethz.ch/Perple_X_options.html
Perple_X_option.dat

```
Computational options used by Perple_X are controlled via the computational
option file. This file is normally named Perple_X_option.dat. This file
contains several options to adjust your plot and thermodynamic data.
Sometimes VERTEX of BUILD indicates errors which might be caused by
limitations in the Perple_X_option.dat file. The error will always indicate
which parameter needs to be changed in order for the model to run
correctly. You can always take a look at the help-site described above for
further explanation of the described parameters in the file.
```

The current data base components are:
NA2O MGO AL2O3 SIO2 K2O CAO TIO2 MNO FEO O2 H2O CO2
Transform them (Y/N)?
n

This is the part where you have to use your bulk rock chemical composition (mainly provided via an EMP or XRF analysis). Since we are using the bulk rock chemical composition of major elements you don't have to change the data base components. Since the percentage of P_2O_5 is irrelevant (especially for a metapelitic system), you can discard this one for further calculation. If you want to include it, say **y** to transform them and follow the next steps.

Calculations with a saturated FLUID (Y/N)?
y

Here the system is assumed to be saturated with respect to a fluid phase, rather fluid stability and composition is a function of the physical conditions. This closed system model requires that the fluid components are specified as thermodynamic components (below). There are problems with such a model, but the closed system model for water-CO_2 bearing systems is certainly less arbitrary (and probably more realistic) than the petrological artifice of assuming that the system is saturated with respect to a fluid with a fixed composition. Although, since I was working with metapelitic crustal rocks I assumed an important amount of water to be present. If you are for example working with granulites or granitic rocks the saturation of water is highly arbitrary and the saturated fluid should be set to **n**.

Select the independent saturated FLUID components:
H2O CO2
Enter names, 1 per line, press <enter> to finish:

For C-O-H fluids it is only necessary to select volatile species present in the solids of interest. If the species listed here are H2O and CO2 (which it is), then to constrain O2 chemical potential to be consistent with C-O-H fluid speciation treat O2 as a saturated component.

H2O

When you have significant amounts of CO_2 fluids present you can also include CO_2. In these metapelitic rocks there is however no CO_2 fluid present and hence neglected.

Calculations with saturated components (Y/N)?
n

Use chemical potentials, activities or fugacities as independent variables (Y/N)?
n

Select thermodynamic components from the set:
NA2O MGO AL2O3 SIO2 K2O CAO TIO2 MNO FEO O2 H2O CO2
Enter names, left justified, 1 per line, [cr] to finish:
SIO2
AL2O3
TIO2
FEO
MNO
CAO
MGO
NA2O
K2O

It is convenient to put the major oxides in the order of your excel file, since in the next step you need to type the amounts and this way it is less searching in the document.

Select the fluid equiation of state:

0 - X(CO2) Modified Redlich-Kwong (MRK/DeSantis/Holloway)
…
25 - H2O-CO2-NaCl Aranovich and Haefner 2004

5 (= Holland and Powell CORK model)

Specify computational mode:

1 - Unconstrained minimization
2 - Constrained minimization on a 2d grid [default]
3 - Constrained minimization on a 1d grid
4 - Output pseudocompound data
5 - Phase fractionation calculations
2

If you are interested in making pseudosections use the constrained minimization on a 2d grid.

The data base has P(bar) and T(K) as default independent potentials. Make one dependent on the other, e.g., as along a geothermal gradient (y/n)?
n

Select x-axis variable:

1. P(bar)
2. T(K)
3. Y(CO2)
4. Composition X(C1)* (user defined)
2

Enter minimum and maximum values, respectively, for: T(K)
X1 X2

Dependent of the range on which you want to investigate the compositions. Note T is in Kelvin and not ^{o}C!

Select y-axis variable:

2. P(bar)
3. Y(CO2)
2

Enter minimum and maximum values, respectively, for: P(bar)
Y1 Y2

Specify sectioning value for: Y(CO2)
0

Specify component amounts by weight (Y/N)?
y

Enter weight amounts of the components:
SIO2 TIO2 AL2O3 FEO MGO CAO NA2O K2O
for the bulk composition of interest:
48.32 36.33 1.67 6.09 0.02 0.98 0.81 4.41 1.24 0.13

Output a print file (Y/N)?
n

The print file output is not useful for unconstrained minimization calculations except: 1) if MEEMUM is used, in which case the print file echoes the console output; or 2) an explicit list of the phases considered in the calculation is desired. For constrained minimization the file will show a summary of the computed phase equilibria. Not really necessary, so discarded.

Next a summary of the valid make definitions is made. These definitions can be found in the hpo2ver.dat thermodynamic datafile.

Exclude pure and/or endmember phases (Y/N)?
y

The endmember phases are identified by abbreviated names, in general these abbreviations are defined in the header section of the thermodynamic data file. Phases which you do not need (eg. pyroxenes and olivine phases in a metapelitic system) you can exclude. This diminishes the calculation time for the model and creates less fields in your pseudosection.

Do you want to be prompted for phases (Y/N)?
y/n

If you type **y**. The program views every phase possible and it is your choice if you want it to be included or not. If you know which phases you want to exclude (e.g. fo and fa for olivine) you can say **n** and type the name abbreviations (according to the thermodynamic database) yourself.

Include solution phases (Y/N)?
y

By default all endmember phases and no solution phases (i.e., non-stoichiometric phases) are included in calculations. For example in a pelitic system you can include the plagioclase solid solutions, staurolite s.s, garnet s.s, mica s.s etc. All the possibilities are listed in the solution_model database.

In this file you can see all the possible solid solution models you can include in your system. But be careful: some models need particular changes in the thermodynamic database hp02ver.dat in order to work properly. This is all stated in the solid solution model description, so read it carefully if you choose to use this model.

Example
Choose the Gt(WPH) solid solution model out of the solution_model database. For this model to work properly, you have to include the *endmember names* spss, alm, py, gr, andr, fmn_i, fkho_i and kho_i. The names alm, py, gr and andr you can find in the hp02ver.dat database. The explanation of the other fmni_i, fkho_i and kho_i end members is explained below as dependent of others (e.g. fmn_i = 1 andr + 1 spss – 1 gr). If for example fmn_i was dependent of e.g. fo, you also had to include the fo end member in your model.

Enter solution model file name [default = solution_model.dat]:
solution_model.dat

Select phases from the following list, enter 1 per line, press <enter> to finish:

Bio(TCC)…GlTrTsMr

For details on these models see:
www.Perple_X.ethz.ch/Perple_X_solution_model_glossary.html or read the commentary in the solution model file.

select phases

Now you select the solid solution models you have chosen in the solution_model database.

Enter calculation title:
test_output

Running Vertex

Vertex is a phase diagram calculator. After you've build your model with BUILD you run the program to get your refined results. If the auto_refine option is on calculations are done in two stages: an initial low quality exploratory stage establishes the range of phase compositions; and a final high resolution auto-refine stage. These stages are executed in a single calculation, as done here, only if the value of the auto_refine keyword is auto. Before running VERTEX verify that the auto_refine keyword is set to auto in your copy of Perple_X_option.dat.

Enter the project name (the name assigned in BUILD) [default = my_project]:
test

This is the name you have given to your project in the first place. After this task the program starts calculating. If you have included a lot of solid solutions and end members this calculating can last quite long. Therefore, I advise to let extensional Perple_X calculations run overnight, hence you can use them the following day.

During this processing and auto-refining VERTEX may come up with several warnings as:

warning ver114 the following endmembers are missing for Bio(TCC): ffbi_i fbi

This warning can be solved by including these endmembers in your calculations hence delete them from your "exclude endmember" list in your test.dat file. If the endmember is not annotated in that file, it is a composition of several other endmembers. The meaning of these endmembers can be found in the hp02ver.dat or solution_model.dat file.

warning ver369 failed to converge at T= 673.00 K, P= 72105.3 bar Using Murnaghan EoS, probably for Ghiorso et al. MELTS/PMELTS endmember data. Volume estimated using 3rd order Taylor series.

that indicate unstable numerical behavior of specialized equations of state, most commonly these result because the calibration is being used beyond the range of physical conditions for which it was intended. In general, these warnings have no significant consequences, but if you

have doubts it is possible to eliminate the offending entity (e.g., here endmembers of the pMELTS(G) silicate melt model are causing problems at subsolidus temperatures and pressures far beyond the 4 GPa upper limit for the pMELTS calibration).

More details on the processing can be found on the Perple_X website via: http://www.Perple_X.ethz.ch/Perple_X_66_seismic_velocity.html scrolling down to the VERTEX part.

Finally VERTEX terminates as in the exploratory cycle with a summary of the phase compositions and writes a new auto-refine data file.

Running PSSECT

PSSECT generates PostScript (.ps) graphical output and can be used once the phase diagram section has been calculated with VERTEX. The default plot from PSSECT shows the computed phase relations in the annotated PT space in BUILD.

Enter the project name (the name assigned in BUILD) [default = my_project]:
test

This is basically everything you have to do for running the program. It creates a .ps file which can be viewed with programs like CorelDraw, Adobe Illustrator or Ghostview.

Modify the default plot (y/n)?
n

If you decide to adapt your original PT ranges chosen in BUILD you can do this here. Remember, the plot in BUILD is created for specific PT ranges. Extending these ranges here will bring a white surface since no data is present. Shrinking the area is although possible. Within the perlex_plot_option.dat you can modify the plotting process in PSSECT.

PSSECT finishes and the file can be viewed with above programs. You create plots like (FIGURE X)

Running WERAMI

WERAMI permits the user to extract information from a phase diagram section at a point (operational mode 1), throughout a region (mode 2), or along a line or curve (modes 3 and 4). In our case mode 2 is mostly used since we need to create a PT region diagram.

Enter the project name (the name assigned in BUILD) [default = my_project]:
test

Select operational mode:
1 - properties at specified conditions
2 - properties on a 2d grid
3 - properties along a 1d path
4 - as in 3, but input from file
0 - EXIT
2

Since we need to calculate a region, option 2 is chosen.

Select properties [enter 0 to finish]:
1 - Specific Enthalpy (J/m3)
…
6 - Weight (%) of a component
7 - Mode (Vol, Mol, or Wt proportion) of a phase
8 - Composition (Mol or Wt) of a solution
…
38 - Multiple property output (PHEMGP format)
8

Enter solution or compound name (left justified):
Gt(HP)

Here you enter one of your solid solutions have you included in the calculations in BUILD.

How many components in the numerator of the composition (<13)?
1

Here I chose to calculate the Xmn, Xca, Xmg fraction of garnet. This is done by inserting the composition of the solution (option 8), hence the amount of spessartine (Mn-rich), grossular (Ca-rich) and pyrope (Mg-rich). The formulae will be:

$$X_{mn} = \frac{MnO}{Mno + CaO + FeO + MgO} \quad X_{ca} = \frac{CaO}{Mno + CaO + FeO + MgO} \quad X_{mg} = \frac{MgO}{Mno + CaO + FeO + MgO}$$

Enter component indices and weighting factors for the numerator;
1- SiO2
2- Al2O3
3- TiO2
4- FeO
5- MnO
6- CaO
7- MgO
8- Na2O
9- K2O
10- H2O
6 1
Enter the components in the denominator of the composition (<12)?
Enter zero to use the numerator as a composition
4
Enter component indices and weighting factors for the numerator;
1- SiO2
2- Al2O3
3- TiO2
4- FeO
5- MnO

6- CaO
7- MgO
8- Na2O
9- K2O
10- H2O

4 1 5 1 6 1 7 1

Change it (y/n)?
n

If the calculation is correct you put **n**, otherwise you can start again and say **y.**

This composition will be designated: C1Gt(HP)

Select a property [enter 0 to finish]:
8
Since you need 3 fractions you select option 8 again to start the process over again. When you have calculated all three of the fractions you enter **0**.

Change default variable range (y/n)?
n

Enter number of nodes in the T(K) and P(bar) directions:
100 100

The more nodes in each direction, the more precise the plots will be. Fine plots will be created with nodes between the 50-400. If you have several calculations (e.g. 3 in this case) and you enter a high amount of nodes in each direction, the calculation time will increase significantly.

Output has been written to the 2d tab format file:
test_1.tab

2d tab format files can be processed with:

PSTABLE - a Perple_X plotting program
PERPLE_X_PLOT - a MATLAB plotting script
PYWERAMI - petrol.natur.cuni.cz/~ondro/pywerami:home
spread-sheet programs, e.g., EXCEL

for details on tab format refer to:
Perple_X.ethz.ch/faq/perple_x_tab_file_format.txt

Select operational mode:
1 - properties at specified conditions
2 - properties on a 2d grid
3 - properties along a 1d path
4 - as in 3, but input from file
0 - EXIT
0

WERAMI shuts itself down.

Graphical data which are created by WERAMI can best be viewed with the program PyWerami created by the Czech Ondrej Lexa. It can be downloaded for Windows and Mac from the following website: http://petrol.natur.cuni.cz/~ondro/pywerami:home. PyWerami makes contour and 3D plots which can be further modified with e.g. Adobe Illustrator. With PyWerami you can change the contour interval and zoom in and out from particular areas. Also 3D plots and black/white or colour views can be made.